"NON-METALLIC" COLD-CATHODE ELECTRON EMISSION FROM COMPOSITE METAL-INSULATOR MICROSTRUCTURES

Stevan Bajic, BSc

Doctor of Philosophy

THE UNIVERSITY OF ASTON IN BIRMINGHAM

April 1989

THE UNIVERSITY OF ASTON IN BIRMINGHAM

"NON-METALLIC" COLD-CATHODE ELECTRON EMISSION FROM COMPOSITE METAL-INSULATOR MICROSTRUCTURES

Stevan Bajic, BSc

A thesis submitted for the degree of Doctor of Philosophy

1989

SUMMARY

A detailed investigation has been undertaken into a field-induced electron emission (FIEE) mechanism that occurs at microscopically localised "sites" on uncoated, dielectric-coated and composite-coated metallic cathodes. An optical imaging technique has been used to observe and characterize the spatial and temporal behaviour of the populations of emission sites on these cathodes under various experimental conditions, e.g. pulsed-fields, gas environment etc. This study has shown that, for applied fields of $\leq 20 MVm^{-1}$, thin dielectric ($\leq 750Å$) and composite metal-insulator (MI) overlayers result in a dramatic increase in the total number of emission sites (typically $\geq 30cm^{-2}$), and hence emission current. The emission process has been further investigated by a complementary electron spectroscopy technique which has revealed that the localised emission sites on these cathodes display field-dependent spectral shifts and half-widths, i.e. indicative of a "non-metallic" emission mechanism. Details are also given of a comprehensive investigation into the effects of the residual gas environment on the FIEE process from uncoated Cu-cathodes. This latter study has revealed that the well-known Gas Conditioning process can be performed with a wide range of gas species (e.g. O_2, N_2 etc), and furthermore, the degree of conditioning is influenced by both a "Voltage" and "Temperature" effect. These experimental findings have been shown to be particularly important to the technology of high-voltage vacuum-insulation and cold-cathode electron sources. The FIEE mechanism has been interpreted in terms of a hot-electron process that is associated with "electroformed" conducting channels in MI, MIM and MIMI surface microstructures.

Key words: field electron emission, electron spectroscopy, cold-cathodes, high-voltage vacuum-insulation, gas conditioning, hot electrons.

DEDICATED TO MY MOTHER AND FATHER

ACKNOWLEDGEMENT

It is with great pleasure that I thank my Supervisor Dr R V Latham for his continual encouragement and guidance throughout the course of this work.

I would also like to express my gratitude to Dr N A Cade from the GEC-Hirst Research Centre, Wembley, UK, for many helpful discussions and suggestions on the LB-film studies.

Thanks are due to Messrs B A Lawrence and A M Abbot for affording invaluable technical assistance throughout the long periods spent in the laboratory.

I would like to thank the University of Aston for granting me a studentship and providing the appropriate research facilities.

The support given to this work by the SDIO/IST sponsored programme managed by the Space Power Institute, Auburn University, Alabama, USA is gratefully acknowledged.

Finally, my warmest thanks go to my family for their encouragement and longstanding financial support.

CONTENTS

LIST OF FIGURES

LIST OF TABLES

CHAPTER 1

INTRODUCTION

The term "field emission" is conventionally used when referring to the electron emission process that results from the application of an intense electric field to an atomically clean metal surface. This phenomenon has become a classic textbook subject in physics, and has been explained by Fowler and Nordheim [1] in terms of a quantum mechanical tunnelling effect. There are, however, alternative mechanisms by which electrons can be emitted from, for example, insulating and semiconducting materials. This thesis will be concerned with three types of study on the latter "non-metallic" process, which is now commonly referred to as "field-induced electron emission".

1.1 Electron Emission from High-Voltage Electrodes

Over the past two decades, a number of research groups have provided evidence to suggest that the prebreakdown currents that flow between vacuum-insulated high-voltage electrodes, at fields of ~10-30MVm^{-1}, stem from a "non-metallic" electron emission process that occurs at localised regions on the cathode surface. Previously, it had been assumed [2] that electrons were emitted from metallic microprotrusions, or whiskers, on the cathode, where the local field was enhanced to a value such that Fowler-Nordheim [1] quantum mechanical tunnelling into vacuum could occur, i.e. at fields of ~10^9Vm^{-1}. However, *in situ* SEM probe techniques [3] have now established that the emission is associated with anomolous, micron-sized particulate structures which are composed of both metallic and non-metallic materials. In order to explain the "non-metallic" characteristics of this emission process, a number of mechanisms have been proposed which rely on field-penetration in the insulating regions of the composite metal-insulator (MI) and metal-insulator-metal (MIM) surface microstructures. Most notable amongst these mechanisms have been the filamentary [4,5], dynamic [6,7], hot electron [8,9] and antenna [10] models, of which the hot electron model has been shown to provide the most satisfactory quantitative explanation

of the principle experimental findings. For a detailed account of the characteristics of this emission phenomenon, and a review of the above non-metallic emission models, the reader is referred to section 2.2 in the following chapter.

More recently, attempts have been made to simulate the MI and MIM emission regimes under controlled laboratory conditions, using resin-coated tungsten micropoints [11,12] and artificially-contaminated electrode surfaces [10,13,14]. These simulation studies, which have been shown to convincingly reproduce the "non-metallic" emission process that occurs naturally on HV electrodes, have continued to generate interest in this field, owing to the recognition of their importance to the technological application and fundamental understanding of the "non-metallic" emission process. In the technological context, it is widely recognised that there are a number of electron-beam systems (e.g. electron microscopes) which could benefit from the high-brightness characteristic of a field-emitting, or cold-cathode, electron source. To date, the commercial utilisation of these sources, in particular those based on non-metallic structures, has been limited, primarily owing to the lack of, or relatively rudimentary understanding of the fundamental processes involved in the emission mechanism. From a fundamental viewpoint, it is thus anticipated that the on-going studies into laboratory-fabricated composite microstructures will provide information on the details of the non-metallic emission process, and the factors by which it is influenced (e.g. material composition, and the residual gas environment etc). In fact, it is important to note that this latter objective has far-reaching implications on the operation of a wide range of HV devices and systems, whose performance is ultimately limited by the emission, or leakage, currents which result from the above process. Thus, it is hoped that an understanding of the emission mechanism will enable a technique to be developed which permanently suppresses, or ultimately eliminates, the prebreakdown electron emission from localised sites on HV electrodes.

1.2 Cold-Cathode Electron Sources

Although the majority of electron beam devices, e.g. electron microscopes, cathode ray tubes (CRTs) etc, still rely on electron emission from thermionic cathodes, it is widely accepted that there is a growing need for a new generation of cold-cathode electron sources, whose operating mechanism differs radically from that of the thermionic emitters. Thus, it is hoped that commercial cold-cathode electron sources can be developed that eliminate, or reduce the disadvantages associated with conventional thermionic cathodes, namely their high operating temperatures ($\geq$1000K), limited emission current density ($<100 Acm^{-2}$), long turn-on period, high power consumption, and limited life and stability.

In contrast, the ideal cathode can be characterized by the following factors: an operating mechanism which is insensitive to temperature fluctuations, a current density $>100 Acm^{-2}$, fast modulation of the emitted current, a narrow electron energy distribution, a long operating life, and insensitivity to medium and poor vacuum conditions. Although many of these features have been achieved with both metallic and non-metallic cold-cathode regimes, it is generally found that their performance is limited by inherent instabilities in the emission, and lack of reproducibility. On the other hand, commercial field-emitters in the form of tungsten microtips have been used, for example, in scanning electron microscopes. However, the stable operation of this type of cathode requires not only an ultra-high vacuum ($\leq 10^{-10}$mbar), but also the provision for an *in situ* cleaning, or "flashing" of the tip to remove surface contaminants.

Despite these drawbacks, recent advances in microfabrication techniques have renewed the interest in metallic micropoint cathodes, particularly in the form of planar multi-emitter arrays [15,16] for high-current applications. These emitters, which are commonly referred to as thin-film field emission cathodes (TFFECs), have been successfully incorporated into devices such as vacuum-fluorescent displays [17] and vacuum FETs [18]; in fact, this latter application is presently the subject of much attention, owing to the need for miniature, ultra-fast, radiation-hard devices for military

systems.

Whilst the past two decades have witnessed a growing increase in both the commercial interest and utilisation of metallic field-emitters, an extensive research effort has also been directed towards obtaining stable electron emission from more elaborate non-metallic structures that are compatible with solid-state circuitry, and are based on essentially planar extended-area geometries. Interest in these cathodes began with the discovery of the thin-film tunnel emitter [19] in 1960, which was promptly followed by an active decade of research into the so-called "formed" metal-insulator-metal (MIM) sandwich cathodes [20,21]. However, although these emitters theoretically offered a wide range of desirable emission features, including controllable hot electron energies, their full potential was never realised owing to problems encountered with the stability and reproducibility of the emission characteristics.

More recently, attention has focussed on a number of carbon-based cathodes [22,23], which exploit the ability of carbon to deliver copious emission currents, at low applied fields, via a "non-metallic" emission process. These studies followed from investigations into the emission properties of carbon-fibre micropoint emitters [22] which were found to be mechanically stable, or durable, during operation under the poor vacuum conditions typically encountered, for example, in electron microscopes, i.e. $\geq 10^{-8}$mbar; however, the emission current from these cathodes generally exhibited an unacceptable instability. In an attempt to stabilise the emission from carbon fibre cathodes, *in situ* thermal processing [24] and optically-controlled feedback [24] techniques have been used in prototype CRT tests. However, although these techniques have proved to be relatively successful, the inherent lack of emission stability with the carbon, and other non-metallic cathode regimes still remains a major obstacle in the search for an viable alternative to the conventional metallic field-emitter.

1.3 *In Situ* Electrode Preparation Techniques

The insulation of broad-area high voltage electrodes by vacuum is a vital technological consideration in both the design and operation of a wide range of devices and instruments, e.g. vacuum switches, RF resonance cavities, particle accelerators, and electron microscopes etc. In addition to the insulation requirements of these terrestrial devices, there is now a growing need for the improved insulation, and hence protection, of space-borne devices, in particular, space power systems. It is generally believed that, under ultra-high vacuum conditions (UHV), and with applied fields in the range 10-30MVm^{-1}, the initiation of a breakdown event is associated with the prebreakdown current [25] arising from the localised "non-metallic" electron emission processes described in section 1.1. Since these emission processes are now believed to result from particulate microstructures involving both metallic and non-metallic materials, attempts to minimise the incidence of particulate contamination on electrode surfaces have greatly improved the performance of, for example, RF resonance cavities [26]. However, these electrode preparation methods are costly and technically demanding.

For this reason, considerable interest still exists in two alternative approaches which are routinely employed in the preparation of commercial HV systems, namely (i) the *in situ* electrode conditioning techniques, and (ii) the dielectric-coating of electrode surfaces. Of the most commonly used conditioning procedures, e.g. gas [27-31], current [30,32], glow-discharge [33,34] and spark conditioning [35,36], gas conditioning has become widely recognised as the most effective technique for suppressing any residual electron emission processes, and hence breakdown events. Using this technique, improvements in the voltage hold-off capability of up to five times the unconditioned values have been reported for a range of electrode materials [29]. In addition to the *in situ* conditioning procedures, it is well known that the use of thin dielectric coatings can result in a substantial improvement in the electrical

insulation properties of a HV system. For example, work carried out at CERN [37,38] in the 1960's demonstrated that the use of anodised aluminium cathodes led to a doubling in the voltage performance of large electrostatic particle separators. However, although the above coating and conditioning techniques are routinely employed in the commisioning of HV electrode systems, it is generally recognised that their exact influence on the underlying electron emission process is not fully understood.

1.4 Research Programme

For all of these studies, a novel transparent-anode optical imaging technique has been used to investigate the field-induced electron emission phenomenon as it occurs on a range of extended-area cathodes. This technique, which enables real-time monitoring of the populations of constituent electron emission sites on a test cathode, has been used to study the influence of dielectric and composite metal-insulator (MI) coatings on the emission characteristics of planar metallic cathodes. The present study also includes a detailed investigation into the effect of the residual gas environment on the above process for both the coated and uncoated cathodes.

In chapter 4, an investigation is presented on the spatial and temporal behaviour of populations of emission sites, on uncoated Cu-cathodes, during a period of gas conditioning. In addition to characterizing the site behaviour during the well-known He-conditioning process, the present study has been extended to include the effects of a wide range of common gas species, and, in particular, the influence of the gap voltage and temperature on this process. In chapters 5 and 6, we investigate the field-induced electron emission phenomenon that results from coating planar metallic cathodes with composite MI layers and thin-film dielectrics respectively. Chapter 5 describes a series of experiments on the emission properties of a new type of composite-coated cathode, which is composed of a spun resin layer containing a random distribution of encapsulated conducting particles. The transparent-anode imaging technique has been used to characterize the emission from a range of

composite-cathode regimes under various operating conditions, e.g. poor-vacuum residual gas environments and pulsed-fields etc. This study also included a series of electron spectroscopy measurements on the emission process, and a feasibility study into the possibility of producing new-generation cold-cathode electron sources by this coating technique. Finally, in chapter 6, an investigation in presented on how thin dielectric Langmuir-Blodgett (LB) coatings of varying thicknesses (90-750Å) influence the emission characteristics of planar metallic cathodes. As in the preceding chapters, results will be given from a series of experiments on the spatial and temporal behaviour of the resulting emission phenomenon, and its dependence on factors such as the residual gas environment. Furthermore, this will include a complementary electron energy analysis of the emission process, which sheds further light on the conduction mechanism through multilayer structures.

CHAPTER 2

FIELD-INDUCED ELECTRON EMISSION

Although this thesis is primarily concerned with a field-induced electron emission phenomenon that occurs at composite metal-insulator (MI) microstructures, it is important to put the subject in context by first presenting a brief account of "classical" field emission from atomically clean metals. As will be shown, the "classical" field emission of electrons from metals, embodied by the Fowler-Nordheim theory [1], has proved to be inadequate in explaining the anomalous emission characteristics observed, for example, on commercial, extended-area HV electrodes. Nevertheless, the following review of the theoretical implications of the metallic emission process will enable the distinction to be made between the "metallic" and "non-metallic" processes. A review will also be given of the more recent "non-metallic" emission models which contend to provide a physical basis for interpreting the prebreakdown electron emission phenomenon from vacuum-insulated HV electrodes. In particular, this will include an introduction into the field-induced hot electron emission (FIHEE) mechanism which has been shown to successfully explain most of the fundamental experimental observations.

Finally, the latter part of this chapter is dedicated to a discussion of recent attempts to utilize the electron emission from "non-metallic" regimes in the form of cold-cathode electron sources. This topical section will also include a brief account of a number of recent non-conventional metallic cathodes which are presently the subject of considerable research and commercial interest, e.g. the multitip array emitters.

2.1 Field Electron Emission from Metals

2.1.1 Fowler-Nordheim Theory

The first attempt to explain field electron emission (FEE) from atomically clean metal surfaces was made by Schottky [39], who postulated that the effect was due to the complete reduction of the potential barrier at the metal surface resulting from a combination of the applied electric field and the electron image force. However, this

hypothesis was subsequently found to be inadequate to quantitatively explain the FEE phenomenon. Subsequently, in 1928, Fowler and Nordheim [1] formulated a quantum mechanical model in which electrons tunnel through the Schottky-modified surface potential barrier, which results from the application of a high external electric field at the metal surface. This theory, which provides a satisfactory quantitative interpretation of the emission phenomenon, will be outlined below: for a more comprehensive treatment, the reader is referred to the original paper [1], or the more recent modern reviews by Good and Muller [40] and Van Oostrom [41].

A schematic representation of the Fowler-Nordheim (F-N) model of field emission is given in figure 2.1. In essence, the theory assumes that as the applied electric field at the surface of the metal increases, the potential barrier width encountered by electrons at the Fermi level (FL) becomes so thin that unexcited electrons can directly tunnel through the barrier, at constant energy, into the vacuum. In quantum mechanical terms, this situation is governed by the Heisenberg Uncertainty Principle, and corresponds to a situation where the barrier width becomes comparable to the de Broglie wavelength of the electrons near the Fermi level. For atomically clean metals, tunneling occurs at a surface field of $\geq 3 \times 10^9 Vm^{-1}$, where the barrier width at the Fermi level is $\leq 10Å$.

In order to obtain a quantitative relation for the emitted current density, J, in terms of the applied electric field, F, it is first necessary to apply Fermi-Dirac statistics to calculate the electron supply function $N(W_x)dW_x$, i.e. the flux of electrons arriving at the surface that have normal energy components between W_x and W_x+dW_x. Secondly, it is then necessary to solve the Schrodinger equation using the WKB approximation [42] to obtain the electron transmission coefficient $D(W_x)$, which represents the probability that an electron of energy W_x will be transmitted through the barrier. Thus, the number of electrons with energies in the range W_x and W_x+dW_x tunneling through the surface potential barrier is given by the normal energy distribution $P(W_x)dW_x$, where

$$P(W_x)dW_x = N(W_x)D(W_x)dW_x \qquad (2.1)$$

Figure 2.1 A schematic representation of the metallic field emission process. (From [62]).

Figure 2.2 A comparison of the theoretical Normal and Total energy distributions of field emitted electrons with the experimentally obtained distribution. (From [48]). E_F - Fermi level

Figure 2.3 A schematic representation of field electron emission via a surface resonance state, E_S, which lies close to the metal Fermi level, E_F. (From [53]).

Finally, the total emission current density is obtained by summing over all possible electron energies, i.e.

$$J = e\int_{\text{all E}} N(W_x)D(W_x)dW_x \qquad (2.2)$$

This quantum mechanical formulation then gives rise to the most useful form of the F-N equation, viz.

$$J = 1.54\text{x}10^{-6} \quad \frac{10^{4.54}\phi^{-1/2}}{\phi} \quad F^2 \exp\left[\frac{-6.53\text{x}10^9\phi^{3/2}}{F}\right] \qquad (2.3)$$

where ϕ is the emitter work function in eV. This equation has been experimentally verified, for example, by Haefer [43] and Dyke [44], by measuring the field emission from metallic microtips of accurately known geometries, and hence surface field, over a current range of up to eight orders of magnitude. However, for current densities $\geq 10^6 Acm^{-2}$, J is found to deviate from F-N theory due to the build up of space charge which progressively reduces the field on the emitter surface, and hence the emitted current.

In most practical emission regimes, e.g. micropoint cathodes or "natural" microprotrusion on a planar electrode surface, the field is locally enhanced by a factor

$$\beta = F_{mic}/F_{mac} \qquad (2.4)$$

where F_{mic} is the locally enhanced microscopic field, and F_{mac} is the macroscopic gap field. Thus, since $F_{mac}=V/D$ for a plane parallel electrode geometry, where V is the applied gap voltage and D the electrode gap spacing, one has

$$F_{mic} = \beta V/D \qquad (2.5)$$

Hence, the resulting emission current, I, will be given by substituting this expression, and the local emitting area A_e, into equation 2.3 to give

$$I = 1.54\text{x}10^{-6} \quad \frac{10^{4.54}\phi^{-1/2}}{\phi} \quad \frac{A_e\beta^2V^2}{D^2} \quad \exp\left[\frac{-6.53\text{x}10^9\phi^{3/2}D}{\beta V}\right] \qquad (2.6)$$

Equation 2.6 therefore implies that if the current-voltage (I-V) characteristic of a gap is plotted as $\ln(I/V^2)$ versus $1/V$, known as a F-N plot, a straight line will be obtained with slope

$$m = -6.53 \times 10^9 \phi^{3/2} (D/\beta) \qquad (2.7)$$

and intercept

$$c = \ln \left[1.54 \times 10^{-6} \frac{(10^{4.54\phi^{-1/2}})}{\phi} \frac{A_e \beta^2}{D^2} \right] \qquad (2.8)$$

Therefore, since D is known, and ϕ is tabulated for different metals, the slope of the F-N plot enables the field enhancement factor, i.e. the β-factor of the emitter to be calculated. This may then be substituted into equation 2.8 to determine the emitting area A_e.

2.1.2 Total Energy Distribution of Electrons Field Emitted from Clean Metals

Early studies [45,46] of the energy distribution of electrons field emitted from metals showed, in agreement with F-N theory, that the electrons emerged from just below the Fermi level (FL) of the metal. Subsequently, using an improved high-resolution retarding potential analyser, Young and Muller [47] obtained a much narrower energy distribution than that originally predicted from F-N theory. However, as stated in the previous section, the derivation of the F-N equation only considers the normal electron energy component at the surface, and consequently, gives rise to the so-called Normal Energy Distribution of emitted electrons. This energy distribution would be correct for the case of a perfectly plane emitter, however, for a micropoint, or spherical geometry, the transverse component of energy, conserved in the tunneling process, is transferred to the normal direction once the electron has left the surface. Therefore, by introducing the total electron energy into a modified supply function, Young [48] obtained an expression for the Total Energy Distribution P(E)dE, viz.

$$P(E)dE = \frac{4\pi md}{h^3} \exp(-C) \frac{\exp(E-E_f/d)}{1+\exp(E-E_f/kT)} dE \qquad (2.9)$$

where

$$C = \frac{4e^{1/2}(2m\phi^3)^{1/2}}{3\hbar F} v(y) \qquad (2.10)$$

and

$$d = \frac{\hbar e^{1/2}F}{2(2m\phi)^{1/2}} \frac{1}{t(y)} \qquad (2.11)$$

where $E_f=-\phi$, and v(y) and t(y) are tabulated dimensionless elliptic functions [40,41] from the solution to the F-N equation. Figure 2.2 shows both the Normal and Total Energy Distributions in comparison to the distribution obtained experimentally by Young [48].

2.1.3 Field Emission Through Adsorbates: Resonance Tunnelling

It is well known from experimental observations [49] that the adsorption of a monolayer of adatoms or molecules onto a clean metallic emitter results in a deviation from Fowler-Nordheim emission theory. For an adsorbate on a surface, one would expect the surface work function to change due to the dipole moments associated with the adatoms; however, this hypothesis is found to be inadequate in explaining the experimental data. For example, Ermrich [50] studied the influence of adsorbed N (which has an excited state 1eV below the Fermi level) on the [100] plane of tungsten and, from FEE measurements, observed a slight increase in the effective work function in conjunction with an increase in the emitted current of up to four orders of magnitude; i.e. in contradiction to the F-N tunnelling theory.

Since the field emission of electrons from metals is strongly dependent on the detailed shape of the surface potential barrier, in particular the effective barrier thickness, it is necessary to consider the changes to the surface barrier resulting from the adatom's attractive potential well. This approach was adopted by Duke and Alferieff [51] in their developement of a quantum mechanical resonant tunnelling model

of field emission through adsorbates. This is illustrated in Figure 2.3 for the case of a square adatom attractive potential well with a virtual energy state close to the metal Fermi level (E_f). By applying double barrier potential theory [52], it was shown that the electron transmission probability, and hence barrier penetration, is enhanced if a tunnelling electron arrives from the metal with an energy approximately equal to a bound state of the adatom; i.e. an electron can then tunnel directly through the total barrier, or alternatively, go via the resonant atomic state which is favoured because of the reduction in the total barrier thickness at each stage. Consequently, the emitted electron energy distribution will then display fine structure peaks associated with electrons emitted from adatom energy levels, as illustrated in Figure 2.3.

The contribution to the total emitted current density associated with adsorbate resonance tunnelling has been obtained for various adatoms and surfaces [49] from measurements of the total energy distribution of emitted electrons before and after adsorption. The data from such experiments is typically presented in terms of the enhanced resonance factor, $\mathfrak{R}(E)$, defined as

$$\mathfrak{R}(E) = j(E) / j_m(E) \qquad (2.12)$$

where $j(E)$ and $j_m(E)$ are, respectively, the measured energy distributions with and without surface adatoms. Thus, Figure 2.4 shows the experimentally determined variation in the resonance factor, $\mathfrak{R}(E)$, for the adsorption of Ba and Ca on W[013], where the peaks in the spectra indicate the positions of the resonance centres (E_s in Figure 2.3) with respect to the Fermi level (ε=0).

The resonance tunnelling model of Duke and Alferieff [51] also predicts that electron emission through adsorbates is maximised if the adatom potential well lies in the centre of the tunnel barrier. However, in the case of emission from clean metal surfaces, the tunnel barrier width is typically a few nanometres, whilst the centre of a typical adatom would be, say, 0.2nm from the metal surface, i.e. far from its optimum enhancing position. This therefore accounts for the relatively low values of $\mathfrak{R}(E)$ in figure 2.4. A more detailed account of electron emission through suface adatoms and molecules is given by Modinos [53].

Figure 2.4 Experimental resonance factor, $\mathfrak{R}$, for Ba and Ca on W[013]. (From [53]).

Figure 2.5 An SEM micrograph of a located emission site on a HV electrode. (From [60]).

Figure 2.6 Schematic representations of (a) the initial switch-on I-V characteristic of a virgin cathode, and (b) the F-N plot of the final reversible state. (From [57]).

2.2 Field-Induced Electron Emission from Composite MI Structures

Over the past decade or so, a wealth of experimental evidence has been published which strongly opposes the previously accepted assumption that the localised electron emission from broad-area electrodes, in the applied field range 10-30MVm^{-1}, derives from a Fowler-Nordheim type of field emission process at metallic surface asperities, or whiskers, where the local field is enhanced by over two orders of magnitude. Rather, it is now more generally accepted that this localised emission phenomenon stems from some complex "non-metallic" mechanism. Supportive evidence for this latter hypothesis, and conversely, objections to the former interpretation, are well documented and have been critically reviewed, for example, by Latham [3] and Noer [54]. Therefore, for the purpose of this thesis, the following section will give only a brief account of the major experimental findings which have prompted the most recent models of non-metallic field-induced electron emission from high-voltage (HV) electrodes.

2.2.1 Experimental Evidence in Favour of a Non-Metallic Emission Regime

In order to attribute the electron emission that occurs on HV vacuum-insulated electrodes (for applied fields of typically 10-30MVm^{-1}) with metallic microprotrusions, it was necessary, from typical F-N measurements on these sites, to postulate a geometric field enhancement factor (β) of typically 100-1000, and an emitting area (A_e) of typically 10^{-12}-10^{-8}cm^{-2}. However, at the time of this interpretation, conflicting evidence was frequently appearing which deviated from Fowler-Nordheim metallic emission behaviour: this included for example, non-linear and variable F-N plots [55,56], a characteristic switch-on of emission sites [57], site instability, and current-voltage (I-V) characteristics which displayed an irreversible hysteresis behaviour [55].

Although these early findings were often variable and somewhat inconclusive, they provided the inspiration for a number of groups, notably those of Cox [58], Hurley [59] and Latham [60], to develop new *in-situ* analytical techniques for studying the discrete localised regions on an electrode surface which gave rise to electron emission. However, it was Cox and co-workers [58] who provided the first direct evidence of the physical nature of emission sites. This group used a system involving a planar scanning anode, incorporating a 10μm diameter probe-hole mounted on-axis in a scanning electron microscope (SEM), which enabled both the detection and SEM imaging of a surface region which was known to contain an emission site. Using this technique, these authors consistently failed to detect any metallic microprotrusions with the necessary field enhancing geometries to support a metallic field emission process; on the contrary, an emitting region was commonly found to contain microscopic insulating structures, possibly surface oxide conglomerates, which were often located at surface cracks, or grain boundaries. In addition to these findings, Cox [55] was able to identify the existence of two main types of emission site which, significantly, was later confirmed by Hurley [56] who termed them "a" and "b" sites. Thus, the more common "a" sites generally gave linear F-N plots and initiated breakdown for currents >50μA, and subsequent site destruction. On the other hand, "b" sites were found to exhibit a characteristic current-controlled negative resistance behaviour, and were also observed to breakdown randomly but at the lower currents >10μA, without site destruction.

In a similar study on the identification of possible emitting microstructures, Athwal and Latham [60] used a micropoint anode-probe technique to reveal emitting microstructures in an SEM with an improved resolution of 2-3μm. A typical result obtained by this technique is shown in Figure 2.5, where it is demonstrated how an emission site is invariably associated with an anomalous micron-sized adhering "dust" particle, or surface inclusion, which appears "bright" in the micrograph. This bright appearance was assumed to imply that the emitting microstructure was either an insulating particle, or conversely, a conducting particle that is insulated from the metallic substrate: in fact, *in situ* X-ray analysis measurements have revealed that these

microstructures often contain elements such as C [61,62], S [61,62], and Ag [63].

Another important finding to emerge from the work of Athwal and Latham [57] was the identification of a "switch-on" process for emission sites on a virgin electrode. Thus, although most sites were subsequently found to exhibit a linear F-N behaviour following such a characteristic switch-on event, this behaviour could not be reconciled with the traditional F-N field emission theory. This is illustrated schematically in Figure 2.6(a), where it is shown that as the applied field is increased to approaching $10MVm^{-1}$, a sudden, and irreversible switch-on process occurs in which the electrode gap current "jumps" from effectively zero, to a value which, in practice, can typically vary from 10^{-9} to $10^{-6}A$. This then results in a relatively stable and reversible emission mode; however, as the applied field is further increased, subsequent switch-on processes may occur, which, as can be demonstrated, correspond to the formation of new sites. Figure 2.6(b) shows that the final emission mode generally gives a linear F-N plot for applied fields $<20MVm^{-1}$, where the characteristic β-factor typically ranges from around 200-500.

Prior to Hurley's confirmation of the existence of two types of emission sites, Hurley and Dooley [64,65] had already established that spots of light, or k-spots, could be observed on the electrode surface when electron emission was in progress; this same phenomenon was also previously noted by Klyarfell and Pokrovskya-Soboleva [66]. Hurley and Dooley [64] obtained spectra of the light emitted from k-spots on broad area electrodes by using an image intensifier in conjunction with a photomultiplier and a series of optical filters. The spectrum typically obtained, which is shown in Figure 2.7, could not be interpreted in terms of black body or discharge radiation, but instead, was believed to be associated with an electronic process, such as electroluminescence, which can occur in insulating and semiconducting materials. In conformation of this hypothesis, measurements of the light output intensity versus $V^{-1/2}$, where V is the applied voltage, yielded a straight line, which is in agreement with the characteristic Alfrey-Taylor law of electroluminescence [67]. Furthermore, Hurley [59] obtained experimental evidence to confirm that electron emission sites and k-spots were directly related, and was thus able to assume from spectral measurements, that the emission

Figure 2.7 The spectrum of light emitted from a typical k-spot on a HV electrode. (From [64]).

Figure 2.8 Electron energy spectra obtained from (a) a reference tungsten micropoint emitter, and (b) an emission site on a broad-area electrode. E_F - Fermi level. (From [73]).

Figure 2.9 The field dependence of the spectral shift, S, and the half-width, f, of a typical sub-site on a Cu-electrode. (From [9]).

stemmed from a semiconductor-like material with a band gap of ~2 to 3eV: in fact, Hurley [68] measured the optical k-spot spectra for a range of cathode materials, and obtained evidence to suggest that the spectra, and hence electron emission, were related to the electronic properties of the ambient oxide film on the cathode. However, it is important to note that recent measurements by Latham and Fielding [69] consistently failed to detect any electroluminescence at emission sites. These authors have suggested that the earlier reports of light emission may, in fact, have been due to an X-ray fluorescence phenomenon associated with field emitted electrons impinging onto the nearby anode.

More recently, Latham and co-workers have developed a high resolution hemispherical electron spectrometer facility to study the fundamental emission processes as they occur naturally on broad-area electrodes; the details of the design and operation of this facility have been given elsewhere [70-72]. The spectroscopic studies reported by Allen and Latham [73], Athwal and Latham [74], and Bayliss and Latham [75] provided the most convincing and comprehensive evidence to suggest that a non-metallic emission mechanism was operating at anomalous surface microstructures. In an early application of this technique, Allen and Latham [73] were able to compare the energy distributions of electrons emitted from a clean tungsten micropoint and a "natural" site on a HV electrode; this result is reproduced in Figure 2.8. Thus, whilst the metallic emission spectra shown in Figure 2.8(a) appears as predicted in section 2.1.2, the "natural" site spectra differs considerably in that, (a) all electrons are emitted from states below the substrate Fermi level, (b) the half-width (FWHM) is significantly broader than for the metallic spectrum, and (c) the spectrum is considerably more symmetrical. Furthermore, the spectra from natural sites were often found to be multipeaked. In a follow up to this study, Athwal and Latham [74] found that the spectral shift, S, and the half-width, f, of natural broad area sites were both strongly dependent on the applied field, such as shown in Figure 2.9.

In more recent experiments, Bayliss and Latham [75] showed, in agreement with the earlier findings of Cox [58], that an emission site is often composed of several

discrete emission centres, termed sub-sites. An electron optical image of a typical emission site, obtained by Bayliss and Latham [75], is shown in Figure 2.10. Using this technique, with its improved input lens assembly, it was shown that each sub-site gave a unique single-peak energy spectrum with a characteristic field dependence: furthermore, this result was assumed to justify the observation of multipeaked emission spectra, which were obtained in earlier studies [63] where the site imaging capabilites were limited.

In conclusion, it can be stated that the findings of these electron spectroscopy studies, and the aforementioned earlier studies, have collectively provided strong evidence against a simple metallic microprotrusion field emission model, whilst yielding important information concerning the electronic processes involved in the emission phenomenon. The remainder of this section will be devoted to a brief review of the most recent models of non-metallic field-induced electron emission which have been proposed in an attempt to explain the experimental observations.

2.2.2 The Filamentary Model

In an attempt to provide a qualitative explanation of his cathode electroluminescence observations, Hurley [59] proposed the filamentary model of electron emission, based on the well-known Ovshinsky "switching" phenomenon [76] that occurs in thin film metal-insulator/semiconductor-metal (MIM) devices. This type of switching behaviour, as discussed by Dearnaley et al [77] and Adler et al [78], is observed particularly in metal oxides, nitrides, flourides and semiconducting glasses of nanometre to micrometre thicknesses, when a high field of typically 10-100MVm^{-1} is applied via the metal electrodes. As a consequence, the device changes from a non-conducting "off" state to a conducting "on" state, where the sample resistance may change by a factor of up to 10^8. The conducting "on" state was believed to be associated with the formation of conducting "filaments" or "channels" within the insulating/semiconducting matrix, which, in turn, were then responsible for the observed phenomena such as microscopically localised electroluminescence and

Figure 2.10 The emission image of a single site, showing how a site is typically composed of a number of sub-sites. (From [75]).

Figure 2.11 The simultaneous production of electroluminescence and electron emission from an electroformed conducting filament in an oxide impurity. (From [5]).

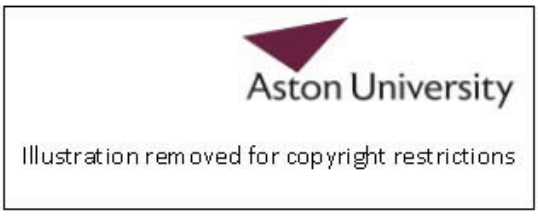

Figure 2.12 A schematic representation of the metal-insulator (MI) emission regime showing how conducting channels are formed in an insulating microinclusion. (From [9]).

electron emission [59,68]. Furthermore, if the field was applied for a sufficient length of time (i.e. ≥1ms), the conducting filament became "electroformed" through the dielectric, corresponding to a permanent or semi-permanent rearrangement of atoms or molecules within the filament region (see Dearnaley [79]).

In the context of a high voltage electrode assembley, Hurley assumed that this same process could occur at isolated points in the ambient oxide film on the cathode at applied fields of $\geq 10 MVm^{-1}$. Under these circumstances, the resulting "electroformed" conducting filaments would then provide the necessary local field enhancement at the dielectric/vacuum interface for conventional Fowler-Nordheim field emission of electrons to occur, i.e as illustrated schematically in Figure 2.11. In comparison with the Dearnaley [79] filamentary model, Hurley [59] assumed that "hot" electrons, produced by acceleration across high resistance sections of a filament, would subsequently be scattered from such regions into the surrounding oxide, and could thus give rise to electroluminescence via impact ionisation, or recombination processes, as described by Hickmott [80]. Furthermore, it was assumed that junction effects at the metal/oxide interface could account for the behaviour of the so-called "b" sites [56], i.e. those which were found to display a region of negative resistance in their current-voltage (I-V) characteristic.

2.2.3 The Dynamic Field Emission Model

This model was recently published by Halbritter [81], and proposes that electron emission from broad-area electrodes is associated with the presence of low-density hydrocarbon surface impurities. It is assumed that there exists a continuous population of filled electron traps within the impurity band gap, and that, for an applied field of $F \sim 10^7 Vm^{-1}$, electrons will be stochastically emitted from these traps. These electrons, which are susequently heated to an excess energy of $E_{kin} = e\Delta x F \geq \Delta E$, produce excited atomic states within the impurity which relax by the emission of electrons, photons, and atoms (i.e. gas desorption). Furthermore, this process generates a positive charge distribution which locally enhances the field by a factor

$\beta>1$, such that $F^*=\beta F$, which, in turn, leads to an enhanced tunnelling current from the metal and interband traps. Successive impact ionisation events then rapidly establish a localised electron avalanche, i.e. the formation of a high conductivity channel, which generates the hot electrons for the emission process; in fact, this localised avalanching effect is known to occur non-destructively in, for example, SiO_2 [82] at fields of $\sim 10^8 Vm^{-1}$. However, only the high energy electrons are able to penetrate the surface barrier due to the increased positive charge density : the other electrons, which loose energy through inelastic collisions, eventually neutralise the positive charge, which terminates the emission process. This therefore leads to a pulsed electron emission phenomenon under dc field conditions, where the time constant is estimated by Halbritter [81] to be of the order of a nanosecond for 100Å-sized impurities.

In order to satisfy the conditions for avalanching, the mean-free-path of electrons, λ_e, in the impurity must be comparatively large; accordingly, Halbritter assumes that this process could occur in low-density irregular hydrocarbons where λ_e can be as large as 200Å. However, recent experiments by Niedermann et al [61] have shown that most emitting particles appear to be free from significant hydrocarbon concentrations, and furthermore, there is no experimental evidence to date which confirms the major conclusions of the model, viz. that the emission can be externally triggered by photons, and that electrons are emitted via a pulsed mechanism for dc fields.

2.2.4 The Hot Electron Model

This model has been progressively developed by Latham and co-workers [9,71,83,84] in an attempt to explain the "non-metallic" electron emission characteristics (described in section 2.2.1) of localised sites on broad-area HV electrodes. It is based on a similar idea to that proposed for the switching phenomenon observed in chalcogenide MIM devices [76-79], in which it is assumed that "conducting" channels, or filaments, are created within a dielectric medium under the

influence of an applied field. Although this section will deal with the case of hot electron emission from metal-insulator (MI) microstructures, it will be shown in section 2.2.5 how a similar process is believed to occur with MIM microstructures.

The assumed structure of an emission site is shown schematically in Figure 2.12, where it is seen to consist of some "foreign" dielectric-like inclusion in the surface of a metallic electrode. It is further assumed that the inclusion has dimensions of ~0.1-1μm in the direction of the applied field, F, such that for gap fields of 10-20MVm^{-1}, it can support a voltage drop of ~2-3 volts, i.e. comparable to the electron affinity of the dielectric. This latter assumption is supported by the micropoint anode-probe evidence, described in section 2.2.1, which suggests that naturally occurring emitting particles are typically of these dimensions.

(i) The Switch-on Mechanism

As discussed by Halbritter [85], it is assumed that the surface microinclusion will be only partly crystalline and impure, such that it contains a distribution of both trapping states and donor centres. A further requirement of this model is that, under low field conditions, the metal-insulator (MI) interface forms a blocking contact [86], otherwise electrons would be free to flow from the substrate, thereby charging the insulator and so screening the metal substrate from the applied field. In addition, it may be assumed that there will be microscopic locations at the MI interface where there exists a favourable tunnelling contact, such as could be created by local impurity atoms providing the necessary donor centres to produce marked band bending. Under zero field conditions, the energy band diagram of this localised region will appear as shown in Figure 2.13(a).

When the external field is first applied, it is anticipated that most of the potential drop across the insulator will occur at the contact since this region has a lower electron density than the bulk. As the external field is progressively increased, the situation shown in Figure 2.13(b) will arise, i.e. where the conduction band edge is lowered to the Fermi level (Fl), so that electrons can tunnel from the substrate in the

Figure 2.13 A sequence of band diagrams illustrating the switch-on process of the hot electron model. (From [9]).

Figure 2.14 The field and potential distribution associated with an emitting channel. (From [9]).

conduction band of the insulator. With increasing field, these electrons will eventually fill all the electron traps which exist just below the conduction band edge throughout the thickness of the insulator. Further increments in the field will result in more electrons tunnelling from the metal, but because the bulk traps are now full, these electrons will fill the surface states at the insulator-vacuum (IV) interface. This latter effect, depicted in Figure 2.13(c), results in an effective screening of the external field which, in turn, raises the conduction band edge, thus preventing further tunnelling from the substrate. Because of this screening effect, it will now require several increments in the external field before the band structure approaches the situation shown in Figure 2.13(d), when electrons can again tunnel from the metal. These electrons will experience a relatively high field as they are swept towards the IV interface, where, through scattering processes, they will raise the effective temperature, T_e, of electrons stored near the insulator surface. Hence, if the concentration of electrons in this "bunch" is high enough, there will be sufficient energy to raise T_e to the threshold required for initiating thermionic emission over the reduced Schottky barrier.

For continuous electron emission by this process, it is necessary for the system to experience a transition. Thus, as the electrons at the vacuum surface are preferentially emitted, the surface field will be greatly enhanced relative to the bulk field, which will result in a further lowering of the surface barrier and an increase in the electron temperature; it follows that both of these effects will tend to push the system towards a highly conducting state. As discussed by Mott [87] in his double-injection model, it is then assumed that the dynamic charge distribution existing within the channel will rapidly achieve dynamic equilibrium. This will then adjust itself to give the highest density a short distance into the insulator, thus stabilising the IV interface field at a high value as illustrated in Figure 2.13(e), which represents the emitting "on" state of an emission site. In fact, the "knee" in the conduction band edge must be quite close to the IV interface, probably a few times the hot electron mean-free-path (~500Å), otherwise the relaxation of hot electrons in this high-field surface region would prevent emission over the surface barrier.

The essential feature of this switch-on mechanism is that it does not require a

permanent structural change of the insulator in the channel region; rather, the channel is essentially "memorised" by the charge distribution. It therefore follows that, if the applied field is reduced to zero for short time, and then re-applied, it is unlikely that a similar switch-on process will be observed; i.e. as is typically found for the emission sites on broad-area HV electrodes [57].

The field distribution associated with the emitting "on" state of a conducting channel is shown in Figure 2.14. In this figure, the field enhancement factor, β_1, refers to the ratio of the vacuum field immediately above the filament tip, F_{tip}, to the macroscopic electrode gap field, F_o. Similarly β_2 is the ratio of the average field within the filament, F_{fil}, to the insulator field well away from the channel, F_{ins}. Thus, since $F_{ins}=F_o/\varepsilon_r$, where ε_r is the relative permitivitty of the insulator, it can be shown that

$$F_{tip}/F_{fil} = \varepsilon_r (\beta_1/\beta_2) \qquad (2.13)$$

where $\beta_1 \geq \beta_2$.

(ii) The Emission Current Density

To aid the discussion, a more detailed band diagram of the emitting "on" state of a conducting channel is given in Figure 2.15. If now the same asumptions are made as above, i.e. that the electronic properties of the high-field surface region are quasi-metallic, the emission current density will be given by the Murphy and Good [88] expression for the case of high-field thermionic emission, i.e.

$$J = \frac{4\pi me}{h^3} \frac{\pi/N}{\sin(\pi/N)} k^2T_e^2 \exp\left[\frac{-(\phi-b(F/a_1)^{1/2})}{kT_e}\right] \qquad (2.14)$$

where

$$N = \frac{kT_e}{b}\left[\frac{F}{a_1}\right]^{-3/4} \qquad (2.15)$$

Figure 2.15 A detailed band diagram representation of the on-state of an emitting channel. Fl - Fermi level, vb - valence band, cb - conduction band. (From [9]).

Figure 2.16 The current-voltage characteristic of a typical sub-site showing the transition from contact- to bulk-limited behaviour. (From [9]).

Here, N is a factor determining the shape of the energy spectrum, and typically has values of $N \leq 1.6$ [9]. Since the hot electron model critically depends on the injection and transport of electrons to the IV surface region, it follows that the emission current density will be influenced by the electronic properties of both the MI contact junction and the bulk of the insulator. When a channel is switched-on, the current density, J_T, tunnelling through the MI contact junction will be given by [89-91]

$$J_T = \frac{5.56\times10^{-14}}{\varepsilon^*\phi_o} N_D (V_C+P_M-P_I) \exp\left[-3.6\times10^{13}\left(\frac{\phi_o 3\varepsilon^*}{N_D (V_C+\phi_M-\phi_I)}\right)^{1/2}\right] \quad (2.16)$$

where ϕ_o is the contact barrier height, ε^* the high-frequency dielectric constant of the insulator, N_D the donor density and V_C the contact voltage drop due to the applied field. This equation predicts a sharply rising current with applied voltage (i.e. a rapidly falling contact resistance) that is essentially independent of temperature. In the bulk region, the low-field current density will be given by [89-91]

$$J_o = e\mu \frac{V_b}{d} N_c \left(\frac{N_D}{N_T}\right)^{1/2} \exp\left[-\left(\frac{E_D+E_T}{2kT_e}\right)\right] \quad (2.17)$$

where N_c is the effective density of states on the insulator, N_D and N_T are the donor and trap densities respectively, μ the electron mobility and V_b the bulk potential drop due to the applied field. This equation applies if $E_T >$ Fermi level $> E_D$, where all these levels are just below the conduction band edge, and nearly all the electron traps are filled. However, for high fields, where the Poole-Frenkel effect [92] operates (i.e. field-assisted thermal ionisation of donors and traps), the bulk conductivity becomes field dependent, and is of the form

$$J = J_o \exp\left[\frac{e}{kT_e}\left(\frac{eV_b}{\pi\varepsilon\varepsilon_o d}\right)^{1/2}\right] \quad (2.18)$$

It may now be noted that a contaminated insulator (i.e. containing donor centres) is required not only to produce a thin MI depletion region, but also to give the bulk a finite

conductivity.

If the insulator contains a high donor density ($N_D > 10^{24} m^{-3}$) and a high trap density ($N_T > 10^{25} m^{-3}$), the contact depletion region will be very thin, and the bulk conductivity will be low (see equation 2.17). As discussed by Simmons [89-91], it is then possible for a contact-limited to bulk-limited transition to occur, where the Poole-Frenkel [92] conduction process becomes dominant. In this case, it is usual to illustrate this behaviour by plotting ln I versus $V^{1/2}$, which usually enables the contact- and bulk-limited regions to be clearly identified. Thus, referring to Figure 2.16, which shows a typical example of the current-voltage data obtained from spectral measurements on a single emission site on a HV electrode [9], it will be seen that there is strong evidence to suggest that a contact-bulk-limited transition occurs with the hot electron emission process.

(iii) The Energy Distribution of the Emitted Electrons

In this section, we will briefly consider the energy distributions of electrons emitted via the above hot electron emission mechanism. Referring to the band diagram of Figure 2.15, it will be seen that the total drop in energy, S^*, from the metal Fermi level (Fl) to the insulator Fermi level will be given by the sum of the potential drops, V_c and V_b, in the contact and bulk regions of the insulator respectively; i.e.

$$V_c + V_b = S^* = S + \phi_I - \chi \qquad (2.19)$$

where S is the measured spectral shift. The energy distribution of electrons emitted via a high-field thermionic process has been considered in some detail by Murphy and Good [88], although the analysis of these authors was in terms of the normal energy distribution P(W) (defined in section 2.1.1). In the hot electron model, Bayliss and Latham [9] were able to calculate the total energy distribution of emitted electrons for the present regime in terms of the original Murphy and Good analysis. This derivation, which is beyond the scope of this section, has yielded the following expressions for the

spectral shift, S, and the spectral half-width (FWHM), f :

$$S = AkT_e - b(F/a_1)^{1/2} \qquad (2.20)$$

and

$$f = \frac{kT_e\,(2.3\pi kT_e - 1.3b(F/a_1)^{3/4})}{\pi kT_e - b(F/a_1)^{3/4}} \qquad (2.21)$$

where a_1 and b are constants given in [9] as $a_1=5.15\times10^{11}Vm^{-1}$ and b=27.2eV. These equations, which predict increasing energy shifts and half-widths with increasing applied field, have been shown to be in agreement with the spectral data obtained from sites on broad-area electrodes, i.e. such as shown in Figure 2.9.

2.2.5 FIEE from Artificial Sites: the MIM Emission Model

The first investigation into the field-induced electron emission (FIEE) arising from intentionally deposited carbon particles on broad area electrodes was due to Athwal et al [10]. In this study, techniques were developed for depositing graphite particles at specific locations on broad-area electrodes, which were subsequently examined in an SEM prior to the emission tests. Thus, the SEM micrographs revealed that a typical carbon deposit was composed of a random distribution of carbon particles, that typically had sub-micron to 10 micron dimensions, and were insulated from the substrate electrode.

Emission measurements, made under UHV conditions, revealed a direct spatial correlation between the location of an artificial carbon deposit and the switch-on of an emission site at anomolously low applied fields of $\leq 8MVm^{-1}$. Thus, Figure 2.17 gives a typical example of the current-field characteristics, and associated F-N plot, obtained from a single carbon emission site. This illustrates (a) the extremely emissive nature of these sites (c.f. a natural site on a broad area electrode (Figure 2.6)) and (b) that the F-N plot can be divided into two linear regions. Here, the low field region is characterised by β values in the range 300-1000, whilst for the high field region, β is typically >1000.

Figure 2.17 A typical example of the current-field characteristic (x) and the associated F-N plot (●) of a carbon site. (From [10]).

Figure 2.18 An example of the type of emission images obtained from artificial carbon sites. (From [13]).

Figure 2.19 A schematic representation of the coherent scattering and emission of hot electrons from an MIM microstructure on a broad-area electrode. (From [13]).

Athwal et al [10] measured the emitted energy spectra from artificial sites and concluded that the emission mechanism was non-metallic in origin, and similar to that occuring at the natural sites described in section 2.2.1. Consequently, from this limited experimental evidence, a qualitative hot electron emission mechanism [10] was proposed, which assumed that the flake-like structure of the graphite particle would form a metal-insulator-metal (MIM) microstructure with the electrode and its ambient oxide layer. It can be assumed from elementary electrostatic principles that the flake, which is electrically "floating" due to the blocking contact provided by the insulator, effectively probes the gap field and assumes a potential which is approximately equal to the equipotential field line at the highest point on the flake. This has subsequently been termed the "antenna effect", and gives rise to a field enhancement, β_{ant}, across the insulator, where

$$\beta_{ant} \approx h/d \qquad (2.22)$$

where h is the maximum height of the particle above the substrate, and d is the thickness of the insulating film. According to this model, as the applied field, F, is increased, a critical insulator field value is reached (~5-20MVm^{-1}), i.e. equal to $\beta_{ant}F$, where a switching process is initiated. This then provides a flux of hot electrons, by a simlar process to that described in section 2.2.4, which are subsequently projected through the flake to be emitted into the vacuum.

In a more detailed study on the electron emission from artificial carbon sites, Xu and Latham [13] obtained emission images from metal-insulator-graphite flake microstructures, such as shown in Figure 2.18. These images were typically found to consist of several regularly orientated segments (Figure 2.18(a)), although in some cases the segments were randomly orientated i.e similar to those obtained by Simmons et al [93] from purpose-fabricated MIM structures. In addition to these observations, single segment images (Figure 2.18(b)) were occasionly obtained which subtended angles $<180^{o}$, whilst exhibiting a well defined outer edge and a diffuse inner edge; furthermore, the segments were found to increase in size, i.e. in a perpendicular

direction, with increasing applied field.

Having established a similarity between their emission images and those of Simmons et al [93], Xu and Latham [13] proposed a model based on the coherent scattering of electrons from a graphite flake, as shown in Figure 2.19. Thus, as originally proposed by Athwal et al [10], the antenna effect of the graphite flake gives rise to a MIM switching process in the critical region shown in the inset of Figure 2.19. As discussed in the hot electron emission model of Bayliss and Latham [9], electrons are injected from the substrate into the conduction band of the insulator layer where they are heated, i.e accelerated towards the top metal film. Subsequently, as described by Simmons et al [93], these electrons will be coherently scattered in the top metal film, where only those with sufficient energy, determined by the Bragg equation, will be scattered in a forward direction. Thus, electrons scattered along path 2 in Figure 2.19 will be emitted into vacuum, i.e provided that they have a velocity vector parallel to the insulator-vacuum interface and large enough to surmount the surface potential barrier.

In this model, Xu and Latham [13] further proposed that the high energy electrons would give rise to the well defined outer edge shown in Figure 2.18(b), whilst conversely, the low energy electrons resulted in the diffuse inner edge. This hypothesis was initially confirmed by preliminary electron spectroscopy measurements [94], and more recently by a more advanced energy-selective electronic imaging technique developed by Xu and Latham [95]. Finally, it should be noted that a more detailed account of FIEE from artificial carbon sites, including the effects of photo- and thermal-stimulation, has been given by Xu [96].

2.3 Purpose-Fabricated Cold-Cathode Electron Sources

In addition to extending the present understanding of the fundamental principles of field-induced electron emission from metals and non-metallic composite structures, there exists a parallel incentive to develop a commercial cold-cathode electron source which, it is hoped, will ultimately supersede the conventional

thermionic emitter and its practical shortcomings. In pursuit of this objective, limited success has been achieved, to date, using a variety of metallic micropoint emitter designs. On the other hand, although the commercial potential of a non-metallic cold cathode is widely recognised, and has been the subject of extensive research since the 1960's, attempts to utilise such cathodes have so far proved relatively unsuccessful. In this section, an account will be given of the concepts and relative merits etc, of a variety of cold-cathode regimes which have generated a commercial interest over the past few decades.

2.3.1 Metallic Micropoint Field-Emitters

In practice, it is not possible to obtain useful F-N electron emission from extended area planar cathodes. This is primarily due to technological problems encountered (a) in producing a sufficiently uniform emitter surface, and (b) in the use of high operating voltages without the risk of electrode breakdown. For this reason, practical field emitters are produced in the form of metallic micropoints, or needles, with typical tip radii of ~100nm or less. These micropoints are commonly formed by electrolytically etching thin wires [97], although other methods exist, e.g. corona discharge etching [22].

The material of an ideal field emitter should possess several properties if stable cathode operation and a reasonable lifetime are to be realised. For example, high values of electrical and thermal conductivities, coupled with a high melting point, are required to minimise the effects of Joule heating, which can ultimately lead to tip melting. Furthermore, a high mechanical strength is required to prevent disintegration of the tip by forces imposed on the emitter due to the high surface electric field ($\geq 10^9 Vm^{-1}$). On the basis of these requirements, tungsten has been a favourite choice of material, although other materials, e.g. lanthanum hexaboride (LaB_6) and low temperature (230K) mercury whiskers have been used.

In addition to the basic material requirements, the stability and lifetime of tungsten micropoint emitters is further limited by the effects of the residual gas

environment in which they operate. In particular, bombardment of the tip by ionised residual gas molecules results in a continual sputtering of the emitter material, which, in turn, leads to emission instability and a reduced lifetime. This sputter damage can be quite severe when He gas is present; in contrast, it is interesting to note that hydrogen has the opposite effect, in that it produces very little sputtering and permits field emission operation at pressures of ~10^{-2}mbar. In addition, factors such as the surface adsorption of residual gas molecules, and the diffusion of impurities to the emitter surface, are also found to reduce the stability of the emission owing to subsequent changes in the surface work function. In practice, the majority of these instabilities are reduced by operating under ultra-high vacuum (UHV) conditions ($\leq 10^{-10}$mbar), and by frequently heat treating, or "flashing" the tip (see [98]) to remove surface contaminants. Furthermore, heating, or outgassing the anode assembly is also found to be beneficial in reducing residual gas-based instabilities.

As far as the widespread use of field emitters in concerned, many devices [101] have been "bench tested" with a field emission electron source, in particular, those requiring high current densities (10^7Acm^{-2}), a relatively high current (e.g. 30A from pulsed multitip arrangements), and current modulation at microwave and optical frequencies [99]. However, although emitter lifetimes of many thousands of hours have been achieved, problems still remain in obtaining sufficient emission stability. Despite this, the past decade has witnessed a renewed interest in the use of metallic micropoint emitters as alternatives to thermionic cathodes in electron microscopes. This interest has largely been due to their potentially superior cathode qualities in practical applications, e.g. source brightness, source size, electron energy spread, and lifetime; in this context, a comparison of the emission capabilities of commercially available field-emitting and thermionic cathodes is given in Figure 2.20.

In addition to the conventional micropoint emitters, more elaborate point-geometries have been investigated over the past few years, e.g. the low-dimensional micropoint cathodes [100]. In these cathodes, the dimensions of the emitter are comparable to the mean-free-path of electrons in metals (~500Å), which results in an increase in emission due to a decrease in the interaction of the supply electrons with the

	Field emission (Cold cathode)	LaB_6	Tungsten Filament
Brightness ($A/cm^2 \cdot sr$)	10^9	10^7	10^6
Virtual source (Å)	$<10^2$	10^5	$>10^5$
Energy spread (eV)	0.2	1.0	1.0
Service life (h)	>1,000	1,000	40
Operating vacuum (Pa)	10^{-7}	10^{-5}	10^{-3}

Figure 2.20 A comparison of the emission characteristics of three commercially-available electron sources.

Figure 2.21 A schematic cross-section of a single emitter from a multi-emitter Spindt TFFEC. (SiO_2 thickness ~ 1.5μm). (From [16]).

Figure 2.22 A typical Fowler-Nordheim plot for a 5000-tip Spindt cathode. (From [16]).

lattice. Consequently, emission current densities as high as $10^{10}Acm^{-2}$ have been obtained from prototype cold-cathodes which utilise this principle.

2.3.2 Multitip Array Emitters: The Spindt Cathode

The use of array cathodes consisting of a large number of individual metallic microtips has become increasingly popular for applications requiring high operating currents and high current densities. Although these cathodes were originally developed in the form of closely-packed conventional tungsten microtips [101], recent advances in microfabrication techniques have lead to a new generation of multitip array emitters [15,16], of which, the Spindt-type thin film field-emitting cathode (TFFEC) has shown the most potential as a practical electron source. It should however be pointed that, although the Spindt array cathode has recieved the most attention from a commercial viewpoint, similar microfabricated emitter arrays have been produced and studied at other centres, for example, at the UK Fulmer Research Institute and the US Naval Research Laboratories. The details and findings of these research programmes have been published respectively by Rivlin et al [102] and Gray et al [18,103].

Figure 2.21 shows the schematic cross-sectional structure of a single emitter from a Spindt array. The cathode is constructed from a silicon substrate (<111> p-type) with a thermally-grown silicon oxide film (~1.5μm thick), onto which is deposited a molybdenum gate film (~0.5μm thick). An array of holes is then micromachined in the gate film and SiO layer, and molybdenum cones are formed through the holes on the silicon substrate; the tips of these cones are centred in the holes and lie in the plane of the Mo gate film. The developement of this fabrication technique has lead to the production of arrays 1mm in diameter with tip densities of up to 10^6 tips/cm^2, i.e. 10,000 tips per cathode [104].

Emission tests on these cathodes have been performed under pulsed field (60Hz) conditions in order to reduce the total power dissipation at high current densities. In practice, a negative pulsed voltage (≤200V) is applied to the tips, whilst

the gate is earthed and the collector biased to ~1000V for an emitter-collector distance in the range 2-10mm. Under these conditions, the Spindt cathode geometry ensures that most of the high energy ions, i.e. those originating in the vicinity of the collector, will strike the gate as opposed to the emitting surface. A more detailed account of the experimental arrangement and testing procedure is given by Spindt et al [15] and Forman [16]. In operation, the Spindt cathode is found to emit for a gate voltage of ~120V, i.e. corresponding to a tip-gate field of $\sim 10^9 Vm^{-1}$; at these low current densities, the emission current I_e is independent of the collector voltage, V_c, which is typically held at 1000V. Subsequently, if the gate voltage (V_g) is further increased, I_e increases exponentially according to the Fowler-Nordheim relationship, i.e. as shown in the F-N plot of Figure 2.22, which was obtained from a 5000-tip cathode. By assuming a traditional metallic F-N emission mechanism, it appears that as the emitter current density approaches $5Acm^{-2}$, or approximately 10μA/tip, the space charge density, ρ, directly above each individual emitter, becomes sufficiently large to decrease the rate of increase in I_e with increasing V_g; hence the F-N plot in Figure 2.22 deviates from an ideal linear relationship at higher current densities. As illustrated in Figure 2.23, the effect of this space-charge limitation on the total emission, or collector current, can be reduced by increasing the collector voltage (V_c), i.e. reducing ρ. However, for a constant gate voltage, I_e is found to saturate with increasing V_c (Figure 2.23), which corresponds to the maximum F-N current available at a particular gate voltage. These experimental observations confirm, or strongly imply, that Spindt cathodes operate by the "metallic" Fowler-Nordheim electron tunnelling mechanism.

Using a 60Hz pulsed gate voltage, maximum peak current densities of around $12Acm^{-2}$ have been achieved from 5000-tip arrays with a total emission current of 100mA [16]. However, current densities in excess of $55Acm^{-2}$ have been obtained from smaller 16-tip arrays at a current level of ~1.4mA; in this case, the lower current density from the larger arrays is believed to be due to collector power-handling limitations which are observed at the higher emission current levels. Although the array cathodes are capable of operating satisfactorily at these current levels and densities, many cathodes fail at emission currents ≥50mA. These failure modes are most

Figure 2.23 Variation in the collector current versus collector voltage for a Spindt cathode. Emitter voltage = 197 volts. (From [16]).

Figure 2.24 The cross-sectional structural model for high-modulus carbon fibre. (From [110]).

Figure 2.25 An SEM micrograph showing the "tip explosion" damage that can occur during the initial switch-on of a carbon-fibre emitter. (From [113]).

commonly in the form of an electrical "short circuit" between the gate and emitters, resulting from localised arc discharges, which, in turn, render the cathodes inoperable: this irreversible damage is presently believed to be associated with a degassing phenomenon [16]. Finally, despite the problems encountered at high current levels, 100-tip array cathodes have been tested at a peak current level of 2mA, for a 60Hz supply, and have attained lifetimes, under continuous operation, in excess of eight years [15].

2.3.3 Carbon Fibre Cathodes

In recent years, carbon fibre micropoint field emitters have been studied as a possible electron source for electron beam devices, since their emission current is generally found to be insensitive to poor vacuum conditions (~10^{-5}mbar) when compared with conventional tungsten emitters. These carbon-based emitters have commonly been in the form of carbon fibres [22,105-107], or glassy carbon fibres [108,109]. The first recognition that carbon fibres could provide a stable field emission regime was due to Baker et al [22], who used 7μm diameter fibres which had been shaped into suitable emitter profiles by a controlled corona discharge in air. Using a point-to-plane geometry, these authors obtained emission currents >100μA at an applied voltage of a few kV for single emitting tips. Furthermore, in the pressure range 10^{-8}-10^{-7}mbar, the lifetime of the emitters was found to exceed 2400 hours for an emission current of 10μA, but reduced to 500 hours at an emission current of 100μA.

Following these preliminary investigations, Lea [106] and English et al [107] assessed the suitability of a hybrid emitter in which high-strength carbon fibres were coated in tungsten and then electrolytically etched in a solution of 1M potassium hydroxide to form single emitter tips. However, emitters produced in this manner were found to be fragile, and consequently, the emission current was limited to 5μA by the onset of destructive processes. The emission images from these carbon fibre cathodes were shown to consist of many small sub-sites which, at the time, were attributed to the F-N "metallic" emission of electrons from multiple microprotrusions on the tip surface.

In similar, but more recent studies, Latham and Wilson [110,111] observed electroluminescence and non-metallic electron emission spectra, such as described in section 2.2.1, from carbon fibre emitters, and hence concluded that the emission was not in fact due to field enhancing microprotrusions as was previously assumed. In order to provide an physical basis for their non-metallic hot-electron emission model, i.e. similar to that considered in section 2.2.4, these authors considered the cross-sectional structure of a carbon fibre, which, as illustrated in Figure 2.24, is known to have a concentric, three-zone, skin-sheath-core structure [112]. It follows therefore, that when a fibre is electrolytically etched, the exposed surface of the conical end form will contain amorphous carbon structures (typically $<1\mu m$ in diameter) whose insulating properties could conceivably result in the formation of both MI and MIM surface microstructures; in fact, the recent emission images obtained by Xu and Latham [13] from carbon fibre emitters strongly support the contention for a hot electron model based on a MIM regime.

Although the above studies on carbon fibres proved to be reasonably successful in terms of current density capabilities and current stability under poor vacuum conditions, their use as practical cold cathodes was limited due to instabilities in the emission images, i.e. a spatial instability associated with the random "switch-on" and "switch-off" of individual emission sub-sites. Thus, in a practical situation, such as a prototype CRO tube incorporating a carbon fibre field emitter, the switching instability was shown to result in non-uniform line traces and a "flickering" screen image [113]. In an attempt to reduce the instability, Latham and Salim [24] developed an optically-controlled external feedback loop which eliminated the low-frequency fluctuations (<10Hz) in the emission current. Furthermore, a thermal processing technique [24] was used, where the emitter is baked *in situ* ($p \leq 10^{-8}$mbar) at $250^{o}C$ for 36 hours, and was found to significantly reduce the cathode instability, as well as the incidence of "tip explosion" events, i.e. commonly observed during the initial switch-on of a virgin tip (see Figure 2.25).

2.3.4 Composite MI Micropoint Emitters

These emitters were originally conceived in a simulation study, undertaken by Latham and Mousa [11,12], on the field-induced emission of electrons from composite metal-insulator (MI) structures, such as described in section 2.2.1. These authors fabricated emitters consisting of a tungsten micropoint cathode overlayed with a sub-micron layer of epoxylite resin, and obtained convincing evidence in support of a non-metallic electron emission mechanism, as proposed earlier by Latham and co-workers [71,83]. Furthermore, from a technological point of view, these composite emitters were shown to exhibit several potential qualities in relation to commercial cold-cathode electron sources.

The composite microemitters were prepared from electrolytically-etched, 0.1mm diameter tungsten wires with tip radii in the range 30-100nm. Following a period of ultrasonic cleaning, the tips were dipped, using a micrometer-controlled vertical carriage, into a bath of epoxylite resin, where the number of successive dips determined the final coating thickness. The resin overlayer was then subjected to a curing process [12], which finally resulted in a resin thickness, determined in a transmission electron microscope (TEM), of typically 0.04-0.2μm. To investigate the general current-voltage (I-V) characteristics and emission images obtained from these emitters, a simple point-to-plane field emission microscope facility was utilised with a tip-screen distance of ~10mm. Thus, referring to curve B of Figure 2.26, it is seen that as the applied voltage is slowly increased across a typical virgin emitter, a point is reached, V_{sw}, where the emission current "switches-on" to a stable, but saturated value, I_{sat}. The saturated region extends to a higher voltage, V_{max}, where current instabilities and "tip explosions" may occur, and to a low voltage limit, V_{sat}, below which, the emission current falls to zero ($<10^{-12}$A) at a threshold value, V_{th}. The region between V_{th} and V_{sat} is found to exhibit a hysteresis behaviour on subsequent re-cycling of the applied voltage, where, for voltages less than V_L (Figure 2.26), the I-V data gives a linear F-N plot. Furthermore, Figure 2.26 compares the composite emitter I-V characteristic with that of the same micropoint prior to coating with a

Figure 2.26 A comparison of the I-V characteristics of an uncoated W emitter of tip radius ~30nm (curve A), and that obtained after coating with a 200nm thick layer of resin (curve B). (From [11]).

Figure 2.27 Projection images obtained for (a) a clean tungsten emitter, and (b) after coating with a 150nm layer of resin. I_e= 4.5μA in each case. (From [11]).

Figure 2.28 The idealised energy band diagram of a thin-film tunnel emitter. Applied voltage = V_d. (From [101]).

dielectric layer: from a technological point of view, this demonstrates how the dielectric coating results in a significant lowering of the threshold voltage and operating voltage required to obtain an emission current equal to I_{sat}. In this investigation, I-V measurements were obtained for a variety of substrate radii and resin coating thicknesses (0.04-0.2μm), where it was generally observed that (i) the switch-on field, F_{sw}, and I_{sat} were typically $10^9 Vm^{-1}$ and 5μA respectively, (ii) V_{th} was typically one-tenth the value of V_{sw}, (iii) the F-N slope of a coated emitter was typically ~1/4 that of the corresponding uncoated emitter, and finally (iv) V_{max} was typically equal to $2V_{sat}$.

The emission image of a composite micropoint emitter, which was obtained directly from the phosphor screen of the field emission microscope (FEM), was typically found to consist of a single very bright spot with no apparent internal structure, i.e in contrast to typical FEM images obtained from a metallic emitter [114]. The images obtained from a tungsten emitter, before and after coating with a 150nm layer of epoxylite resin, are shown respectively in Figures 2.27(a) and (b) for an emission current of 4.5μA. From these images, it is seen that the composite emitter is a very much brighter, in fact, a six times brighter electron source at an equivalent emission current. Additional measurements also showed that the emission images increased in diameter with increasing applied field. Furthermore, from observations of such images over a time scale of ~100 hours, it was established that the resin coated emitters were significantly more stable, and gave higher (current) signal-to-noise ratios than the conventional tungsten emitters.

From measurements of the emitted electron energy distributions from composite micropoint emitters, Latham and Mousa [11] confirmed that the emission mechanism was non-metallic in origin, where, as described in section 2.2.1, the spectra had significantly wider half-widths (≤300meV), and were typically displaced below the substrate Fermi level by up to 1eV: these characteristics were subsequently found to be functions of the emission current. Thus, from the evidence of the I-V data, emission images and spectral measurements, Latham and Mousa [11] proposed a hot electron emission model, based on the model described in section 2.2.4, in which hot electrons are emitted from a conducting channel formed in the dielectric layer at the apex of the

emitter. According to this model, it is assumed that both the current saturation and current dependence of the emission images were due to the onset of electron-phonon scattering processes within a channel. Finally, similar experimental findings have been obtained from more recent experiments on MI micropoint cathodes fabricated from a variety of insulating coatings [115,116].

2.3.5 The Thin-Film Tunnel Emitter

The concept of electron tunnelling, discussed in section 2.1.1, could, in principle, be used to transfer electrons across an extremely thin dielectric layer (≤100Å) of a metal-insulator-metal (MIM) sandwich structure, as modelled in the papers of Stratton [117] and Simmons [118]. In this process, it is assumed that no interaction takes place in the thin dielectric where, provided that the potential drop across the electrodes is greater than the top metal work function (in most cases 4-5eV), electrons can gain sufficient energy to surmount the surface barrier, and be emitted into vacuum: this further assumes that the top electrode is sufficiently thin (<50Å) so that electron absorption is minimised. The idealised energy diagram of this emission regime is given in Figure 2.28.

Mead [19,119] attempted to utilise this principle as the basis for a thin-film sandwich cold-cathode which theoretically offered a wide range of hot electron energies, a high current density, and would be insensitive to temperature fluctuations. However, his experimental observations on Al-Al_2O_3-Al structures were found to deviate considerably from the theory. Typical tunnel, vacuum emission, and transfer ratio characteristics of similar cathodes [120], with an oxide thickness of 30Å, are given in Figure 2.29(a), where the transfer ratio, α, is defined as the ratio $\alpha = I_e/I_e+I_s$, where I_e and I_s are the emitted and sandwich currents respectively. Thus, it is shown how the cathode initially emits at an applied voltage of ~4V, and is capable of delivering currents of $>10^{-5}$A. However, the low values of α ($<10^{-3}$) demonstrate the inefficiency of these cathodes, whilst the monotonic decrease in α with the sample

Figure 2.29 (a) Voltage dependence of the sandwich current I_s, emission current I_e, and the current transfer ratio α, for an Al-Al_2O_3-Al tunnel emitter. (b) The dependence of α on the thickness of the Au overlayer in an Al-Al_2O_3-Au tunnel emitter. (From [120]).

Figure 2.30 Current-voltage (I_s-V_s), electron emission (I_e-V_s) and electroluminescence (I_L-V_s) characteristics of a "formed" Al-Al_2O_3-Au cathode. (From [20]).

voltage (V) suggests that the hot electrons can be absorbed in the oxide and/or top electrode. Finally, Figure 2.29(b) shows how α is found to decrease in an exponential manner with increasing top electrode thickness.

In order to gain some insight into the electronic processes responsible for these non-ideal characteristics, Kanter and Feibelman [121] and Savoye and Anderson [122] analysed the energy spectra of the emitted electrons. The spectra obtained were found to have a maximum value well below the fermi level of the base electrode, thus impying that a considerable loss of electron energy had occured during transport through the tunnel structure. Furthermore, by assuming an attenuation length of 100Å in the upper Au-electrode, an attenuation length of ~20-30Å was deduced for electrons in Al_2O_3. From these measurements, it was proposed [122] that electron losses in the insulator were due to the creation of optical phonons; this process would require a loss of 0.1eV per interaction, which is consistent with the fact that $k\theta_D$ ~0.1eV, where θ_D is the Debye temperature for Al_2O_3.

Finally, tunnel cathodes have been produced with extremely thin (20-40Å) dielectric layers [117,118] in an attempt to reduce the electron energy losses, and hence increase the emitter efficiency. However, despite these efforts, commercial research interest in the thin-film tunnel cathode has faded, owing primarily to practical problems such as their short lifetime, lack of reproducibility, non-linear emission characteristics and inefficiency.

2.3.6 The "Formed" MIM Cold-Cathode

The main drawbacks associated with the thin-film tunnel emitter have, over the past two decades or so, directed more interest towards the so-called "Formed" metal-insulator-metal (MIM) cathodes [20,21,123]. These are essentially MIM sandwich devices, similar to the tunnel emitter in design, however, with a thicker insulating layer of typically 200-1000Å, and a top metal electrode of thickness 100-200Å. Although these emitters have more recently been discarded as potential commercial cold cathodes, i.e. for similar reasons to those described in the last section,

the processes and princples involved in their operation are generally important, and valid to a variety of non-metallic field emission regimes.

If the voltage V_s, applied to the electrodes of a fresh MIM sample is increased, a value is reached where the sample conductivity "switches" to a high "on" state, i.e. as described in section 2.2.2. The value at which this irreversible change occurs is known as the "forming" voltage, V_F, and typically occurs at a voltage of ~2-10V for these devices. In addition to the increased conductivity of the sample, formed MIM devices are found to exhibit (a) intense electron emission, (b) a region of voltage-controlled negative resistance, (c) electroluminescence and (d) swithing and memory effects, which are collectively referred to as the anomolous properties of a formed MIM device. Furthermore, it is found that all these phenomena, including electron emission, are observed for both normal and reverse voltage polarity.

In the early 1960's, it was proposed that these MIM devices could be utilised as low voltage solid-state cold-cathode emitters. The first detailed study of electron emission into vacuum from these devices was made by Hickmott [124,125,126], who found, using Al-Al_2O_3-Au structures, that electron emission developed simultaneously with electroluminescence following a characteristic switch-on at V_F~2V. Figure 2.30 shows the relationship between the sample current I_s, emission current I_e, and electroluminescent intensity I_L for a fully formed Al-Al_2O_3-Au sample. Using an imaging screen and optical microscope, the point of inflection in the I_e-V characteristic was shown by Hickmott [126] to indicate a transition from uniform to localised electron emission; thus, for voltages ≥4.5V, the emission became localised, i.e. arising from discrete emission centres. Furthermore, Figure 2.30 demonstrates the poor efficiency of these cathodes with transfer ratios (defined in section 2.3.5) increasing from 10^{-7} to 10^{-4} with increasing voltage.

From a comparison of the emission distribution patterns with optical micrographs of the upper electrode of a test cathode, Emmer [127] obtained evidence to suggest that there was a direct correlation between emission centres and pin-hole defects. This finding was also confirmed by Biederman [128] who used a scanning electron microscope technique to identify possible emission centres; an example [128]

of an SEM micrograph of a typical emission source is given in Figure 2.31. In an effort to further investigate the influence of the top electrode on electron emission, Hickmott [129], who supposed that electrons penetrated the top electrode, calculated the attenuation length, l_m, of electrons in the electrode using the equation

$$I_e = KI_s \exp(-d_m/l_m) \qquad (2.23)$$

where I_e and I_s are the emitted and sandwich currents respectively, K is a constant and d_m is the thickness of the upper electrode. Thus l_m was calculated to be ~200-300Å, where values as high as 1000-3000Å were obtained in similar studies on Au-SiO-Au cathodes [130]. These authors concluded that electron emission through pin-hole defects in the upper electrode was the reason behind the incorrect (too high) values of l_m, derived from equation 2.23.

The electron emission images obtained from formed MIM emission sites have been observed by Simmons et al [93] on a flourescent screen situated a few centimetres from the sample, and at a voltage of 1-3kV. These images were found to consist of diffuse patches for $V_s<8V$, but for $V_s>8V$, a ring-like pattern composed of individual arcs was obtained, as shown in Figure 2.32. A model of electron emission through pin-hole defects was proposed by Simmons et al [93] in an attempt to explain these non-uniform emission distributions. Thus, it was assumed that some electrons would arrive in the top metal film with little loss in energy, i.e. approximately equal to $V_s+\eta$, where η is the Fermi level of the top electrode. It is further assumed that electrons, arriving at normal incidence to the plane of the electrode, would subsequently be diffracted by the (111) plane of crystallites in the polycrystalline Au electrode at an angle 2θ, where θ is given by the Bragg Law, i.e. $\sin\theta = \lambda/2d_{(hkl)}$, where $\lambda(Å) = 12.2/(V_s+\eta)^{1/2}$ is the de Broglie wavelength of the electrons. It can be shown that, under the experimental conditions described above, hot electrons will be diffracted almost parallel to the plane of the top electrode, will rapidly thermalise, and hence not be emitted. However, if the diffraction occurs in proximity to the edge of a pin-hole, then electron emission into vacuum may be energetically possible. This emission

Figure 2.31 An example of a typical emission source for a "formed" Al-LiF-Au cathode. (Magnification x10,000). (From [20]).

Figure 2.32 The emission images obtained from "formed" MIM sandwich cathodes. (From [93]).

regime is illustrated in Figure 2.33.

More recently, Biederman [131] has criticised the "diffraction" model on the evidence of his electron emission images obtained from Al-LiF-Au and Al-SiO-Au cathodes under both normal and reverse voltage polarity. In the case of electron emission under reverse bias (i.e. with the top electrode biased negatively), Biederman found that the images consisted of full circles with diffused edges, and proposed that hot electrons were emitted from the insulating peripheral edge exposed at a pin-hole defect: i.e. as illustrated two-dimensionally in Figure 2.34. Furthermore, the equipotential distribution resulting from this regime (see Figure 2.34) was assumed to form an electrostatic micro-lens with a defocussing effect for normal voltage polarity, and a focussing effect for reverse polarity.

In addition to these models, several authors published more fundamental, yet somewhat qualitative, models on the physical nature of the forming process and associated phenomena such as hot electron generation, and hence hot electron emission. Thus, for example, Hickmott [126,129] assumed that his anodically deposited oxide layers contained a considerable amount of impurities, so that an impurity band, or acceptor level E_H, appeared approximately at the Fermi level in the oxide band gap. In this model, the forming process involves the ionisation of impurities, thus leading to electrical conduction along the impurity band. Furthermore, as the applied voltage is raised to ~2V (i.e. the threshold for electroluminescence and electron emission), free holes are created at the top of the valence band in the high field region close to the negative electrode, due to electrons tunnelling to the acceptor level E_H. Recombination then gives rise to the emission of photons, which subsequently excite electrons, i.e. those to be emitted, into the conduction band via an Auger mechanism.

Simmons and Verderber [132] have suggested that the forming process arises from the injection of metal ions from the top electrode into the dielectric, which creates an impurity band close to the Fermi level. In this model, electrons are assumed to be injected from the bottom electrode into the impurity band under the influence of the high field in this region; these electrons are subsequently transported to the top electrode via a discrete tunnel-hopping process along impurity states in the dielectric. However, in

Figure 2.33 (a) A band diagram of the emission process from "formed" MIM cathodes. (b) The emission of electrons via diffraction at a pin-hole in the top electrode. (From [93]).

Figure 2.34 The electrostatic microlens effect for electrons emitted from the edge of a pin-hole defect in a "formed" MIM cathode. (From [20]).

order to create hot electrons in the insulator conduction band, it is necessary for the hopping electrons to gain an excess energy of ~1eV from the lattice phonons, i.e. E_C-E_H= 1eV. The resulting hot electrons are then emitted from pin-hole defects in the upper electrode as discussed above.

A full description of the many alternative models of electron emission from formed MIM cathodes, for example, those of Barriac et al, Green et al, Emmer, and the filamentary model of Dearnaley et al, is beyond the scope of this thesis. However, the main conclusions of these models have been extensively reviewed elsewhere [20].

2.3.7 Modified MI Interface Injection: the Si-rich SiO_2 Emitter

The idea of modifying an interface contact in order to enhance the current injection from a semiconductor into a wide band gap insulator, has been utilised in a number of solid-state devices, and can be achieved by the use of graded and stepped band-gap insulators [133]. However, an alternative method of obtaining high-current injection into an insulator at moderate applied fields ($<10^9 Vm^{-1}$) is by introducing a multiphase interface layer composed of metallic or semiconducting crystalline/amorphous structures (typically ≤100Å in diameter) embedded in an insulating matrix. Prior to the discovery of this latter injection method, injection into the conduction band of, say SiO_2, was difficult since direct F-N tunnelling occurs at about the same field at which dielectric breakdown occurs, i.e. ~10MVcm^{-1}. To avoid these problems, the injector method is now used in the Si-rich SiO_2 electron emitter, which has been developed over the past decade by DiMaria and co-workers [134-137], primarily for the purpose of investigating the electron transport properties of SiO_2.

Figure 2.35(b) shows the basic construction of a metal-insulator-semiconductor (MIS) cathode, due to DiMaria and co-workers [135], incorporating a Si-rich SiO_2 injector layer at the S-I interface. The injector layer is chemical vapour deposited (CVD) on top of (100) 2Ωcm p-type or n-type substrates at a moderate temperature of 700°C and a typical thickness of a few 100Å. In this proces, the ratio of concetration of N_2O to SiH_4 during CVD can be varied from 10 to 3, which gives

Figure 2.35 A schematic representation of (a) the band structure, and (b) the device structure of a Si-rich SiO_2 injector cathode biased for electron emission into vacuum. (From [135]).

Figure 2.36 A schematic energy diagram of a reverse bias p-n junction emitter. (From [101]).

approximately 7 to 3% excess atomic Si over stoichiometric SiO_2 respectively. Finally, a SiO_2 layer is deposited to a thickness of a few hundred Å by CVD, prior to the evaporation of a top Al or Au gate film (100-300Å thick). A detailed description of the construction of such devices is given by DiMaria and Dong [134].

The Si-rich SiO_2 layer is believed to be a two-phase mixture of amorphous Si and SiO_2, although evidence suggests [138] that the high annealing temperatures used in the deposition process possibly result in the formation of Si crystallites with diameters of ~10-20Å. Thus, it is assumed that this gives rise to the band configuration shown in Figure 2.35(a), i.e with the device biased for electron emission into vacuum. DiMaria and Dong [134] have proposed that the electric field distortion associated with the two-phase nature of the Si-rich SiO_2 layer is responsible for the enhanced electron injection and hence emission from these devices. Thus it is assumed that direct electron tunnelling occurs between isolated Si regions, followed by a subsequent high-field F-N injection into the SiO_2 due to the local field enhancement. However, these authors have not dismissed the possibilities that alternative conduction mechanisms may operate, for example, Poole-Frenkel [92] conduction and electron heating between Si regions. Detailed accounts of electronic transport phenomena in two-phase materials have been given by Abeles et al [139] and Pfeilsticker et al [140].

Brorson et al [137] directly measured the energy distribution of the emitted electrons using a retarding potential analyser and found that electron heating of ≥2eV, for fields of ≥2MVcm^{-1}, had occured in the SiO_2 layer, i.e. measured from the bottom of the SiO_2 conduction band. Thus, for the electron emission regime shown in Figure 2.35(a), it can be assumed that the hot electrons arriving in the top gate film will be emitted over the vacuum barrier. From a technological viewpoint, these injector cathodes have proved to be essential in the study of the electron transport processes in SiO_2, however, electron emission into vacuum has so far been limited to currents of ~1μA, which is presently believed to be due to the build up of permanent interface space-charge [135].

2.3.8 Semiconductor Junction Emitters: The SiC Cathode

The application of a reverse bias to a p-n junction results in the creation of a high field region in which electrons can be accelerated to energies exceeding the surface vacuum level. Consequently, electron emission into vacuum becomes probable provided that the generation of hot electrons occurs within a mean-free-path length from the vacuum surface. Although this latter condition implies that the emission process will be inherently inefficient, considerable interest has been shown in reverse bias junction cathodes over the past three decades [101,141-143].

A schematic energy diagram of a reverse bias p-n junction emitter, including the associated electron processes, is shown in Figure 2.36. In addition to electron energy losses resulting from phonon scattering in the conduction band, losses may also occur due to interactions with electrons from the valence band in the form of electron-hole pair production. This latter interaction becomes probable when a primary electron acquires an energy in the conduction band which is greater than $1.5E_g$, where E_g is the energy band gap of the host semiconductor [144]. Thus, in order to suppress pair production, one would choose a semiconductor whose electron affinity is sufficiently small in comparison to its band gap. However, in the case of silicon, which was commonly used in early p-n junction cathodes [145], this requirement is not satisfied, which, in turn, is believed to account for the low transfer ratios ($<10^{-6}$), i.e. the ratio of the emitted current to the junction current, typically observed for silicon junction emitters.

In contrast, a material such as α-silicon carbide would be expected to be a more efficient emitter, since, at room temperature, it has a band gap of 3.1eV, and an electron affinity of about 4eV: in agreement with this reasoning, transfer ratios as high as 10^{-4} have been obtained from α-SiC junction cathodes [146]. A schematic of a SiC junction cathode, and its application in a typical cathode ray tube (CRT) is given in Figure 2.37. The construction and pre-test treatments of these cathodes have been described in detail by Brander and Todkill [141]. To observe emission from the SiC p-n junction it is necessary to cut a small recess through the n-type layer to the p-region,

Figure 2.37 A schematic of (a) a practical SiC p-n junction emitter, and (b) its application in a cold-cathode CRT system. (From [141]).

Figure 2.38 The emission pattern from a typical SiC p-n junction cathode. (Recess diameter = 0.5mm). (From [141]).

Figure 2.39 The typical emission characteristic and the effect of caesiating the surface of a SiC emitter. (From [141]).

thus exposing a peripheral area, or "ring", of the junction. This is necessary since the small carrier diffusion length of SiC would normally prevent the emission of hot electrons into vacuum. The resulting electron emission from a cathode of this type, with a hole diameter of 0.5mm, is shown in Figure 2.38. The emission image, which was obtained by electrostatic focussing in a CRT, suggests that the total emission current originates from a large number of discrete regions on the periphery of the junction, known as microplasmas, where the major junction avalanche current flows [141]. According to Brander [142], it is further assumed that the presence of a heavily C-doped oxide layer provides donor electrons to enhance the junction, and hence emission currents following activation at ~500°C. Furthermore, the degrading, or "poisoning" effect observed following exposure to water vapour is attributed to the oxidation and subsequent removal of the carbon donors. In practice, the emission currents obtained from these cathodes are found to vary from sample to sample, but in general are in the range 10^{-7} to 10^{-5}A for junction currents of a few tens of milliamps [141]. A typical emission characteristic of a SiC junction cathode is given in Figure 2.39, where the effect of lowering the cathode work function by depositing a surface layer of caesium is shown to increase the emission level by typically one or two orders of magnitude. In general, the emission current I_e and junction current I_j are found to obey an approximate law of the type

$$I_e = CI_j^{\gamma} \qquad (2.24)$$

where C is a constant and γ is typically found to vary from 1 to 9, although its true relation to the emission phenomenon is not understood.

As far as commercial cold-cathode applications are concerned, SiC junction cathodes offer currents and operating voltages that are compatible with solid state circuitry (≤15V), can be modulated at frequencies above 1MHz, and furthermore, have been operated in excess of 15,000 hours under UHV conditions without any observable deterioration in their emission characteristics [141]. In addition, more recent work on (p-GaAs)-(n-AlGaAs) junction emitters [143] has demonstrated that efficiencies as high as 4% can be obtained at current densities of up to 7Acm^{-2}.

2.3.9 The Negative Affinity Emitter

Electrons in the conduction band of a semiconductor or insulator are prevented from escaping into vacuum by the surface potential barrier, χ, measured from the bottom of the conduction band, and termed the electron affinity of the solid. For an interface between a typical semiconductor, for example Si or GaAs, and vacuum, χ is of the order of 4eV. However, it has long been known that the electron affinity of these surfaces can be lowered by depositing monolayer quantities of alkaline metals, for example caesium, and their oxides [147]. Furthermore, it is posible to create an effective negative electron affinity if band bending occurs near the surface, due to electric charge residing in surface states. This is illustrated for a p-type semiconductor in Figure 2.40. Here, a positively charged surface on the p-type semiconductor repels the positive holes from the immediate vicinity of the surface, thus exposing a fixed distribution of negative "acceptor centres" in the volume of the semiconductor. Consequently, a "depletion region" is formed under the surface, whose potential variation perpendicular to the surface plane gives rise to the band bending voltage, V_{BB}, shown in Figure 2.40. The effective affinity for electrons in the bulk (to the left of S') is clearly

$$\chi_{eff} = \chi - V_{BB} \qquad (2.25)$$

Thus, if V_{BB} is greater than the original electron affinity χ, then χ_{eff} is negative, and conduction electrons in the bulk effectively "see" no vacuum barrier. The mechanism by which caesium, and caesium oxide, produces a negative electron affinity has been explained by an electronegative-electropositive surface dipole effect, and has been reviewed by Swanson and Strayer [148]. However, work with photoemitters [149] and thermionic cathodes [150] has shown that even lower surface barriers are obtained from thick layers (many monolayers) of caesium oxide, although the mechanism is not yet understood, despite continued interest in this field; in fact, recent evidence [151,152] suggests that a quantum size effect may influence the electronic properties of

the sub-oxides that are used, for example, in oxide-coated thermionic emitters.

In the case of a practical negative affinity emitter, the band bending must occur over a distance which is smaller than the mean-free-path of hot electrons (say 50Å). For this reason, the width of the depletion region in Figure 2.40 is minimised by heavily doping the p-region with a high density of acceptors ($\sim 10^{21} cm^{-3}$), which, in ionising, produces steep band bending at the surface. Negative affinity emitters have been produced in this manner, using a Si [100] surface activated to a negative affinity with a caesium oxide monolayer [153]. The electrons for the emission process are supplied to the conduction band of the p-layer as minority carriers by means of a forward biased p-n junction, i.e using an n-type substrate. Cathodes of this type, with an active area of diameter 0.1mm, have been operated at pulsed currents of 7mA, current densities of $225 Acm^{-2}$, and efficiencies of up to 10% [147]. However, despite these promising emission characteristics, the requirement of an ultra high vacuum, and the need to maintain contamination-free surfaces, has so far limited the use of these field emitting cathodes.

2.3.10 Additional Cold-Cathode Regimes

The latter part of this chapter has been devoted to a review of some well established cold-cathode regimes that have spurred research interest in this field. However, owing to both the diversity of this subject and the vast literature that it encompasses, it has not been possible to include details on all such emitters. Accordingly, in an attempt at completeness, this section will briefly present and give reference to some additional well-known cold-cathode emitters.

The characteristics of gold-island film cathodes [154,155] have been shown to closely resemble those of the "formed" MIM cathodes described in section 2.3.6. These cathodes essentially consist of a thin Au film of thickness ~1000Å, deposited on an insulating substrate, which undergoes an electroforming process when biased in the normal conduction direction at ~5V. This process results in the formation of a discontinuous (or island) region due to a localised thermal rupturing of the film.

Electron emission from these cathodes has been shown to be located in this island region, which has a typical width of ~10μm, and is found to exhibit a transition from hot electron to F-N emission at a bias of ~8V; here, the hot-electron emission phenomenon is believed to originate from MIM structures composed of gold and the substrate, or a derivative of the substrate material.

Emission into vacuum has also been achieved, in a similar manner to the gold-island cathodes, however, using electroformed carbon films [156,157]. As in the above case, emission from the carbon cathodes is known to occur at the electroformed high-resistance discontinuous region, i.e. close to the virtual cathode resulting from this process [156]. It is further believed that hot electrons are generated in a high-field region, situated ~0.5μm from the virtual cathode, where they are subsequently scattered and emitted into vacuum. The angular and energy distributions of electrons emitted from such devices have been studied by Araki and Hanawa [157].

The "oxide cathode" [101] first generated interest amongst technologists in the 1950's where it originated from a study of the field-induced secondary emission (Malter effect) from MgO [158]. These cathodes are fabricated by depositing a porous MgO layer, typically 30-50μm thick, onto a nickel substrate prior to activation by a heat treatment in oxygen, or air, at a reduced pressure. In order to obtain electron emission, it is first necessary to "trigger" the cathode surface by UV irradiation, or electron bombardement, under the influence of an applied field; following this procedure, the emission is sustained soley by the aplied field. In operation, the oxide cathode is capable of delivering currents of a few hundred milliamps almost uniformly over the active surface area. However, from a practical point of view, the use of these cathodes is generally found to be limited due to excessive current instabilities and their delayed response to changes in the applied field. Although the emission mechanism operating with oxide cathodes remains relatively unknown, a number of models have been proposed which generally involve secondary electron and avalanching processes associated with the porous oxide layer (see [159]). More recently, however, advances [151,152] in the understanding of the role of oxides and sub-oxides in the lowering of

surface work functions may provide a fundamental insight into the emission mechanism of these and other non-metallic cold cathode regimes.

Finally, the recent technological advances made in high-temperature (T_c) superconductors [160] may provide the impetus for a renewed interest in superconducting field emitters [101], which, as in the case of the low-dimensional emitters, theoretically offer a high efficiency owing to the increase in the supply of electrons to the emitting surface.

Figure 2.40 An illustration of the negative affinity, χ_{eff}, achieved by band bending in a surface depletion region on a p-type semiconductor. (From [147]).

CHAPTER 3

EXPERIMENTAL SYSTEMS

The most widely used method of investigating the electron emission phenomenon associated with a field-emitting cathode or a HV electrode regime involves measuring the total current-voltage (I-V), and hence the F-N characteristic of the test gap. However, as described in section 2.2.1, the field-induced electron emission from extended-area cathodes is invariably localised, and arises from discrete emission centres, or sites. Consequently, for the purpose of locating, or "imaging" the individual emission sites that contribute to the total emission current, a number of specialised experimental techniques have been developed over the past two decades, e.g. the anode-probe systems described in section 2.2.1. These diagnostic techniques, which have been reviwed in detail by Latham [3], have provided a further insight into the total emission characteristics of such cathodes. For the present study of cold-cathode electron emission from extended-area emitters, an ultra high vacuum (UHV), high-voltage testing facility has been developed to incorporate a novel transparent-anode electrode module, which provides a direct, real-time site distribution imaging capability. In this chapter, an account is given of the above cathode testing facility, including associated features such as a cathode hot-stage and gas handling/monitoring systems etc, whose versitility enables a range of *in situ* emission measurements to be performed in a single vacuum environment. In addition to this main facility, details are also given of a further two systems, namely a high resolution electron spectrometer and a complementary high-voltage pulse facility which has been developed for use in conjunction with the main transparent-anode imaging system.

3.1 The Basic Experimental Facility

The electron emission characteristics of the laboratory-fabricated cold cathodes used in the present study were measured in the purpose-built ultra high vacuum (UHV) test facility which is shown schematically in Figure 3.1. This facility basically consists of a high-voltage electrode module which provides a plane-parallel

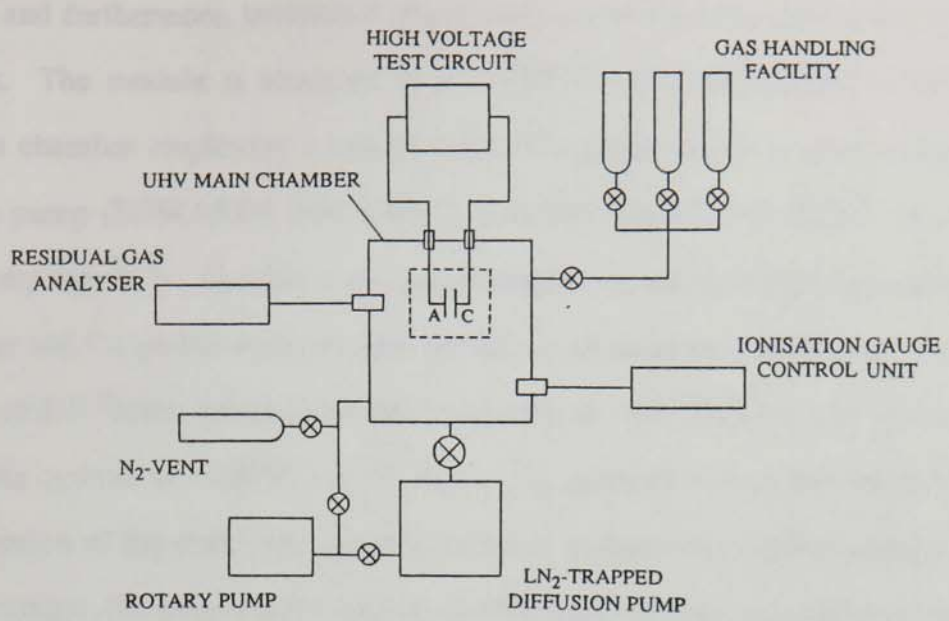

Figure 3.1 A schematic layout of the UHV high-voltage cathode testing facility.

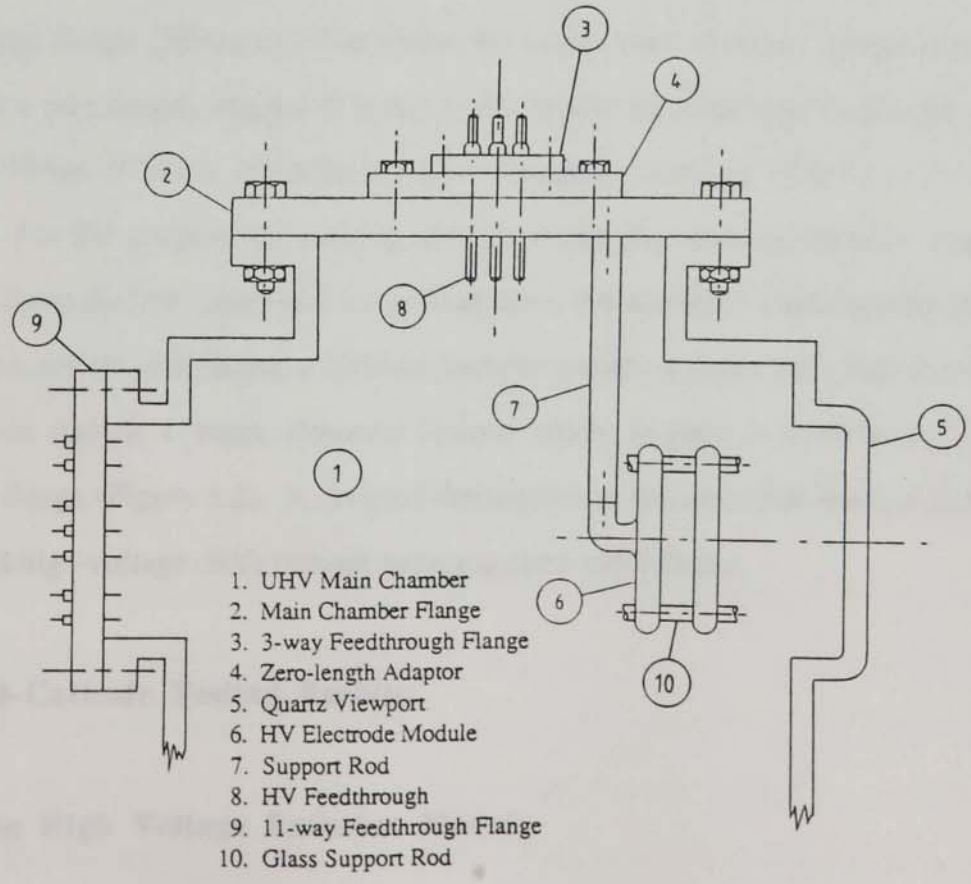

Figure 3.2 A schematic showing the basic arrangement of the HV electrode module and electrical feedthrough flanges in the main chamber.

test gap, and furthermore, includes a transparent anode for site distribution imaging purposes. The module is mounted in a VACUUM GENERATORS (VG) UHV specimen chamber employing a standard liquid nitrogen-trapped, water cooled, oil diffusion pump (EDWARDS E04, $600ls^{-1}$) and associated EDWARDS-5 two-stage rotary pump ($5m^3h^{-1}$). The above vacuum arrangement, which incorporates all-metal, knife edge and Cu gasket seals, enables emission measurements to be made at a base pressure of $\leq 10^{-8}$mbar, where an optimum pressure of $\sim 10^{-10}$mbar can be achieved by baking the system at ~200°C for 18 hours. In order to reduce the water-vapour contamination of the chamber, and thus maintain a clean vacuum following routine sample changes, the system also includes an additional nitrogen inlet valve for venting the chamber to atmospheric pressure.

Figure 3.2 illustrates the basic arrangement of the electrode module and associated electrical feedthroughs in the main chamber. Here, the main high-voltage, 3-feedthrough flange (70mm O.D.) is connected to the main chamber flange (200mm O.D.) via a zero-length adaptor (114mm O.D.), whilst an additional 11-feedthrough flange (114mm O.D.) is available for low voltage connections (<2kV) to the test module. For the purpose of viewing and recording the cathode emission images obtained from the transparent-anode arrangement, the electrode module is mounted adjacent to, and directly facing a 100mm-diameter quartz viewport via a stainless steel support rod (length 115mm, diameter 13mm) which, in turn, is fixed to the main chamber flange (Figure 3.2). A detailed description of the electrode module and the associated high-voltage (HV) cathode testing system now follows.

3.2 Cold-Cathode Testing Facility

3.2.1 The High Voltage Emission Module

The current-voltage characteristics, site distribution and stability data for the

cathodes used in this study were obtained using the plane-parallel electrode module and its associated testing circuitry shown schematically in Figure 3.3. Here, the electrode regime is seen to consist of a 14mm-diameter, extended-area test cathode, which is electrically isolated from the vacuum system via a 10mm-thick pyrophyllite insulating block, and is preset with a known separation (typically 0.5mm) from a transparent tin oxide coated anode. In practice, the electrode separation is adjusted by translating the stainless steel anode holding-structure along the three insulating glass support rods (Figure 3.2). Thus, under normal testing conditions, electron emission is obtained by applying a high positive potential to the anode which is derived from a BRANDENBURG 807R d.c EHT supply (0-30kV). In this system, the EHT supply is connected to the anode via an oil-immersed current limiting resistor whose value depends on the emission capability of the particular test cathode. To complete the basic test circuit, the cathode is connected to earth via a KEITHLEY 414S series picoammeter, which is capable of measuring emission currents in the range 1pA-10mA. For the purpose of determining the current stability of a particular cathode, the 1V full scale deflection (f.s.d.) output from the 414S picoammeter can be monitored using a JJ CR 552 chart recorder to obtain current-time (I-t) traces.

The versatility of this basic testing facility, and the emission site imaging technique to be described in section 3.2.2, has been further improved by including an *in situ* cathode heating stage. Referring to Figure 3.3, the heater is shown to consist of a 0.1mm-thick, resistive molybdenum heating element (60 x 15mm^2) which is centre-bored and electrically insulated from the test cathode by a 0.1mm mica spacer. The heater is operated by a high power FARNELL H 60/25 stabilised 60V d.c supply, which is capable of delivering a heating element current of up to 25A, and consequently enables the cathode temperature to be elevated during operation to >250^{o}C. As illustrated in Figure 3.3, the cathode temperature is monitored by an inserted chromel/alumel type-K thermocouple probe which is used in conjunction with an automatic cold-junction compensated digital thermometer (RS 612 619).

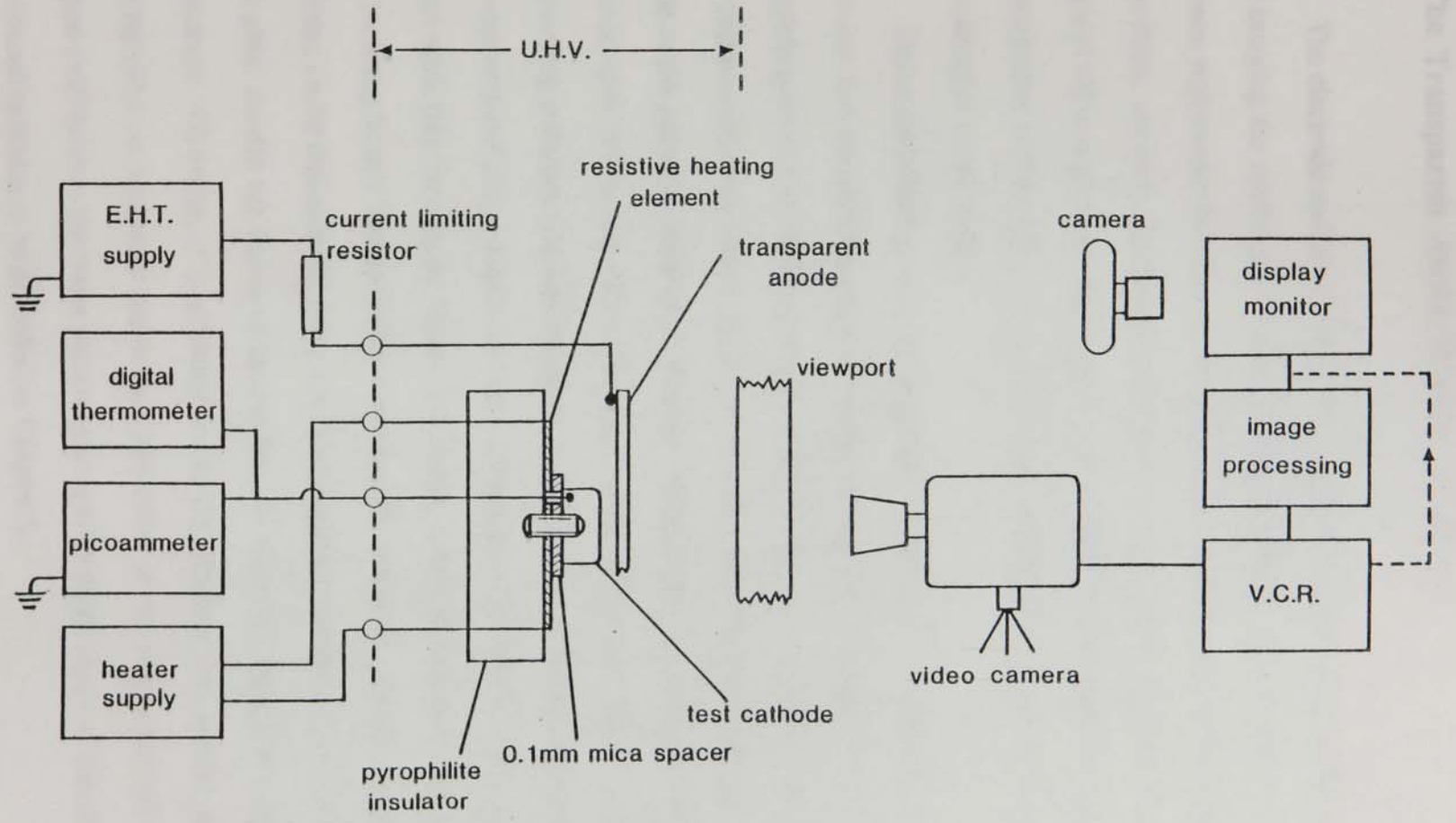

Figure 3.3 A schematic representation of the transparent-anode emission imaging module and experimental systems.

3.2.2 The Transparent Anode Imaging Technique

The electrode module shown schematically in Figure 3.3 provides a means of directly imaging the spatial distribution of the constituent cathode emission sites. In this system, replaceable transparent anodes are produced by coating 50mm-diameter, 2.25mm-thick, optically-flat Pyrex discs with a SnO_2 surface layer. This coating technique [114] is performed at a temperature of ~600°C and results in a conducting, semi-transparent surface film which is strongly adhering due to its partial diffussion into the substrate pyrex surface.

Under the influence of an applied field, electrons are emitted from sites on the test cathode, and are accelerated in the electrode gap to subsequently impinge on the SnO_2 anode surface with typical energies of a few keV. As a consequence, these high energy incident electrons induce optical excitations within the anode surface, and hence give rise to pin points of bluish light that have been termed "anode spots" [161]. Thus, the anode spot formation effectively represents a "carbon copy" image of the corresponding emission site distribution on the test cathode, and can be recorded using either conventional photographic or video techniques. To illustrate the type of result obtained with this technique, Figure 3.4 shows a typical emission site distribution image resulting from a "commercially" polished Cu electrode. Under normal operating conditions, i.e for emission currents <1mA and applied voltages of <15kV, the SnO_2-coated glass anodes are found to be durable and show no significant signs of film deterioration. However, it is generaly found that replacement anodes are required following either an electrode gap breakdown event or prolonged periods of cathode operation (>10 hours); the latter requirement applies particularly to the testing of the carbon-based cathodes to be described in Chapter 5.

At this stage, it should be noted that exploratory tests were also conducted on the suitability of metallic semi-transparent thin film anodes, e.g. glass anodes coated with sputter-deposited Mo films ranging in thickness from 200-1000Å. For this

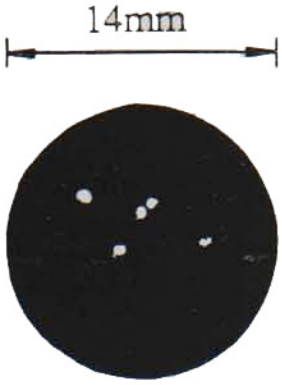

Figure 3.4 A typical example of a site distribution image obtained from a commercially polished Cu-electrode using the transparent-anode imaging technique.

Figure 3.5 A schematic representation of the emission site mapping and electron spectrometer facility. (From [75]).

Figure 3.6 A schematic of the interface lens assembly for the high-resolution electron spectrometer. (From [75]).

application, Mo was initially chosen as a coating medium since it offered a suitable compromise between the ideal anode film properties, viz (a) a high melting point, (b) a high thermal and electrical conductivity, and (c) ease of film deposition. However, although high definition emission images, comparable to the SnO_2 anode images, were obtained from the Mo films, a series of tests have indicated a preference for the use of SnO_2 anodes; the Mo films were invariably found to be fragile, and ultimately limited by their susceptibility to both pin-hole deterioration and localised adhesion failure, i.e. such as typically observed with phosphor screen anodes [114].

3.3 Ancillary Systems

In addition to the basic experimental features outlined in the last two sections, the experimental facility used in this study includes a number of ancillary systems (see Figure 3.1) which were routinely utilised during the testing of the cold-cathodes. In this section, an account will first be given of the residual gas handling and monitoring facility, followed by a description of the video system which has been commisioned for recording the test cathode emission site distribution images.

3.3.1 Gas Handling and Monitoring

In order to study the effects of the residual gas environment on cathode operation, an auxiliary UHV gas handling facility is interfaced to the main chamber for the introduction of any commercially-available gas species to a chosen pressure (typically in the range 10^{-2}-10^{-7}mbar). In practice, the residual gas environment in the experimental chamber is controlled by admitting gases from BOC gas cylinders (BS 341) via a VG MD6MR sapphire/metal UHV leak valve. Here, the main chamber pressure is monitored before and during a cathode testing period using a standard VG VIG8 ionisation gauge and associated ion gauge control unit (VG TCS6), which enable

vacuum pressure measurements to be made in the range 10^{-2}-10^{-11}mbar. In order to maintain a clean, leak-free vacuum, and furthermore, monitor any outgassing effects which may occur during electron emission from a test cathode, a residual gas analyser (RGA) (Vacuum Analyst, VSW Scientific Instruments) is also incorporated into the main chamber via a standard 70mm vacuum port. This analyser measures the partial pressures of all the residual gases in the atomic mass range 1-100, and can be interfaced with a chart recorder to obtain a spectrum of the relative gas pressures; alternatively, the analyser can be used to monitor the partial pressure of a single gas species during cathode operation. It should be noted, however, that although these analysers give a realistic indication of the gases present in the chamber, the quantitative data thus obtained cannot be considered as absolute.

3.3.2 VHS Video Recording of Emission Site Distributions

In previous transparent-anode studies [162] on the spatial imaging of emission sites on broad-area electrodes, a standard 35mm camera was used to record the resulting site distribution images. However, since it is well established [3] that non-metallic electron emission sites on such cathodes are commonly unstable, particularly being subject to random switching instabilities, an effort has been made to upgrade the image recording and analysis technique by using modern VHS video recording and computer image processing techniques. This new recording facility, shown schematically in Figure 3.3, is used to obtain a complete record of the total emission activity on a test cathode during an extended period of cathode operation (typically 20 mins).

The system used in this study esentially consists of a PANASONIC WVP-F10E high-sensitivity colour camera, a PANASONIC NV-G10B high quality (HQ) video cassette recorder (VCR) and a SHARP CV-3707HD 14-inch colour monitor. The camera, which incorporates a 16mm charge coupled device (CCD) high-resolution image sensor, has particular qualities in relation to the recording of emission sites, in

that it offers (a) low-light operation (7lux), (b) operation without "image burn" effects, i.e. such as might be encountered with local breakdown phenomena, (c) the option of on-sceen titles, and (d) can be adapted to accommodate a standard 35mm camera lens and extension tubes for zoom, high-magnification viewing.

For the recording of emission site distribution images from 14mm diameter cathodes, this system is capable of magnifying the total emission image by up to 20 times on the monitor screen, where the resulting images can be subsequently stored onto standard VHS video cassettes. In addition, the audio track is used in conjunction with the built-in camera microphone to record the current and voltage data corresponding to particular site distribution images. In order to obtain a "hard copy" of a site distribution from the video tapes, the recorded images can be "frozen" on the monitor screen using a special "Still Frame" option and subsequently photographed. Alternatively, the images can be transferred to 5.25" floppy disks using digital "frame store" techniques, and can then be computer-analysed using standard image processing software packages.

3.4 The High Resolution Electron Spectrometer

As described in section 2.2.1, the energy analysis of emitted electrons has proved to be a powerful tool in the understanding of the fundamental electronic processes involved in the field-induced electron emission mechanism. In order to obtain energy data for the emission process investigated in this study, a high-resolution electron spectrometer facility has been used. This facility, whose design and operational details have been fully described elsewhere [70-72], is based on a UHV ($<10^{-10}$mbar) hemisperical electron energy analyser which is shown schematically in Figure 3.5.

In operation, an associated electronic drive system is used to spirally scan the test cathode across the anode probe-hole to obtain a "map" of the distribution of

emission sites. Referring to Figure 3.5, the spiral scan generator provides two voltage sequences $V_{x(t)}$ and $V_{y(t)}$ which, when fed to the x and y drive circuits, result in the 14mm diameter cathode being scanned in a 200-turn spiral pattern, i.e corresponding to a line separation of ~40μm. These same voltages are also used to simultaneously scan the spot of a storage oscilloscope to provide a synchronised display of the specimen motion. For the purpose of locating the relative positions of emission sites, a point is reached during the scan when a site directly faces the probe-hole, so that the emitted electrons are collected by the lens assembly directly behind the anode, and the resulting current is measured by picoammeter 1. This signal, together with the total cathode current (picoammeter 2), is fed into the comparator and oscillator circuit which consequently switches to an on-state. The 15V, 10kHz output from the oscillator then activates the z-modulation input of the storage oscilloscope which, in turn, "brights up" the previously extinguished trace. This technique eventually results in an oscilloscope site "map" which represents the relative positions of the individual emission sites on the test cathode. Having followed this procedure, a chosen site can then be manually relocated in front of the probe-hole for energy analysis: in fact, at the time of writing, the specimen drive and electron spectrometer systems are in the process of being upgraded to incorporate a computer-control interface.

Having thus located an emission site for analysis, the emitted electrons pass through the anode probe-hole and enter the interfacing electron lens assembly [71], shown schematically in Figure 3.6. By applying the appropriate lens potentials (supplied from an external voltage divider circuit [71]), the emitted electrons are projected onto a phosphor screen to produce a magnified image of the emission site and its sub-sites, i.e. such as shown in Figures 2.10 and 2.18. Refering to figure 3.6, the phosphor screen incorporates a 0.5mm dian.eter axial probe-hole which serves as the entrance aperture to the input lens assembly of the 50mm diameter hemispherical analysing element. This is based on a similar design to that developed by Kuyatt and Plummer [163], and has been described in detail elsewhere [70]. Hence, this

arrangement enables the electron energy distribution to be measured with respect to the Fermi level (FL) of the substrate cathode, over a scan width of up to 10eV. The calibration of the spectrometer [70] involves using a clean tungsten micropoint emitter, where it has been theoretically predicted by Young [164] that the Fermi level will correspond to a point 73% up the high energy slope of the distribution recorded at room temperature (300K). In addition, this measurement also serves to determine the resolution of the spectrometer, which has subsequently been measured at ≤30meV [70], i.e. as determined directly from the tungsten micropoint distributions using the method described by Young and Kuyatt [165].

3.5 The High Voltage Pulse Facility

The use of pulsed voltages for the routine evaluation and operation of cold-cathode electron sources is becoming increasingly important, particularly for high-current and high frequency applications. From a practical viewpoint, the generation of pulsed waveforms with moderate peak voltages (<1000V), i.e as typically required for micropoint cathodes, poses no technological difficulties; furthermore, frequencies in the MHz range are readily obtainable. However, for the pulsing of high voltages (>1kV) and high currents, serious problems arise in obtaining fast pulse-rise times, owing to a variety of effects [166], which ultimately impose a high frequency limit on the pulsed waveform.

In this section, an account will be given of a pulsed high-voltage testing system which has been developed and interfaced with the existing UHV test facility described in section 3.1. This system, which is shown schematically in Figure 3.7, consists of a high-voltage (HV) pulse generator and an associated current detection circuit, which together enable the real-time monitoring of both the applied voltage and emission current waveforms.

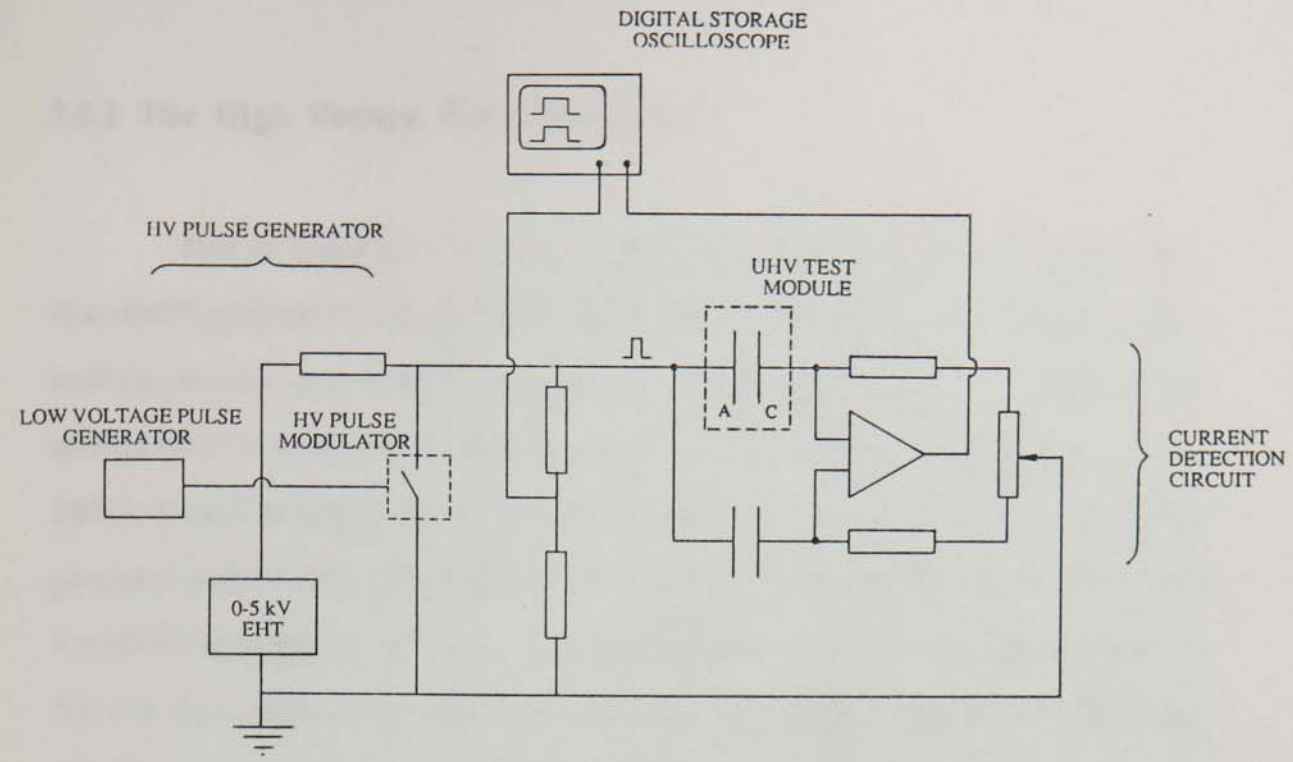

Figure 3.7 A schematic representation of the high-voltage pulse generator and current detection unit.

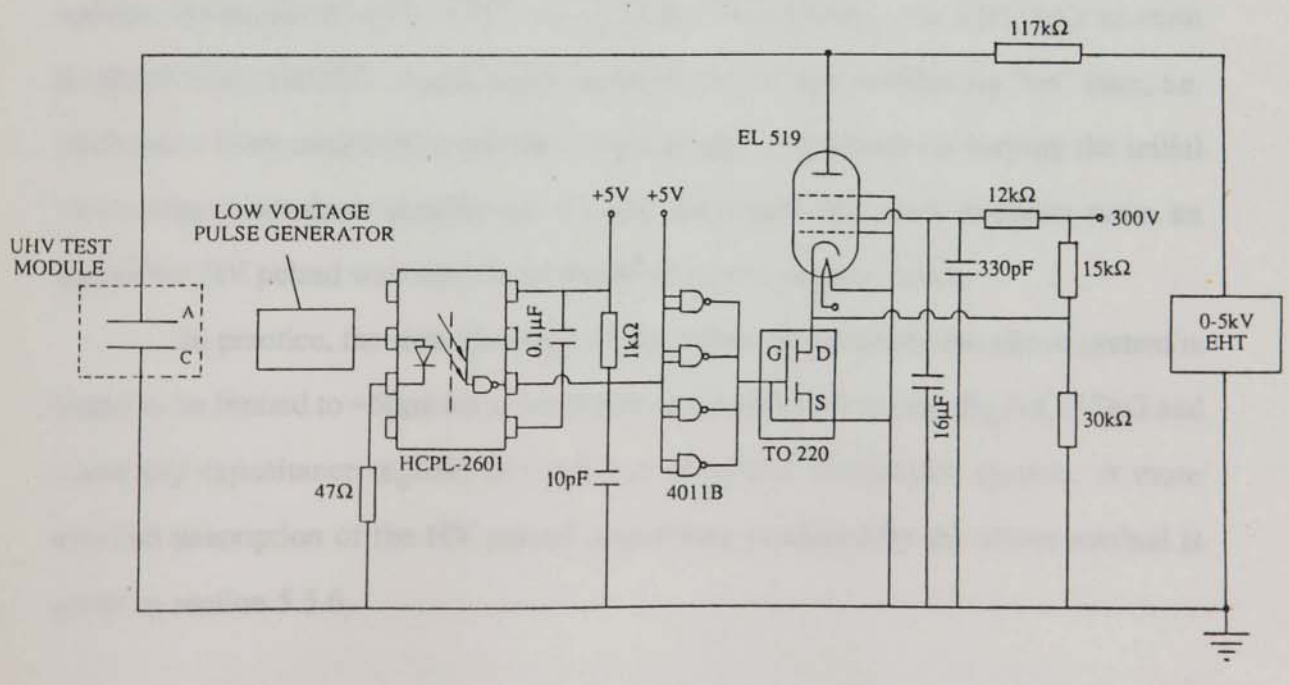

Figure 3.8 A circuit diagram of the hard-valve, high-voltage pulse generator.

3.5.1 The High Voltage Pulse Generator

This is based on a hard-valve HV pulse generator design, as originally described by Johnson [167], and produces a positive high-voltage pulse train at the test module anode via a parallel-feed HV valve modulator [168]. A circuit of this arrangement is given in Figure 3.8, which illustrates how an opto-isolator (HCPL 2601) is used to couple the trigger pulse-train from a standard low-voltage pulse generator (ADVANCE INSTRUMENTS PG 58A) into the common input of a parallel 4 x 4011B logic gate arrangement. This transforms the original trigger waveform into a fast rise time, high-current pulse, which is then fed into the input of a TO220 field-effect transistor (FET). Subsequently, the drain output voltage of the FET is used to modulate the cathode potential of a MULLARD EL519 HV thermionic valve: the 300V grid potential, and the ancillary 5V source to the opto-isolator and logic gates, are supplied from a SOLARTRON VARI-PACK. Thus, when the valve is biased to open curcuit, the variable 0-5kV positive EHT output from an AEI P120 power supply appears at the anode of the UHV test module. Susequently, the EHT falls to earth potential when the FET trigger-pulse biases the valve to a conducting "on" state, i.e. produces a short circuit or "crow bars" the test gap. Therefore, by varying the initial low-voltage waveform parameters, e.g the frequency and mark-to-space ratio, an equivalent HV pulsed waveform is produced at the test module anode.

In practice, the total rise time of the pulses produced by the above system is found to be limited to ~60μs for a current-limiting series resistance (R_L) of 117kΩ and a test gap capacitance ($\varepsilon_o A/d$) of ~5pF, i.e. as used in the present system. A more detailed description of the HV pulsed waveforms produced by the above method is given in section 5.3.6.

3.5.2 The Current Detection Circuit

In order to measure the real transient emission current response of the test cathode to pulsed-field conditions, the system incorporates a tunable RC bridge circuit, shown schematically in Figure 3.7. This circuit utilises an ultra high-speed differential operational amplifier to detect the off-balance bridge voltage, which is directly proportional to the current emitted from the test cathode. Details of the bridge and op amp circuits are given in Figure 3.9.

In this system, the choice of a bridge current detection circuit was based on its ability to compensate for the transient charging/displacement signal, i.e. resulting from the charging of the HV electrode on each pulse cycle; in fact, the present circuit eliminates the charging transient which would otherwise "mask" the emission current signal. Referring to Figure 3.9, the bridge consists of a tunable, parallel RC network, where the capacity in one arm of the bridge is due to the inherent capacitance of the UHV test module: in comparison, the "dummy" HV capacitor (≤10kV) in the opposite arm is fixed at a value of 5pF, i.e. approximately equal to the test module capacitance. Thus, prior to the testing of a cathode under pulsed-field conditions, it is first necessary to tune, or balance, the bridge circuit so that $V_B=0$ for no emission current. This procedure involves the initial application of pulsed peak voltages which are lower than the threshold voltage for electron emission from the test cathode. Under these conditions, the resulting bridge current (i.e the unbalanced charging transient), which is monitored on the oscilloscope screen ($V_B\neq0$), can be effectively eliminated by adjusting the 0-100Ω, 2W-cermet potentiometer. From this point, the bridge can be considered as "tuned" for detecting the transient electron emission current from the test cathode. Subsequently, as $V_{app}(t)$ is increased above the emission threshold value, the cathode begins to emit, which, in turn, results in an off-balance bridge current, and proportional voltage drop, $V_B(t)$, appearing across the bridge. Accordingly, this voltage is amplified by approximately 20 times to give a signal $V_o(t)$ which represents the transient cathode

emission current. This is subsequently fed to one channel of a GOULD ADVANCE OS 4000 digital storage oscilloscope for comparison with the applied voltage waveform.

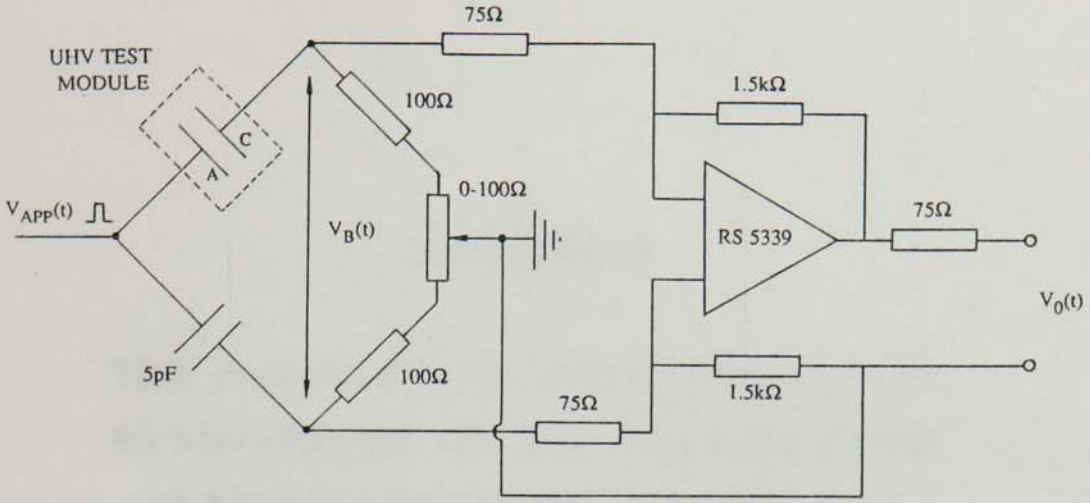

Figure 3.9 A circuit diagram of the RC-bridge current detection unit for pulsed-field cathode operation.

CHAPTER 4

THE INFLUENCE OF THE RESIDUAL GAS ENVIRONMENT ON THE FIELD-INDUCED ELECTRON EMISSION PROCESS: GAS CONDITIONING

4.1 Introduction

Vacuum-insulated high-voltage (HV) electrodes are extensively employed in a variety of practical applications, including industrial, research and space power systems. However, in these applications, it is generally found that their performance is limited by the sudden, and largely unpredictable, breakdown of the vacuum gap which can ultimately render the electrodes inoperable. At present, it is generally assumed [25] that such breakdown events are initiated by electron emission processes that occur at microscopic locations on the electrode surface, where the emission is strongly dependent on these localised surface anomalies. Thus, in order to improve the performance of the electrode gap, i.e. increase its voltage hold-off capability, it is conventional to use an appropriate electrode surface conditioning technique to eliminate, or suppress, the prebreakdown emission processes. Previous research in this field has focussed on four main conditioning techniques, namely gas conditioning [27-31], glow- discharge conditioning, current conditioning, and spark conditioning, where the latter three processes have been reviewed elsewhere by Latham [3].

Of the above conditioning techniques, gas conditioning has proved to be the most widely used and, reportedly, the most effective procedure for suppressing the localised electron emission that is typically observed from high-voltage electrodes in the applied field range 10-30MVm^{-1} [9]. This technique, as originally reported by Lyman et al. [27], Alpert et al. [28], Ettinger and Lyman [29], and later by Buekema [30,31], involves introducing an inert gas (usually He or Ar) into the UHV chamber at a pressure ~10^{-5}-10^{-4}mbar, whilst establishing an initial prebreakdown current of typically 1μA at a constant field approaching that required for normal electrode operation. In these early experiments, Ettinger and Lyman [29] used argon gas at a pressure of ~10^{-3}mbar, and maintained a constant current of ~50μA for a few hours of operation. Subsequently, this procedure led to improvements in voltage hold-off capability of 3 to 5 times the unconditioned values for both copper and tungsten

electrodes.

At the time of these findings, it was generally accepted that the localised electron emission phenomenon was associated with "metallic" Fowler-Nordheim emission that was assumed to occur at isolated "whiskers" or microprotrusions [2] on the electrode surface. Subsequently, a model of the gas conditioning phenomenon was proposed by Alpert et al. [28], which assumed that gas ions, formed in the electron beams emitted by the protrusions, are "funnelled" back onto the protrusions by the converging local field, progressively blunting them by a selective sputtering process, and thus suppressing the emission. In investigating the sputtering interpretation, Bloomer and Cox [169] extended their study to include non-inert gases such as oxygen and mercury vapour. Thus, although these authors observed a significant conditioning effect with the heavier gases, their comparison of the degree of conditioning obtained with Ar and O_2, which are known to have comparable ionisation cross-sections and sputtering powers, yielded contradictory results under identical experimental conditions. In fact, no conditioning effect was observed with Ar at a pressure of ~10^{-6}mbar and an initial prebreakdown current of ~10^{-7}A, which consequently led the authors to postulate that some further mechanism was operating with the active oxygen gas. In a similar series of experiments, Buekema [30] found no significant improvement in the performance of titanium and stainless steel electrodes after conditioning, and furthermore, occasionally observed a de-conditioning effect for high-field situations where the total gap current exceeded 10^{-7}A.

Despite these somewhat sporadic, and inconclusive early findings, gas conditioning now plays a vital role in the routine preparation of, for example, the superconducting RF cavities [174] commonly used in modern particle accelerator systems. However, to date, the conditioning of such devices is largely conducted on a "rule of thumb" basis, where results obtained with identical electrode regimes can often differ quite dramatically: in this respect, it is apparent that there remains the need for a comprehensive study of the gas conditioning phenomenon to alieviate, or otherwise

clarify these inconsistencies. Moreover, since it is now widely recognised that electron emission sites are in fact composed of anomalous, micron-sized particulate structures [3], that promote a "non-metallic" emission mechanism, doubts have arisen as to the validity of the sputtering interpretation of gas conditioning. In particular, there have been informal suggestions as to whether the conditioning phenomenon may arise from induced "electronic" changes to the surface, or bulk, of a dielectric-like emission regime. Consequently, it may be necessary to revise the sputtering model in the light of these speculations and the newly emerging experimental findings.

4.2 Electrode Preparation

For the series of gas conditioning experiments to be described in this chapter, a standard planar-disc cathode was adopted, and incorporated into the transparent-anode electrode module described in section 3.2. These cathodes are machined from Oxygen-Free, High-Conductivity (OFHC) copper rods to a diameter of 14mm, a thickness of 5mm, and also include a 0.5mm edge radius to minimise the effects of field enhancement at the front-face periphery [3]. Furthermore, to enable their accommodation in the electrode module, the cathodes incorporate a centre-tapped 4BA thread, as shown schematically in Figure 3.3. Thus, prior to assembley in the electrode module, the cathode surface is initially ground on a 1200-grade abrasive pad, followed by a series of polishing stages on metallographic diamond-paste wheels, which finally results in a surface finish of $\leq 1\mu m$. Following this procedure, both the cathode and transparent-anode are rinsed with distilled water and then separately cleaned in an ultrasonic methanol bath for ~20 mins to remove any organic surface contamination and loosely adhering particles.

In order to obtain the required electrode gap spacing, and furthermore, ensure a plane-parallel alignment of the electrode assembly, the gap is preset using PVC spacers in conjunction with a pair of identical "dummy" electrodes. Finally, on completing this operation, the cleaned test electrodes are then mounted into the electrode

module, which in turn is inserted into the main vacuum chamber for testing under UHV conditions.

4.3 Experimental Findings

In this section, results will be presented from a study on the effects of the residual gas environment on the spatial and temporal behaviour of populations of "natural" emission sites on planar OFHC Cu-cathodes. This study evolved from a preliminary series of experiments on the He-conditioning of Cu-electrodes, which was subsequently extended to include a wider range of common gas species, namely He, Ar, Ne, N_2, H_2, O_2 and CO. Thus, the present study constitutes a comprehensive reappraisal of the gas conditioning phenomenon, and, as will be shown, has identified a number of experimental consistencies, in particular the "Voltage" and "Temperature" effects, which are crucial to both the fundamental understanding and technological application of the conditioning process. In addition, results will also be presented from a series of measurements on the electron energy spectra of emission sites obtained during gas conditioning, and a complementary investigation into the influence of surface oxidation on the field-induced electron emission process.

4.3.1 He-conditioning of emission sites on planar Cu-electrodes

Although He-conditioning of HV electrodes is a well established procedure, no direct experimental evidence has been presented to date that confirms the basic assumptions of the phenomenon. Here, previous studies have largely been conducted on the basis of indirect measurements of the gap I-V characteristics and breakdown strengths of conditioned electrodes. For the present investigation, a more versatile experimental system, which includes an optical imaging facility, has been used to monitor the spatial and temporal behaviour of a population of emission sites during a

period of He-conditioning.

In this series of experiments, a planar Cu-cathode is mounted in the transparent-anode imaging module, and preset with an appropriate gap spacing (typically 0.3mm), i.e. as illustrated in Figure 3.3. Subsequently, the vacuum chamber and gas supply line are then evacuated to a pressure of ~10^{-8}mbar before applying a slowly increasing positive voltage to the anode until the switch-on of emission sites is observed [9]. Then, having established a stable emission current of ~1μA, He-gas is introduced into the chamber to a pressure of ~10^{-5}mbar. From this point, the conditioning process is set in progress under constant field conditions, and temporal changes in the total gap current are continuously recorded using video techniques whilst complementary photographs are taken of the emission site distribution at 5min intervals.

This experimental technique has been used to investigate the temporal evolution of the He-conditioning process at a constant applied field of ~25MVm^{-1}, i.e. corresponding to a gap voltage of ~8kV. In order to demonstrate the typical manifestation of the gas conditioning effect, Figure 4.1 shows how an initial gap current of I_i~1μA decays in an exponential manner, in the presence of a He environment (p~10^{-5}mbar), to a final equilibrium value of I_f~0.1μA; typically, the "saturation" of the current decay under constant field conditions, i.e the tendency to an equilibrium level, is found to occur after a 15-20 minute period of conditioning. From a practical point of view, Figure 4.1 also illustrates how the current instability is typically reduced following conditioning, for example, from ~20-10% in this case.

For the purpose of demonstrating the corresponding induced-changes in the site distribution resulting from He-conditioning, the sequence of photographs presented in Figure 4.2 shows the temporal variations in a population of emission sites obtained at subsequent stages of the process. Thus, in the 15 minute interval between Figures 4.2(a) and (d), the initial gap current of ~1μA is reduced by approximately one order of magnitude, corresponding to a systematic decrease in the number of dominant emission

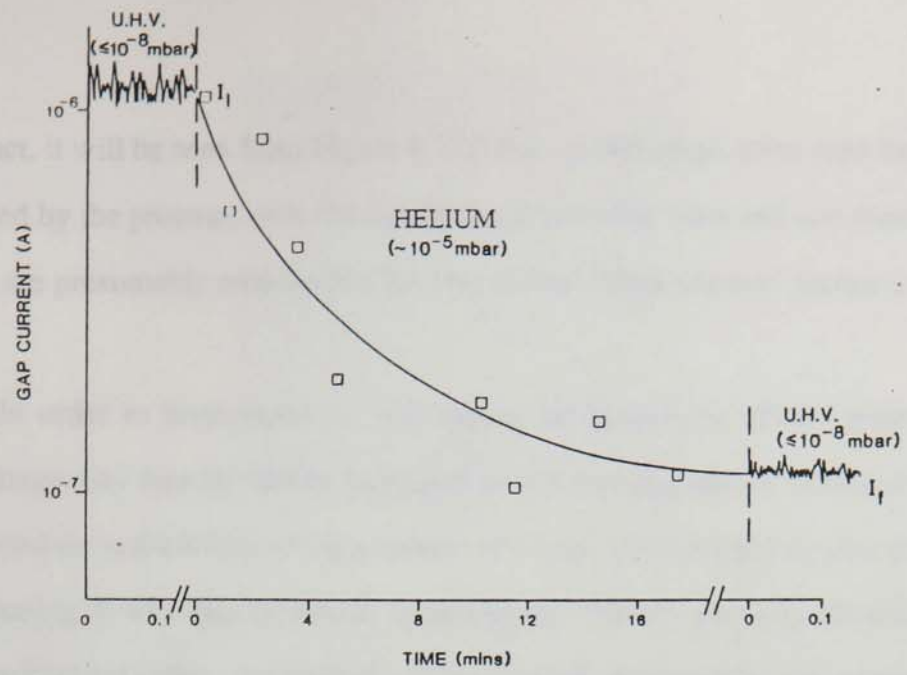

Figure 4.1 A typical experimental demonstration of the gas conditioning effect showing how the gap current, i_g, and its noise level, decays with time in the presence of a He-environment at a pressure of ~10^{-5}mbar, V_g=20kV and d=0.5mm.

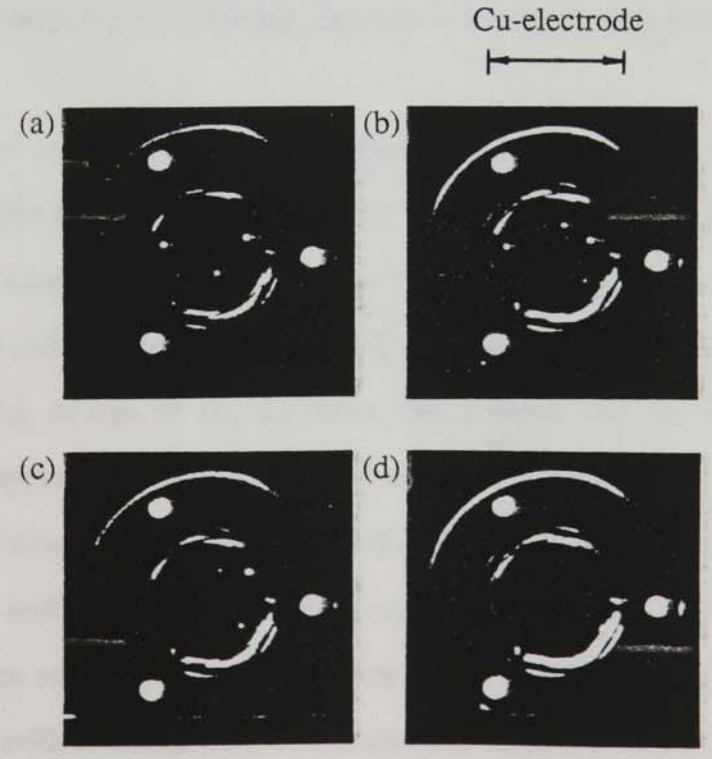

Figure 4.2 Typical site distributions taken at 5 minute intervals during a He-conditioning sequence at ~10kV and a gas pressure of 10^{-5}mbar.

sites. In fact, it will be seen from Figure 4.2(d) that, at this stage, most sites have been extinguished by the process, with the exception of two edge sites and one faint central site which are presumably responsible for the residual "dark current" shown in Figure 4.1.

In order to investigate the full extent, or limitations of this process, the applied voltage may then be further increased until a new population of emission sites have switched-on and are delivering a current of ~1μA. Following a similar period of He-conditioning, it will then be found, as previously, that the new gap current decays to some equilibrium value. Accordingly, this sequence of operations may generally be repeated at incremental increases in the gap voltage before it is found that an upper limit of ~13kV (i.e. E~40MVm^{-1}) is reached, beyond which, no further conditioning occurs: the degree of conditioning obtained at subsequent stages of such an operation is further investigated in section 4.3.3. Thus, Figure 4.3 shows a typical residual site distribution that is observed at the upper limit of the He-conditioning process, and is characterised by a large number of small sites which are found to be immune to further conditioning.

In order to determine whether the conditioned sites are permanently extinguished by this process, the gap voltage is increased, under UHV conditions, beyond its final conditioned value. Thus, Figure 4.4 shows the resulting site distribution for the cathode shown in Figure 4.2, where the gap voltage has been cycled to 14kV following delays of (a) 20 mins, (b) 3 days, and (c) 3 weeks after conditioning. By applying a spatial correlation technique developed in a previous study [162], it can be established that the conditioned sites, shown in Figure 4.2, have failed to re-appear, thus indicating that the conditioning process is permanent under these conditions and time scales. Furthermore, from a fundamental viewpoint, Figure 4.4 also illustrates the evident difference between site distributions obtained under identical conditions, and clearly demonstrates that the site distributions are unstable over a time scale ≥hours, i.e. indicating inherent switching-instabilities.

Figure 4.3 Typical emission site distribution at the He-conditioning limit of V_g~13kV (E_g=40MVm^{-1}).

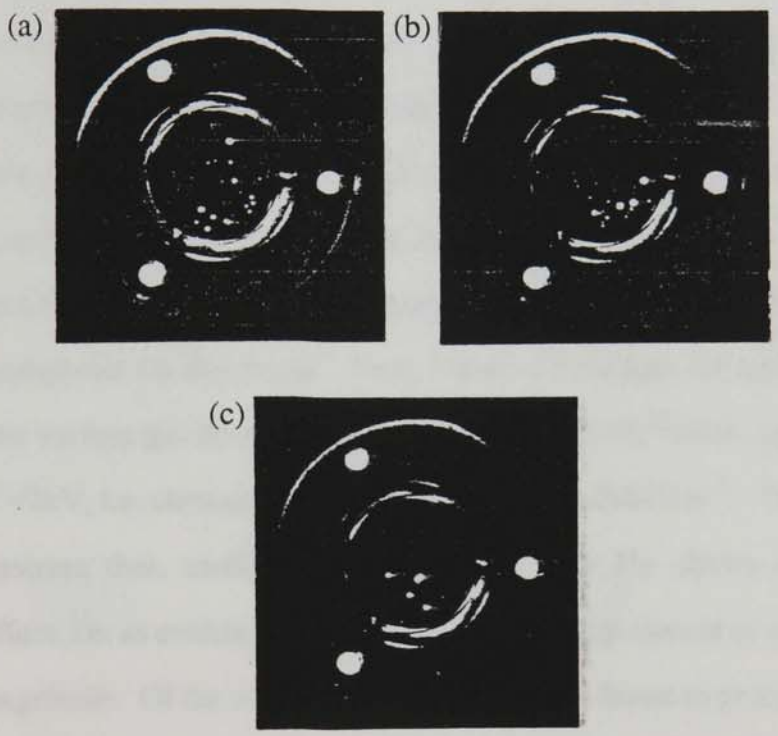

Figure 4.4 Spatial correlation of emission sites recorded at V_g~14kV, following delays of (a) 20 mins, (b) 3 days and (c) 3 weeks after conditioning.

4.3.2 An extended study of Gas Conditioning under moderate voltage conditions for an extended range of gas species

Having established the effectiveness of He-conditioning in extinguishing, or otherwise reducing electron emission processes under moderate voltage (≤10kV) and field (≤30MVm^{-1}) conditions, it was considered necessary to perform a similar series of experiments to compare the relative conditioning effectiveness of an extended range of gas species, under the same experimental conditions as described in the previous section. These measurements were considered to be important both in the fundamental context of understanding the underlying conditioning mechanism, and furthermore, in determining the influence of the residual gas environment on, for example, the routine operational characteristics of a practical cold-cathode electron source.

In this study, comparative measurements have been made, under identical experimental conditions, on the influence of seven different gas species (He, Ar, Ne, N_2, H_2, O_2 and CO) on the spatial and temporal behaviour of typical populations of emission sites on planar Cu-electrodes. Thus, Figure 4.5 collates the total gap current responses for the various gas environments at a pressure of ~10^{-5}mbar, and a moderate gap voltage of ~7kV, i.e. corresponding to a gap field of ~20MVm^{-1}. These findings clearly demonstrate that, under these conditions, only He shows a significant conditioning effect, i.e. as evidenced by a reduction in the gap current of approximately one order of magnitude. Of the remaining gases, only Ar is found to promote a similar, although far less dramatic suppression of the total emission current. In comparison, Ne, O_2 and CO generally result in a small increase (typically <50%) in the mean current level over a 20 minute period, and furthermore, significantly de-stabilise the mean current level; this latter effect is particularly prominent with an O_2 or CO environment. Finally, Figure 4.5 also shows how N_2 and H_2 appear to play a relatively inactive, or passive, role, where speculation exists as to whether an N_2 environment may even significantly stabilise the gap current.

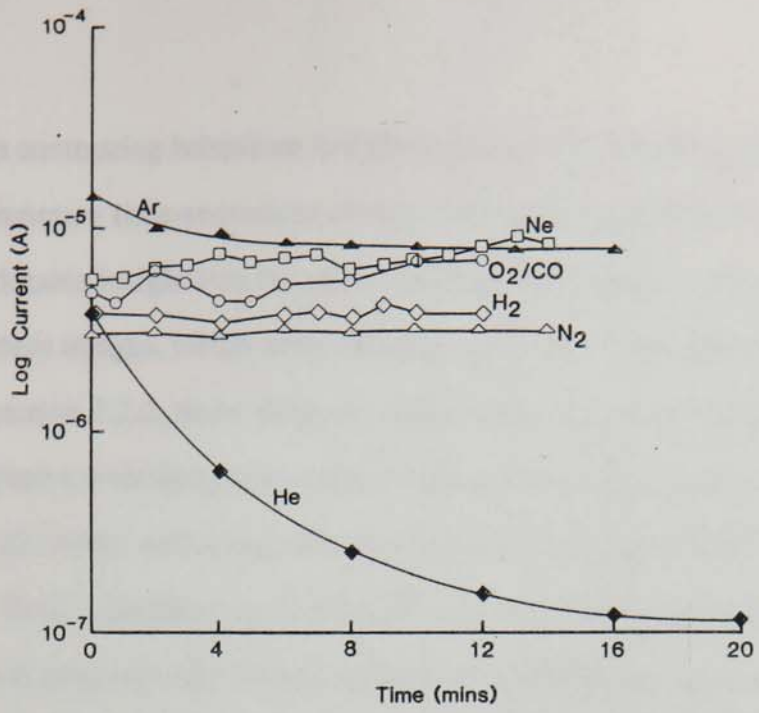

Figure 4.5 Plots showing how the total gap current varies with time under various residual gas environments at a pressure of 10^{-5}mbar, and a field of 20MVm^{-1}. (Gap voltage = 7kV).

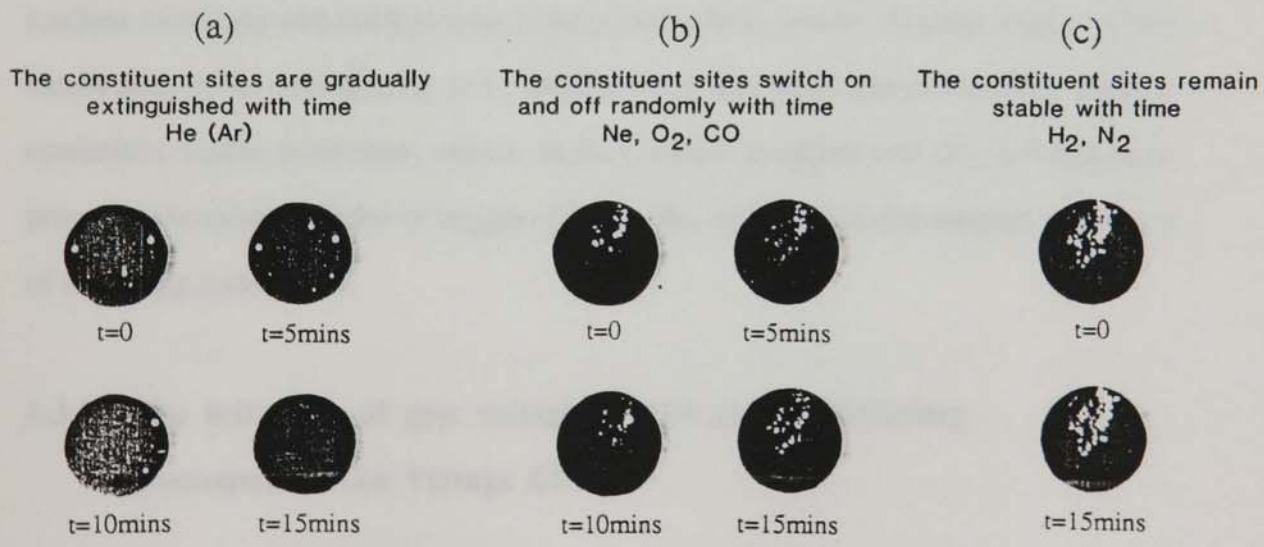

Figure 4.6 Sequences of emission images at a constant field of 20MVm^{-1}, showing how the temporal evolution of site distributions depends on the residual gas environment. (Gap voltage = 7kV). (a) He and Ar, (b) Ne, O_2 and CO, and (c) H_2 and N_2.

This contrasting behaviour to different gas environments is further illustrated in the complementary time-sequences of emission images shown in Figure 4.6, which provide considerable insight into the physical origin of the current responses shown in Figure 4.5. These images, which were obtained using the transparent-anode technique described in section 3.2.2, show three alternative ways in which a population of sites can typically evolve with time, under the influence of the various gas environments at a pressure of ~10^{-5}mbar, and a constant gap field and voltage of 20MVm^{-1} and 7kV respectively. Thus, with He, it is shown in Figure 4.6(a) how the initial population of emission sites is progressively reduced with time, until finally, all dominant sites are extinguished; a similar, although far less dramatic effect is observed with Ar, where however, it is generally observed that a persistent site population remains after the 20 minute conditioning period. In contrast, with O_2, CO and to some extent Ne, there is an apparent random variation in the site population with time (Figure 4.6(b)), without any systematic reduction in the total number of sites. In fact, from an detailed analysis of the images in Figure 4.6(b), it is apparent that the individual sites are prone to random switching and corresponding fluctuations in intensity. Finally, Figure 4.6(c) shows that, in the case of a H_2 or N_2 environment, the initial site distribution remains essentially stable with time, where, in fact, video recordings of this process have provided tentative evidence to suggest that N_2 may even reduce the inherent occurence of switching instabilities.

4.3.3 The influence of gap voltage on the gas conditioning phenomenon: the Voltage Effect

In the previous section, it was demonstrated how chemically-dissimilar gas environments give rise to quite contrasting patterns of electron emission behaviour, under identical experimental conditions, where only He and Ar result in a significant "conditioning", or suppression of the gap current. In comparison, previous

publications [169,170] have claimed to have observed the conditioning phenomenon with O_2, for similar applied fields, however, at a higher gap voltage of 13kV, i.e. as opposed to the moderate 7kV used in the present study. Moreover, during the course of experiments on He-conditioning, it was observed that the "emissivity" of a particular cathode, i.e corresponding to the range of gap voltages required for normal operation, appeared to influence the degree of conditioning obtained over a 20 minute period; in particular, it was noted that conditioning did not occur at voltages <5kV. Collectively, these observations, including the high-voltage limitation revealed in section 4.3.1, provided an incentive for a further series of experiments designed to determine the influence of the gap voltage, V_g, on the gas conditioning phenomenon.

In order to assess the importance of V_g, a Cu-cathode was successively conditioned at an increasing gap spacing, typically in the range 0.3-1.0mm, whilst maintaining a constant gap field of ~20MVm^{-1}. This procedure was repeated for a number of common gas species, at a pressure of ~10^{-5}mbar, whilst monitoring the current suppression obtained at each successive gap voltage. Thus, Figure 4.7 illustrates how the effectiveness of the He-conditioning process depends on the gap voltage, V_g, as it is successively increased from 5 to 7, 9, 11 and 13kV. From these plots, it is clearly seen that the He-conditioning effect is voltage-dependent, where, in the voltage range 5-11kV, the degree of conditioning increases asymptotically with increasing V_g.

Since it was observed in section 4.3.2 that Ar also promotes a conditioning effect, although to a lesser degree, an experiment was conducted to compare the relative effectiveness of both the He and Ar processes over a range of gap voltages. In order to facilitate a systematic analysis of the type of data obtained in such experiments, it is convenient to define a "coefficient of conditioning", C_c, given by the fractional reduction of the gap current under constant field conditions, i.e

$$C_c = (I_i - I_f)/I_i \qquad (4.1)$$

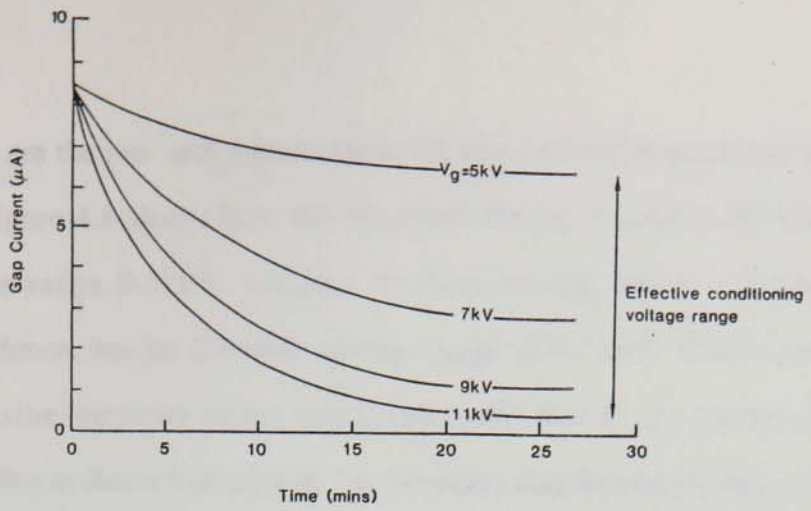

Figure 4.7 The "voltage" effect: an illustration showing how the degree of He-conditioning, at a constant field of 20MVm^{-1}, depends on the gap voltage V_g.

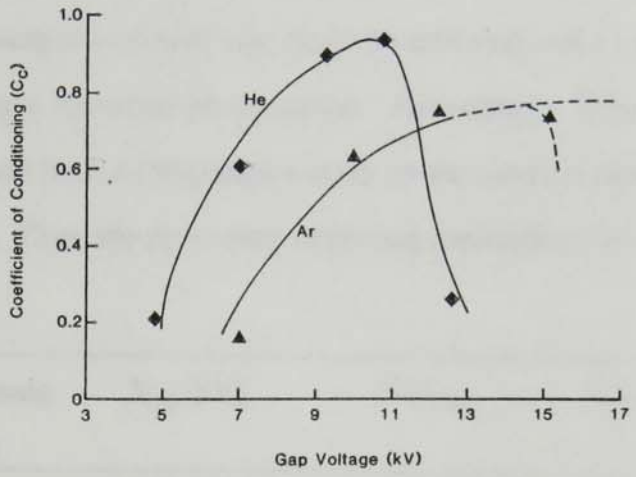

Figure 4.8 A further illustration of the voltage effect: namely how the optimum conditioning voltage depends on gas species.

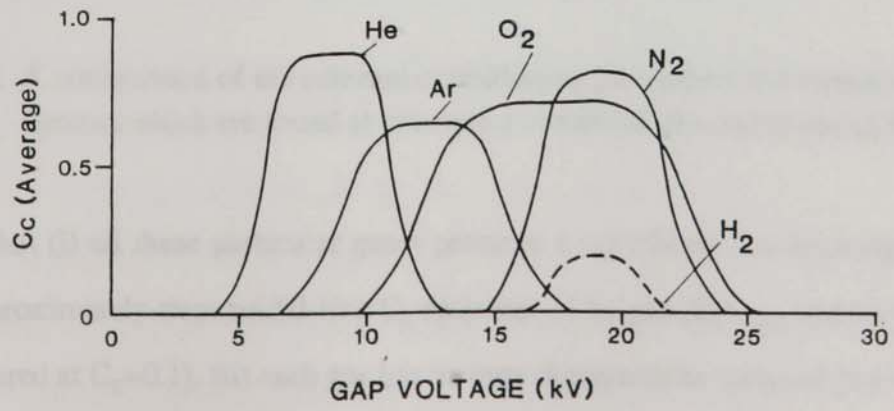

Figure 4.9 A comparison of how the coefficient of gas conditioning, C_c, varies with voltage for each of the gases studied.

where I_i and I_f are the pre- and post-conditioned gap currents respectively (see Figure 4.1). Thus, Figure 4.8 shows how the He-conditioning process is effective for gap voltages in the range 5-11kV, whereas Ar-conditioning, which exhibits a similar voltage dependence, has an effective voltage range of 8-15kV. Consequently, these findings lead to the important technological conclusion that Ar can indeed give rise to a comparable effect to that achieved with He, provided that the conditioning procedure is conducted at a higher gap voltage; however, in this context, it is generally found that Ar gives rise to lower values of C_c at comparable gap voltages, i.e. $C_c(He)>C_c(Ar)$.

Having established a voltage dependence for the gas conditioning process, the present investigation was further extended with a view to acertaining whether a systematic conditioning of emission sites could be achieved with the non-inert, or active gases, i.e intimating a universal phenomenon. Accordingly, Figure 4.9 presents the collated data obtained from a comparative study on the conditioning capabilities of H_2, He, Ar, O_2 and N_2. Thus, the three most important conclusions to be drawn from this

Conditioning Gas	V_{oc} (kV)	$(C_c)_{max}$	ΔV_o (kV)
He	9.0	0.9	7.0
Ar	12.5	0.65	9.0
O_2	17.0	0.75	13.0
N_2	19.0	0.85	7.5

Table 4.1. A comparison of the relevant conditioning parameters for various gas species which are found to promote a beneficial gas conditioning effect.

figure are that (i) all these particular gases promote a significant conditioning effect, with an approximately trapezoidal-like C_c-response of height $(C_c)_{max}$ and base width ΔV_o (measured at C_c=0.1), (ii) each gas has its own characteristic range of gap voltages (with varying values of ΔV_o) over which it is effective, and (iii) there is a significant spread in the maximum values of C_c among the gases, with H_2 providing the least

convincing evidence of promoting a beneficial conditioning effect. To highlight these observations, Table 4.1 compares the values of V_{oc}, $(C_c)_{max}$ and ΔV_o for He, Ar, O_2 and N_2, where V_{oc} is the optimum conditioning voltage, taken as the mid-point of each corresponding plateau region in Figure 4.9.

4.3.4 High temperature annealing of conditioned emission sites: the Temperature Effect

A number of reports have been published on the use of temperature cycling in the routine commisioning of high-voltage electrodes, both in conjunction with [175], and without [62] the use of complementary gas conditioning processing. However, although temperature cycling has proved to be beneficial in respect to improving voltage hold-off capabilities, its direct influence on conditioned sites has, to date, been largely ignored, possibly owing to the general acceptance of the sputtering model of conditioning. More recently, as described in section 4.1, questions have been tentatively posed as to whether the gas conditioning phenomenon could arise from some form of surface, or even bulk "electronic" process, whose permanence could quite conceivably be vulnerable to temperature annealing, i.e. similar to the effects commonly encountered in semiconductor processing [176]. Thus, in pursuit of a clearer understanding of the gas conditioning mechanism, a series of measurements have been undertaken, with the present experimental facility, on the influence of moderate high-temperature annealing ($\leq 300^{o}C$) on conditioned electron emission sites.

In this study, a planar Cu-cathode is first conditioned with He for a period of ~20 minutes until the gap current decays to an equilibrium level. At the end of this period, the chamber is evacuated to UHV ($\sim 10^{-8}$mbar), and the cathode temperature is elevated under zero-field conditions to $250^{o}C$ for 2 hours. Subsequently, after the cathode has returned to room temperature, the conditioning voltage is then re-applied across the electrode gap, under UHV conditions, and further measurements are made

on the resulting current-voltage (I-V) characteristic. In addition to these measurements, site distribution images are also recorded at subsequent stages of the above experiment.

An illustration of the typical effect of temperature annealing on the permanence of the conditioning process is given in Figure 4.10. Thus, prior to the heat treatment, the cathode is conditioned at ~10kV which reduces the gap current from 10.5μA to 1.5μA. If the cathode is then subjected to a 2 hour period of *in-situ* heating, as described above, it is found that, on re-applying the same gap voltage to the cooled cathode (i.e. 10kV), the current suppression previously achieved by conditioning is largely reversed; in fact, it will be seen that the gap current is restored to a value approaching its pre-conditioned level.

As shown in Figure 4.11, the effect of temperature annealing can be further demonstrated by comparing the Fowler-Nordheim (F-N) plots (see section 2.1.1) of the gap at subsequent stages of the experiment. Thus, Figure 4.11 shows how the F-N plot of the virgin cathode is first modified by He-conditioning, i.e. corresponding to a lowering of current levels and a reduction in the field-enhancement, or β-factor of the gap from 367-272. Subsequently, after a 2 hour *in-situ* bake at 250°C, it is shown that the gap characteristic has largely recovered, with β having increased from 272-356.

Finally, Figure 4.12 shows a sequence of constant-voltage site population images obtained at sequential stages of the above procedure for a single emission site. Thus, Figures 4.12 (a) and (b) demonstrate the decrease in site intensity, resulting from a period of gas conditioning, where the site current is reduced from 10μA to 2μA respectively. Subsequently, following temperature annealing, the site current is restored to ~6mA, i.e corresponding to an increase in the site intensity, as shown in Figure 4.12. Hence, the evidence obtained from these direct observations of the site images strongly suggest that the recovery of the total gap current , as a result of temperature annealing, is directly associated with changes in the "emitting state" of a conditioned site, i.e. as opposed to a possible thermal activation of new sites on the test cathode.

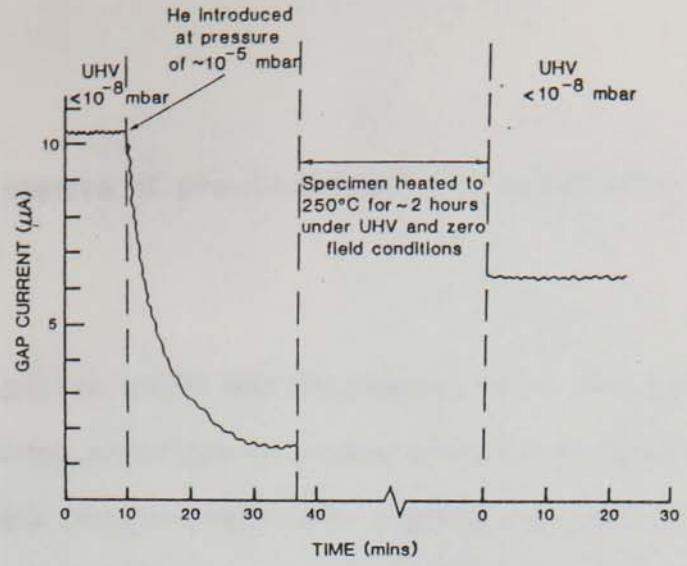

Figure 4.10 The "temperature" effect: an illustration of how a zero-field temperature cycling partially reverses the He-conditioning effect.

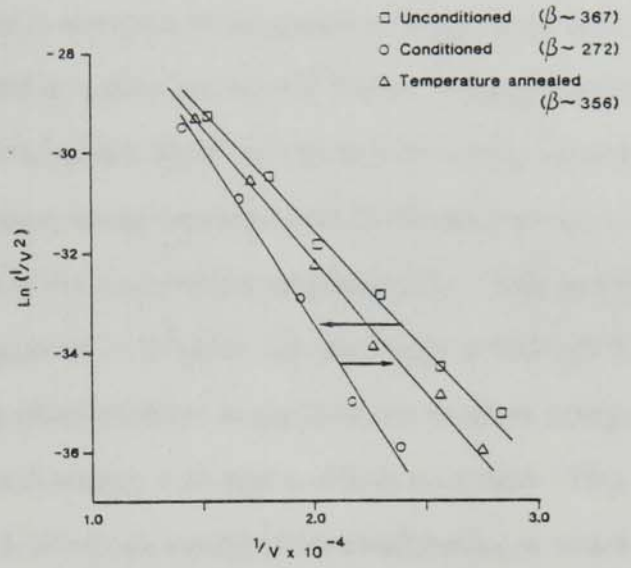

Figure 4.11 A sequence of F-N plots showing how the I-V characteristics of a vacuum gap is influenced, first by the gas conditioning, and then by a subsequent thermal cycling.

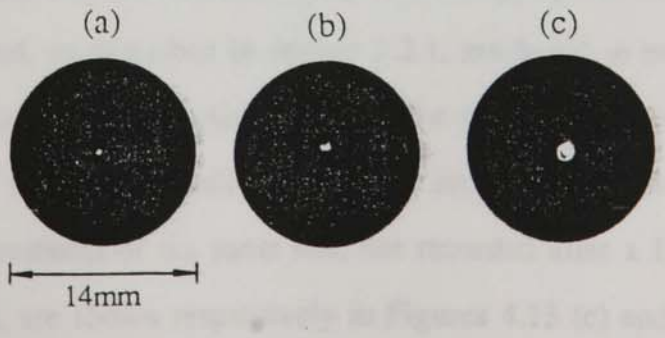

Figure 4.12 A sequence of constant-voltage emission images for a single site (a) before conditioning, (b) following a 15min period of He-conditioning, and (c) after 2 hours of cathode heating at ~200°C. (V_g=7kV).

4.3.5 The electron spectra of pre-conditioned and conditioned emission sites

In order to gain an insight into the physical nature of the conditioning mechanism, and thus further investigate the possible existence of a mechanism based on an "electronic" process, complementary electron spectroscopy measurements were made to determine how the fundamental emission properties of sites change during gas conditioning. These measurements were made possible by the versatility of the versatile purpose-built electron spectrometer described in section 3.4. Thus, for this investigation, a test cathode is mounted on the specimen stage of the spectrometer, and the main chamber evacuated to a pressure of ~10^{-9}mbar. Having established a stable distribution of emission sites, an individual site can then be axially located as described in section 3.4, and its emission image focussed onto the fluorescent screen by applying the appropriate potentials to the electrostatic lens assembly. Prior to introducing the conditioning gas at a pressure of ~10^{-5}mbar, the site image is first left to stabilise for ~15 minutes before being photographed; in addition, its electron energy spectrum is analysed using a 5 volt total energy scan and a 100ms scan time. This procedure is then repeated following a 5-10 minute period of He-conditioning in which it is possible to observe a partial conditioning of the fluorescent-screen site image.

The typical changes observed in the emission characteristics of individual sites before and after a period of conditioning are shown in Figure 4.13. Thus, Figures 4.13 (a) and (b) show respectively the emission image and energy spectrum recorded before He-conditioning, and, as described in section 2.2.1, are found to exhibit the typical characteristic of a "non-metallic" emission process, i.e displaying a spectral shift below the Fermi level of the substrate electrode and a broad spectral half-width (FWHM). Similar measurements of the same site, but recorded after a 10 minute period of He-conditioning, are shown respectively in Figures 4.13 (c) and (d), and clearly reveal that there is a decrease in site intensity and size following conditioning. Furthermore, a similar comparison of the electron spectra reveals a spectral shift of

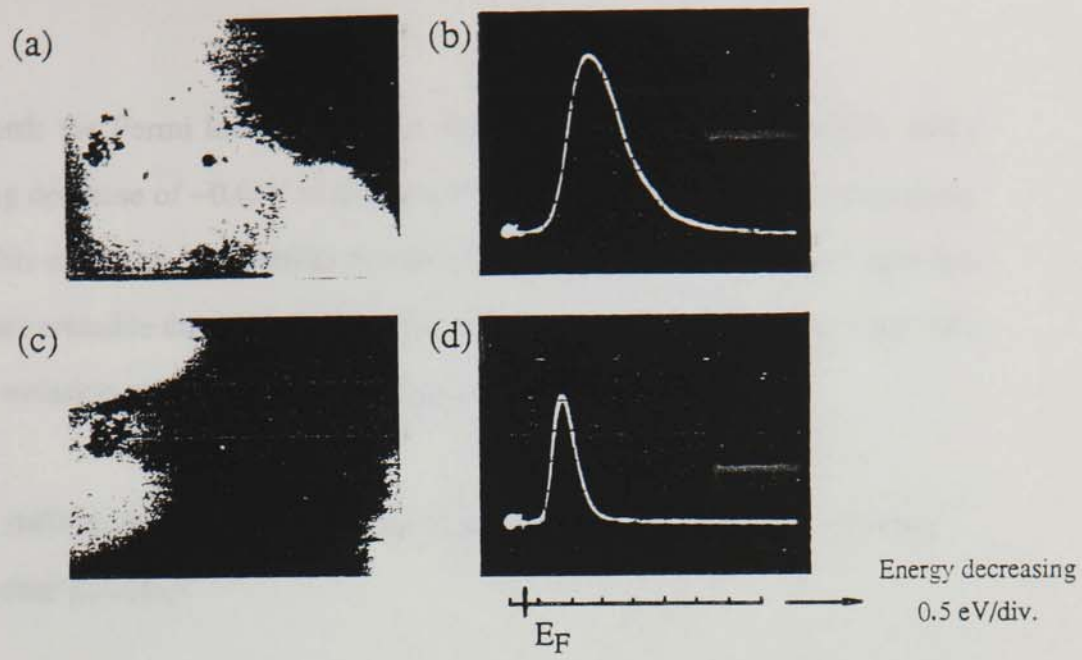

Figure 4.13 Emission site images and associated electron energy spectra recorded (a, b) before and (c, d) after a period of conditioning.

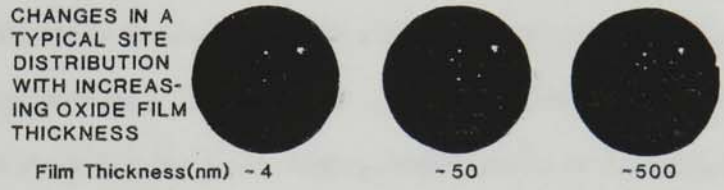

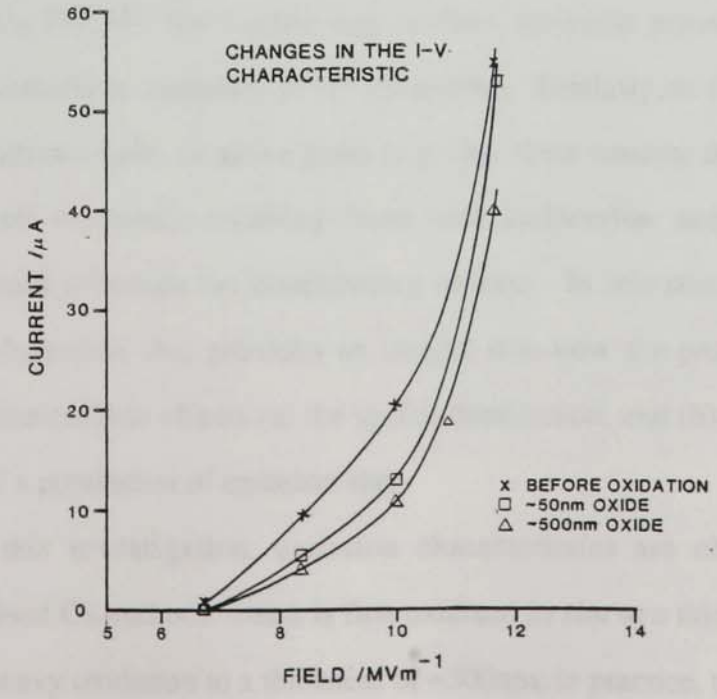

Figure 4.14 The effect of increasing oxidation on the electron emission characteristics of a planar Cu-electrode.

~0.4eV towards the Fermi level (FL), i.e a shift to higher electron energies, and a corresponding decrease of ~0.6eV in the spectral FWHM as a result of conditioning. Thus, from this evidence, and similar results obtained with Ar-conditioned emission sites, it appears probable that intrinsic changes are induced in the "electronic state" of a non-metallic emission regime as a result of conditioning.

4.3.6 The influence of surface oxidation on the field-induced electron emission process

The influence of surface oxidation on prebreakdown electron emission processes is an important consideration from both a fundamental and technological viewpoint. From a fundamental perspective, it could be anticipated that the oxidation of an emission site could result in changes to the surface electronic properties, e.g. work function, or, in the extreme case, could literally consume (if metallic), or "bury" a site. In fact, in an attempt to exploit the technological implications of the latter effect, there has been a growing trend towards the use of surface dielectric coatings, e.g. MgF_2 [177] and Al_2O_3 [37,38], for suppressing electron emission processes, and hence improving the insulation capability of HV electrodes. Similarly, in the context of gas conditioning with non-inert, or active gases (e.g. O_2), there remains the possibility that surface chemical reactions, resulting from both surface/ion and surface/neutral interactions, could influence the conditioning process. In this section therefore, an experiment is described that provides an insight into how the progressive *in-situ* oxidation of a test cathode effects (a) the spatial distribution, and (b) the total gap I-V characteristic of a population of emission sites.

For this investigation, emission characteristics are obtained from an ambiently oxidised Cu-cathode which is first oxidised *in situ* to a thickness of ~50nm, followed by a heavy oxidation to a thickness of ~500nm; in practice, the 50 and 500nm layers are grown at a temperature of ~150°C during exposure to atmospheric-oxygen

and atmospheric-air environments respectively. Thus, the typical effect of increasing oxide thickness on the spatial distribution of a population of emission sites is shown in Figure 4.14(a). This illustrates how the site distribution remains virtually unaffected for both moderate and heavy surface oxidation, where no significant changes are observed in the intensity of the dominant sites. The corresponding current-voltage (I-V) characteristics obtained at subsequent stages of oxidation, are given in Figure 4.14(b), where it is found that a small, but significant decrease is observed in the total gap current at a given field, as a result of increasing oxide thickness. Thus, from a comparison with the gas conditioning results described in sections 4.3.1, 2 and 3, it appears justifiable, at this stage, to conclude that the effects of surface oxidation on the behaviour of "natural" emission sites are generally of second-order importance.

4.4 Discussion

In this chapter, results have been presented from a comprehensive investigation into the well-known gas conditioning phenomenon, where, from a fundamental viewpoint, the findings of sections 4.3.3 and 4.3.4 have established the existence of a further two, and hitherto unknown, effects, namely the voltage and temperature-dependence of the conditioning mechanism. Traditionally, the gas conditioning effect has been interpreted in terms of an ionic sputtering process [28], however, it is presently believed that the existence of both the "voltage" and "temperature" effects cast doubt on the general validity of the sputtering interpretation and highlights its inability in providing a fundamental physical basis for explaining these related phenomena. In addition to the technological implications of the new experimental findings, it is further believed that the above effects lend support to the recent speculations of a conditioning model based on an "electronic" mechanism. Consequently, the present discussion will aim to provide an alternative explanation of the gas conditioning phenomenon in terms of a newly proposed "electronic" model.

This discussion will conclude with a re-appraisal of the technological benefits and limitations associated with the gas conditioning technique.

4.4.1 A proposed "electronic" model of gas conditioning

In order to provide a physical basis for an electronic interpretation of the gas conditioning effect, it is first necessary to refer back to section 2.2.1 and re-introduce the experimentally established concept that electron emission sites are invariably associated with anomolous, micron, or submicron-sized particulate structures involving non-metallic materials. Accordingly, the following model of gas conditioning will be based on the metal-insulator (MI) emission regime, described in detail in section 2.2.4, in which hot electrons are produced within conducting channels "formed" in the insulating medium (Figure 4.15(a)), and are thus emited quasi-thermionically as shown in the band model of Figure 4.16.

In terms of this model, the mechanism that is currently under consideration involves the formation, and subsequent implantation of high energy ions (e.g. He^+ or Ar^+) into the non-metallic region of the field-emitting microstructure. More specifically, it is assumed that these ions are formed by impact ionisation within the narrow beams of electrons emitted from individual sites (Figure 4.15(a)), i.e. as originally proposed by Alpert et al [28], and that these ions are subsequently funnelled back by the local converging field to impact on the emission centres with maximum energies given by the total gap voltage, e.g. ~10keV in the case of He-conditioning. Under these conditions, it can first be assumed that ions will be implanted to depths >100Å below the surface of an emitting microstructure [176,178,179], and secondly, that the implanted ions, either directly or indirectly, will form electron traps in the vicinity of the metal-insulator interface, i.e. as illustrated in Figure 4.16(b). Electrons captured by these traps would then "shield" the metal-insulator (MI) interface from the external field, and hence raise the conduction band edge towards the metal Fermi level (FL). Initially, this process will lead to a reduced MI barrier field, accompanied by a

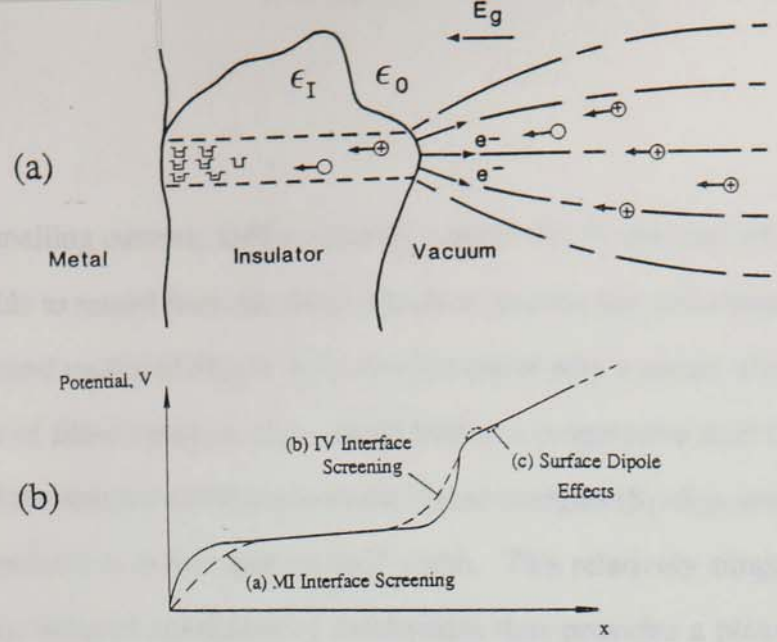

Figure 4.15 (a) A schematic representation of a metal-insulator (MI) emission site showing how electrons are emitted from conducting "channels" that have "formed" in the insulating medium. (b) The assumed potential distribution in the channel region, where the dotted lines represent the modifications due to MI interface, IV interface and surface dipole moment effects respectively.

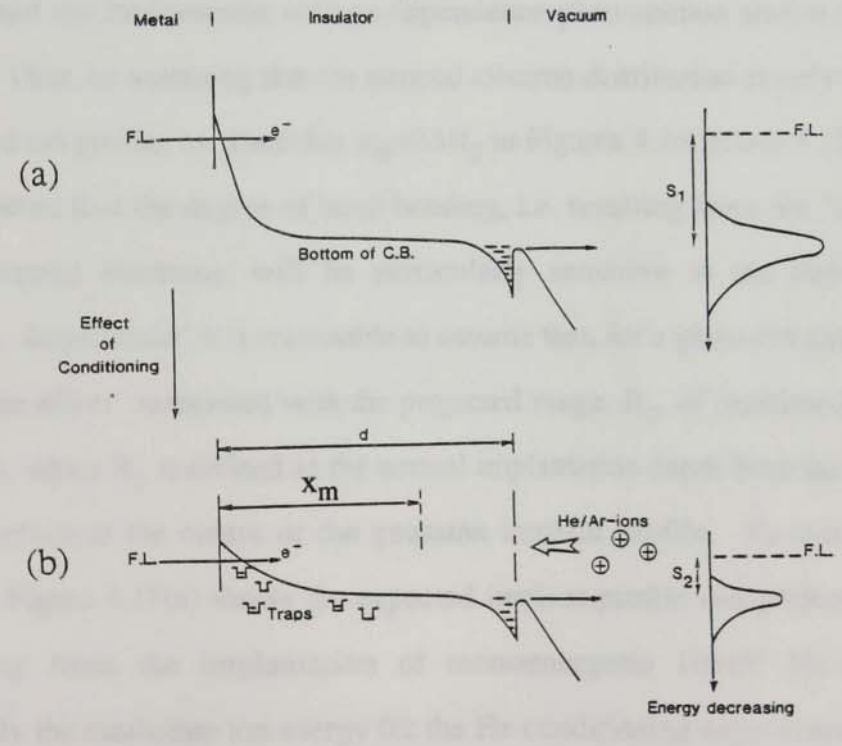

Figure 4.16 A band diagram representation of an "electronic" model of the gas conditioning phenomenon: (a) before and (b) following a period of conditioning under constant-field conditions. Here, the electron energy spectra are shifted by an amount S (eV) with respect to the Fermi level of the substrate cathode.

- 131 -

reduced tunnelling current, until eventually a point will be reached where electrons are no longer able to tunnel from the metal substrate, and the site will consequently cease to emit. The band model of Figure 4.16 also illustrates why a period of conditioning, i.e. the creation of filled electron traps, could lead to a progressive shift (S) in the energy spectrum of the emitted electrons towards higher energies ($S_1>S_2$), accompanied by an associated reduction in the spectral half-width. This relatively simple concept of an electron-trap induced conditioning mechanism thus provides a plausible qualitative explanation of the observed suppression of the electron emission process, as shown in Figures 4.1 and 4.2, and the corresponding spectral changes obtained as a result of conditioning (see Figure 4.13).

From a further consideration of the ion implantation dynamics associated with the mechanism illustrated in Figure 4.16, it can be shown how the above model also provides a basis for interpreting the the constant-voltage current responses of Figure 4.5, and the fundamental voltage-dependence phenomenon shown in Figures 4.8 and 4.9. Thus, by assuming that the trapped electron distribution closely resembles the implanted ion profile, i.e. such that $x_m \approx 2\Delta R_p$ in Figures 4.16(b) and 4.17(a), it can then be expected that the degree of band bending, i.e. resulting from the "screening" effect of trapped electrons, will be particularly sensitive to the depth of ion implantation. In particular, it is reasonable to assume that, for a given ion energy, there will be a "size effect" associated with the projected range, R_p, of implanted ions (see equation 4.2), where R_p is defined as the normal implantation depth from the insulator-vacuum interface to the centre of the gaussian implant profile. To illustrate this mechanism, Figure 4.17(a) shows the expected implant profile and projected range, R_p, resulting from the implantation of monoenergetic 10keV He-ions (i.e. approximately the maximum ion energy for the He-conditioning experiments) into an assumed SiO_2 emission microstructure [178]. From an analysis of the collated data of Table 4.2, which shows the relative masses [180], atomic numbers and projected ranges [178] of the various gas species used in the present study, it is apparent that the

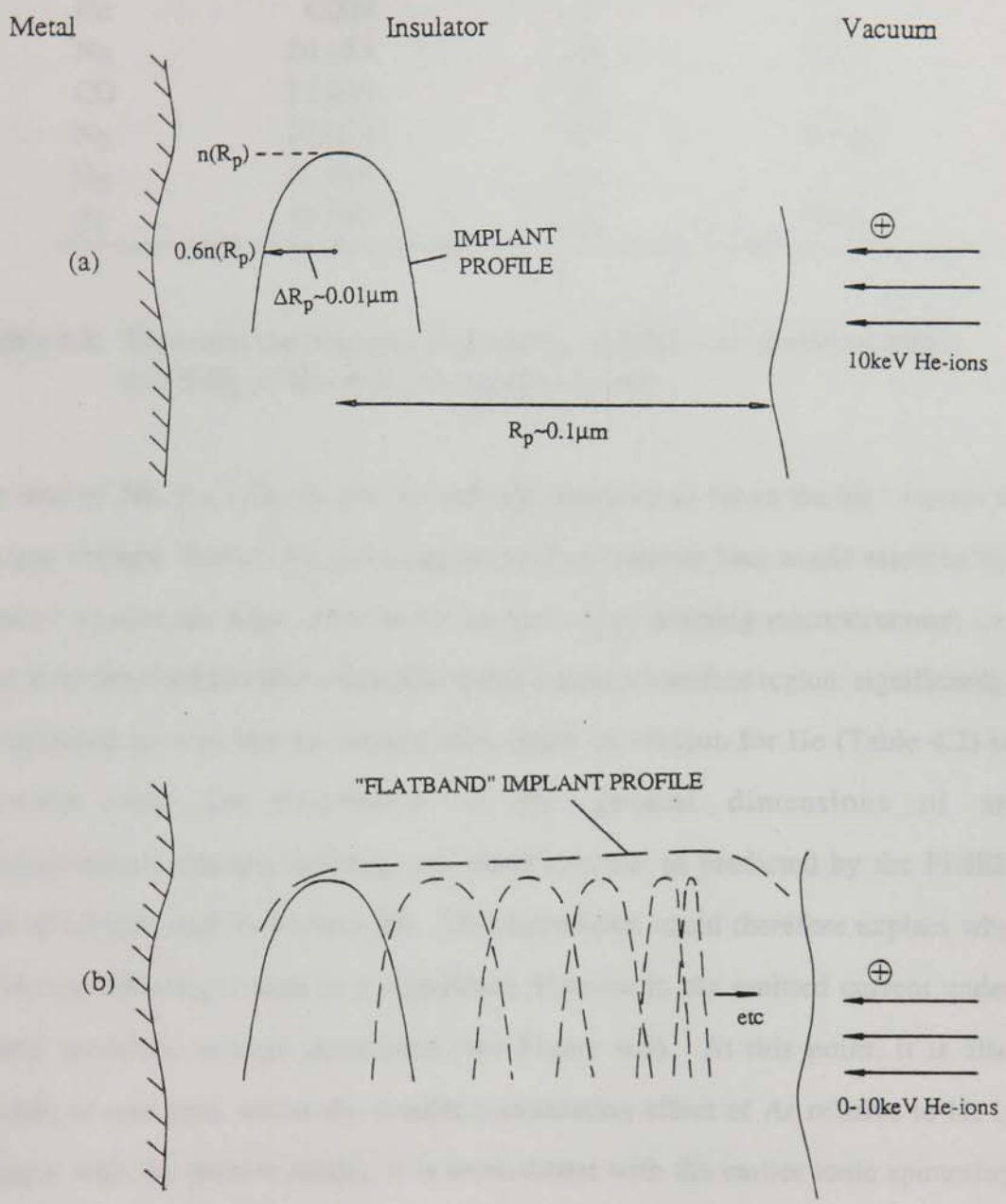

Figure 4.17 A schematic of the implant distributions resulting from the implantation of (a) monoenergetic 10keV He-ions, and (b) 0-10keV ions into a typical insulating microstructure.

Gas ion	Molecular Mass, M	Atomic Number, Z	Projected Range, R_p, at 10keV (μm)
H_2	2.016	2	0.06
He	4.003	2	0.1
Ne	20.183	10	0.02
CO	28.010	14	-
N_2	28.014	14	0.007
O_2	31.998	16	-
Ar	39.948	18	0.01

Table 4.2. The molecular masses [180], atomic numbers and projected ranges (for SiO_2 [178]) of the gas species studied.

larger ions of Ne, N_2, CO, O_2 and Ar will not penetrate as far as the He^+ ions at a given gap voltage. Rather, the projected range of the heavier ions would result in the formation of electron traps close to the surface of an emitting microstructure, i.e. remote from the electronically vulnerable metal-insulator interface region: significantly, it is important to note that an implantation depth of ~0.1μm for He (Table 4.2) is consistent with the estimation of the general dimensions of an insulating/semiconducting emitting microstructure, i.e. as predicted by the FIHEE model of Latham and co-workers [9]. This hypothesis could therefore explain why only He-conditioning results in a significant decrease in the emitted current under identical moderate voltage conditions (see Figure 4.5). At this point, it is also important to note that, whilst the smaller conditioning effect of Ar relative to He is consistent with the present model, it is inconsistent with the earlier ionic sputtering model of gas conditioning [28]: i.e. the latter suggests that Ar would have a greater conditioning effect, since its sputtering yield is approximately three orders of magnitude greater than that of He [181] at a given voltage.

Referring to Figure 4.17(a), it has been shown by Schiott [182] that the projected range, R_p, of a particular gas species will be approximately proportional to the incident ion energy, E_{ion}, such that

$$R_p \approx C \frac{M_2}{M_1} M_2 \frac{(Z_1^{2/3}+Z_2^{2/3})^{1/2}}{Z_1 Z_2} E_{ion} \quad \text{(in } \mu g\ cm^{-2} \text{ and keV)} \qquad (4.2)$$

where the subscripts 1 and 2 refer to the incident ion and target masses and atomic numbers respectively, and $C(M_2/M_1)$ is a tabulated correction factor [179,182]. In addition therefore to the species-dependent "size effect" associated with the present conditioning model, it is apparent that the depth of ion implantation, and hence the resulting trap distribution, will also be dependent on the energy of the incident ions, where the maximum ion energy is given by eV_g in electron volts. Consequently, by increasing the gap voltage, V_g, during conditioning with the larger gas species, e.g. Ar, it could be anticipated that the modified insulator region, shown as x_m in Figure 4.16(b), will penetrate further into the emitting channel region, i.e. resulting in an increased screening effect at the MI interface, which, in turn, will lead to a similar current suppression to that obtained with the lighter He-ions at a lower gap voltage. In fact, the effect of the trapped electron distribution on the MI interface barrier (shown in case (a) of Figure 4.15(b)) can be approximated by assuming that the negative charge distribution for the maximum energy ions is contained within a sphere of radius ΔR_p (Figure 4.17(a)), so that the "screening" field strength, E_s, at the MI interface is given by

$$E_s = \frac{1}{4\pi\varepsilon} \frac{Q}{r^2} \qquad (4.3)$$

where r is the distance from the interface to the centre of the charge distribution and Q is the total trapped charge given by $(4/3)\pi(\Delta R_p)^2\rho$ for a uniform charge density ρ. The sensitivity of the MI barrier field to the depth of ion implantation thus provides a tentative explanation of the voltage-dependence curves of Figures 4.8 and 4.9, where, in support of the implantation model, a general correlation is observed, viz. the low-penetration species (R_p in Table 4.2) require higher optimum conditioning voltages, V_{oc}, to achieve comparable degrees of conditioning.

From a consideration of the original sputtering model [28] of gas conditioning in which emitting microprotrusions were assumed to be progressively blunted by ion bombardment, it is presently believed that such a mechanism could not provide a physical basis for the evidence of Figures 4.10, 4.11 and 4.12, which indicate that a significant reversal of the conditioning effect is brought about by an extended period of cathode heating. Referring to the "electronic" model of Figure 4.16, one could anticipate that, although annealing temperatures of ~250°C, as used in the present study, would be sufficient to release electrons from shallow traps which may exist up to 0.05eV below the insulator conduction band, subsequent recapturing of electrons would be expected to maintain the "screening", and hence conditioning effect, following the annealing process; i.e. such first-order temperature effects could not adequately explain the observed "temperature" effect in terms of the present "electronic" model. However, since the temperature reversal of the conditioning process is found to be permanent, even after cooling to room temperature, it appears reasonable to postulate that the "temperature" effect could result from a thermally-induced change in the electron trap profile and/or concentration, such as might be due to both lattice defect annealing [176,179] and implant impurity diffusion [176,179]. In the latter case, both lateral and normal diffusion would be expected to broaden the implant distribution shown in Figures 4.16(b) and 4.17(a), hence reducing the trap concentration adjacent to the MI interface of an emitting channel and partially reversing the conditioning effect. Furthermore, from a consideration of both the defect annealing process and the Fick diffusion laws [176], one would expect the decrease in the trap cocentration, and hence the degree of conditioning reversal, to increase with both annealing temperature and time.

4.4.2 Further considerations of an "electronic" conditioning model

From the outset, the proposed "electronic" model of gas conditioning has

been based on the assumption of a submicron surface dielectric emission regime, i.e. as shown schematically in Figure 4.15(a). However, although the non-metallic microstructure concept, and the associated field-induced hot-electron emission (FIHEE) model described in section 2.2.4, has been developed in some detail over the past decade or so [9], it is apparent that no direct evidence exists as to the exact material composition, or electronic structure, of the bulk or interface regions shown in the band model of Figure 4.16. Furthermore, whilst the present "electronic" conditioning model has largely considered the effects of ion implantation in the MI interface region, the possibility of trap formation in the high-field IV interface region (see case (b) in Figure 4.15(b)) has not yet been considered. Although it is still envisaged that MI interface screening will play a major role in the conditioning mechanism, it is important to mention a futher two related phenomena which could be expected to significantly contribute to the level of ion-induced electronic changes in the vicinity of the surface region (≤100Å), namely the "real gap" non-monoenergetic distribution of the incident ions, and the indirect formation of electron traps due to lattice disorder effects [176]. Firstly, it is important to note that the "electronic" model described in the previous section considers only the maximum energy ions, i.e. those which originate from the immediate vicinity of the anode (e.g. ~10keV ions in the case of He-conditioning). However, in practice, it can be reasonably assumed that the formation of ions, and hence the incident ion energy distribution, will be statistically determined by the ionisation potentials and ionisation cross-sections of the gas species studied. To assist the discussion, a comparison of the relevant parameters of the conditioning gases is given in Table 4.3. Referring to Figure 4.17(b), it can be assumed that ions of a given characteristic energy will each give rise to a corresponding gaussian implant profile with a characteristic distribution, ΔR_p, and projected range, R_p. As a consequence, one would expect the resulting total implant profile to tend towards a "flatband" distribution (shown in Figure 4.17(b)), hence extending the expected filled-trap population to the IV interface surface region; in fact, the detailed shape of this total

Gas Species	Ionisation Potential (eV)	Relative Ionisation X-section
H_2	15.4	1.1
He	24.5	0.2
N_2	15.5	2.5
O_2	12.0	2.5
Ar	15.7	3.6

Table 4.3. The ionisation potentials and relative ionisation X-sections of the gas species studied. (From [180]).

profile will be governed by the probability of residual gas ionisation at various points in the interelectrode gap [181,183]. In addition to the modified implant profile, a second effect which can be expected to increase the density of traps in both the bulk and the IV interface regions of an emitting channel can be explained from a consideration of the energy loss mechanisms associated with the implantation of high energy ions. It follows that when energetic ions enter a target substrate, they lose their energy in a series of electronic and nuclear collisions, until they finally come to rest in the host lattice. However, whilst electronic collisions, which dominate at the higher energies (typically tens of keV), generally give rise to electronic excitations and pair production processes, only nuclear collisions can transfer sufficient energy to displace atoms from the lattice (e.g ~15eV for Si), hence resulting in lattice disorder. Therefore, since nuclear collisions can be expected [178] to be the dominant energy loss mechanism for the ion species and energies used in the present conditioning experiments, it is anticipated that damage in the form of lattice disorder will start from the very surface of an emitting microstructure. Furthermore, by assuming that the lattice defects give rise to trapping centres, as is invariably found with ion-implanted SiO_2 [184], it follows that the increased surface trap density could influence the "screening" of the IV interface, and hence the mobility of the "hot" electrons which are required to be generated within a few mean-free-paths from the emitting channel surface, i.e. ~100Å

[9].

In order to explain why, for example, O_2 or CO exhibit a significant de-stabilising, or even de-conditioning, effect at moderate gap voltages of ≤10kV (see Figures 4.5 and 4.6), it may be necessary to consider the chemical/electronic nature of these gases and their subsequent reactions with the surface of an emitting microstructure. Thus, in contrast to the relatively "passive" effect of the less active gases, e.g. N_2 and H_2 (Figures 4.5 and 4.6), O_2 can be expected to drastically modify the electronic surface states of an emitting regime, thus influencing surface phenomena such as resonant tunnelling [53] and surface dipole reductions in the barrier field (see case (c) in Figure 4.15(b)): the "active" nature of O_2 has been previously demonstrated by numerous studies using metallic micropoint emitters [53,114].

Whilst the exact role of the surface in non-metallic field-induced electron emission is not fully understood, it seems plausible, from a consideration of the oxidation experiments described in section 4.3.6, to conclude that although surface chemical reactions may influence the short term emission stability of sites, such processes could not soley be expected to give rise to the gas conditioning phenomenon observed with O_2; i.e. as was tentatively suggested by Bloomer and Cox [169]. From a fundamental viewpoint, it has previously been recognised that the electrode surface oxidation process, described in section 4.3.6, gives rise to a significant increase in both the shift and half-width of the energy spectra of emitted electrons [86], i.e. consistent with an increase in the number of electron-lattice scattering events prior to emission. However, whilst this latter observation implies that emission sites are effectively "buried", or "encroached on", by an oxide overlayer, it is clear from Figure 4.14 that this has very little effect on the emission characteristics of individual sites. These findings are technologically important since they imply that the process of coating electrodes with thick-oxide overlayers (≤500nm) cannot be relied upon to extinguish, or reduce the prebreakdown currents that ultimately limit their use in vacuum-insulated HV circuits. Furthermore, the use of thick-oxide coatings, which may include loosely-

adhering conglomerate regions, is likely to result in an undesirable mechanical de-stabilisation of the microtopography of an electrode surface.

The present discussion has highlighted a number of processes which could be expected to influence the behaviour of electron emission sites under poor vacuum conditions (i.e. $\leq 10^{-5}$mbar). In particular, a model has been proposed in which the well-known gas conditioning phenomenon is explained in terms of the creation, and subsequent implantation of energetic (a few keV) ions into a "non metallic" emitting microstructure. However, owing to the apparent complexity [9], and lack of detailed knowledge of the emission regime, it should be stressed that, whilst the above model provides a basis for tentatively explaining the experimental data presented in section 4.3, the details of such a conditioning model remain necessarily speculative. It seems appropriate therefore to end this discussion with a brief mention of some alternative mechanisms which may play an important role in the gas conditioning phenomenon, e.g. sputtering[179] and ion-induced surface diffusion [185,186] etc. Thus, although sputtering has not featured in the present model, it may be premature, at this stage, to ignore the effects of surface sputter damage on a "non-metallic" emitting microstructure; in fact, the characteristic "fall-off" in the sputtering yield for low energy ions ($\leq$10keV), with increasing ion energy, could account for the characteristic energy dependence and limitation of the conditioning effect, as shown in Figures 4.8 and 4.9. It may also be appropriate to consider the effects of ion-induced surface diffusion [185,186], and/or diffusion of ions into the bulk of an emitting microstructure under the influence of an applied field. Finally, it is apparent that, in order to assess the importance of the contending physical mechanisms, any future modelling of the gas conditioning effect would benefit from a complementary analysis of the energy flux distribution of the ions and neutral atoms impacting on an emission centre.

4.4.3 The technological implications

From a technological viewpoint, the results presented in this chapter confirm earlier reports [27-31] describing the effectiveness of He gas-conditioning in significantly reducing the prebreakdown, or leakage currents that flow between vacuum-insulated high-voltage electrodes. In addition, the important new findings presented in the voltage dependence curves of Figure 4.9 indicate that the gas conditioning phenomenon is not limited to the inert gases; rather, it is found that a comparable conditioning effect can be achieved from a range of gas species, provided that the technique is conducted within the characteristic voltage range of each particular gas species. Thus, in order to capitalise on these findings, it is apparent that a more sophisticated conditioning procedure is required than that currently employed in the routine He-conditioning of HV vacuum devices. It follows, for example, that as a device is progressively conditioned, i.e. its applied voltage is gradually increased, it will be necessary to change the conditioning gas to "match" the corresponding voltage range, and hence maximise the degree of conditioning at each stage of the process; otherwise, as must frequently occur with the conventional He-conditioning process, where voltages in excess of 10kV are routinely employed, it will be found that the benefits derived from the treatment will prematurely "saturate". On the basis of the limited data presented in Figure 4.9, it therefore appears that the most appropriate sequence of gases for conditioning a device to ~20kV would be He $\rightarrow$ Ar $\rightarrow$ O_2 $\rightarrow$ N_2. Alternatively, it may be more convenient to use a single mixture of gases, e.g. He, Ar and O_2, which collectively provide a high coefficient of conditioning over the available range of gap voltages (see Figure 4.9); in fact, it is interesting to note that argon-oxygen mixtures [187] have been used in preference to pure argon for the glow-discharge conditioning of niobium surfaces such as used in RF superconducting cavities. Ultimately, however, it has to be recognised that the technological effectiveness of the gas conditioning technique could well be limited, particularly in the case of *in situ* conditioning with "fixed" electrode devices, by the progressive switch-

on of new emission sites resulting from the increased gap field. Similarly, although it can be generally concluded that gas conditioning represents a reliable technique for the suppresion of, for example, the spurious electron emission currents that degrade the performance of superconducting RF cavities [174,175], it is important to note that the present study provides no quantitative data on the effectiveness of gas conditioning in raising the voltage hold-off capability of HV electrodes.

A further technological limitation of the gas conditioning procedure is indicated by the findings of Figures 4.10, 11 and 12, which show that an appreciable reversal of the effect can occur following the temperature cycling of conditioned electrodes up to $\geq 200^{o}C$. Consequently, this phenomenon could be expected to threaten the potential insulating capabilities of a number of practical devices which may be subject to routine temperature fluctuations, e.g. space-borne devices, RF cavities in the presence of multipacting effects, and electron tube devices that include an internal heater. It also follows that the long-term performance of a conditioned electrode could be degraded by a similar, although slower, room-temperature "annealing" process which may occur over a time scale of a few weeks, or more.

Finally, mention should be made of the Current/Voltage Conditioning procedure [30,32], in which the required operating voltage of a device is achieved by incrementally raising the applied voltage and allowing the gap current to decay to a steady-state value at each stage. This conditioning phenomenon, which typically occurs over a similar time scale to the gas conditioning process, i.e. ~20-30 mins, has traditionally been interpreted in terms of the influence of high fields on electrode microprotrusions, loosely adhering particles and micro-reservoirs of occluded gas [3]. Frequently, this technique is used at only modest vacuum levels of $\geq 10^{-6}$mbar, such as in sealed-off devices and electron microscopes, where the residual gases will be predominantly N_2 and O_2. It follows therefore, that since the gas conditioning effect is now believed to be a "universal" gas phenomenon, i.e. not limited to the inert gases, the decay in gap current following current conditioning is probably largely due to the

mechanism discussed in this chapter; i.e. the current and gas conditioning effects could well be one and the same phenomenon.

CHAPTER 5

COLD-CATHODE ELECTRON EMISSION FROM COMPOSITE-COATED EXTENDED-AREA CATHODES

5.1 Introduction

Although the indirectly-heated, low-ϕ thermionic cathode remains the most common method of obtaining electron emission for practical electron beam systems and devices, there are however certain specialised applications, e.g. high resolution electron microscopes, that require an electron optically "bright" source, and in these cases the tungsten micropoint field-emitter has, over the past decade, emerged as a viable replacement. However, in view of the stringent practical requirements associated with the operation of a tungsten field-emitter, e.g. an ultra-high vacuum ($\leq 10^{-9}$mbar) and a frequent tip "flashing" procedure [98,114], it is generally recognised that there exists a need for an alternative and more robust type of field emitting cold-cathode. Consequently, a variety of non-conventional emission regimes have been investigated over the past two decades, including the "non-metallic" cathodes described in section 2.3. Prominent among these have been the studies of carbon-based emitters (e.g. single fibre micropoints [22,110,111] and felts [23], etc), where the particularly attractive technological feature of such emitters is their ability to operate at the relatively poor vacuum conditions of commercial devices ($\leq 10^{-6}$mbar).

Coincidently, the propensity of carbon to promote the field emission of electrons was further reinforced by recent independent studies [61] of the prebreakdown electron emission process that occurs on HV electrodes, where it was established that "natural" microscopic emission sites are frequently associated with carbon-based surface particulate contamination. In a follow up to these studies, this phenomenon was experimentally simulated by a number of groups [10,13], by depositing "artificial" carbon particles on a planar electrode surface, and demonstrating that they invariably gave rise to electron emission at the anomolously low fields of $\leq 10 MVm^{-1}$. It was also established from electron spectroscopy studies by Latham and co-workers [74,111] that both "natural" prebreakdown sites and the carbon fibre regime exhibit similar "non-metallic" emission characteristics, which was subsequently

interpreted in terms of a field-induced hot electron emission model [8,9] based on a metal-insulator (MI) emitting microstructure. In fact, it was the accumulation of evidence in support of this model that prompted Latham and Mousa [11,12] to undertake the simulation study discussed in section 2.3.4, in which the emission properties of resin-coated tungsten microtips were investigated. From this study, the authors obtained convincing evidence that confirmed the existence of a non-metallic MI emission mechanism, and furthermore, established the importance of sub-micron insulating resin layers in significantly, if not dramatically, enhancing the electron emission current from a previously uncoated cathode at a given applied field.

In an attempt to collectively capitalise on the technological implications of the above findings, an attempt was made to combine the desirable emission features obtained independently with the carbon particle and resin-coated regimes to obtain a new type of electron source. Thus, the idea of a "hybrid cathode" was conceived, in which a metallic cathode is coated with a composite layer consisting of carbon particles suspended in a resin matrix. This concept has subsequently been realised in the present study by the development of a new emitter fabrication technique. Although in its infancy, the composite coating technique has been used to fabricate a range of extended-area multi-emitter cathodes from various insulating and non-insulating materials, where ultimately, it is envisaged that these will form the basis of a new generation cold-cathode electron source. In fact, an incentive for this study follows from the recent interest in the application of multi-emitter cathodes in, for example, "radiation hard" microvalve arrays, ultra-fast device applications and matrix-addressed flat displays.

A further aim of the present investigation is to simulate the effects of various surface particulate contaminants on the insulating capabilities of a vacuum-insulated high-voltage electrode regime. Thus, whilst specialised electrode surface preparation techniques [26] have been developed to reduce surface contaminantion, and hence raise the electrode voltage hold-off capability, it is generally found that particulate

contaminants cannot be totally avoided in many commercial HV electrode systems. From a technological point of view, it is therefore very important to determine whether there are certain combinations of electrode and contaminant particle materials that would be unfavourable to the high voltage engineer.

In this chapter, details are presented of an investigation into the emission characteristics and operating capabilities of the new extended-area composite-coated cold-cathodes fabricated from a range of materials. For these studies, the transparent-anode imaging technique described in section 3.2.2 has been used to characterize and evaluate the respective emission characteristics of these cathodes. With a view to assessing the commercial cold-cathode potential of the C-composite emitter, an extended study has also been conducted on the influence of a variety of experimental parameters on this regime (e.g. gas environment, pulsed-fields, stability, etc).

5.2 Composite-cathode fabrication technique

The extended-area composite-coated cathodes used in this study are essentially a progression from the "artificial" particulate-contaminated cathodes described in section 2.2.5, but, with the added feature of the nominal resin "encapsulation" of particles. In the first stage of the emitter fabrication technique, a 14mm-diameter OFHC Cu electrode is polished and ultrasonically cleaned as described in section 4.2. The cleaned electrode is then horizontally mounted on a vertical translator, which enables the inverted electrode face to be dipped into a shallow bath of epoxylite resin (Clark Electromedical Instruments) containing a suspension of the chosen conducting, or semiconducting particles, e.g. C or MoS_2, etc; for the present study, the suspensions typically conformed to a particle/resin ratio of ~0.1g/ml. Following withdrawl from the suspension, the cathode is immediately transferred to the spinner module, and mounted as shown schematically in Figure 5.1. Here, the purpose-built spinner consists of a cradle-mounted, vertical d.c motor, which, when used in conjunction with a variable 0-6V d.c power supply, can controllably attain

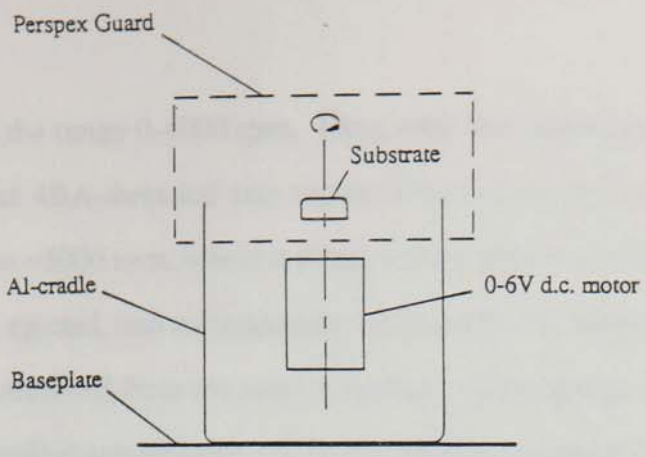

Figure 5.1 A schematic of the spinning module used for coating the substrates with a composite metal-insulator film.

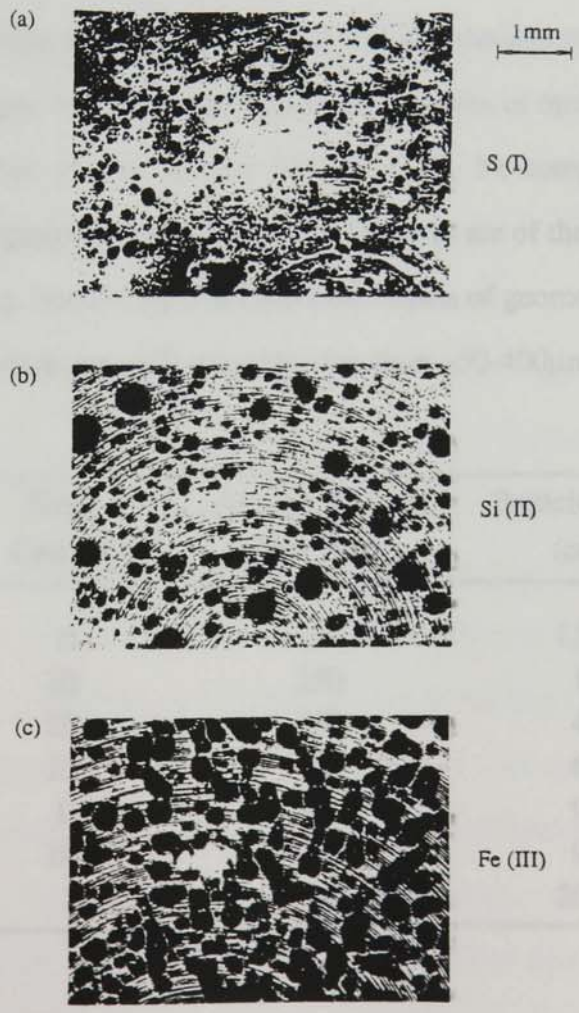

Figure 5.2 Low-magnification (x20) optical micrographs of typical group I, II and III cathode surfaces. (a) a S-composite, (b) a Si-composite and (c) an Fe-composite coating.

speeds of rotation in the range 0-4000 rpm. Thus, with the suspension-coated cathode accommodated on the 4BA-threaded axis mount (Figure 5.1), the speed of rotation is gradually increased to ~3000 rpm, where it remains for a period of ~30 secs until all the excess suspension is ejected, and subsequently collected by the perspex guard. At this stage, the cathode is removed from the spinner module and immediately transferred to a thermostatically-controlled sample oven where it is initially subjected to a heat treatment [12] of 30 mins duration at ~100°C, followed by 30 mins at ~180°C to complete the curing of the resin. Finally the resulting cathode is allowed to cool to room temperature, and is then stored for a period of at least 24 hours in a vacuum-desiccator prior to testing under UHV conditions.

To illustrate the type of composite-cathode surface coatings resulting from this fabrication technique, Figure 5.2(a)-(c) shows typical examples of optical micrographs taken at normal incidence to the surface of the S, Si, Fe-composite cathodes respectively. These micrographs indicate that the composites are of the form of a single layer, resin/particle coating, containing a random distribution of geometrically irregular and dissimilar particles, which generally range in size from ~50-400μm.

Particle Type	Size Category	Average Particle Size (μm)	Particle Density (cm^{-2})
C	II	130	1263
MoS_2	III	250	172
Au	III	250	409
SiC	III	225	682
Si	II	130	963
Fe	III	225	909
S	I	50	2054

Table 5.1. The relevant coating parameters of the seven composite-cathode types.

In the present study, the composite-cathode fabrication technique has been used to produce a variety of resin-based extended-area composite cathodes from a range of conducting and semiconducting particles. For the purpose of characterizing the cathode coatings, Figure 5.3 and Table 5.1 show respectively the particle size distributions and general coating parameters obtained from a detailed optical microscopy study of the seven cathode-types. In interpreting Figure 5.3, it should be noted that the particle size distributions represent the profiles of the corresponding frequency histograms sampled at a class width of ~30μm. Thus, referring to these data, it will be seen that the seven particle types can be generally classified into three size categories (termed groups I, II and III), and generally exhibit a similar distribution profile. Finally, in addition to the above analysis, a more detailed study of the composite coating structure will be presented in section 5.3.8.

5.3 Experimental Findings

In this section, results are presented from a series of electron emission tests on the various composite-coated cathode types listed in Table 5.1. For these measurements, the total I-V characteristics and site distribution images were obtained using the plane-parallel transparent-anode emission module described in section 3.2, where, unless otherwise stated, tests were made at a base pressure of ~10^{-8}mbar, with a 2.2MΩ current-limiting resistor and an interelectrode gap spacing (i.e. as determined with an uncoated test cathode) of 0.5mm. Two types of measurement have been performed for characterising the fundamental emission capabilities of the composite-coated cathodes; thus, sections 5.3.1 to 5.3.5 describe experiments conducted under dc-field conditions, whilst in section 5.3.6, results are presented from an investigation into the pulsed-field operation of these emitters. Finally, sections 5.3.7 and 5.3.8 include results from (i) a complementary electron spectroscopy study and (ii) an investigation into the cross-sectional structure of the composite cathode coatings.

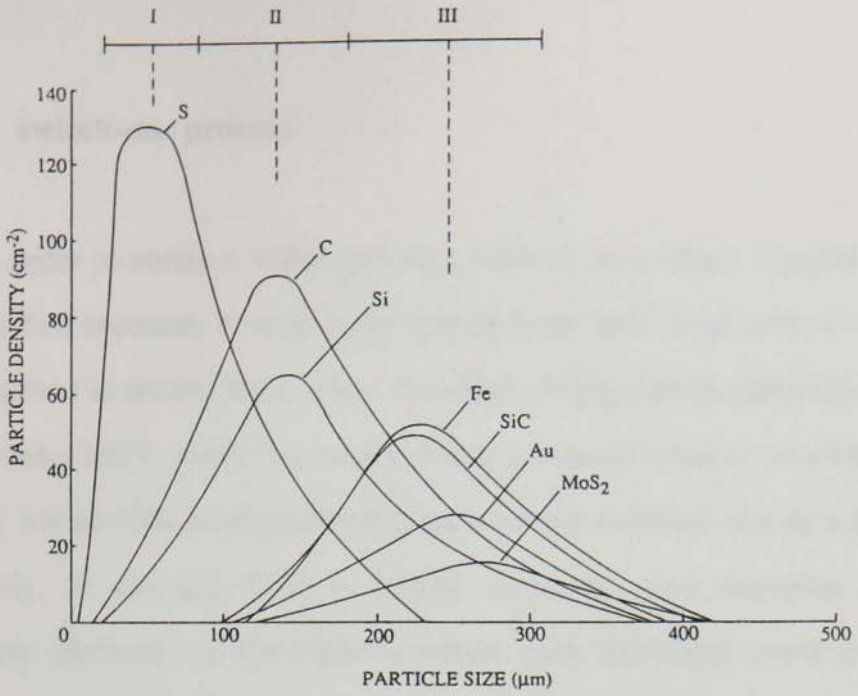

Figure 5.3 An analysis of the particle size distributions for the seven composite-cathode types. Here, the distributions represent the profiles of the corresponding frequency histograms obtained for a class width of 50μm.

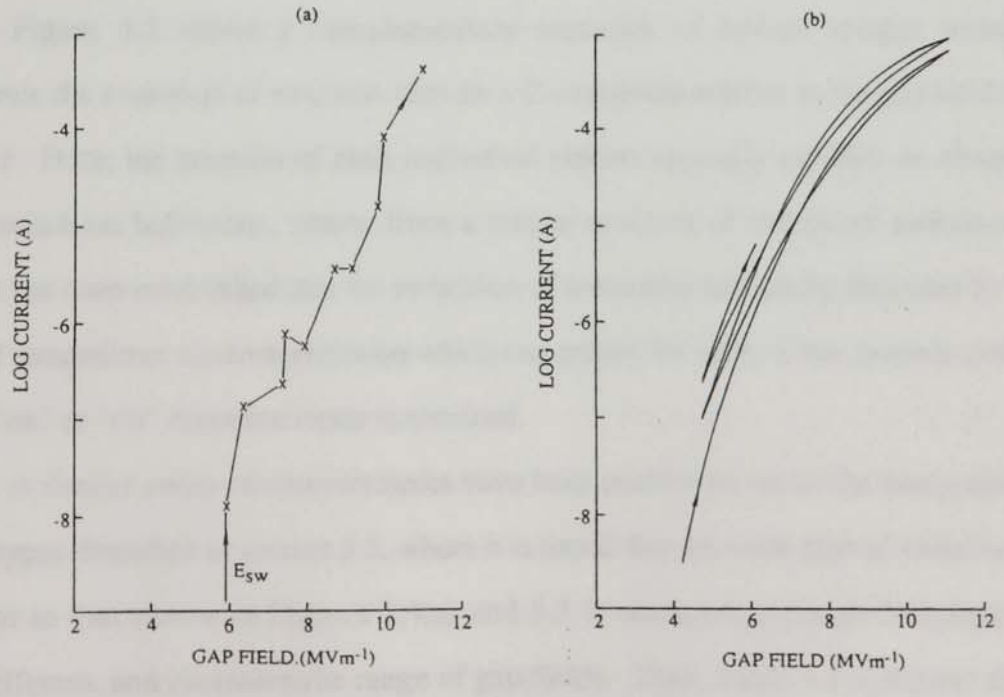

Figure 5.4 An example of (a) the typical switch-on of a virgin C-composite cathode, and (b) the hysteresis effect obtained for the initial voltage cycling of the same cathode.

5.3.1 The switch-on process

In order to obtain a stable emission mode from a virgin composite-coated cathode, it is first necessary to subject the cathode to an "activating" switch-on process, such as described in section 2.2.1. Here, the electrode gap field is gradually increased from zero, under UHV conditions, until the first switch-on event is observed, i.e. the sudden and irreversible establishment of an electron emission site at a field E_{sw}. Subsequently, as the gap field is further increased, new emission sites are progressively "formed" on the cathode, where each individual event is detected simultaneously by the transparent-anode imaging technique and the corresponding step-like increases in the total recorded gap current. To illustrate the switch-on process of a virgin composite-coated cathode, Figure 5.4(a) shows the typical characteristic obtained from a C-composite emitter. By applying the transparent-anode imaging technique to this sequence of events, it is found that the discrete "steps" shown in Figure 5.4(a) generally correspond to the switch-on of a new emission site. To illustrate this process, Figure 5.5 shows a complementary sequence of optical images which demonstrate the evolution of emission sites on a C-composite emitter as the gap field is increased. Here, the creation of each individual emitter typically exhibits an abrupt "flash" switch-on behaviour, where, from a similar analysis of individual switch-on events, it has been established that the switch-on of some sites is initially followed by a period of intermittent electron emission which can persist for up to a few seconds until a stable "on" or "off" emission mode is obtained.

A similar series of measurements have been performed on all the composite-cathode types described in section 5.2, where it is found that the same typical switch-on behaviour to that shown in Figures 5.4(a) and 5.5 is obtained, although frequently, over a different, and characteristic range of gap fields. Thus, Table 5.2 compares the typical values of the macroscopic gap switch-on field (E_{sw}) obtained with each composite type, and illustrates how all types exhibit a low-field switch-on characteristic

with typical values of E_{sw} in the field range 6-12MVm^{-1}.

Composite Cathode	C	MoS_2	Au	SiC	Si	Fe	S
E_{sw} (MVm^{-1})	6	6	7	7.5	10	10	12

Table 5.2. A comparison of the typical switch-on fields, E_{sw}, for the virgin composite-coated cathodes.

Referring to Table 5.2, it will be seen that the composite cathodes have been listed in order of increasing switch-on field, where a considerable difference, i.e a factor of 2, is typically observed between the respective values of E_{sw} for the C and S-composite emitters. Finally, it should be noted that although these values are generally reproducible, switch-on fields as low as 2MVm^{-1} have occasionally been observed during extended tests on the C-composite cathodes.

5.3.2 Current-Voltage (I-V) characteristics

Having established a population of emission sites as described above, the applied field is then cycled a number of times, typically in the field range 0-20MVm^{-1}, until it is found that a stable and reversible current-voltage (I-V) characteristic is obtained for each of the composite-cathode types. Thus, Figure 5.4(b) shows the effect of the initial field cycling following the switch-on of a virgin C-composite cathode, and clearly demonstrates an "exercising" effect in which the emissivity of the cathode progressively increases for increasing-field half-cycles, until a reversible I-V characteristic is obtained after typically 2 or 3 cycles. Subsequently, from an extended series of measurements on the range of composite-cathode types, it is generally observed that a similar behaviour to that shown in Figure 5.4(b) is obtained; however, the degree of exercising varies somewhat randomly, i.e. typically over a field span of

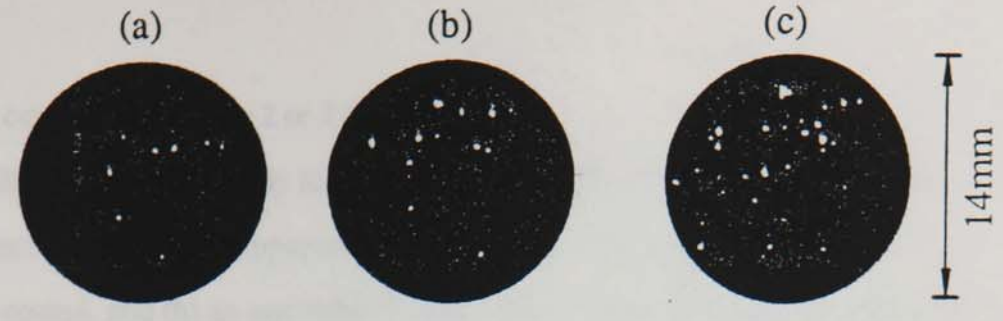

Figure 5.5 Optical images demonstrating the evolution of emission sites during the initial switch-on of a virgin C-composite cathode. (a) V_g=8kV, (b) V_g=10kV and (c) V_g=12kV.

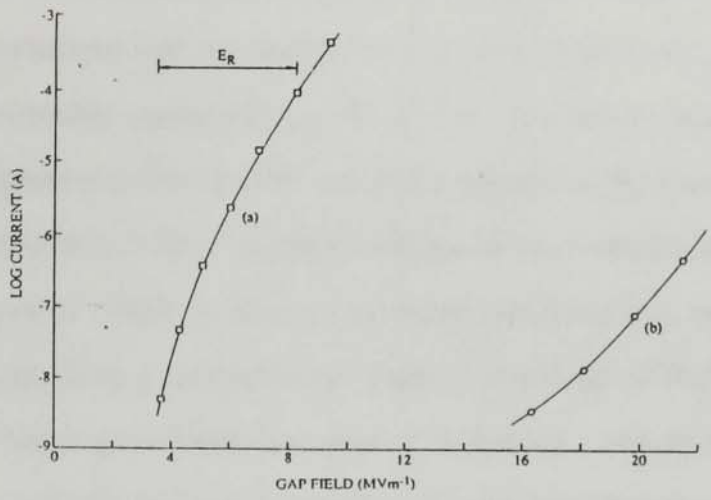

Figure 5.6 A comparison of the reversible I-V characteristics of (a) a typical C-composite coated cathode, and (b) an uncoated Cu-cathode.

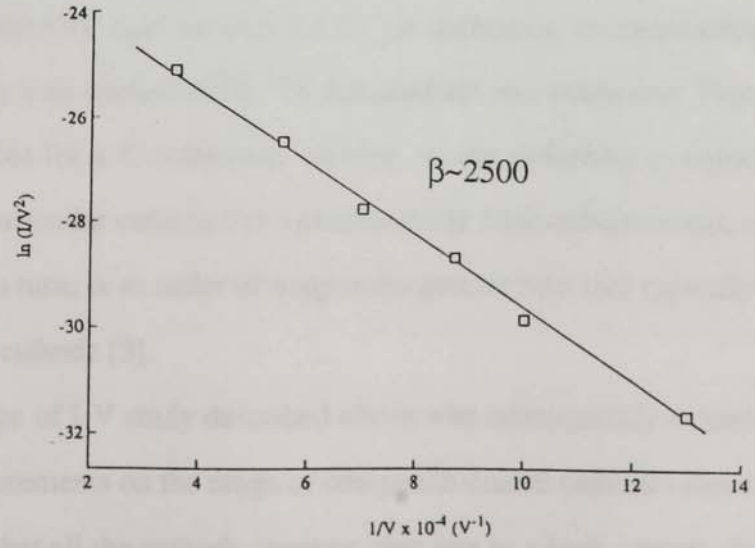

Figure 5.7 A Fowler-Nordheim (F-N) plot obtained from the reversible I-V characteristic of a typical C-composite cathode.

$1MVm^{-1}$ at a current of 1μA, for 2 or 3 field cycles.

To illustrate the extremely high level of emission obtained from the composite cathodes, Figure 5.6 shows a comparison between the stable I-V characteristics of (a) a C-composite coated, and (b) an uncoated Cu-electrode. These plots highlight how the composite cathode exhibits a steady low-current emitting state ($\sim 10^{-10}$-10^{-9}A) at an extremely low macroscopic gap field of $\sim 3MVm^{-1}$, where subsequently, by increasing the gap field beyond this region, the emission current rises rapidly, until finally, currents in excess of ~1mA are obtained at $\geq 10MVm^{-1}$ ($V_g \sim 3kV$); in fact, this emission behaviour can be correlated with an increase in the total number of emission sites contributing to the recorded current (see section 5.3.3). In addition to these general observations, it is important to note that the composite cathode current has not saturated over this field range; in fact, current measurements above 1mA could not be obtained with the present system owing to both anode power-handling and power supply limitations. However, from a comparison of curves (a) and (b) of Figure 5.6, it is apparent that the C-composite cathode is capable of delivering a current of ~1mA at a lower field than that typically required to switch-on the emission from an uncoated Cu-electrode.

It is interesting to note that an analysis of the I-V characteristic shown in Figure 5.6 reveals that the C-composite cathode exhibits a linear Fowler-Nordheim (F-N) emission behaviour (see section 2.1.1), i.e indicating an exponential rise in the emission current with applied field. To demonstrate this behaviour, Figure 5.7 shows a typical F-N plot for a C-composite emitter, where, referring to equation 2.7, it is found that this particular cathode has a characteristic field-enhancement, or β-factor, of ~2600, which, in turn, is an order of magnitude greater than that typically obtained for an uncoated Cu-cathode [3].

The type of I-V study described above was subsequently extended to include a series of measurements on the range of composite-coated cathodes listed in Table 5.1. These revealed that all the cathode-systems give rise to a high current characteristic at relatively low gap fields, however, significant differences were found in the general

emissivity of the cathode types. Thus, Table 5.3 compares the respective β-values and the operating field range, E_R, associated with each cathode type, where E_R is defined as the range over which the total emission current increases from 10^{-9}- 10^{-4}A.

Composite Cathode	Current at 10MVm^{-1} (μA)	Operating Field Range E_R (MVm^{-1})	β -factor
C	500	2.5- 9.0	2571
MoS_2	400	5.0-11.5	1552
Au	80	5.0-15.0	753
Si	30	3.5-17.0	1705
SiC	15	6.5-16.5	595
S	10	6.5-16.5	572
Fe	1	7.5-25.0	623

Table 5.3. Typical electron emission characteristics of the seven composite-cathode types listed in order of decreasing emissivity.

Thus, whilst all the composite cathodes are capable of delivering total currents in excess of 0.1mA in the field range ~10-25MVm^{-1}, it is clear from Table 5.3 that there is a considerable difference between the I-V characteristics of the highly emissive C and MoS_2 composites and the lower emission level obtained from the Fe composite, i.e greater than an order of magnitude at a moderate gap field of 10MVm^{-1}. To illustrate these differences, the cathodes shown in Table 5.3 have been listed in order of decreasing emissivity, i.e as determined by their respective emission currents at 10MVm^{-1}; in fact, this trend is also reflected, to a large extent, in both the relative positions and widths of the respective operating ranges, and the corresponding values of β. In addition to these general emissivity trends, a comparison of Tables 5.2 and 5.3 reveals a further correlation between the emissivity of a particular cathode and its switch-on field, E_{sw}. Thus, it is generally observed that the most emissive cathodes, e.g. C and MoS_2, initially switch-on at the lower field values of ~6MVm^{-1}.

5.3.3 Site Distribution Images

Having established the switch-on and total current-voltage emission characteristics in the previous sections, the transparent-anode imaging facility, described in section 3.2.2, has been used to investigate the spatial distribution and temporal behaviour of the electron emission sites on the composite-coated cathodes. In this section, results will be presented from video recordings of the site distributions obtained during the routine evaluation of the seven composite-coated cathode types described in section 5.2.

Following the characteristic switch-on sequence of a typical composite test cathode, the optical imaging facility reveals that the resulting electron emission current stems from a population of localised emission centres, or sites, which are randomly distributed over the cathode surface. To illustrate this behaviour, Figure 5.8 shows the corresponding site distribution images obtained at successive increases in the gap field for the reversible emission characteristic of a typical C-composite emitter. From a comparison of the I-V characteristic of Figure 5.6, and the site distribution images of Figure 5.8, it is apparent that the rapid increase in the emission current with increasing gap field can be correlated with a corresponding increase in the number of emission sites; in fact, an increase in the gap field from ~7 to 10MVm^{-1} results in a ten-fold increase in the number of sites contributing to the total emission current, i.e from ~5 to ~50 sites. A particularly significant feature of the image shown in Figure 5.8(c) is the large number of sites that have switched-on at the relatively low macroscopic field value of ~10MVm^{-1}, which, in turn, serves to illustrate the extremely high emissivity of the composite-coated cathodes when compared with an uncoated conventional Cu-electrode [75]. To further highlight this observation, Figure 5.9 compares the respective site distributions typically obtained at the same gap field of 10MVm^{-1} for (a) an uncoated Cu-electrode, (b) a resin-coated Cu-electrode and (c) a C-composite test cathode. Significantly, from a vacuum-insulation viewpoint, it is clear from Figure 5.9(b) that

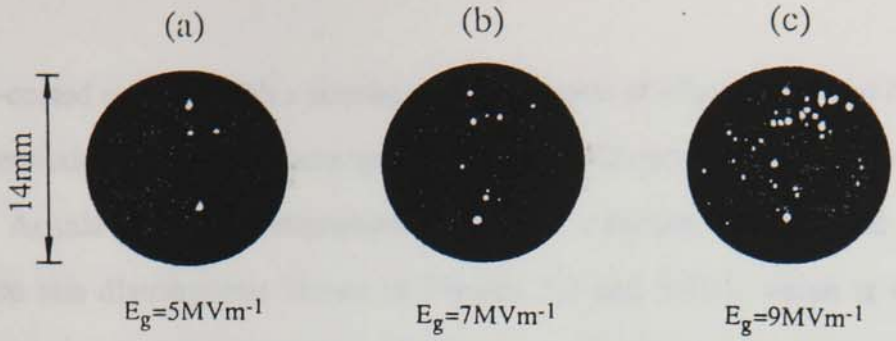

Figure 5.8 A sequence of optical images illustrating the increase in the number of emission sites with increasing gap field for the reversible characteristics of a C-composite emitter.

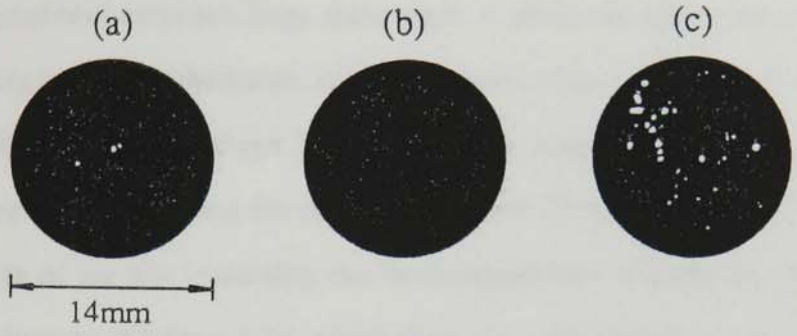

Figure 5.9 A comparison of the typical site distribution images obtained at a gap field of 10MVm^{-1} for (a) an uncoated Cu-cathode, (b) a resin coated Cu-cathode and (c) a C-composite cathode.

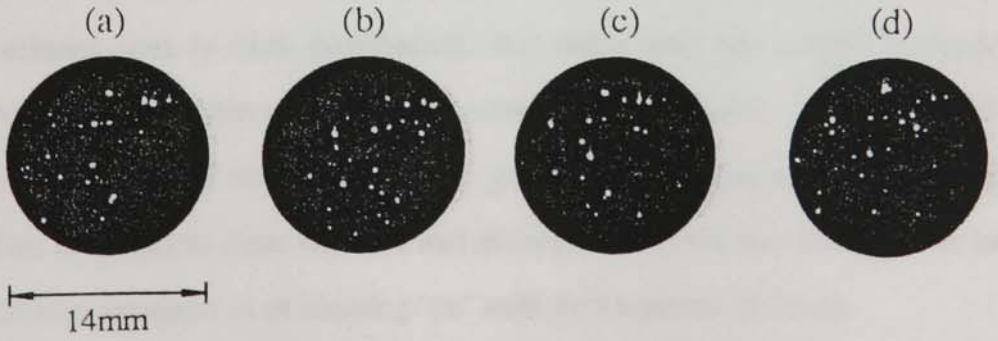

Figure 5.10 A time sequence of constant-field site images illustrating the spatial instability of a typical C-composite cathode. E_g=10MVm^{-1}, I_e=0.5mA, time interval = 3mins.

the resin-coated cathode, with a nominal resin thickness of ~7μm, shows no discernible electron emission following an attempted switch-on field cycle of up to 40MVm^{-1}.

At this point, it is important to describe a further characteristic of the C-composite site distributions shown in Figures 5.8 and 5.9(c), which is inherently hidden owing to the "still frame" nature of these images; i.e. the images represent only a "frozen" record of a site population at a particular gap field and time. However, from a video analysis of the process over a time scale of 20 mins, it is revealed that some sites (generally less than 20%) exhibit a random switching instability, with varying time scales of a few seconds, or less, to a few minutes; this behaviour, including the occasional intermittent emission from some sites, is generally more pronounced with the low-intensity sites. Furthermore, it has also been noted, particularly with the C-composite regime, that 1 or perhaps 2 sites are seen to host occasional "explosive" or "flashing" events, thus indicating the existence of a non-destructive instability. In fact, the general form of the site instability can be demonstrated to a certain extent by the time-sequence images of Figure 5.10, which show the long-term temporal variations in a typical C-composite cathode site population for a constant gap field of ~9MVm^{-1} and a total emission current of ~0.5mA. Thus, it will be seen that, of the 60 or so sites that can be identified in the 9 minute period between Figure 5.10 (a) and (d), only 60-70% of these sites are in an emitting "on" state at any particular frame reference. In addition to this spatial instability, it is also evident from a comparison of, for example, the 5 most dominant sites in each distribution, that many sites are subject to random variations in intensity with time, under constant-field conditions. At this point, it is interesting to note that the Si-composites generally gave rise to the most stable populations of emission sites, where it was generally observed that ≥90% of the total number of sites remained in an emitting "on" state over a period ≥10mins.

Hitherto, the general site distribution characteristics of the composite-coated cathodes have been described in terms of the images obtained from the C-composite emitters. However, in order to gain an insight into the emission characteristics of all

the composite-cathode regimes, and their corresponding site capabilities, a comparative study has been performed on the complete catalogue of site data obtained from extensive video recordings of each cathode-type. Thus, Figure 5.11 (a)-(d) compares the typical constant-current (10^{-4}A) site distributions obtained for the Si, SiC, Au and MoS_2 cathodes respectively, and highlights the differences in the resulting emission modes for the various composites. In particular, these images show the variation in the total number of sites required to attain a total current level of 10^{-4}A for each cathode, i.e ~50 for MoS_2 and ~12 for Si. It follows that such data can be used to estimate values for the average emission current per site, i_s, i.e. defined as the total emission current divided by the total number of sites. Thus, Table 5.4 compares the number of sites per cm^2, n_s, and hence the average site currents, i_s, typically obtained for the seven composite-cathode types at a current level of 10^{-5} and 10^{-4}A respectively.

Composite	$I_e=10^{-5}$A		$I_e=10^{-4}$A	
cathode	n_s (cm^{-2})	i_s (μA)	n_s (cm^{-2})	i_s (μA)
C	0.7	5.0	4.7	14.0
MoS_2	14.0	0.5	32.7	2.0
Au	6.7	1.0	13.3	5.0
Si	2.7	2.5	8.7	7.7
SiC	11.3	0.6	29.3	2.2
S	4.7	1.3	26.7	2.5
Fe	3.3	2.0	22.7	2.9

Table 5.4. Collated data of typical emission site densities, n_s, and average site currents, i_s, for total emission currents of 10^{-5} and 10^{-4} A.

Referring to Table 5.4, it will be seen that, with the exception of the C, Si and Au emitters, the cathodes generally give rise to a similar emission characteristic for individual sites, where, at a current level of 10^{-4}A, the average site currents typically lie within the range 2-3μA, i.e as obtained from the site images shown in Figure 5.11(b)

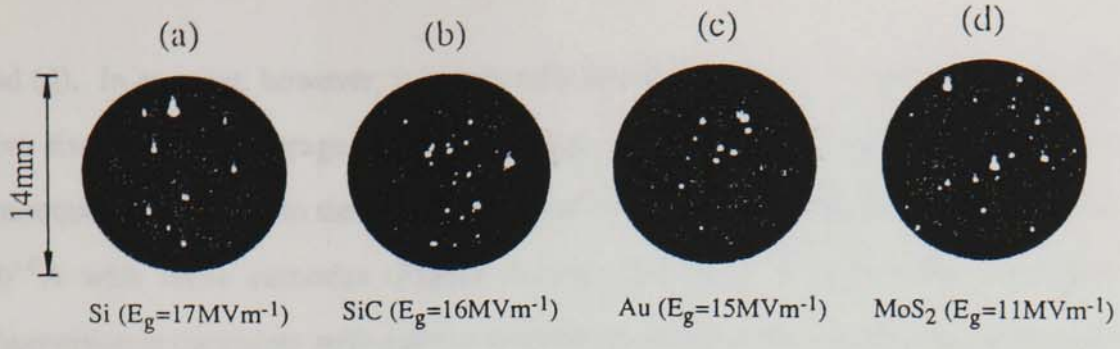

Figure 5.11 A comparison of the typical site distribution images obtained for (a) a Si, (b) a SiC, (c) an Au, and (d) an MoS_2-composite cathode for a total emission current of 10^{-4}A.

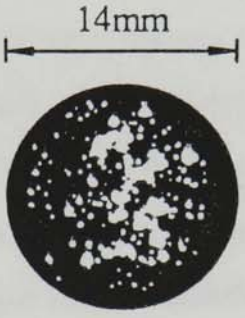

Figure 5.12 A typical site distribution image of a high site density SiC-composite emitter. E_g=14MVm^{-1}.

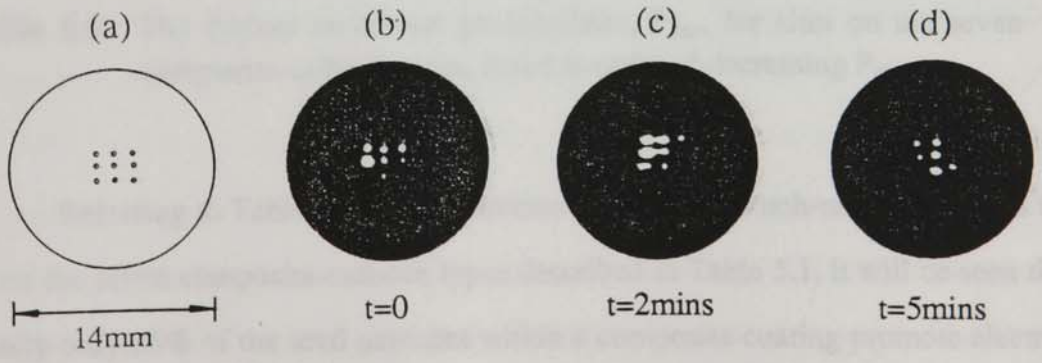

Figure 5.13 (a) A schematic of a 3 x 3 multiemitter composite-array cathode. (b) - (d) A time sequence of constant-field images for a SiC composite array cathode. E_g=10MVm^{-1}.

and (d). In contrast, however, it is generally found that the C, Si and Au-composites give rise to higher average site currents, e.g. of the order i_s~14μA for C, which is consequently reflected in the lower number of sites required to deliver a total current of 10^{-4}A with these cathodes (Figure 5.11(a) and (c)). Significantly, this latter observation is consistent with a direct correlation between the average site current and the general emissivity (Table 5.3) of a particular composite-cathode type, which, with the exception of the MoS_2 emitter, is satisfied to a certain extent by the range of i_s data presented in Table 5.4. In this respect, although the MoS_2 cathodes are generally found to be very emissive and capable of delivering a total current of 10^{-4}A at a low gap field of ~11MVm^{-1}, it is evident, from a comparison with the C-cathode parameters in Table 5.3, that the high MoS_2 emissivity is a direct result of the high site density, n_s, i.e as opposed to a high i_s-characteristic of the individual MoS_2 sites. This observation highlights the importance of a further cathode parameter, namely the switch-on probability of sites, P_{sw}, which is defined as the percentage of the total number of particles that are found to emit for gap fields of ≤20MVm^{-1}.

Composite-cathode	MoS_2	C	Au	SiC	Fe	S	Si
P_{sw} (%)	22.3	5.1	3.3	2.6	2.5	2.4	2.2

Table 5.5. The typical switch-on probabilities, P_{sw}, for sites on the seven composite-cathode types, listed in order of decreasing P_{sw}.

Referring to Table 5.5, which collates the typical switch-on probabilities for sites on the seven composite-cathode types described in Table 5.1, it will be seen that typically only ≤5% of the total particles within a composite coating promote electron emission for these applied fields. Furthermore, it is shown how the C and MoS_2 particles, which are well-known for stimulating emission at low fields from high-voltage electrodes [62], convincingly give rise to the highest values of P_{sw}, i.e. 22.3%

and 5.1% respectively. As will be discussed later, Table 5.5 also provides evidence for the existence of a "size effect", in which the large-particle composites (Figure 5.3) generally give rise to more emission sites per total number of particles.

In addition to characterizing the site distribution behaviour of the seven composite-cathode types used in the present study, the transparent-anode imaging facility has been used to evaluate the performance of two modified prototype cathodes based on the same composite sub-structure. The motivation for these studies stemmed from the considerable commercial interest in both the extended-area "uniform" emission and single-emitter regimes, discussed in section 2.3, where it was considered of technological importance to assess the feasibility of (a) significantly increasing the emission site density of the composite-coated cathodes and (b) producing an array cathode consisting of a two-dimensional ordered array of single emitters on an extended-area substrate.

5.3.3(i) High Site Density Cathodes

In an attempt to fabricate a high site density emitter, a standard 14mm-diameter Cu-electrode was coated with a double density composite layer (~1000 SiC particles cm^{-2}), which was originally spun from a 0.2 g/ml suspension as described in section 5.2. The resulting site distribution image obtained following the characteristic switch-on of this SiC-composite cathode is shown in Figure 5.12. From this, it is evident that a high site density of $n_s > 130 cm^{-2}$ is obtainable from these emitters at a relatively low gap field of ~$14 MVm^{-1}$. However, whilst this demonstrates the potential level of emission obtainable from such surfaces, it is generally difficult to increase the site density beyond, say, $150 cm^{-2}$ with the SiC-composites, owing to both the inherent particle density limitation imposed by the present spinning technique and the comparatively low switch-on probability, $P_{sw} = 2.6\%$, of this regime (see Table 5.5).

5.3.3(ii) Composite Array Cathodes

For the second prototype cathode, a modified fabrication technique was used to produce a 3 x 3 multi-emitter array cathode which is shown schematically in Figure 5.13(a). To achieve the desired degree of control required to fabricate these emitters, it is necessary to "deposit" the composite array layer in successive stages, where initially, this involves coating the Cu-substrate electrode with a spun resin layer of nominal thickness ~7μm. Subsequently, the chosen particles are individually deposited onto the uncured resin layer using a needle-point vertical carriage manipulator to form a 3 x 3 two-dimensional particle array with a nearest neighbour distance of ~1mm (Figure 5.13(a)). Following this procedure, the uncured resin is heat treated, as described in section 5.2, prior to spinning and subsequently curing an additional top resin layer, which encapsulates the existing array in a dielectric matrix. Figure 5.13(b)-(d) shows a time sequence of constant-field site images obtained during a 5 minute video recording of a 3 x 3 SiC-composite array cathode produced from 400μm-sized particles. Whilst these images further demonstrate the inherent site instability associated with the composite emitters, it is apparent that each of the 9 "doped" regions shown schematically in Figure 5.13(a) have successfully given rise to a centre of electron emission over the 5 minute test period at the relatively low gap field of ~10MVm^{-1}. In spite of the obvious differences in the individual site intensities at this field, and the occasional appearance of "twin sites" (e.g Figure 5.13 (c)), it is clear from such feasibility experiments that the location of individual emission sites can be controlled to a considerable extent using the modified composite fabrication technique. Furthermore, in view of the inherent particle density limitations of the spun-composite fabrication technique (section 5.2), it appears justifiable to conclude that the above modified fabrication process could substantially increase the site density, n_s, on the proposed "uniform" emission cathodes, such as shown in Figure 5.12.

5.3.4 Emission current stability

Referring to the site distribution images of Figure 5.10, it is apparent that the constituent sites on a typical composite-coated cathode are inherently subject to random switching instabilities, which consequently give rise to fluctuations in the total gap current during cathode operation. To investigate the relative level of current instability associated with all the seven composite-cathode types studied, temporal fluctuations in the gap current have been monitored in the form of chart recorder, current-time (I-t) traces under identical experimental conditions. As an example of the type of data obtained in this series of measurements, Figure 5.14 demonstrates the total current stability associated with a typical C-composite cathode operating at a mean current level of (a) 10^{-5}A, (b) 10^{-4}A and (c) 10^{-3}A, for a period of ~120 secs. Referring to trace (a) of Figure 5.14, it will be seen that, at the lower current levels ($<10^{-4}$A), the composite-cathode emission current generally exhibits a step- and/or spike-like behaviour, such as commonly observed with single-emitter carbon tips [24,109]: furthermore, the "frequency" of these fluctuations is shown to increase significantly with increasing current level (traces (b) and (c)).

In order to undertake a systematic analysis of the data obtained from these I-t measurements, it is conventional to define a current stability parameter, S, as the mean current fluctuation per mean current level, expressed as a percentage, i.e. such that

$$S=\Delta I_e/I_e \times 100\% \qquad (5.1)$$

where ΔI_e and I_e are shown in Figure 5.14(a). Thus, it can be concluded from Figure 5.14 that the stability of the C-composite cathode improves quite markedly with increasing current level. In quantitative terms, it was found from a extended analysis of the available data, that the value of S decreases almost exponentially from ~50% to 2% in the current range 10^{-6}-10^{-3}A. However, it is also evident from a comparison of

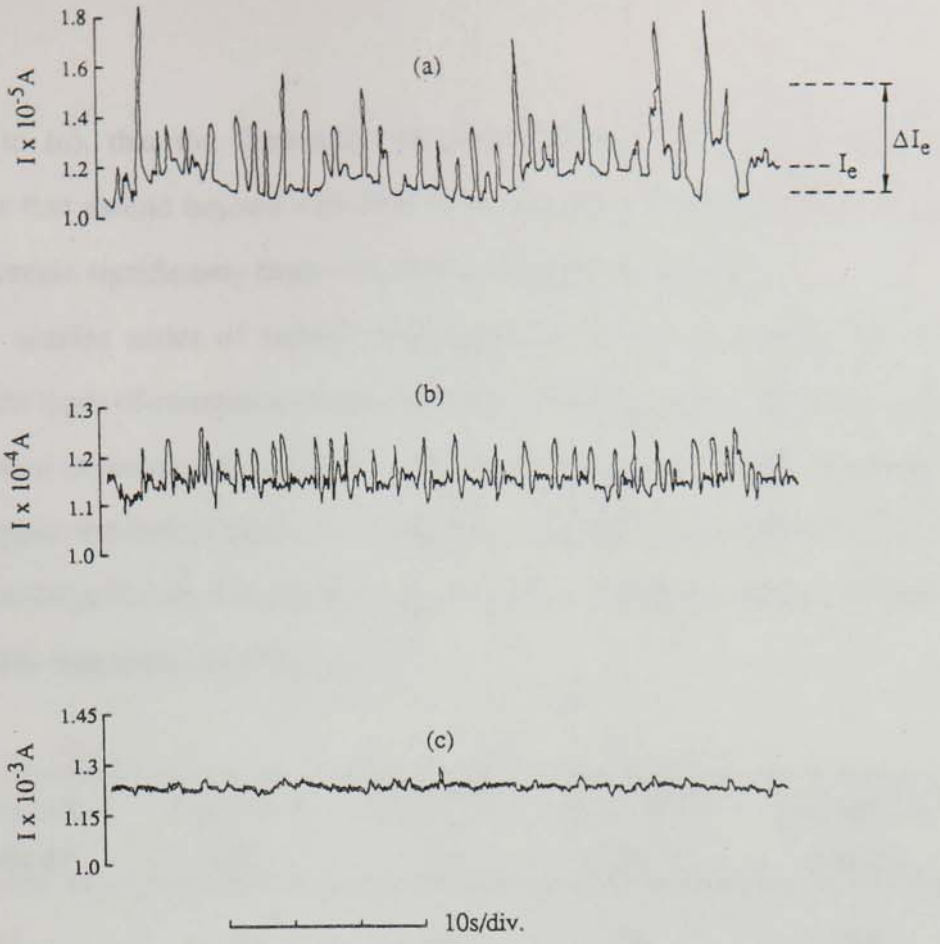

Figure 5.14 An example of the temporal stability of a typical C-composite cathode operating at a total current level of (a) 10μA, (b) 100μA and (c) 1mA. The stability, S, is defined as $\Delta I_e/I_e$ x 100%.

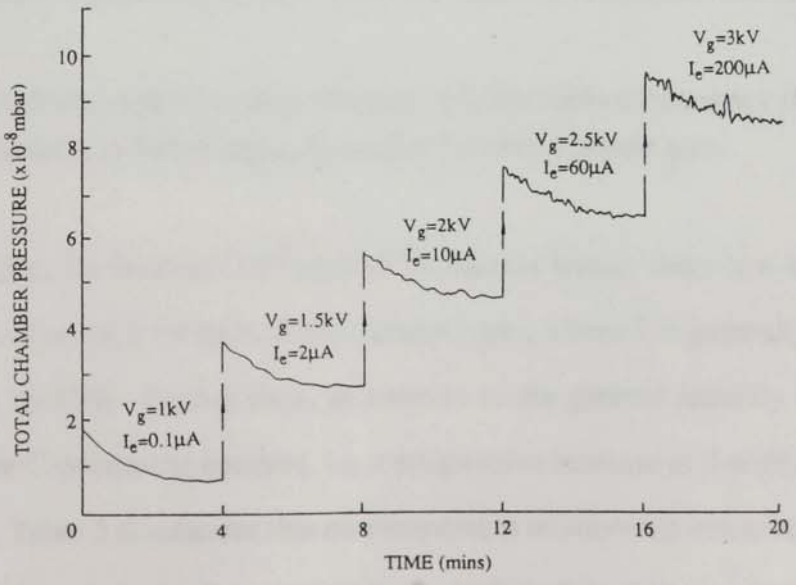

Figure 5.15 A typical example of the operational outgassing effect showing how the total chamber pressure increases linearly with gap voltage during the operation of a C-composite cathode.

traces (a) to (c), that the fluctuation frequency (F_f), defined as the number of fluctuations that extend beyond ~10-20% of ΔI_e from the mean current level (I_e), is found to increase significantly from ~34, to 60 to 94min^{-1} respectively.

A similar series of stability measurements have been conducted on the remaining six types of composite-coated cathodes to compare their respective stabilities under identical experimental conditions. These findings are summarised in Table 5.6, which compares the typical values of the stability, S, the fluctuation frequency, F_f, and a further instability factor, defined as the product of the fractional stability (S/100) and the fluctuation frequency, i.e $(\Delta I_e/I_e) \times F_f$.

Composite Cathode	S at 10^{-5}A (%)	S at 10^{-4}A (%)	F_f at 10^{-4}A (min^{-1})	$(\Delta I_e/I_e) \times F_f$ (min^{-1})
C	33	15	54	8.1
MoS_2	21	49	84	41.0
Au	18	46	57	26.0
Si	8	15	66	9.9
SiC	48	12	96	11.5
S	26	22	98	21.8
Fe	32	23	81	18.6

Table 5.6. Collated data of typical stability (S), fluctuation frequency (F_f) and instability factor ($F_f\Delta I_e/I_e$) values for each cathode type.

It will be seen that, for both the 10^{-5} and 10^{-4}A current levels, there is a significant variation in the values of S for each of the cathode types, where S is generally found to lie in the range 10-50%. Furthermore, in contrast to the general stability behaviour obtained with the C-composite emitters, i.e. a progressive increase in S with increasing I_e (Figure 5.14), Table 5.6 indicates that no comparable relationship exists between the values of S and the corresponding current level; in fact, it is seen, for example, that MoS_2, Au, and Si clearly depart from such behaviour. However, despite this

observation, a correlation is clearly evident between the tabulated values of S and the instability factor ($F_f\Delta I_e/I_e$) at $I_e \sim 10^{-4}$A. These values appear to imply that the C, Si, and to some extent SiC-composites give rise to the most stable emission currents under identical experimental conditions. In view of the practical importance of this finding, the influence of I_e on the instability factor will be considered in more detail in section 5.3.5(d). Finally, from a technological viewpoint, it is significant to note that the mean current level (I_e) of all the composite cathode-types is found to be stable during the 30 minute testing period used in the present study.

5.3.5 An extended study on the emission stability of C-composite cathodes

From first-order feasibility considerations, it is apparent from the evidence presented in the above sections, that the composite-coated cathodes exhibit exciting cold cathode emission features, where high current operation (≥1mA) is generally obtainable at moderate applied fields of <20MVm^{-1}. In particular, the C-composite cathodes have been shown to possess the most desirable emission features amongst the emitters studies, and offer a promising compromise between (a) low-field operation, (b) high average site currents and (c) a favourable total current stability. However, in the realisation of practical cold-cathode electron sources, such as envisaged for example in the 3 x 3 array of single emitters shown in Figure 5.13, there exists a technolgical requirement of individual site stability, which, as demonstrated in Figure 5.10, has so far proved difficult to achieve with the cathodes tested in this study. Therefore, for the purpose of investigating the origin of the spatial and temporal instability of these emitters, a series of experiments have been performed on the C-composite regime, with the ultimate objective of improving the existing cathode performance by utilising both thermal processing and reverse-field pre-treatments. In addition, the present study also includes an investigation into two further experimental phenomena which are of considerable technological importance, namely the operational outgassing process and

the influence of the residual gas environment on the cathode performance.

5.3.5(a) Thermal pre-treatment

The thermal annealing of a virgin cathode prior to operation has been shown by a number of workers [11,12,24] to drastically reduce both the spatial and temporal emission instabilities, as well as reducing the incidence of "explosive" events during the initial switch-on process. This annealing process typically involves heating the cathode, under UHV conditions, to a temperature of 150-250°C for a period of ≥20 hours. Hence, to investigate the influence of thermal pre-processing on the C-composite cathode, a procedure was developed whereby a virgin cathode was heated *in situ* to a temperature of ~200°C for ~24 hours , and was then left to cool to room temperature before applying a slowly increasing field across the electrode gap. Following this proceedure, it is typical to observe a similar type of unstable cathode switch-on characteristic, such as shown in Figure 5.4(a); furthermore, the transparent-anode imaging facility reveals a similar switch-on behaviour including "flashing" or "explosive" events. Having established a stable distribution of emission sites, it is found, in contrast to previous studies, that both the current instability and the spatial instability have significantly increased when compared with the untreated-cathode stabilities shown in Figures 5.10 and 5.14. Furthermore, by applying the same thermal processing to previously used C-composite cathodes, it is generally found that the same, or a similar level of de-stabilisation results, where, from I-t traces, it is typically observed that the stability, S, decreases by a factor of 2 in the current range 10^{-6}-10^{-4}A, e.g. from 32% to 60% at I_e~10^{-5}A. Moreover, this process is typically found to result in a 20-30% increase in the fluctuation frequency, F_f, of the total emission current, e.g from 54min^{-1} to 66min^{-1} at I_e~10^{-4}A.

5.3.5(b) Reverse-polarity processing

In a further investigation into the influence of various pre-treatments on the operating characteristics of the C-composite cathodes, a cathode was subjected to an extended period of reverse-field processing, i.e. with the test "cathode" biased with a positive potential. This technique is commonly used in the preparation of metallic micropoint field emitters, where it is known to reduce the adsorbed gas layer via a field desoption process [114]. In these experiments, the reverse field is gradually increased across the electrode gap to a value of ~7MVm^{-1} (V_g~2kV), where it is then held constant for a period of 30 mins. Under these conditions, it is typical to observe 2 or 3 "sites" through the transparent anode, which together deliver a stable gap current of ~10^{-4}A, and furthermore, appear to be located in the positions of the dominant electron emission sites obtained previously under the normal field polarity. For the purpose of determining the origin of the reverse-field sites, both the "normal" and "reverse" emission images can then be viewed through the video or photographic system, at an increased electrode gap spacing of ~2mm. Thus, from a comparison of the respective "planes of foci", it is found that the bluish pin points of light corresponding to the reverse sites originate from the the surface of the test cathode. From this evidence, it appears likely that the reverse-field current stems from a field emission process associated with the carbon contamination that is invariably present on the transparent anode, i.e as opposed to ion emission, or a continuous gas ion or field desorption [114] process from the composite-coated surface. Hence, it can be anticipated that the above procedure results in a continual bombardment of the dominant sites on the C-composite cathode by electrons with energies of ~2keV.

To investigate the influence of electron bombardement on the stability of the C-composite cathodes, I-t traces have been obtained for a number cathodes both prior to and following a 30min period of reverse-field conditioning, i.e. as described above. From a comparison of such measurements, it is generally revealed that no discernable

changes occur in the I-V characteristics of the C-composite cathodes. However, these measurements have shown that a slight, if not negligible, increase (≤5%) is occasionally observed in the values of the stability, S, and the fluctuation frequency, F_f, following a period of reverse-field processing.

5.3.5(c) Operational outgassing effects

The liberation of gases from an electron emission regime is an important technological consideration, since the onset of excessive outgassing during operation could ultimately threaten both the stability of the cathode and the UHV environment, which, in turn, may be of crucial importance in certain applications. Moreover, it could be anticipated from an analytical viewpoint, that the characteristics of the gas emission may provide an insight into the fundamental processes involved in the underlying field-induced electron emission mechanism and associated phonomena such as cathode stability, etc. For this purpose, the residual gas analysis technique (described in section 3.3.1) has been used to investigate the degree and nature of the outgassing phenomenon observed during the operation of a test C-composite cathode.

During the routine evaluation of the C-composite emitters, significant increases are invariably observed in the total chamber pressure, where the resulting pressure level, and its fluctuations, appear to be generally dependent on the level of electron emission and the stability of the test cathode respectively. To illustrate this behaviour, Figure 5.15 shows the typical variation in the chamber pressure for successive increases in the total gap voltage and hence emission current. From this, it is observed that the total pressure increases by approximately one order of magnitude over the characteristic operating range of the C-composite cathode. A more detailed analysis of this "staircase" pressure response, and the corresponding emission parameters shown in Figure 5.15, reveals that the outgassing phenomenon displays a linear voltage-dependence, i.e. as opposed to a current dependence. Furthermore, from similar experiments with an increased electrode gap spacing, it has been established that

the level of outgassing is independent of the gap field. Referring to Figure 5.15, it is also shown how the constant-voltage pressure levels typically decrease, in an exponential-like manner, to an equilibrium value over a period of ~4mins; in contrast, the corresponding fluctuations in these levels are found to increase with increasing voltage, and hence emission current. In view of this latter observation, it should be noted that the pressure fluctuations generally increase with the corresponding current fluctuation frequency of the emitter, F_f, where the most significant fluctuations can be correlated with the onset of the "explosive" site phenomenon described in section 5.3.3.

In order to determine which particular gas species give rise to the observed total pressure increase, mass spectroscopy measurements have been performed in the atomic mass range 1-100, both before and during cathode operation. This comparative analysis reveals that the most significant partial pressure increases occur in the H_2, O_2 and CO peaks, where, at a gap voltage of ~2.5kV and a current level of ~10^{-4}A, increases of 400, 300 and 200% are typically observed for the above gas species respectively; in fact, these findings are similar to those reported in earlier studies [188] on the outgassing effects associated with field-emitting cathodes.

In a similar study to investigate the influence of the emission current and gap voltage on the liberation of a particular gas species, a comparative study was undertaken on the outgassing effects associated with the three main residuals identified above, i.e. H_2, O_2 and CO. Thus, as in the case of the total pressure (Figure 5.15), it is found that the degree of outgassing for each of the three residuals appears to exhibit a voltage dependence, such as shown in the respective plots of Figure 5.16. It is also seen from these plots that the partial pressure of each residual increases linearly with increasing gap voltage c ver the normal range of operating voltages, i.e corresponding to emission currents in the range 10^{-6}-10^{-4}A.

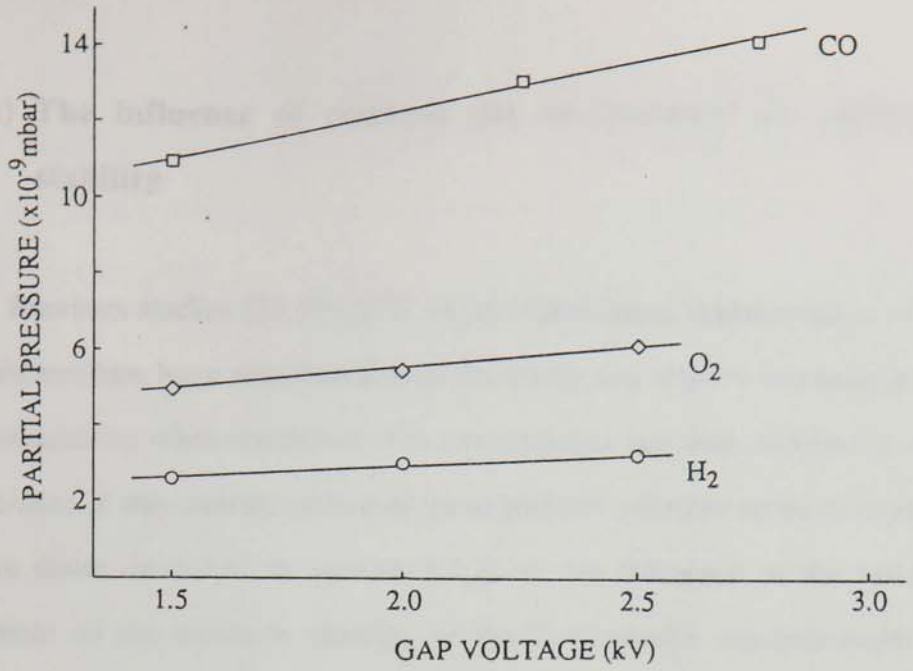

Figure 5.16 The linear voltage dependence of the three main outgassing residuals liberated during the routine operation of a C-composite cathode.

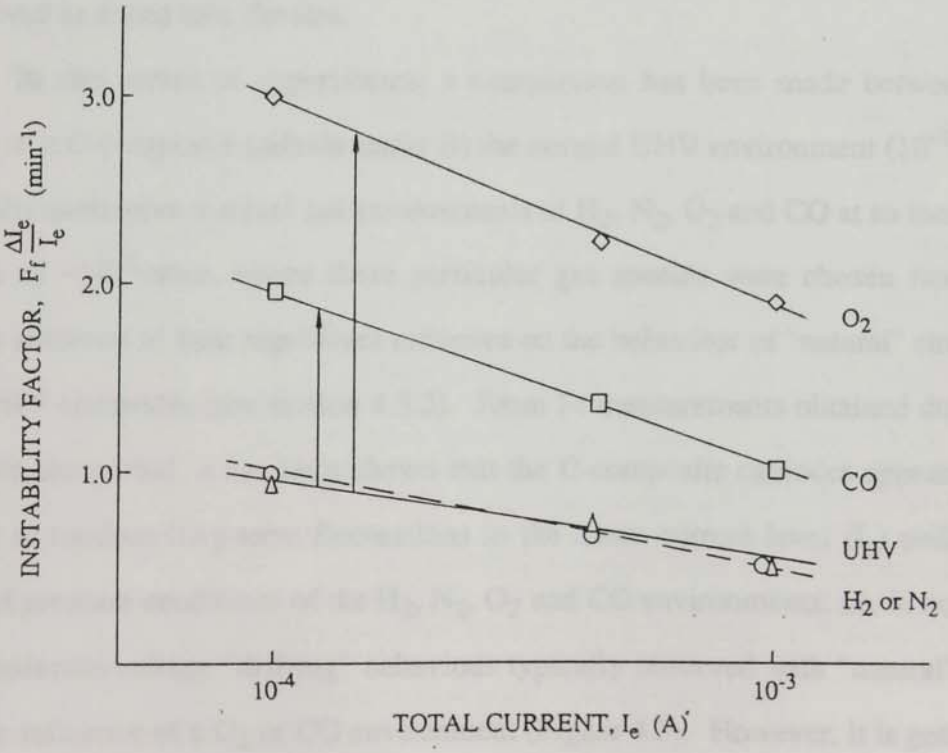

Figure 5.17 The influence of O_2, CO, N_2 and H_2-environments on the instability factor for a typical C-composite cathode operating at various current levels. P=10^{-5}mbar.

5.3.5(d) The influence of residual gas environment on cathode stability

Previous studies [22,106,107] on the operational characteristics of carbon-based field-emitters have established their durability and relative insensitivity to poor vacuum conditions when compared with conventional tungsten micropoint cathodes. In this context, it was considered important to perform a further series of experiments, similar to those described in section 4.3.2, on the influence of the residual gas environment on the emission stability of the C-composite emitters under normal operating conditions. These measurements are of technological interest, in that they provide an insight into the anticipated performance, or capabilities, of a practical composite-coated cathode which may well be expected to operate under pressure fluctuations and "commercial vacuum" conditions ($\leq 10^{-6}$mbar), e.g. as typically encountered in sealed tube devices.

In this series of experiments, a comparison has been made between the stability of a C-composite cathode under (i) the normal UHV environment (10^{-8}mbar) and (ii) the alternative residual gas environments of H_2, N_2, O_2 and CO at an increased pressure of $\sim 10^{-5}$mbar, where these particular gas species were chosen from the previous evidence of their significant influence on the behaviour of "natural" emission sites on HV electrodes (see section 4.3.2). From I-t measurements obtained during a 10 minute test period, it has been shown that the C-composite cathodes appear to be resistant to random long-term fluctuations in the mean current level (I_e) under the increased pressure conditions of the H_2, N_2, O_2 and CO environments, i.e. in contrast to the moderate-voltage "drifting" behaviour typically observed with "natural" sites under the influence of a O_2 or CO environment (Figure 4.5). However, it is generally found that the short-term stability, S, and the fluctuation frequency, F_f, of the total current is increased slightly; for example, from 2 to 2.4% and 36 to 44 min^{-1} respectively for H_2 or N_2, and from 4 to 6.5% and 40 to 47min^{-1} for O_2, at a current

level of ~10^{-4}A. As shown in Figure 5.17, these small changes in the emission stability, resulting from operation under different gas environments, can be illustrated in more detail from an analysis of the variation of the instability factor, $\Delta I_e/I_e \times F_f$ with the total current level, I_e. Thus, in addition to illustrating the linear "current dependence" of the instability factor, Figure 5.17 shows how the underlying influence of each particular gas environment varies significantly, although from a practical viewpoint very slightly, from the extremely passive H_2 and N_2 gases to the more active O_2 and CO environments. Furthermore, the transparent-anode imaging technique has revealed that the corresponding residual gas site distributions remain essentially unperturbed from the inherent level of UHV instabilities (Figure 5.10), i.e. in contrast to the dramatic site instability induced by, for example, an O_2 environment on the natural emission sites shown in Figure 4.6.

In the previous chapter, it was demonstrated how emission sites on "natural" HV electrodes are sensitive to operation under an increased pressure environment (~10^{-5}mbar) of, for example, He in the gap voltage range 5-11kV; in this case, the emission current is found to decay to an equilibrium level over a period of ~20 mins. For the present investigation into the influence of the residual gas environment on the operational characteristics of the C-composite cathodes, a series of He-conditioning tests, similar to those described in section 4.3.1, were undertaken under constant field conditions (<10MVm^{-1}), and at operating gap voltages of 7, 9 and 11kV respectively. These tests generally revealed that no conditioning effect, i.e. a suppresion of the emission current, is observed with the C-composite cathodes for emission currents in the range 10^{-6}-10^{-3}A. Thus, it can be generally concluded from the data presented in this section that the C-composite cathodes are extremely resistant, or "robust", and are relatively unaffected during operation under poor vacuum conditions.

5.3.6 Pulsed-field operation

The study of pulsed-field electron emission from the present composite

cathodes can be considered to provide an invaluable insight into both the physical mechanisms responsible for the emission phenomenon and the potential operational characteristics of such cathodes in, for example, high-frequency vacuum devices. As to the former consideration, it is presently believed that electron emission from metal-insulator (MI) microstructures is critically sensitive to the electron interface conditions and charge transport mechanisms existing within an emitting microchannel [9]. Thus, it could be anticipated that these mechanisms will be sensitive to fast modulations ($\leq\mu$s) in the applied field. From a technological viewpoint, it is also important to determine whether the composite cathodes described in this chapter are capable of operating at high frequencies, i.e. as is required in, for example, vacuum FET device applications [18,103]. Finally, a further incentive for these studies follows from previous investigations into the performance of tungsten [189] and carbon [24] micropoint emitters, where it was found that a significant decrease in the emission noise can be obtained by decreasing the pulse-duration of the periodic applied waveform, i.e. reducing the duty cycle.

For the present investigation, the high-voltage pulse generator and current detection circuits, described in section 3.5, have been used to undertake a preliminary study on the pulsed-field electron emission from the composite-coated cathodes. The general form of the high-voltage pulse and resulting emission current response of a typical C-composite cathode is illustrated in Figure 5.18(a), which shows a typical "low resolution" (200μs/div) result obtained with the present pulse testing facility at a pulse repetition frequency of 100Hz. Whilst this result indicates that the emission current from a composite cathode can be modulated to "reproduce" the driving waveform under these conditions, it is necessary to refer to the high resolution (20μs/div) traces of Figures 5.18 (b) and (c) to determine the real-time transient current response of these emitters. To aid the interpretation of these results, Figure 5.19 presents a schematic of a typical single-pulse, voltage and current response, and defines the characteristic parameters used to describe Figures 5.18 (b) and (c), i.e. in terms of

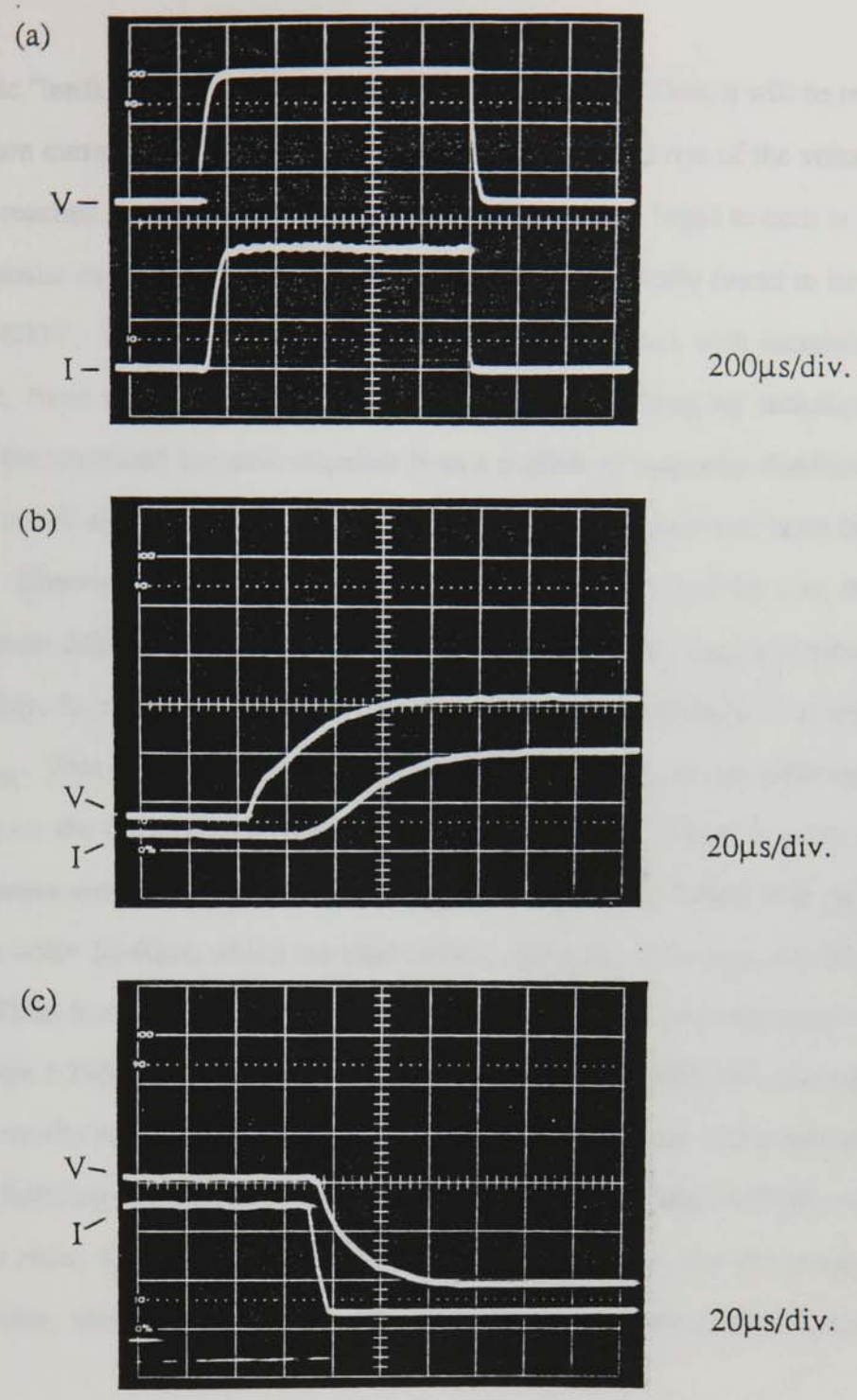

Figure 5.18 (a) Typical low-resolution, and (b) and (c) high-resolution single-pulse, voltage and current responses for the pulsed-field operation of a C-composite cathode.

the characteristic "leading"- and "trailing"-edge time constants (τ). Thus, it will be seen how the emission current remains at a zero value during the initial rise of the voltage until a point is reached (V_{TH}) when the first emission site, or sites, begin to emit at I_o ; for the C-composite cathodes, this threshold voltage,V_{TH}, is typically found to lie in the range 500-800V. Beyond V_{TH}, the emission current increases with increasing voltage, which, from an application of the transparent-anode imaging technique, corresponds to the integrated transient response from a number of randomly distributed emission sites which are progressively "activated" as the applied field increases (see section 5.3.3). However, referring to Figures 5.18(b) and 5.19, it will be seen that there is an inherent delay in the emission current response, such that I_{max} is obtained after a time delay, Δt, measured from the point where the pulsed-voltage reaches a maximum V_{max}. This is an important finding since the delay, Δt, would ultimately impose a limit on the frequency of operation of these cathodes. From a series of pulsed-field measurements on the C-composite cathodes, it was found that Δt is typically of the order 20-40μs, whilst the total current rise time, τ_2, is typically 90μs for τ_1= 80μs. Thus, from a technological viewpoint, the pulsed-field current response depicted in Figure 5.18(b) implies that a systematic reduction in the HV pulse duration (T_1) would eventually result in a distortion of the current transient due to the inherent delay time Δt. Refering to Figures 5.18(b) and 5.19, it will be seen that for $T_1 \leq \tau_1 + \Delta t$, the current rise time, τ_2, would be prematurely "clipped", which, for the present pulsed-field facility, ultimately imposes a square wave frequency limit of $\leq 1/2(\tau_1+\Delta t)$, i.e. $\leq$5kHz.

In contrast to the relatively slow emission current response to the "leading edge" of the HV pulses, it will be seen from Figure 5.18(c) that the emission current falls rapidly to zero over a time constant, τ_4, of ~10μs. As in the case of the leading edge response, the time interval over which this switch-off occurs appears to be determined by the time taken for the voltage to drop below the same threshold value, V_{TH}, defined above; i.e for voltages below V_{TH}, the emission sites cease to emit.

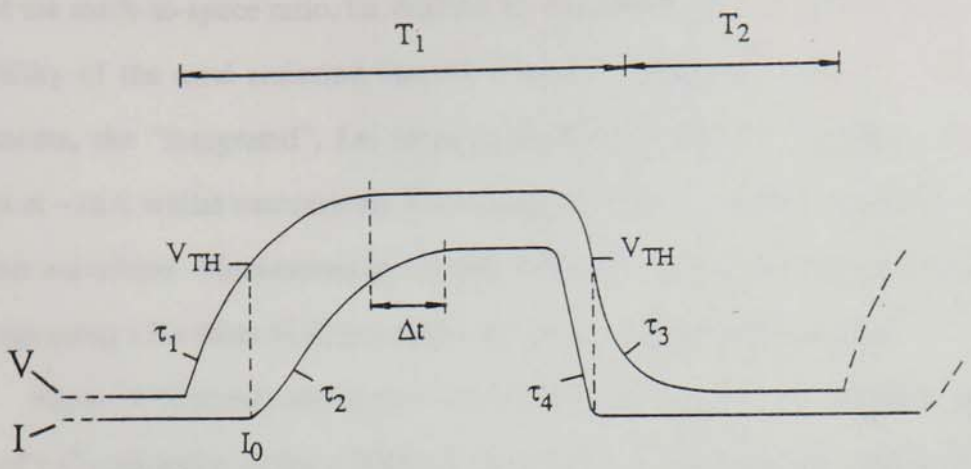

Figure 5.19 A schematic of a typical single-pulse, voltage and current response for a C-composite cathode. τ - rise and fall time-constants.

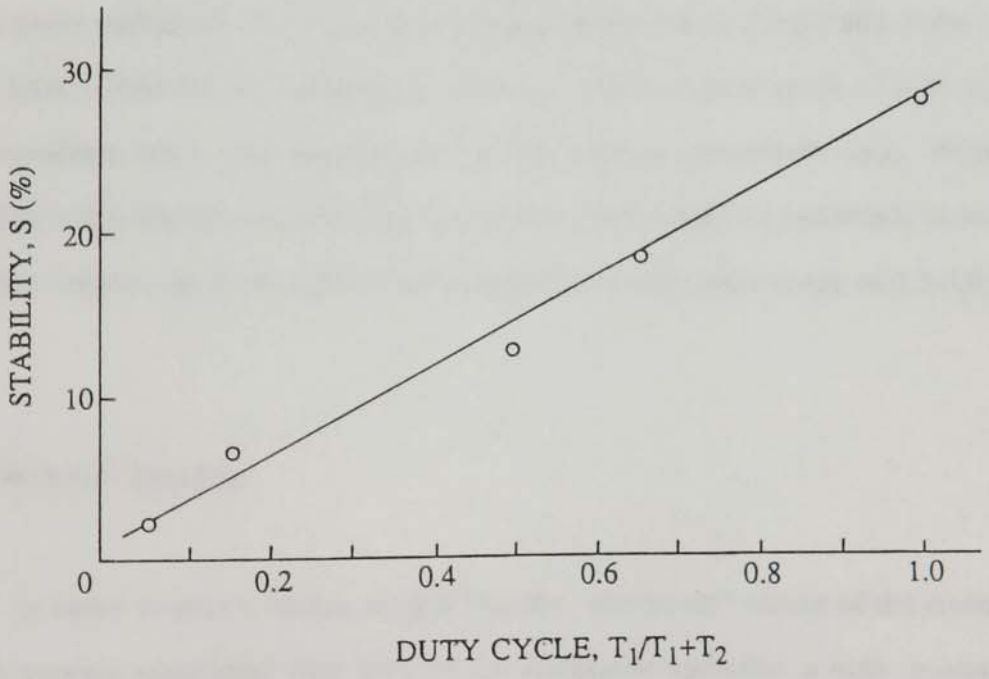

Figure 5.20 Variation in the total current stability, S, with pulse duty-cycle for the pulsed-field operation of a C-composite cathode. Pulse repetition rate = 100Hz.

A second series of measurements have also been undertaken to determine the effect of the mark-to-space ratio, i.e. defined as the ratio of T_1 to T_2 in Figure 5.19, on the stability of the total emission current from a C-composite cathode. For these experiments, the "integrated", i.e. total, current from the test cathodes was kept constant at ~1μA whilst successively decreasing the mark-to-space ratio of the 100Hz HV-pulse waveform. Fluctuations in the total emission current were then monitored at each stage using a Keithley 414S picoammeter and associated chart recorder.

Figure 5.20 shows the typical variation in the stability, S (defined in section 5.3.4), of a C-composite cathode obtained for a series of mark-to-space ratios from dc to 1:15. In this plot, the abscissa represents the "duty cycle" of the pulsed waveform, i.e. the ratio of the pulse "on" time to the total pulse period, which, referring to Figure 5.19, is given by T_1/T_1+T_2. Thus, it is found that the stability, S, is significantly improved, i.e. decreased in magnitude, by decreasing the pulse duration (T_1) for a constant pulse period (T_1+T_2). For the C-composite emitters, S typically decreases linearly from ~30% for dc operation to ~2% at a reduced duty cycle of 0.06 for a 100Hz waveform and a total emission current (i.e. average current) of ~1μA. Finally, it should be noted that the constant-total-current condition requires a systematic increase in the peak currents per pulse from 0.02-0.16μA over a duty cycle range of 0.5-0.06 at 100Hz.

5.3.7 Electron Spectra

In order to gain a further insight into the "electronic" nature of the electron emission process associated with sites on the composite cathodes, a high resolution electron spectrometer, described in section 3.4, has been used to analyse the energy distribution of the emitted electrons for a range of gap fields. The UHV spectrometer system, which was calibrated against a tungsten "metallic" field emission spectrum [70,71], enables the resulting electron energy distributions to be displayed relative to the Fermi level of the metallic substrates used for the composite-coated cathodes.

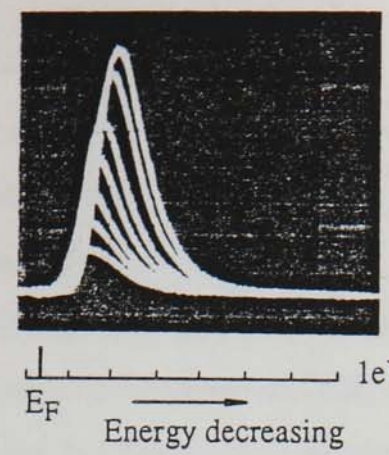

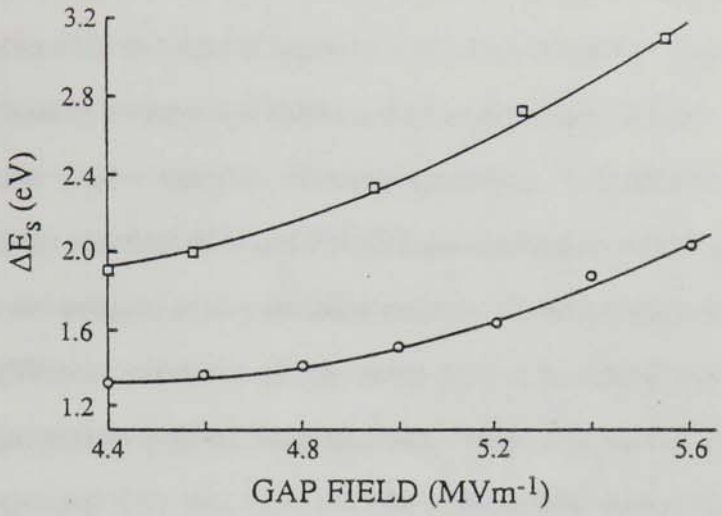

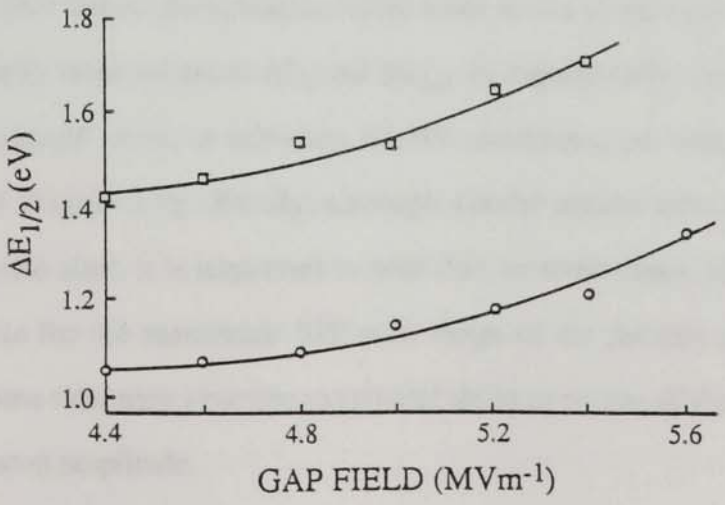

Figure 5.21 Typical spectral characteristics of a C-composite emission site. (a) A sequence of electron spectra obtained at incremental increases in the gap field. (b) and (c) The field-dependence of the spectral shift, ΔE_s, and half-width, $\Delta E_{1/2}$, respectively.

From an application of the electron optical imaging facility of the spectrometer, it is revealed that the images of individual composite emission sites are invariably composed of discrete sub-sites, such as typically observed with "natural" HV electrode sites, and shown in Figure 2.10. Thus, Figure 5.21(a) shows a typical example of the type of electron energy spectra obtained from a single C-composite sub-site at incremental increases in the gap field. From this result, it is clear that these spectra are indicative of a "non-metallic" electron emission process, in which the spectra display (a) a shift to lower energies (>1eV) with respect to the substrate Fermi level, (b) a significantly broader full-width at half maximum (FWHM), and (c) a more symmetrical profile than a metallic emission spectrum. It is also shown in Figure 5.21(a) how both the spectral shift and FWHM are dependent on the gap field, i.e. in sharp contrast to the behaviour of a metallic emitter. From an analysis of the spectra obtained from different sub-sites of the same site, it is found that these exhibit independent single-peaked spectral characteristics. Thus, Figures 5.21(b) and (c) show respectively the spectral shift (ΔE_s) and FWHM ($\Delta E_{1/2}$) field dependence of two sub-sites of a typical C-composite site. These plots indicate that electrons are typically emitted from ~1-3eV below the substrate Fermi level with a broad energy distribution of typically ~1-2eV: these values of ΔE_s and $\Delta E_{1/2}$ are significantly greater than those obtained from "natural" sites, or sub-sites, on HV electrodes, i.e. where $\Delta E_s \leq 1.5$eV and $\Delta E_{1/2} \leq 0.5$eV (Figure 2.9). Finally, although similar results have been obtained from SiC-composite sites, it is important to note that, in some cases, electron spectra were unobtainable for the maximum 10V scan range of the present system; i.e. an indication that some sites may give rise to spectral shifts in excess of the 10eV limit of the instrumental scan amplitude.

5.3.8 Metallographic X-sections of the composite-cathode coatings

For the purpose of investigating the geometrical and structural composition of

the cathode coatings used in the present study, a combined metallographic cross-sectioning [190] and optical microscopy technique has been used to observe the typical microstructures that exist within the C-composite coatings described in section 5.2. To obtain a cross-sectioned cathode specimen by this technique, the cathode is initially sectioned perpendicular to its surface plane using a rotatory milling tool. Subsequently, the resulting section is transferred to a METASERVE automatic mounting press, where it is partially encased in a thermosetting Bakelite mould to ensure that the composite coating remains intact during the final sectioning and polishing stages. Following this procedure, the surface deformation zone, i.e. that resulting from the initial sectioning and moulding process, is then removed by a series of grinding operations to a grade-1200 finish, until finally, the cross-sectioned surface is polished for a period of ~2 to 3 days on a 1μm-finish vibratory polisher.

Having prepared a metallographic sample of a C-composite coating, the constituent microstructures are then viewed, and subsequently photographed at a magnification of x4000 using a POLYVAR-MET wide-field optical microscope. Thus, the optical micrographs of Figure 5.22 show cross-sections of four typical examples of the type of microstructures found within a used C-composite coating. These microstructures, which are typically representative of a particular regime that is the most prominent feature throughout the cathode coating, indicate that the coating is composed of graphite flakes, or particles, of various geometries which are suspended, or otherwise encapsulated at random orientations in a surface resin matrix approximately 7μm in thickness. From a detailed examination of these and similar micrographs, it can be further concluded that (a) the graphite particles appear to be isolated from the Cu-substrate by a resin layer of thickness 1μm or less, (b) a similar sub-micron resin layer extends to the upper surface of a particle, and (c) there appea s to have been a significant deformation to the Cu-substrate surface in the region immediately adjacent to the underside of a particle (micrographs (b) and (c)).

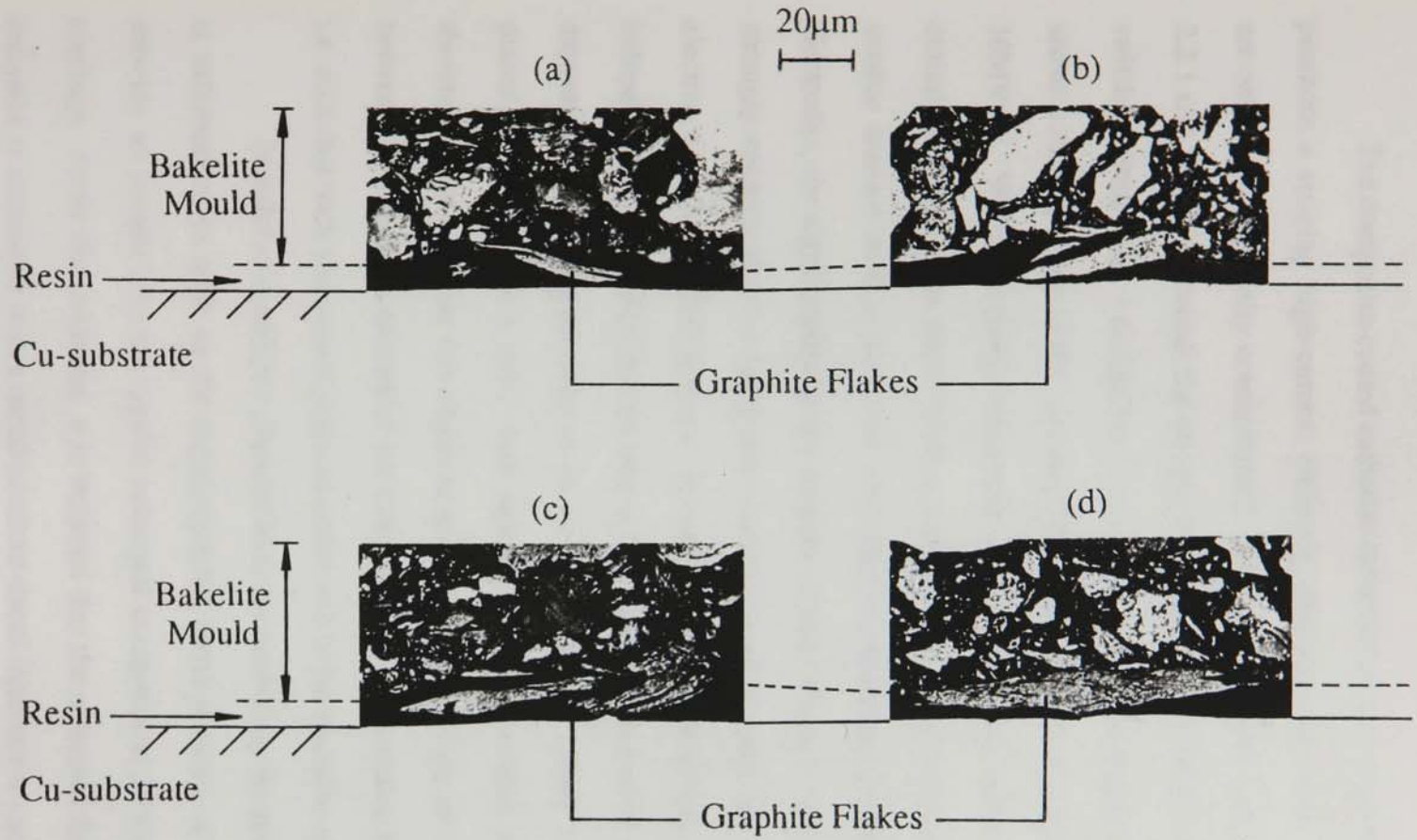

Figure 5.22 Metallographic cross-sections of four typical microstructures found within a used C-composite cathode coating.

5.4 Discussion

The composite-coated cathodes described in this chapter have been shown to promote a striking high-current emission characteristic when compared with the uncoated and artificially contaminated electrodes discussed respectively in sections 2.2.1 and 2.2.5. In general, the composite cathodes are notable for their extremely low switch-on fields (E_{sw} = 6-10MVm^{-1}) and a subsequent reversible I-V characteristic that shows a rapid increase in the total emission current to ~1mA at applied fields as low as 10MVm^{-1}. Whilst the transparent-anode imaging technique has revealed that the above emission phenomenon stems from a population of localised emission sites, i.e. in a similar manner to that observed with the uncoated and artificially contaminated electrodes, the significantly larger number of sites obtained at these low field levels strongly suggests that the composite coatings may be promoting a new field-induced electron emission (FIEE) process. In support of this contention, it has recently been independently established that the above characteristics cannot be obtained by (i) soley depositing conducting particles on an electrode surface [13,96], or (ii) soley coating a planar electrode with a spun resin layer [191], as described in section 5.2. It is therefore proposed that the observed emission arises from an intimate association between the substrate, embedded particles and the encapsulating dielectric resin layer, i.e. such that each component plays an active role in the emission mechanism.

In order to establish a physical basis for modelling the emission mechanism, it is informative to refer to the metallographic cross-sections of Figure 5.22 which provide an insight into the typical structural composition of the present composite coatings. From this evidence, it is believed that the observed field-induced electron emission is associated with a metal-insulator-metal-insulator-vacuum (MIMIV) regime involving a particular type of microstructure such as shown schematically in Figure 5.23. As described in section 5.3.8, it can be assumed that the geometrically irregular particles (Figure 5.23) will have maximum dimensions of up to ~400μm, and will be encapsulated in a resin layer of nominal thickness ~7μm. Furthermore, the thickness of

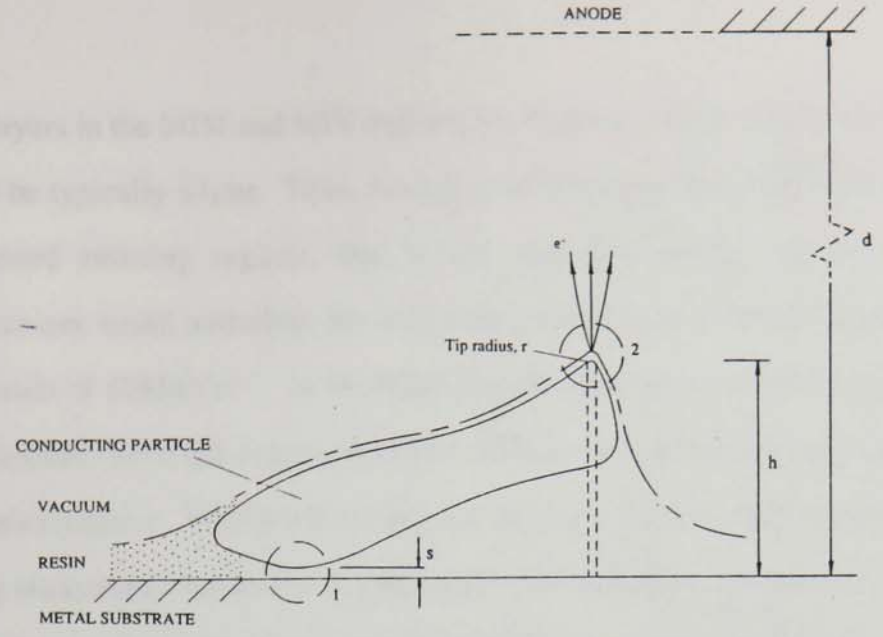

Figure 5.23 A schematic representation of field-induced electron emission via a two-stage switch-on mechanism associated with a MIMIV microstructure.

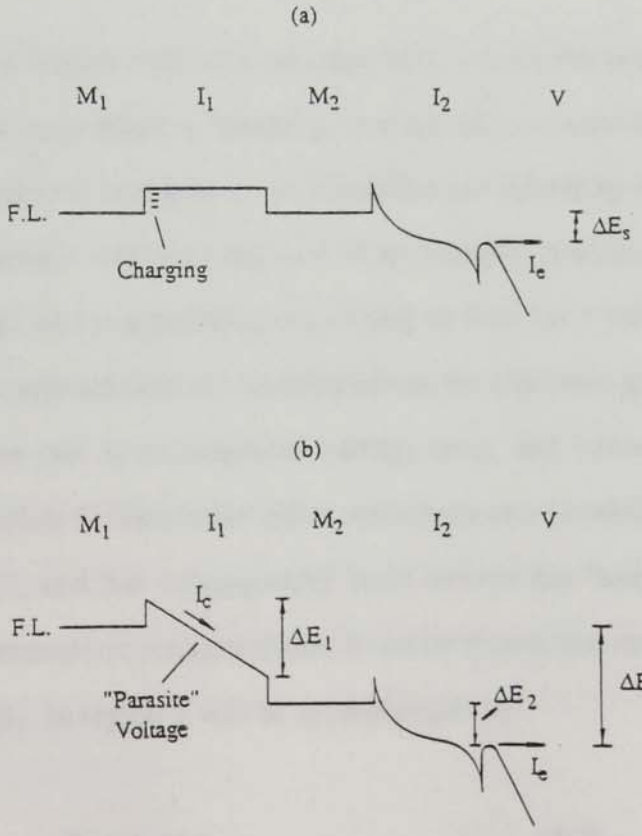

Figure 5.24 A band diagram representation of the two-stage emission mechanism from (a) a charged conducting particle and (b) an electrically "floating" particle. M-metal, I-insulator.

the resin layers in the MIM and MIV regions, i.e. regions 1 and 2 respectively in Figure 5.23, will be typically ≤1μm. Thus, having established the basic physical features of the proposed emitting regime, one is left with the question as to how these microstructures could stimulate the emission of electrons at the anomolously low applied fields of ≤10MVm^{-1}. In the following section, an account will be given of a newly proposed two-stage switch-on model of field-induced electron emission from a MIMIV microregime. Whilst this model, which is based on the well-known dielectric switching phenomena that occur in MIM and MIV structures, provides an insight into the possible emission mechanism operating with the composite-coated cathodes, it will also serve to illustrate the complexity of such an emission regime.

5.4.1 The two-stage switch-on "antenna" model

Referring to Figure 5.23, it is assumed that, during the initial application of the external field, the resin forms a "blocking" contact [86] between the metal substrate and the conducting particle in region 1. As discussed previously by Latham [192], it is assumed that the particle will play the role of an isolated conductor, such that it is electrically "floating" and at a potential depending on how far it probes the gap field. Consequently, as the applied field is increased across the electrode gap, the potential of the particle will give rise to an enhanced voltage drop, and hence field, across the dielectric layer in region 1. This latter effect was previously identified by Latham and co-workers [10,192], and has subsequently been termed the "antenna effect" [62]. From elementary electrostatic considerations, it can be shown that the magnitude of the field enhancement, β_1, in region 1 will be approximated by

$$\beta_1 = h / ks \qquad (5.2)$$

where h is the elevation of the particle above the substrate, s is the dielectric layer

thickness and k is a geometric factor such that typically $1 \leq k \leq 2$. At some critical value of applied field, it is assumed that a "primary" switch-on event [76-78] occurs in region 1, i.e. when a narrow channel within the dielectric layer switches from a non-conducting to a conducting state. At this stage, let us assume that this then leads to a current avalanche between the substrate and the conducting particle, i.e. a localised dielectric breakdown event [193], and, as a result, the potential of the particle falls rapidly (≤1ns) to the substrate potential. As a consequence, there will be a sudden enhancement in the surface field directly above the "charged" particle, particularly at any localised protruding sub-feature such as in region 2 of Figure 5.23. In fact, the magnitude of the surface field enhancement occuring at such a feature can be estimated by considering the idealised "conducting spike" (shown dotted in Figure 5.23), for which the enhancement factor, β_2, will be approximated by

$$\beta_2 = h / r + 2 \qquad (5.3)$$

which reduces to $\beta_2 = h / r$ for $r \ll h$ [3]. The suddenly enhanced field appearing across the surface dielectric film in region 2 then gives rise to a "secondary" MIV switch-on process, as described in section 2.2.4, and leads to the emission of electrons via a field-induced hot electron emission (FIHEE) mechanism [8,9] associated with a conducting channel, or channels, "electroformed" within the surface dielectric layer immediately above the conducting particle.

In order to ascertain whether the above emission mechanism could occur with the present composite regime, it is convenient to express the MIM and MIV switch-on fields in terms of the relevant geometrical enhancement factors (equations 5.2 and 5.3), and the macroscopic gap field, E_g, i.e.

$$E_{MIM} = hE_g / \varepsilon_r ks \qquad (5.4)$$

and

$$E_{MIV} = hE_g / \varepsilon_r r \qquad (5.5)$$

where ε_r is the relative permittivity of the dielectric medium. Referring to sections 5.2 and 5.3.8, it can be estimated that the MIM dielectric thickness (s) of the present composite microstructures will be of the order ≤1μm, whilst the particle elevations (h) above the substrate will be typically ≥100μm. Thus, assuming a macroscopic gap field (E_g) of typically 5-10MVm^{-1}, i.e. comparable to the typical composite-cathode switch-on fields, equation 5.4 would imply that E_{MIM}≥100MVm^{-1}, which is well within the field range typically required for dielectric breakdown processes to occur [193]. In further support of this contention, it is important to refer again to the cross-section optical micrograph results presented in section 5.3.8, which strongly suggest that "substrate melting" frequently occurs in the MIM region of a composite microstructure, i.e. such as might be due to the thermal dissipation associated with a localised dielectric breakdown process. Furthermore, if the assumptions of the two stage switch-on model are correct, it follows from equation 5.3 that surface field enhancement factors as low as, say, β_2 = 2-5 would be sufficient to promote a "secondary" MIV switch-on process within the dielectric layer above the conducting particle; i.e. so that equation 5.5 yields E_{MIV} = 10-30MVm^{-1} [9] for an applied field (E_g) of typically 5MVm^{-1}.

Whilst it is quite conceivable that the MIM and MIV switching events could occur with the particular composite microstructures described in sections 5.2 and 5.3.8, it can also be anticipated that the resulting emission mechanism, particularly the initial switch-on process, will be sensitive to the "size" of the conducting particles. Thus, referring to equation 5.4, it follows that the larger particles would be expected to "switch-on" at the lower applied fields owing to the inherently greater antenna effect associated with these structures. From a comparison of the particle size distributions of the composite cathodes (Figure 5.3) and the corresponding cathode switch-on fields (Table 5.2), it can be shown that there is indeed evidence to suggest the existence of a size effect. Thus, it will be seen that (i) the group II and III particles have comparable maximum particle sizes of ~400μm, and evidently, comparable switch-on fields (i.e. E_{sw}~6-9MVm^{-1}), and (ii) in contrast, the smaller (≤200μm) group I particles (e.g. the

S cathodes) require significantly higher switch-on fields of the order $12MVm^{-1}$. It is also important to note that the evidence for a "size effect" is further substantiated in Table 5.5, which indicates that the large-particle composites generally promote high switch-on probabilities, P_{sw}, i.e. the fraction of the total number of particles that give rise to emission sites.

Whilst it seems probable that the particle size may influence the switch-on of the emission process, it is not clear whether a similar relationship exists between the particle size and the general emissivity (e.g. β-factor, average site current, etc) of the composite cathodes listed in Tables 5.3 and 5.4. For example, a comparison of the C, Si and S size-distributions with the corresponding cathode β-factors and average site currents, listed in Tables 5.3 and 5.4 respectively, would suggest a positive correlation, i.e. the larger the particle, the higher the level of emission. However, this correlation does not extend to the complete range of emission data, where, in particular, it will be noted that the larger group III particles, i.e. MoS_2, Au, SiC and Fe, cannot equal the exceptionally high levels of emission obtained from the C-composite regime. In conclusion, therefore, it has been shown that whilst a size effect may influence the emission from particulate microstructures to some extent, i.e. as tentatively suggested in an independent study undertaken by Niedermann [62], it is apparent that a more comprehensive explanation of the experimental data will need to take into account a wider range of physical parameters.

5.4.2 Factors likely to influence the two-stage emission mechanism

In the previous section, it was considered how the presence of conducting particles within a surface dielectric coating could stimulate the emission of electrons at low applied fields. The new two-stage emission mechanism that emerged from the above discussion was shown to provide a basis for comparing the basic emission characteristics of the composite-coated cathodes with the structural composition of the composite surface microfeatures. However, whilst it seems plausible to assume that

electrons could be emitted from channels "formed" within the dielectric layer above an embedded particle, i.e. following a primary "switch-on" process across the dielectric layer between the particle and the substrate (see Figure 5.23), it appears that a more detailed analysis of the physical phenomena associated with such an emission mechanism is required in order to gain a better understanding of the experimental observations.

In the two-stage "antenna" model described in the previous section, it is assumed that the switch-on of the emission process occurs following the charging of an isolated conducting particle so that its potential becomes equal to the substrate potential. However, although evidence exists in support of a dielectric breakdown mechanism between some particles and the substrate, we have not yet considered whether the charging of the particle is a "transient" or "permanent" state of the emission process. In fact, an alternative mechanism may exist in which the potential of the particle is maintained at an equilibrium value, i.e. such that the the net flow of charge into the particle is equal to the rate of electrons emitted into vacuum. This latter mechanism would imply that a finite resistance region exists between the substrate and the particle (region 1 in Figure 5.23), which could support a steady state MIM conduction mechanism; a process that could result, for example, from the formation of either "electroformed" conducting filaments [77,78], or metallic filaments due to an electromigration process [194-197] following the initial MIM switch-on event.

To illustrate the difference between the two MIMIV mechanisms considered so far, Figure 5.24 shows the probable band configurations of (a) electron emission from a charged particle following an MIM brekdown event, and (b) emission from an electrically "floating" particle involving a steady state MIM conduction mechanism. In both cases, it is assumed that electrons are emitted into vacuum via the type of MIV hot electron emission process, discussed in section 2.2.4, that results from field penetration into the surface dielectric layer [9]. Whilst the band models of Figure 5.24(a) and (b) could account for the experimental observation of a shift (ΔE_s) in the energy spectra of

the emitted electrons to energies below the Fermi level (FL) of the substrate metal, it is important to note that the spectral measurements of section 5.3.7 indicate that anomolously large spectral shifts of $\Delta E_s \geq 3eV$ (perhaps even greater than 10eV in some cases) are typically obtained from emission sites on the composite-coated cathodes. These large shifts may in fact be due to the process shown in Figure 5.24(b) in which the the total shift, ΔE_s, is enhanced by the "parasite" voltage drop, ΔE_1, appearing across the MIM region, i.e. such that $\Delta E_s = \Delta E_1 + \Delta E_2$ where ΔE_2 may be of the order ~1eV [9].

In both the cases depicted in Figure 5.24, it can be anticipated that the emission from the composite microstructures will be particularly sensitive to the MIM conduction process, and hence the "charge state" of the conducting particle. In fact, it is likely that both the MIMIV emission processes described above could exist in a dynamic state, such that the potential of the particle fluctuates about a mean position as a result of a dynamic inbalance in the MIM conduction current (I_c) and the emission current (I_e). In order to estimate a likely frequency for this behaviour, the situation can be simplified by assuming that the emitted current per site (I_e) effectively "drains" the supply of electrons from a charged particle of radius, r, i.e. in a repetitive pulsed manner. By comparing the capacitance of an isolated sphere with the emitted current (I_e), it follows that the repetition rate, or "frequency", f, of this process can be approximated by

$$f = I_e / 4\pi r \varepsilon_0 \varepsilon_r V_p \qquad (5.6)$$

where ε_r is the relative permittivity of the resin and V_p is the potential of the particle. Thus, assuming that $I_e = 5\mu A$, $\varepsilon_r = 4$, $r = 100\mu m$ and $V_p = 5V$, equation 5.6 yields a frequency, f, of the order 10MHz. Although rapid fluctuations in the charge state of the particle may result from an MIMIV-type emission mechanism (c.f. the dynamic emission model [6,7] discussed in section 2.2.3), it is apparent that the slow "energy

spectra acquisition time" of the present spectrometer facility (i.e. approximately 0.2s per spectra) would not resolve the "fine structure" of this process. Rather, the "integrated" spectral characteristics obtained over this slow acquisition time may give rise to a broadening of the measured spectral half-widths ($\Delta E_{1/2}$ in Figure 5.21(c)), i.e. as a result of the rapid fluctuations in the particle potential, and hence spectral shift. In addition to these effects, it is also likely that the inherent capacitance, and transient charging phenomenon, will influence the pulsed-field emission characteristics of the composite-coated cathodes; in fact, the characteristic time delay ($\Delta t \sim 40\mu s$) of the I_e-response to pulsed-field conditions (see section 5.3.6) may well be related to the capacitance of the isolated conducting particles, and similarly, the capacitive/reactive characteristics of the dielectric/filamentary components of the emission regime.

From a comparison of the present spectral data with those obtained from a study into the thermal stimulation of FIEE from composite microstructures [198], it can be postulated that the broad energy distributions associated with sites on the composite-coated cathodes may arise from a local heating phenomenon resulting from the two-stage emission mechanism. In fact, as shown in the cross-section micrographs of Figure 5.22, there is convincing evidence to suggest that local temperatures may exceed ~1000°C in some regions of such a microstructure, i.e. sufficient to melt the underlying Cu-substrate. In order to assess the likelihood of an enhanced particle temperature during operation of the composite emitters, it can be shown that, neglecting heat losses, the temperature rise, ΔT, in an isolated sphere of radius, r, will be given by

$$\Delta T = 3Wt / 4\pi r^3 \rho c \qquad (5.7)$$

where W is the total power dissipation, t the time, ρ the density and c the specific heat capacity of the particle. Assuming that the total power is given by $W=I_eV_p$, i.e. typically a few tens of microwatts, it follows from equation 5.7 that the rate of rise in temperature (dT/dt) will be typically ~$1Ks^{-1}$ for a metallic particle of radius $r=100\mu m$. From this estimation, it therefore seems unlikely that the bulk temperature of an

emitting particle will be significantly raised above room temperature under steady state conditions, i.e. as determined by the inevitable heat loss mechanisms. However, it may be possible for local "hot spots" to exist on the upper surface of an emitting particle, e.g. due to the power dissipated from an emitting channel into an adjacent protruding surface sub-feature. In fact, from a direct comparison with the spectral data obtained by Xu and Latham [198] on temperature-stimulated emission from composite microstructures, it would be necessary to assume local temperatures in excess of ~800°C to explain the broad spectral half-widths ($\Delta E_{1/2} \geq 1eV$) observed with the present emission mechanism. Localised heating effects could be associated with, for example, ohmic loss in microscopic electromigrated filaments which may form at the MI interface (M_2I_2 in Figure 5.24) following an initial switch-on process where the current density could exceed $10^7 Am^{-2}$ [195]. In turn, it can be anticipated that local temperature fluctuations in the vicinity of an emission site will influence the thermally-stimulated emission mechanism, which may ultimately give rise to the site distribution and current instabilities described in sections 5.3.3 and 5.3.4 respectively. Furthermore, in some cases, the dominant heat loss mechanisms (e.g. conduction, radiation and possibly the Nottingham effect [3,25]) operating at an emission site may not be adequate to prevent a thermal overload, particularly for high individual site currents of ≥50μA. This overheating may then account for the occurrence of the occasional "explosive", or "flashing" site phenomenon described in section 5.3.3, and the de-stabilization of the composite cathode currents for large duty cycles under pulsed-field conditions (Figure 5.20). Moreover, one would also expect the degassing effects which may occur at individual emission sites to be sensitive to variations in the local temperature. However, although the origin of the gas evolution observed during operation of the composite-coated cathodes is not entirely clear, the linear voltage (as opposed to field) dependence of this phenomenon (see Figures 5.15 and 5.16) implies that the outgassing may, in fact, be due to electron-stimulated gas desorption from the anode surface [3].

5.4.3 The technological potential of the composite-coated cold-cathodes

It is well established that there is a growing need in the vacuum device industry for the development and utilisation of a variety of specialised field-emitting electron sources, which, as described in section 1.2, have several important technological advantages when compared with conventional thermionic cathodes. For example, the development of reliable, extended-area cold-cathodes could be expected to reduce the power consumption in modern microwave power tubes [199], whilst single micropoint and multi-emitter arrray cathodes have already been incorporated respectively into electron microscopes [200] and prototype vacuum microvalve devices [18]. Thus, having established the general emission characteristics of the composite-coated cathodes in section 5.3, there remains the question as to whether these emitters could form the basis for a new generation of cold-cathode electron sources for commercial vacuum devices. In this section, an account is given of the relative merits, and similarly, the limitations of the present composite cathodes in relation to their potential use as (i) extended-area, high-current sources, and (ii) single or multi-emitter array point sources.

5.4.3(i) Extended-area, high-current cathodes

In order to achieve the high-power outputs (≥1kW) required for present-day microwave applications [199], the electron gun assemblies of modern vacuum microwave tubes must be capable of producing electron beam currents of typically 0.1-1A. In practice, this is achieved using extended-area oxide-coated [150] thermionic cathodes, where beam current densities of typically $5Acm^{-2}$ are readily obtainable with a beam diameter of typically 0.4 cm. Thus, for a cold-cathode electron source to be compatible with these devices, it would be neccessary to develop a "uniform" extended-area ($\leq 1cm^2$) field emitter with a current density capability of up to $1Acm^{-2}$.

From a consideration of the electron emission data presented in sections 5.3.2 and 5.3.3, it will be seen that the present composite-coated cathodes have already achieved a relatively high-current capability (≥1mA) over an extended cathode area of ~2cm^2, and show every promise of achieving a significantly higher performance. However, although the present measurements on these first-generation prototype composite cathodes have, so far, only achieved total-area current densities of the order 10^{-3}Acm^{-2}, it is important to note that (i) the power limitation of the present testing facility limits the total emission current to only a few mA, and (ii) the maximum particle "loading" (i.e. particle density) of the composite coatings is inherently limited by the present coating technique. However, assuming that each emission site on, for example, a C-composite cathode is capable of delivering currents of ~20μA, one would require a total of ~5000 sites to obtain a total emission current of ~0.1A (c.f. the typical microwave tube current requirement). It follows that if each C-particle has a diameter of ~100μm, then the maximum particle loading for a cathode area of 1cm^2 will be ~10^4 particles. Therefore, by assuming that at least 5-10% of these particles will give rise to an emission site (as indicated in section 5.3.3), one could expect a total emission current of the order 0.1A.

From the above estimation, it appears that the composite-coated cathodes could, in principle, be capable of delivering currents of the order ≥0.1A, i.e. comparable to the electron gun capabilities of commercial power tubes. However, in order to fulfil this objective, it will be necessary to improve the composite-cathode fabrication technique to produce coatings with particle densities of ~10^4cm^{-2}. Although it seems unlikely that this could be achieved using the "spinning" technique described in section 5.2, it may be possible to fabricate high particle density emitters using the "layer" process, described in section 5.3.3(ii), in which the MIMI composite coating structure is constructed in successive stages.

On the other hand, an alternative approach to increasing the emission site density of the composite cathodes would be to increase the fundamental switch-on probability, P_{sw}, of the individual particles. Thus, if the implications of the "antenna" effect, described in section 5.4.1, are correct, then an increase in P_{sw} could be achieved

by increasing the particle size. However, since this would ultimately limit the number of particles per cathode, a better approach, particularly with the flake-like particles, e.g. C and MoS_2, might be to align the flakes in the direction of the applied field, i.e. increasing h in equations 5.4 and 5.5. This could possibly be achieved by an "electrostatic alignment" process in which the uncured cathode coating is subjected to an external electric field prior to curing the resin component.

5.4.3(ii) Single emitter and multi-emitter array cathodes

In addition to the high-current cold-cathode applications described above, there are a number of electron beam and vacuum tube devices, e.g. high resolution scanning electron microscopes [200] and X-ray tubes, which have exploited the technological advantages of a field emission electron source. As described in section 2.3.2, recent advances in solid state fabrication technology have also led to the development of a new class of multitip array cathodes which are currently being incorporated into a number of prototype miniature vacuum tube devices, e.g. vacuum FETs [18] and high resolution matrix-addressed displays [17]. In view of the technological interest in single and multi-emitter electron sources, it is therefore appropriate at this stage to consider the practical potential of the composite-coated cathodes described in this chapter.

Referring to Table 5.4, it will be seen that the typical emission sites on a composite cathode are quite capable of delivering average currents of the order $\geq 5\mu A$. In fact, in contrast to the current saturation typically observed with uncoated, or dielectric-coated tungsten micropoints, one could expect to draw total emission currents of $\geq 15\mu A$ from a single carbon site at applied fields as low as $\sim 10 MVm^{-1}$. Thus, in conjunction with a suitable extractor-anode aperture, these single emitters could, in principle, supply ample beam currents in the range 10^{-9}-10^{-6}A, i.e. as typically required for scanning electron microscope (SEM) applications. Furthermore, from a

consideration of the tests described in section 5.3.5(d) on the effects of the residual gas environment, it can be anticipated that, in addition to the high-current, low-field capability of the composite sites, the structural and emission stability of these emitters will be preserved during operation under the poor vacuum conditions ($\geq 10^{-6}$mbar) of a typical electron microscope or sealed-tube device ; i.e. in contrast to the more fragile performance of tungsten micropoint emitters which are found to be very susceptible to damage under these conditions. Although the single-emitter composite cathodes would be relatively simple to fabricate using either the "spinning" or "layer" techniques (see sections 5.2 and 5.3.3(ii) respectively), it is probable that many of the emitters ($\leq 30\%$) would be subject to intolerable switching instabilities, as shown for a population of C-composite sites in Figure 5.10. However, whilst the present study provides no firm conclusion as to the geometrical or structural factors which influence the site instability, the results of section 5.3.3 tentatively suggest that stable, high-current ($\geq 5\mu A$) sites could be reproducibly obtained from the larger particle structures ($\geq 300\mu m$), particularly in the case of the Si-composites which were notable for their low levels of site switching instability.

In considering the suitability of the composite cathodes for multi-emitter array applications, it is apparent, as demonstrated in Figure 5.13, that the inherent switching instabilities of some sites would be expected to limit the reliability of a practical device based on the present composite array structures. However, a certain degree of instability may be tolerable for array applications which rely on the integrated current from a large number of individual emitters, e.g. vacuum fluorescent displays. Whilst it may be possible to produce large-scale ($\geq$cm), high-voltage ($\geq$1kV) displays using an improved high particle density coating technique, the development of matrix-addressed structures, such as described by Holland et al [17], would, for practical vacuum device applications, require low voltage biasing. For this purpose, it may be possible to operate the present composite-coated cathodes at low-voltages by incorporating a thin-film, semi-transparent metallic overlayer onto the existing composite coatings. Thus,

provided that this anode-film is sufficiently thin (≤500Å), electrons could be transmitted through the anode into vacuum for voltages of, say, ≤100V (c.f. section 2.3.5).

Whilst the dimensions of the particles used in the present composite-cathode coatings (i.e. ≤400μm) ultimately limit the miniaturisation of any possible device structures, it is important to note that, for many device applications, only a few emitters would be neccessary to deliver a total emission current of ~100μA. In contrast, the vacuum field-effect transistors (FETs) developed by Gray et al [18] require a 4x10 array of Si field-emitters to obtain a significant voltage and power gain; in operation, these cathodes are found to saturate at a total current of only 1μA. Finally, despite the simplicity of obtaining high currents from the composite cathodes, it is important to note that the pulsed-field measurements presented in section 5.3.6 imply that the relatively slow switch-on time of these emitters (i.e. ≥90μs) would ultimately limit their use to devices requiring modulation at frequencies below a few kHz only.

CHAPTER 6

FIELD-INDUCED ELECTRON EMISSION THROUGH LANGMUIR-BLODGETT (LB) MULTILAYERS

6.1 Introduction

As discussed in earlier chapters, it is well established that the prebreakdown currents that flow between vacuum-insulated high-voltage (HV) electrodes stem from a field-induced electron emission (FIEE) process [3,54] that originates at microscopically localised regions on the cathode surface. This emission phenomenon, which typically occurs at gap fields of ~10-30MVm^{-1}, i.e approximately two orders of magnitude less than that predicted from "metallic" Fowler-Nordheim field emission theory [1], has been shown by Latham and co-workers [60,63] and Niedermann et al [61,62] to be associated with isolated anomolous surface microstructures which frequently contain both metallic and non-metallic elements. Recently, electron spectroscopy studies by Latham and co-workers [73-75] have further established that the emission from "natural" sites on HV electrodes occurs at energies of a few hundreds of meV below the the cathode Fermi level and gives rise to broad energy distributions (≥0.2eV). These observations, which are consistent with a non-metallic emission mechanism, subsequently led to the development of a field-induced hot electron emission (FIHEE) model [8,9] based on a metal-insulator (MI) microregime.

In a recent simulation study [13], the "non metallic" MI emission regime, assumed to operate at "natural" sites, has been reproduced under controlled laboratory conditions by coating electrolytically-etched tungsten microtips with a thin layer (≤0.5μm) of epoxylite resin. Whilst this study reproduced the characteristic "switch-on" phenomenon, and indicated that the emission stemmed from "electroformed" conducting filaments which penetrate the dielectric overlayer, i.e. as is assumed to occur at non-metallic microstructures on HV electrodes, it also established that the process of coating emitters significantly enhances the emission current for a given applied field.

It was therefore decided to investigate the influence of sub-micron dielectric coatings on the electron emission properties of planar extended-area cathodes. For this

study, a series of experiments have been conducted on a range of cathodes coated with Langmuir-Blodgett (LB) multilayers. The LB coating technique [201], which has recently recieved renewed attention as a result of the growing interest in molecular electronics, was chosen for this particular application for a number of reasons; these include ease of film deposition, reproducibility and, in particular, its ability to produce relatively defect-free dielectric films with thicknesses controllable on an Å scale. In the present study, this coating process has been used to fabricate planar MI structures which have not only been used to investigate the HV insulation properties of the coated cathode regime, but also to provide an insight into the switching, electrical conduction and electron emission phenomena in planar MI devices. It is further hoped that an understanding of the fundamental processes involved in field-induced electron emission through dielectric coatings will provide a basis for the fabrication, and hence application of planar MI cold-cathode electron source devices. In fact, the idealised concept of "writing" emission sites at pre-programmed cathode locations, such as might be achieved by locally modifying the electronic/chemical properties of the LB coating, could provide a basis for producing a wide range of cold-cathodes structures which, in turn, could be used in the "future technology" of, for example, radiation-hard microvalve devices which require a planar array of cold, fast-response emitters [15,16,18,103].

In this chapter, results are presented from an investigation into the emission properties of a range of LB-film coated cathodes based on 14mm-diameter metal substrate electrodes. In addition to obtaining the total current-voltage (I-V) characteristics of each cathode, the transparent-anode imaging technique, described in section 3.2.2, has been used to characterise and compare the spatial and temporal nature of the emission phenomenon observed for both uncoated and LB-coated cathodes. Finally, the emission process has been further investigated by comparing the electron energy distributions obtained from a number of emission sites on the LB-coated cathodes for a range of applied fields.

6.2 Langmuir-Blodgett (LB) cathode-coating technique

Organic molecules can be synthesised which have one functional group attracted to water (hydrophilic) and another repelled by it (hydrophobic). In order to satisfy both groups, such molecules adsorb at a water-air surface with the hydrophobic groups on top, i.e. out of the water. The resulting surface layer can then be compressed into a closely packed layer, one molecule in thickness, which may then be transfered onto a solid substrate by a dipping process. This technique produces a single-layer Langmuir-Blodgett (LB) film on the substrate, which is highly ordered, though non-crystalline. The total thickness of these LB coatings can be controlled by the size of the particular molecule and the number of layers deposited, e.g. in the formation of multilayer structures.

In this chapter, an investigation is presented on the field-induced electron emission from LB-coated extended-area metallic cathodes. The cathode samples were produced by depositing insulating multilayers of ω-tricosenoic acid, in the thickness range 90-750Å (monolayer thickness≈30Å [202]), onto 14mm diameter Cu-electrodes, which were pre-coated with ~1000Å of a chosen substrate metal. The ω-tricosenoic acid ($H_2C=CH(CH_2)_{20}CO_2H$) was prepared [203] and deposited at the GEC-Hirst Research Centre [204] using the dipping technique described by Peterson [205]. In this process, the acid was spread as a 10^{-3}M 1,1,1-trichloroethane solution onto a pure water subphase (Eglastat Spectrum) and compressed to a surface pressure of 35mNm^{-2}. Multilayer samples were then produced by lowering (0.1 mm s^{-1}) and raising (0.05 mm s^{-1}) the substrate electrode the required number of times, as shown schematically in Figure 6.1. This technique has been used in the present study to produce ten LB-film coated cathodes with Ag, Au, and W-substrates and varying film thiknesses in the range 90-750Å. The relevant substrate and coating parameters of these samples are given in Table 6.1, where the cathodes are listed in order of increasing film thickness.

Figure 6.1 A schematic of the Langmuir-Blodgett (LB) film deposition process in which the total film thickness is obtained by dipping the substrate the required number of times. (From [201]).

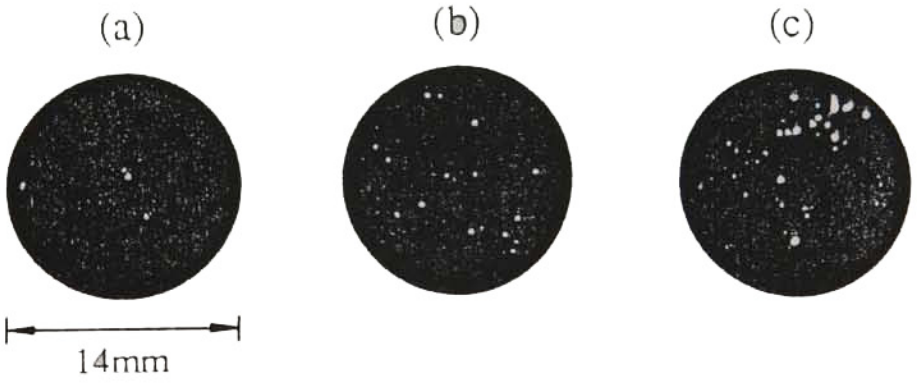

Figure 6.2 A comparison of the typical site distribution images obtained at a field of ~10MVm^{-1} for (a) an uncoated Cu-electrode, (b) an LB-coated cathode, and (c) a C-composite cathode.

6.3 Experimental Findings

The LB-film coated cathodes listed in Table 6.1 were stored in a vacuum desiccator for at least 24 hours prior to their insertion into the transparent-anode electrode module shown schematically in Figure 3.3. Emission measurements were then made at a preset electrode gap spacing of 0.3mm for d.c. fields in the range 0-30MVm^{-1}, using the circuit shown in Figure 3.3 (R_L=140MΩ). For the purpose of reducing the risk of cathode contamination due to anode debris, the emission tests on each cathode were performed using a new, ultrasonically-cleaned transparent-anode, and at a chamber pressure of ~10^{-8}mbar. In addition to these measurements, further characterisation of the emission process has been afforded by an investigation into the energy spectra of emitted electrons using the high resolution electron spectrometer described in section 3.4.

6.3.1 The switch-on process

When an electric field is first applied to a virgin LB-coated cathode, it is found that, as in the case of both the commercial HV electrodes and composite-coated cathodes described in sections 2.2.1 and 5.3.1 respectively, electron emission is only obtained following a characteristic switch-on process, in which emission sites are progressively "formed" on the test cathode. The typical switch-on characteristic of an LB-coated cathode is found to exhibit a similar behaviour to that shown for the composite-coated cathodes in Figures 5.4(a) and 5.5. However, in contrast to the composite-coated cathodes, this process is found to occur at the higher field values of typically 20MVm^{-1}, and furthermore, typically involves the formation of ≤30 emission sites per cathode for gap fields up to 30MVm^{-1}. To illustrate the contrasting patterns of emission site switch-on behaviour for the extended-area cathodes described in this and the previous two chapters, Figure 6.2 compares the site distribution images typically

obtained following the switch-on of (a) an uncoated Cu-electrode, (b) a LB-coated cathode, and (c) a C-composite cathode, for gap fields of ~10MVm^{-1}.

Table 6.1 summarises the switch-on fields, E_{sw}, obtained for the two uncoated Ag "control" cathodes, and the ten LB-coated cathodes shown in order of increasing coating thickness. From these measurements, it can be concluded that the LB-coated cathodes generally switch-on in the field range ~10-25MVm^{-1}, which is significantly, although not drammatically, lower than the fields generally required to obtain emission from the uncoated Ag control cathodes (E_{sw}~30MVm^{-1}) and the uncoated HV electrodes described in section 2.2.1. It is also significant to note that the LB-coated Au-cathodes were found to switch-on at the lowest fields of ~10MVm^{-1}; in fact, as will be described in the following sections, these cathodes were generally found

Cathode	Number of LB Layers	Coating Thickness (Å)	Switch-on Field E_{sw} (MVm^{-1})
Ag	uncoated	0	33.3
Ag	uncoated	0	26.6
"	3	90	23.3
"	7*	210	22.3
"	9	270	18.3
W	9	270	23.3
Au	9	270	13.3
Ag	15*	450	22.3
"	17	510	18.0
W	17	510	13.3
Au	17	510	10.0
Ag	25	750	21.6

Table 6.1. A comparison of the switch-on fields, E_{sw}, observed for virgin uncoated and LB-coated cathodes composed of various substrates and film thicknesses.

to give rise to substantially higher emission currents than the Ag and W-substrate

cathodes at the anomolously low gap fields of $\leq 10 MVm^{-1}$. Finally, although the collated data of Table 6.1 indicates that there is a considerable variation in the values of E_{sw} for these cathodes, it appears that there is no obvious correlation between E_{sw} and the corresponding LB coating thicknesses.

6.3.2 Reversible emission characteristics

Following the characteristic switch-on of emission sites on the virgin LB-coated cathodes, it is then found that, on cycling the gap field, the newly established population of emission sites give rise to a reversible emission characteristic. In this section, results will be presented from a comparative study, using the transparent-anode imaging technique, of the reversible current-voltage (I-V) characteristics and site distribution images obtained for the range of cathodes listed in Table 6.1.

6.3.2(i) I-V characteristics

In contrast to the uncoated control samples, the LB-coated cathodes were generally found to deliver substantial emission currents of $>1\mu A$ at gap fields of $\leq 15 MVm^{-1}$. To illustrate the typical I-V behaviour of these cathodes, Figure 6.3 compares the reversible characteristics obtained from three LB-coated Ag samples with coating thicknesses of (a) 510Å, (b) 270Å and (c) 90Å. As illustrated in Figure 6.3(c), it is found that the initial field cycling of an LB-cathode typically gives rise to a hysteresis behaviour that exhibits a decrease in emissivity with successive cycling of the gap field, until finally, a reversible I-V characteristic is typically obtained after three cycles, i.e. such as shown in curves (a) and (b). Thus, curve (a) shows how the emission current increases rapidly over five orders of magnitude with increasing gap field, to deliver currents of $\sim 100\mu A$ at moderate gap fields of $\sim 15 MVm^{-1}$. In fact, from a detailed analysis of the full range of I-V data, it is found that the emission currents

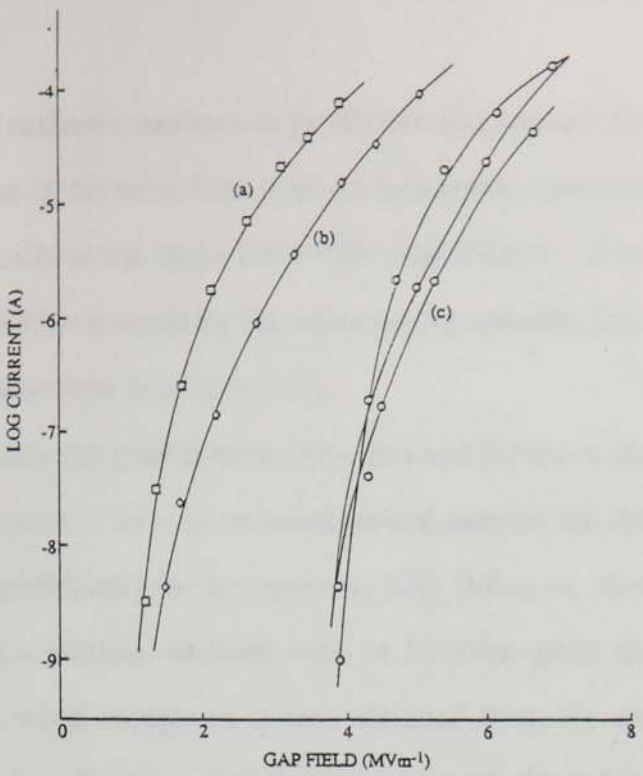

Figure 6.3 An example of the reversible I-V characteristics obtained following the switch-on of three LB-coated cathodes with film thicknesses of (a) 510Å, (b) 270Å and (c) 90Å. The typical initial I-V hysteresis behaviour of these cathodes is shown for sample (c).

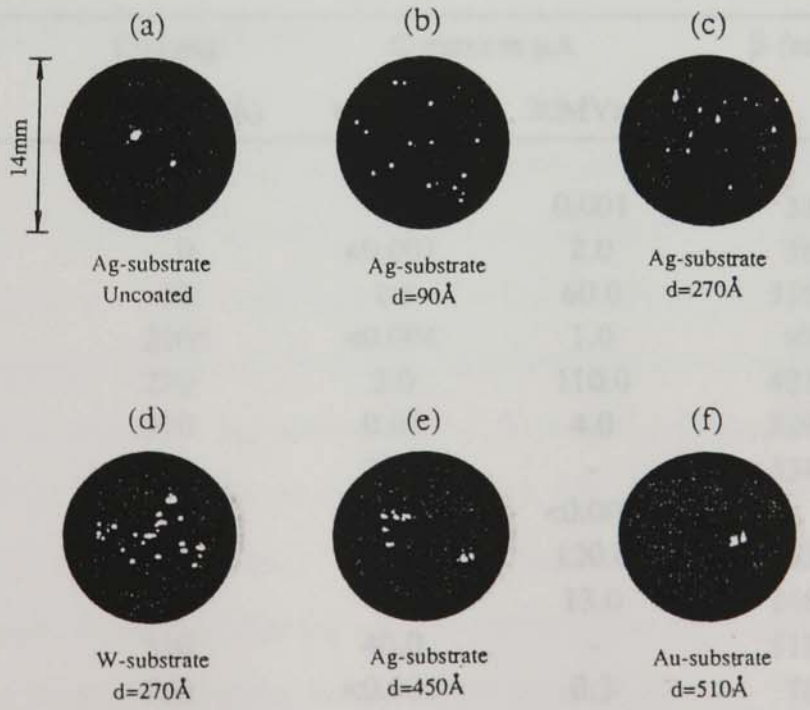

Figure 6.4 Typical populations of emission sites obtained from (a) an uncoated Ag-cathode, and (b) - (f) various LB-coated cathodes of film thickness, d. (Total current level ~10^{-4}A)

from all the LB-coated cathodes increase in an exponential manner, and give rise to a linear Fowler-Nordheim (F-N) behaviour with corresponding characteristic β-factors (see section 2.1.1) typically in the range 1000-5000; significantly, these compare with typical values of β~200-500 obtained for the uncoated Ag cathodes (see Table 6.2) and the HV Cu-electrodes described in section 2.2.1.

Table 6.2 collates the general emissivity data and β-factors obtained from the reversible I-V characteristics of the two uncoated control samples and the ten LB-coated cathodes. These data, particularly the anomolously high β-factors, strongly imply that the process of coating a metallic cathode with an LB-film gives rise to enhanced electron emission, i.e. when compared to that obtained from the uncoated control samples. Furthermore, it is clear that the LB-coated Au-cathodes exhibit an extremely high emission characteristic (β>5000) for gap fields of ≤10MVm^{-1}. However, as will be shown in the following section, the total emission current from the LB Au-cathodes is associated with only 1 or 2 emission sites, and "saturates" at a total current of ~50μA.

Cathode	Coating	Current in μA		β-factor
	Thickness (Å)	10MVm^{-1}	20MVm^{-1}	
Ag	0	0	0.001	384
Ag	0	<0.001	2.0	583
"	90	1.8	60.0	3150
"	210*	<0.001	1.0	991
"	270	3.0	110.0	4210
W	270	0.01	4.0	2892
Au	270	30.0	-	5344
Ag	450*	0.0	<0.001	-
"	510	14.0	120.0	4639
W	510	0.5	13.0	2483
Au	510	40.0	-	5132
Ag	750	<0.001	0.3	781

Table 6.2. A comparison of the reversible emission characteristics obtained from uncoated and LB-coated cathodes.

Lastly, it is apparent that there is a significant spread in the tabulated parameters of Table 6.2; however, no correlation appears to exist between these data and the LB-film thicknesses of the coated cathodes.

The transparent-anode imaging technique, described in section 3.2.2, has revealed that the increase in current from the LB-coated cathodes can be correlated with a progressive increase in the number of emission sites, i.e. in a similar manner to that shown in Figure 5.8 for the composite-coated cathodes. However, as will be shown in the following section, it is important to note that the emission currents from the LB-coated cathodes generally stem from a smaller population of sites, i.e. typically ≤30 as opposed to ≥100 sites for the composite emitters. Finally, it should be noted that, having established a stable population of emission sites on the LB-coated cathodes, it is found that, on repeating the field cycling over a period of days, the I-V characteristics and the corresponding emission site distributions remain unchanged provided that UHV conditions are maintained.

6.3.2(ii) Emission site distributions

In order to characterize the spatial and temporal behaviour of a population of emission sites on an LB-coated cathode, a VHS video recording of the corresponding site distribution was made over a testing period of ~10mins. Thus, Figure 6.4 shows examples of the typical emission site distribution images recorded at a total current level of 10^{-4}A for (a) an uncoated Ag-cathode and (b)-(f) typical LB-coated cathodes composed of various substrates and coating thicknesses. These indicate that the LB-cathode emission currents stem from a "stable" population of discrete emission sites which are randomly distributed over the cathode surface, and vary significantly in relative size and intensity. At this point, it should be noted that the "halo" effect observed at some sites is, in fact, due to secondary electron emission from the anode which occurs at gap voltages of typically ≥7kV (c.f. the spot on a CRO screen). From

a comparison of the distributions shown in Figure 6.4, it will be seen that the LB-cathodes invariably give rise to more emission sites (>10) than obtained from the uncoated Ag control cathodes or indeed a typical HV Cu-electrode, where it is typical to find only 1 or 2 sites at ~20MVm^{-1}. This latter observation serves as the most convincing evidence of the influence of such dielectric coatings on the emission characteristics of an extended-area "metallic" cathode. From a detailed analysis of these site distribution images, one can obtain values for the site density, n_s, and average site current, i_s, for each cathode. Accordingly, Table 6.3 collates the n_s and i_s data obtained at a total emission current of I_e~10^{-4}A for the range of LB-cathodes used in the present study. From this, it will be seen that the LB-coated samples typically give rise to ~10-30 emission sites per cathode (i.e. for a total surface area ≈ 1.5cm^2) at gap fields of <30MVm^{-1}, which, in turn, corresponds to average site currents of typically 2-10μA. Table 6.3 also reveals how the total emission current from the LB-coated Au-cathodes is associated with only 1 or 2 emission sites (see Figure 6.4(f)); here, the saturation of the total Au-cathode emission currents at ~50μA implies a maximum site current of ~25-50μA for these cathodes.

Cathode	Coating Thickness (Å)	Site density, n_s, at $I_e=10^{-4}$A (cm^{-2})	Average site current, i_s, at $I_e=10^{-4}$A (μA)
"	90	16	4.0
"	210*	8	8.3
"	270	12	5.3
W	270	23	2.8
Au	270	1	-
Ag	450*	15	4.3
"	510	20	3.3
W	510	16	4.0
Au	510	2	-
Ag	750	7	9.1

Table 6.3. Collated data from an analysis of stable populations of emission sites on the LB-coated cathodes.

However, it can be generally concluded from the site parameters of Table 6.3 that the stable emission characteristics of the LB-coated cathodes are independent of the coating thickness.

In all cases, the LB-cathode site distribution images were found to be extremely stable and were not subject to the random site switching instability such as shown for a typical C-composite cathode in Figure 5.10. However, individual sites were ocassionally observed to vary slightly in intensity under constant-field conditions. In fact, from an analysis of the current-time (I-t) traces obtained under constant-field conditions, it is generally found that the LB-coated cathodes give rise to current stabilities, S, and fluctuation frequencies, F_f, i.e. as defined in section 5.3.4, of typically $\leq 2\%$ and $60min^{-1}$ respectively for emission currents of $\geq 1\mu A$. This stability is an order of magnitude improvement on that of a typical composite-coated cathode, i.e. where S typically lies in the range ~10-50% (see Table 5.6).

6.3.3 Emission characteristics during and following exposure to various gas environments

From a technolgical viewpoint, it was considered important to determine whether the reversible characteristics of an LB test cathode were reproducible following the routine venting of the vacuum chamber to atmosphere or various residual gas environments. The need for such measurements follows from previous observations of the degrading effects of, for example, "wet" air on the electron emission from the SiC junction emitters described in section 2.3.8. In order to study the effects of various gas environments on the LB-coated samples, the cathodes were exposed to a single-species environment at atmospheric pressure for a duration of 1 hour. Following this procedure, the chamber was re-evacuated to $\sim 10^{-8}$mbar prior to repeating the emission measurements described in sections 6.3.1 and 6.3.2. The above procedure was successively repeated for each cathode with N_2, O_2, H_2, He and "wet" air

environments respectively.

On reapplying the gap field to these LB-coated cathodes, emission current of <1μA were immediately obtained for fields <10MVm^{-1}; i.e. in contrast to the virgin cathodes, no further switch-on process was required to obtain a stable population of emission sites. The resulting I-V characteristics obtained after each treatment were generally found to be comparable to the respective virgin characteristics given in section 6.3.2(i). In fact, the effect of the various gas treatments on the I-V characteristics of a particular cathode appeared to vary randomly, although typically within the hysteresis limits shown, for example, in curve (c) of Figure 6.3. Moreover, it was generally observed that a pre-exposure to wet air gave rise to the maximum emission currents at a particular gap field.

A comparison of the emission site distribution images obtained before and after a 1hour exposure to the above environments has indicated that the original site population is virtually unaffected and resistent to this treatment. However, from a video analysis of the constant-field distribution images, it is generally revealed that a pre-exposure to the above gases results in a slight de-stabilisation of the emission sites, and hence total emission currents. This slight decrease in stability can be correlated with occassional fluctuations in the intensity of some sites, which, in turn, results in a total current stability, S (defined in section 5.3.4), of typically ~5-10%, i.e. in contrast to S≤2% for the virgin LB-coated cathodes. Similarly, the de-stabilising trend has also been observed when re-introducing previously used LB-cathodes into the vacuum system; an observation which seems to imply that there is an "ageing" process in which the long-term performance of these cathodes is slightly degraded without the suppression of the constituent emission sites.

In addition to these tests, measurements have been made on the stability of a population of LB-sites during operation under poor vacuum conditions. Thus, Figure 6.5 compares the current-time traces for a typical Ag LB-coated cathode before and after the introduction of an atmospheric leak into the vacuum chamber , i.e. for

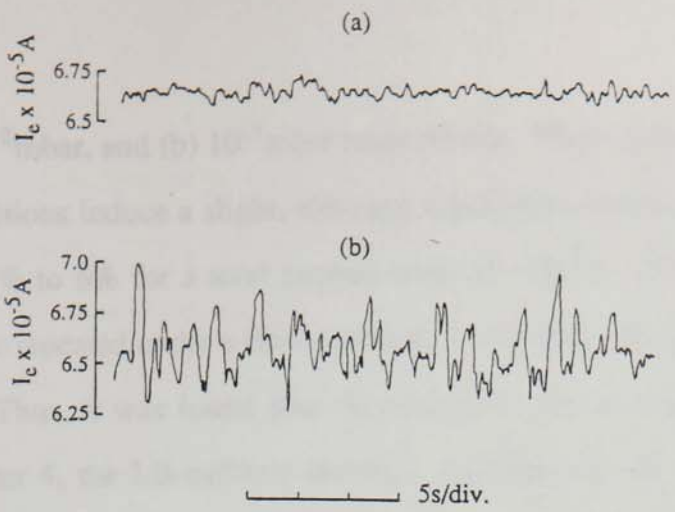

Figure 6.5 A comparison of the temporal stability of an Ag LB-coated cathode operating at residual gas pressures of (a) 10^{-8}mbar, and (b) 10^{-5}mbar. (Coating thickness = 330Å).

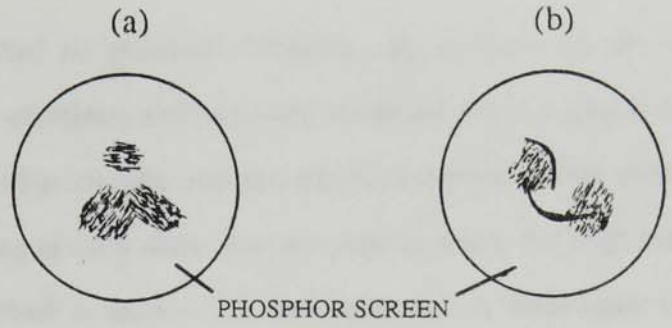

Figure 6.6 An illustration of the projected LB-site images typically obtained from the interfacing lens assembly of the electron spectrometer.

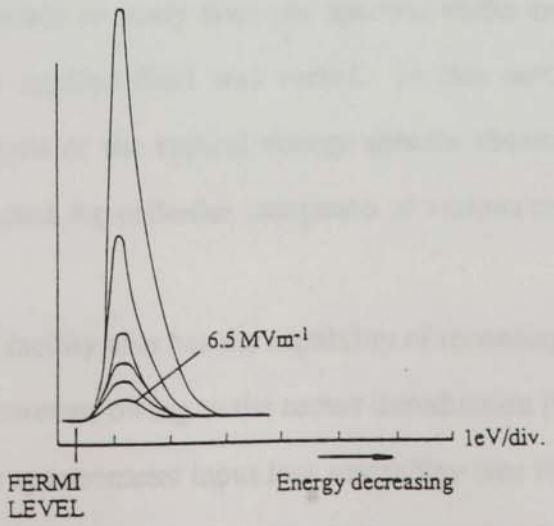

Figure 6.7 A series of energy spectra obtained at 0.3MVm^{-1} incremental increases in the gap field for a single sub-site on an LB-coated Ag cathode.

pressures of (a) 10^{-8}mbar, and (b) 10^{-5}mbar respectively. These traces show that the poor vacuum conditions induce a slight, although significant, decrease in the current stability from S=2% to 6% for a total current level of ~10^{-5}A. Finally, the above measurements were repeated under a He-environment, and for increasing gap voltages of up to ~10kV. Thus, it was found that, in contrast to the uncoated Cu-cathodes described in chapter 4, the LB-cathode emission currents and site populations are immune, or resistant, to the He-conditioning process, i.e. such that no reduction is observed in the total emission current under constant field conditions.

6.3.4 Electron energy spectra of emission sites on LB-coated cathodes

As indicated in previous chapters, an analysis of the electron energy distributions of the electrons emitted from localised sites on extended-area cathodes provides an invaluable insight into the physical nature of the associated emission mechanism operating at such sites. For the present study, the high resolution electron spectrometer described in section 3.4, has been used to investigate the field-induced electron emission process that occurs at microscopic sites "formed" on the LB-coated cathodes. This spectrometer facility, with a 25meV resolution, provides a means of directly recording a spectrum and referencing it with respect to the substrate Fermi level. Thus, it was possible to study both the spectral shifts and the spectral half-widths (FWHM) as the applied field was varied. In this section, results will be presented from an analysis of the typical energy spectra obtained for a number of emission sites on LB-coated Ag-cathodes composed of various coating thicknesses in the range 210-450Å.

This analytical facility also has the capability of recording emission images of individual sites [75]. However, owing to the recent introduction [95] of electron beam deflection plates into the spectrometer input lens assembley (see Figure 3.6), total-area, high-magnification images of the sites could not be recorded for the present study. Accordingly, an alternative approach was used in which the specimen, and hence the

site image, was manually scanned across the available "line of sight" region of the phosphor imaging screen. Using this method, it was possible to determine and re-construct the total spatial composition of the LB-cathode emission images. Thus, the schematic of Figure 6.6 shows two examples of the type of site images obtained from these cathodes. These images indicate that the sites are typically composed of a number of sub-sites, i.e. similar to those obtained for "natural" sites on HV-electrodes (see Figure 2.10). However, in addition to the generally diffuse appearance, and overlapping of the sub-sites, it is found that many images (≥50%) also contain "arc-like" components, with varying sizes and random orientations, i.e. as shown in Figure 6.6(b).

Having located a particular emission site for analysis, a given sub-site image was located over the analyser probe-hole, and emission spectra were obtained over a range of gap fields (typically 5-10MVm^{-1}) for a total energy scan width of 10eV. These measurements revealed that the individual LB sub-sites typically give rise to unique single-peaked spectra, although double-peaked distributions [71,83] were ocassionally observed at some sites (≤5%). To illustrate the type of spectral sequences obtained from LB emission sites, Figure 6.7 shows a series of energy distributions for a single sub-site on an LB-coated Ag-cathode with a coating thickness of 450Å. These spectra, which were recorded at incremental increases in the gap field from ~6.5 to 8MVm^{-1}, indicate that the underlying emission process is non-metallic in origin, where, for a particular gap field, the distributions exhibit (i) a peak shift (≥1eV) below the substrate Fermi level, (ii) a broad half-width (FWHM) of ≥0.5eV, and (iii) a considerable degree of symmetry. From a close examination of these spectra, it is revealed that, in common with "natural" sites on HV electrodes [74,75], the corresponding shifts and half-widths vary significantly as the gap field is increased. To highlight the field-dependence of the above parameters, Figure 6.8 shows the typical variations in the shift, ΔE_s, and the half-width, $\Delta E_{1/2}$, obtained from the series of spectra shown in Figure 6.7; this also shows the field-dependence of the spectral

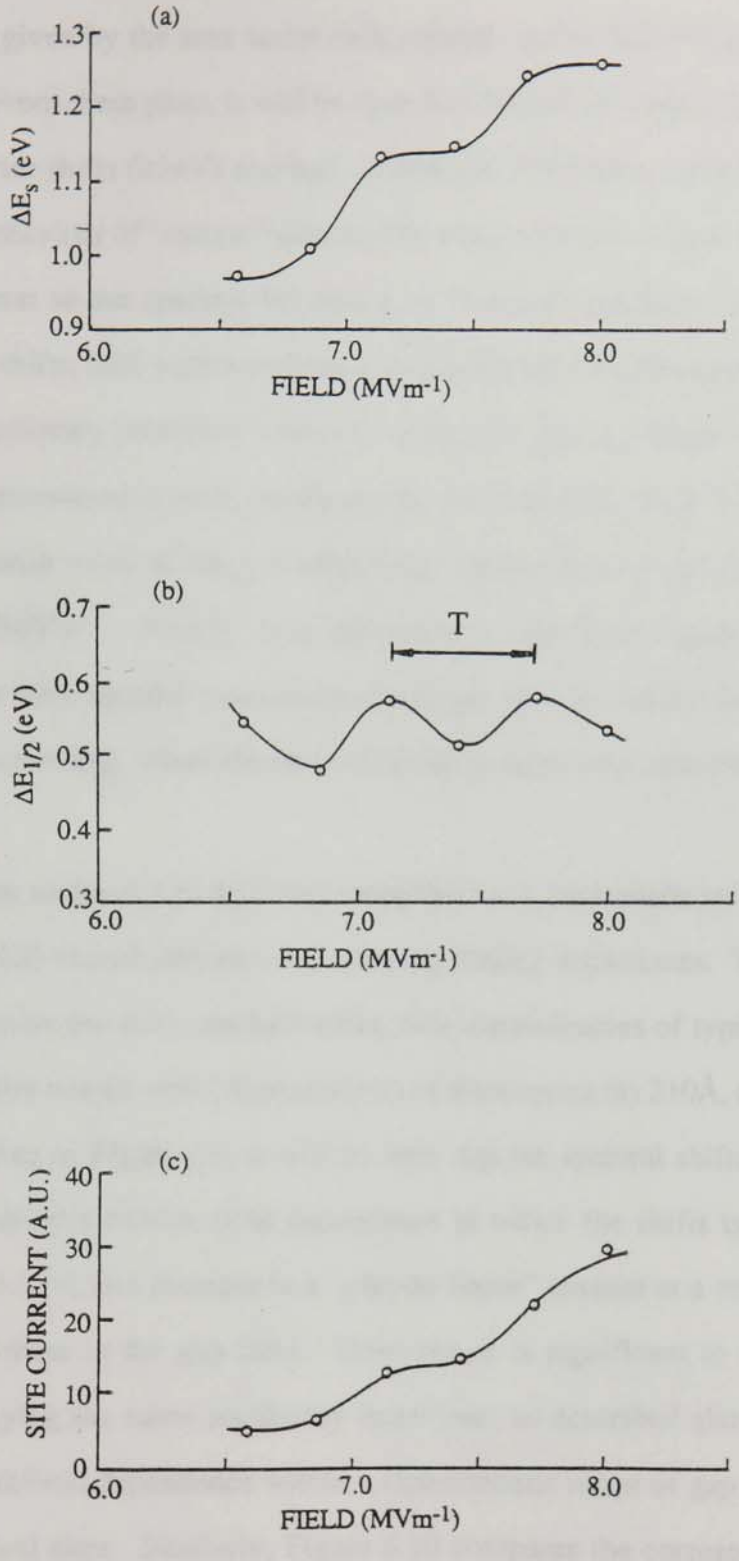

Figure 6.8 Typical variations in (a) the spectral shift (ΔE_s), (b) the spectral half-width ($\Delta E_{1/2}$), and (c) the site current, for a single LB sub-site.

current, which is given by the area under each spectra, and is directly proportional to the site current. From these plots, it will be seen that the LB sites typically give rise to significantly greater shifts (≥1eV) and half-widths (≥0.5eV) when compared with the typical spectral behaviour of "natural" sites on HV electrodes (see Figure 2.9).

In contrast to the spectral behaviour of "natural" emission sites, it is also apparent that the shifts, half-widths and site currents for the LB-sites appear to exhibit an anomolous oscillatory behaviour within an estimated data aquisition accuracy of ± 0.02eV. This phenomenon is most prominent for the half-width data, where it is also evident that the mean value of $\Delta E_{1/2}$ is effectively independent of the gap field in the field range ~6-8MVm^{-1}. Finally, it is important to note from Figure 6.8 that the oscillations of the three spectral parameters of a single sub-site exhibit the same phase and frequency relationship, where the interval between successive maxima, or minima, is T~0.6MVm^{-1}.

A similar series of spectral measurements have been made on a number of emission sites on LB-coated cathodes with varying coating thicknesses. Thus, Figures 6.9 and 6.10 compare the shift and half-width field dependencies of typical emission sites on Ag-cathodes coated with LB-multilayers of thicknesses (a) 210Å, (b) 450Å and (c) 330Å. Referring to Figure 6.9, it will be seen that the spectral shifts for sites on these cathodes exhibit a similar field dependence in which the shifts typically vary between 0.8 and 1.5eV, and increase in a "pseudo-linear" manner at a rate of ~0.1eV per 1MVm^{-1} increase in the gap field. However, it is significant to note that, in addition to displaying the same oscillatory behaviour, as described above, each site gives rise to a shift/field dependence within a characteristic range of gap fields which varies for individual sites. Similarly, Figure 6.10 compares the corresponding half-widths for the series of spectra considered in Figure 6.9. These plots, particularly cases (a) and (b), indicate that each site gives rise to a similar oscillatory behaviour, where the mean value of the half-width increases only slightly (typically ≤0.05eV) over the range of gap fields. However, as is found with the shift plots, it is important to

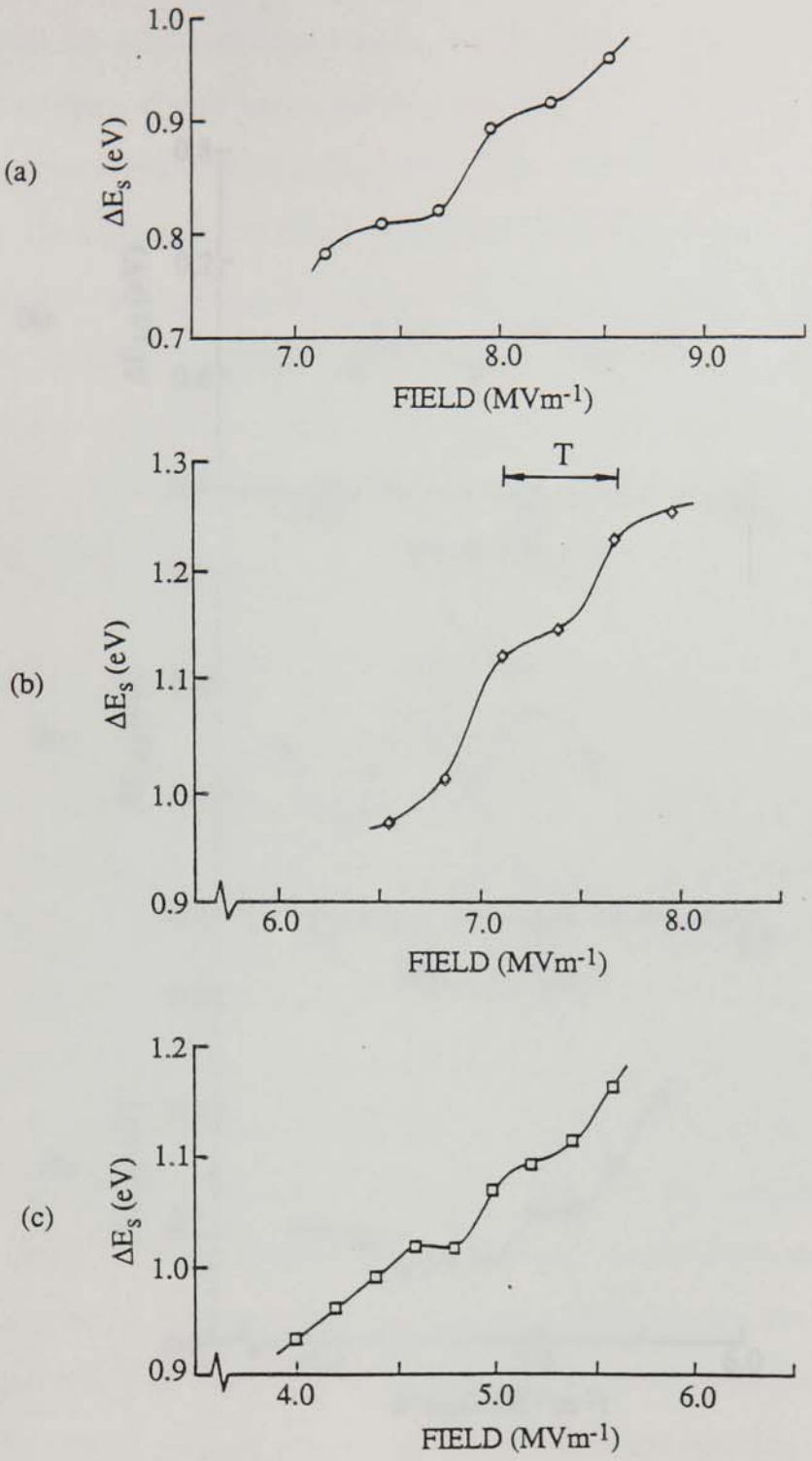

Figure 6.9 Examples of the field-dependence of the spectral shifts (ΔE_s) obtained from single sub-sites on three Ag LB-cathodes with coating thicknesses of (a) 210Å, (b) 450Å and (c) 330Å.

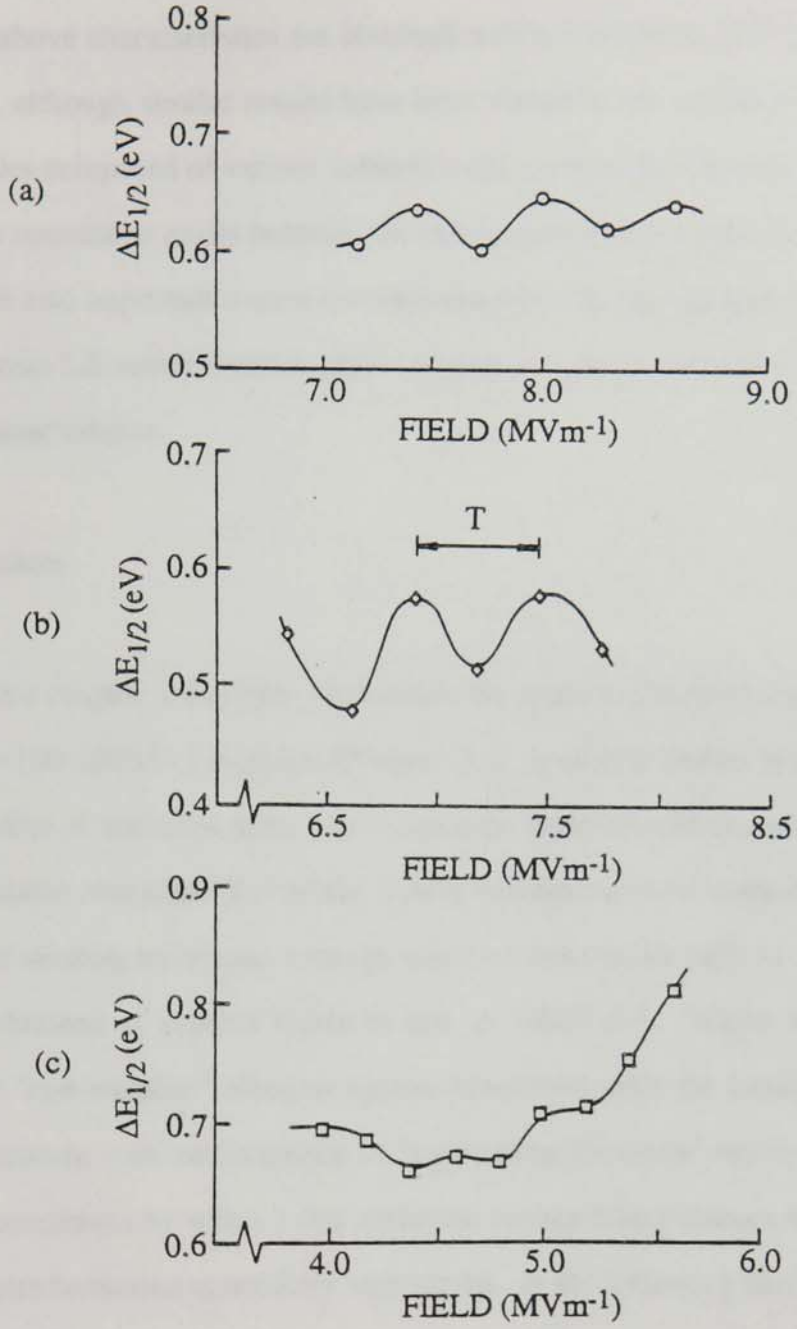

Figure 6.10 The corresponding spectral half-width ($\Delta E_{1/2}$) field-dependence for the LB sub-sites considered in Figure 6.9.

note that whilst the half-widths vary with a similar "period" ($T=0.6MVm^{-1}$), the spectral characteristic of each site is shifted with respect to other sites along the field axis, i.e. the above characteristics are obtained within a different field range for each site. Finally, although similar results have been obtained for a range of sites on LB-coated cathodes composed of various substrates and coating thicknesses, it is generally found that no correlation exists between the above spectral parameters and the coating thickness: it is also important to note that electron spectroscopy studies on a number of sites on the same LB-coated cathode yield substantial differences in the field, shift and half-width characteristics.

6.4 Discussion

In this chapter, it has been shown how the process of coating a planar cathode with a thin (~100-1000Å) Langmuir-Blodgett (LB) overlayer results in an increase in the total number of emission sites, and hence total emission current, when compared with the emission characteristics of the typical uncoated control-cathodes. By using this dielectric-coating technique, average emission currents as high as 10μA per site have been obtained at applied fields as low as $10MVm^{-1}$. Whilst the switch-on process, and "non-metallic" electron spectra associated with the localised emission sites, are consistent with the formation of "conducting filaments" within the dielectric coating, the conditions by which a thin dielectric surface film enhances the probability of emission site formation is not fully understood. In the following section, a number of mechanisms will be discussed that are likely to influence the emission of electrons through LB multilayers.

6.4.1 Possible Emission Mechanisms

(i) Idealised Filamentary Emission

As a first approach to explaining the emission properties of these cathodes, let us follow the models of Dearnaley et al [77] and Adler et al [78] on dielectric switching in metal-insulator-metal (MIM) structures, and assume that electrons are emitted from conducting channels, or filaments, that are "formed" within the LB film structure, and effectively form a conducting bridge across the planar dielectric coating from the metal substrate to vacuum. This planar MIV regime with an embedded filament is shown schematically in Figure 6.11(a). As discussed in section 2.2.4, it is further assumed that the formation of such conducting filaments is initiated at random locations on the cathode due to the presence of localised preferential MI interface conditions [8,9] which promote the injection of electrons from the metal substrate into the conduction band of the insulator. This process then leads to the steady-state emission mechanism illustrated in Figure 6.11(b), in which electrons tunnel from the metal substrate and are then transported along the conduction band, under the influence of the applied field, to be subsequently emitted over, or through, the surface potential barrier into vacuum [9]. Although this process has previously been assumed to involve the generation and emission of hot electrons, particularly at the IV interface [9], it is important at this stage to note that the LB films used in the present study are known to have a negative electron affinity [206], so that electrons arriving at the IV interface may effectively encounter no barrier.

By assuming that the emission regime depicted in Figure 6.11(b) maintains its dielectric properties (i.e. under low-current conditions), it can be anticipated that the measured spectral shift, ΔE_s, will be approximately equal to the "static" voltage drop in the LB overlayer, so that the internal field, F_i, is given by

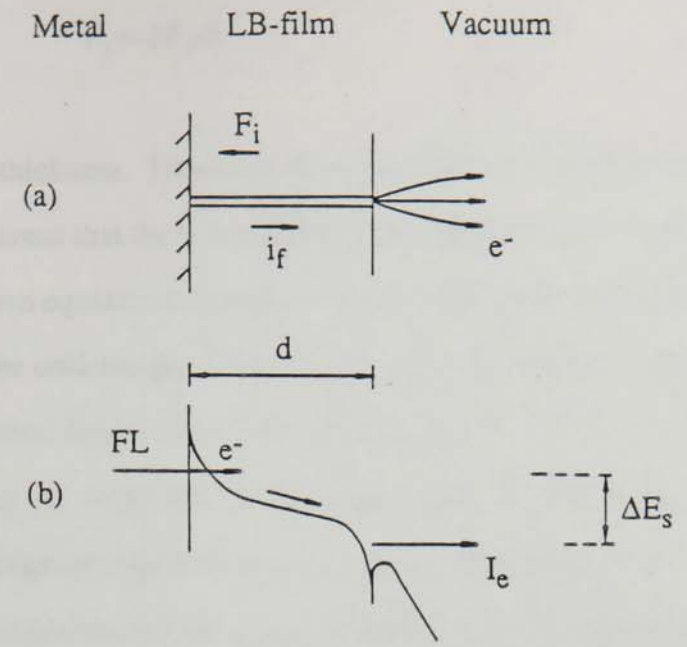

Figure 6.11 (a) Electron emission via an "electroformed" conducting filament in an ideal planar metal-LB film regime. (b) The band configuration of the steady-state filamentary emission process. FL- Fermi level, ΔE_s- spectral shift.

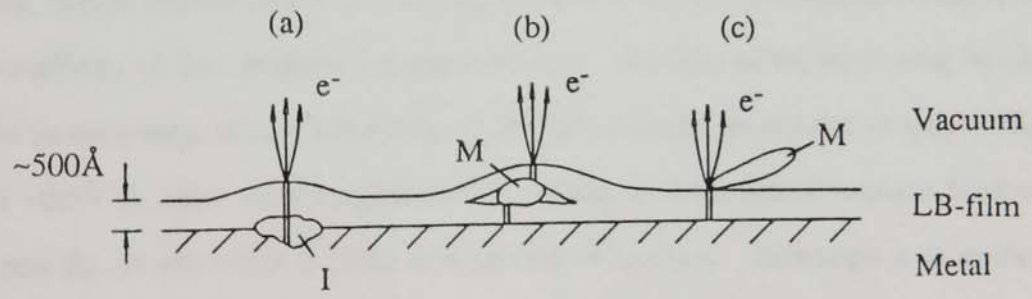

Figure 6.12 A schematic representation of three forms of LB-film contamination which could promote a filamentary emission process. M- metal, I- insulator.

$$F_i = \Delta E_s/d \qquad (6.1)$$

where d is the film thickness. However, from an analysis of the spectral shift data of Figure 6.9, it is apparent that there is a discrepency between the values of the internal field, as obtained from equation 6.1, and the "static" film field values, approximated by E_g/ε_r, where E_g is the uniform gap field. In fact, by assuming ε_r=2, the above analysis implies that the internal field is enhanced typically by a factor of ~10. To resolve this discrepancy, it may be necessary to consider some further factors which could influence the emission mechanism, e.g. the ohmic loss associated with electronic transport along a conducting filament, and a possible negative charge accumulation at the IV interface region. Taking account of these factors, the total spectral shift will then be given by an expression of the form

$$\Delta E_s = (k_i E_g/\varepsilon_r)\, d + i_f R_f \qquad (6.2)$$

where i_f and R_f are respectively the filament current and resistance, and k_i is the internal field reduction factor to account for negative charge accumulation at the IV interface. However, charge accumulation may be negligible with the present regime owing to the negative affinity of the LB-films, i.e. such that k_i=1. In terms of the remaining factors, it would be necessary, in case (c) of Figure 6.9, for example, to assume an $i_f R_f$ voltage drop of ~0.5V in order satisfy equation 6.2, which, in turn, would imply a filament resistance R_f, of the order 0.1MΩ at a current of i_f=5μA. Although it is unclear whether these filaments are metallic in nature, previous experiments with LB [195,196], and oxynitride [21] MIM sandwich structures of comparable film thicknesses, have indicated a similar conducting, even metallic [195,196], filament formation process. In particular, the study on the LB-MIM structures reavealed that both low-resistance (a few tens of mΩ) and high-resistance (~1MΩ) conduction could exist, where the latter process exhibited a $\log I \propto V^{1/2}$ behaviour, i.e. characteristic of

Poole-Frenkel conduction [92] or Schottky emission [120], and therefore non-metallic conduction through the organic LB-film. However, whilst the high filament resistances obtained with the LB-coated cathodes may imply that inelastic processes occur during transport along the conduction band of the LB-film, it is not possible at this stage to exclude the existence of metallic filaments. For example, with the present LB-cathodes, metallic filaments may form as a result of electromigration of the underlying metal substrate following initial local current densities of $\geq 10^7 Am^{-2}$ [195].

(ii) Contamination-induced Emission

With the knowledge that surface contaminant microstructures play a crucial role in stimulating field-induced electron emission from "natural" uncoated HV electrodes [3], it is therefore appropriate to consider the possibility of an emission mechanism that is initiated by the presence of substrate and/or film contamination. Thus, for the LB-coated cathodes described in this chapter, it can be anticipated that surface particulate contamination will be present both prior to and following the film deposition process. It follows therefore, in common with studies on "natural" electrodes that have been exposed to a laboratory environment, that both the substrate and film surfaces may be contaminated by a density of both metallic and non-metallic particles as high as 10^6-10^7 cm^{-2}, and with typical dimensions $\leq 1\mu m$. To aid the discussion, Figure 6.12 shows, schematically, three forms of particulate contamination that are likely to exist with the present LB-coated cathode regime. It is also shown how, in each case, these microstructures could promote a hot electron emission mechanism via the formation of conducting filaments within the dielectric regions. As described in section 2.2.5, it is currently believed that the presence of conducting particles on an ambiently oxidised cathode surface can, through the antenna effect, give rise to an enhanced field, and hence dielectric switching phenomenon, in the MIM oxide junction region. Similarly, it is quite conceivable that this same emission mechanism [13] could occur on a contaminated LB-coated cathode, i.e. as shown in

case (c) of Figure 6.12. With such a regime, it can be expected that the relatively thick (~100-500Å) LB-coatings on the present cathodes will provide a good "blocking contact" [86] between the substrate and any conducting surface contaminants. Moreover, if we assume a contaminant particle of dimensions ~1μm, an LB film thickness of ~0.05μm and $\varepsilon_r \approx 2$, then, as described in section 5.4.1, it can be estimated that the field enhancement (β_1) in the MIM dielectric region will be given by $\beta_1 \approx 1/(0.05 \times 2) \approx 10$, i.e. comparable to the field enhancement factors deduced from the spectral shift data of Figure 6.9 and equation 6.1. From a comparison of this process with the same phenomenon occuring on "natural" uncoated Cu-electrodes, it is important to note that the thin (~50Å) semiconducting surface oxide on the uncoated cathodes may, in some cases, be insufficient to provide an adequate blocking contact between the metal substrate and the conducting particle. As a result, the particles are rendered susceptible to charging under the influence of an applied field, which, in turn, eliminates the antenna field enhancement, and hence the probability of an emission site switch-on event occuring in the MIM junction region (see Figure 6.12(c)). This factor could therefore provide an explanation for the observation that a greater number of emission sites occur with the LB-coated cathodes (see Figure 6.4). It follows from the above reasoning, that the insulating properties of the LB-coatings may also promote an MIMI-type emission process from conducting particles that are encapsulated by the dielectric film, i.e. as shown in Figure 6.12(b). The details of this latter emission mechanism have been discussed in section 5.4. Finally, in further support of a contaminant-induced MIM emission process, it is significant that the individual site images described in section 6.3.4, frequently include "segmented features"; an observation that has previously been interpreted in terms of the coherent electron scattering [13] of hot electrons in the top metal layer of an MIM microstructure.

(iii) Surface Charging

In contrast to the geometric field-enhancing features of the contaminant microstructures shown in Figure 6.12, it is also possible that a contamination-free dielectric coating could provide an alternative basis for supporting a field enhancement through a surface charging effect. Thus, for a planar dielectric-coated regime, such as shown in Figure 6.11(a), the total electric displacement, D, is given by $\mathbf{D} = \varepsilon_0\mathbf{E} + \mathbf{P}$ where E is the electric field intensity arising from the free charge density σ_f on the conducting electrodes, i.e. the external field, and P is the dielectric polarisation associated with the bound surface dielectric charge σ_b, which opposes E. It follows therefore that the presence of an additional free charge density, for example, a localised positive charge σ_i on the upper surface of the dielectric, will result in a corresponding field enhancement across the film. Similarly, in the case of a contaminated film region, e.g. case (b) in Figure 6.12, it is possible that the charge density will be enhanced due to the effects of surface charge migration at an asperity [186]. Although no immediate evidence of a charging mechanism is given by the present measurements, previous models [74] of field-induced electron emission through a dielectric medium have included the effects of MI and IV interface field enhancement due to the migration of electron and hole carriers formed by impact ionisation within the bulk of the dielectric. However, since the initiation of impact ionisation processes requires injected electrons to gain an energy of ~1.5 times the bandgap (E_g), it is unlikely that this process will occur in the wide bandgap of the present organic LB-films (E_g~10eV).

In addition, there are other processes which may influence the charging of the dielectric overlayer, e.g. the ionisation of interband impurity levels. Thus, if we assume that the large spectral half-widths of typically ≥0.5eV (see Figure 6.10) indicate the average electron heating energy that can occur in the conduction band, then it is probable that ionisation of shallow interband impurities could occur, i.e. from a few tenths of eV below the conduction band: here, one possible source for such film

impurities may be from contaminant particles which are known to frequently contain foreign elements, e.g. S and C [62]. Furthermore, an initial charging mechanism may also be enhanced, for example, by exoemission [207,208] from shallow traps within the bulk of the insulator, i.e. implying that the switch-on mechanism need not necessarily be initiated by electron tunnelling at the metal-insulator interface (c.f. the hot electron emission model of section 2.2.4). However, since "formed" emission sites on LB-coated cathodes are typically "memorised", even after long periods (a few weeks) of exposure to ambient atmosphere, it is suggested that MI interface charging [74], or metallic filament formation, would be more likely to provide a permanent site memorising effect; i.e. as opposed to localised positive charging of the dielectric surface, which would be susceptible to discharge in atmosphere.

6.4.2 Electron Emission Spectra

To conclude this discussion, we will briefly consider some further implications of the spectral findings of section 6.3.4; in particular, the observation of an anomolous oscillatory-type behaviour in the spectral shifts (ΔE_S) and half-widths ($\Delta E_{1/2}$) with increasing applied field: indeed, it should also be noted that similar spectral data have been reported in independent studies on oxide-coated cathodes [86]. Since no precise quantitative explanation of these effects is available at present, it is the aim of this discussion to make some tentative suggestions as to the origin of these observations.

(i) Hot Electron Model

Referring to equation 2.21, which gives an expression for the spectral half-width $\Delta E_{1/2}$ as derived in the hot electron model, it will be seen that $\Delta E_{1/2}$ has the interesting property that it can either increase or decrease with increasing applied field, depending on the relative change in the hot electron temperature, T_e, at the insulator-

vacuum (IV) interface. As discussed by Bayliss and Latham [9], and Xu [96], the hot electron temperature will depend on a number of factors, in particular, the local field in the surface region of the insulator, and the energy loss mechanisms in this region due to electron-phonon processes [209]. Since the insulator field, and hence hot electron generation, will be particularly sensitive to any stored negative charge which may exist at the surface of an emitting channel, one could then speculate as to whether the oscillations in $\Delta E_{1/2}$ could be associated with fluctuations in the stored-charge distribution as the applied field is increased. Thus, in terms of the hot electron model, it will be seen in Figure 2.15 that the total energy (in eV) available for generating hot electrons will be

$$\Delta E = (d\beta_2/D\varepsilon)V_o + \chi - \phi_i - S - V^* \qquad (6.3)$$

where V^* represents the screening effect of the stored negative charge. Furthermore, assuming that the hot electron temperature, T_e, is a linear function of ΔE, i.e. following the approach of Bayliss and Latham [9], we have

$$k(T_e - T_o) = \alpha e \Delta E \qquad (6.4)$$

where α is a factor which represents the energy loss to lattice phonons. Although these two expressions demonstrate the dependence of the hot electron temperature, T_e, on the field conditions and the energy loss mechanisms in the surface region of an emitting channel, one can only speculate, at this stage, as to the details of these processes. Considering the lattice phonon effects, it is likely that the complex, large-molecule structure of the LB films will provide a wide spectrum of characteristic phonon-loss modes for conduction band electrons. Consequently, the oscillatory spectral behaviour, described in section 6.3.4, may be related to the particular absorption frequencies and harmonics of the multilayer film structure.

(ii) Bragg Diffraction Effects

As a final speculative contribution to the discussion, attention is drawn to the important experimental observation (see Figures 6.9 and 6.10) that the "period", T, for the oscillatory behaviour of the spectral shifts and half-widths is apparently a constant, and independent of the total film thickness. This tends to suggest that the observed behaviour is a function of some property of the films themselves, where one obvious factor is that all the cathodes will share a common feature, namely the spacing between the LB monolayers which form the multilayer LB-coating structure. One is therefore tempted to enquire whether Bragg diffraction effects at the LB-film planes could influence the spectral characteristics, and hence the emission process that is observed at these sites.

Considering a one-dimensional Bragg diffraction model [210] for electrons injected into an LB structure of layer spacing D, we would have, for the first and second order diffraction maxima, the conditions

$$\begin{aligned} n\lambda_1 &= 2D \\ \text{and} \quad (n+1)\lambda_2 &= 2D \end{aligned} \qquad (6.5)$$

where λ_1 and λ_2 are the de Broglie wavelengths associated with electrons of energy, E; i.e. $\lambda(\text{Å})=12.2 / E^{1/2}$ where E is in eV. From these conditions, it can be shown that the difference in wavelength, $\Delta\lambda=\lambda_1-\lambda_2$, will be equal to the lattice spacing D (in our case ~30Å) for n=1, which, in turn, implies an energy difference $\Delta E=0.2$eV between the first- and second-order maxima. Referring to Figure 6.10, it is interesting to note that the 0.1eV fluctuations in the measured $\Delta E_{1/2}$ values are comparable with the above estimation of ΔE. It is therefore possible that as the electrons approach the IV interface, and are progressively heated above their thermalised ground state in the bottom of the conduction band, they successively acquire sufficient energy to satisfy the above condition.

CHAPTER 7

CONCLUSIONS

In the last three chapters, detailed and independent accounts have been given on the influence of (i) the residual gas environment, (ii) metal-insulator composite coatings, and (iii) LB-dielectric coatings on the field-induced electron emission from extended-area planar cathodes. The experimental findings which emerged from these studies have been shown to collectively provide further evidence in support of a "non-metallic" hot-electron emission mechanism in which the dielectric coatings play the crucial role of supporting a localised "conducting" filament formation, and hence emission, process for applied field of typically 5-20MVm^{-1}. In this chapter, we will briefly summarise the principle experimental findings and the conclusions to be drawn from these investigations. This will also include a brief assessement of the technological implications arising from these studies, and similarly, suggestions for future work.

7.1 Gas conditioning

An optical imaging technique has been used to monitor the spatial and temporal evolution of populations of electron emission sites on planar Cu-electrodes in the presence of various residual gas environments (notably He, Ar, N_2, O_2 and H_2) at a total chamber pressure of ~10^{-5}mbar. This technique has confirmed that the well-known He-conditioning phenomenon, i.e. the "quenching" of the prebreakdown emission current under constant field conditions, can indeed be attributed to a gradual reduction in emission from all sites with time; i.e. as predicted by the traditional sputtering theory [28]. However, from a comprehensive study of this phenomenon, a number of other important, but previously unknown, effects were revealed, viz.

(i) that all gases can apparently promote a comparable conditioning effect, although only within their own characteristic gap voltage range (i.e.typically within a spread of 10kV),

(ii) for a particular gas species, the degree of conditioning is dependent on the gap voltage, and

(iii) that the conditioning effect is reversible, i.e. as evidenced by an increase in the total gap current of a previously conditioned cathode, under constant field conditions, following an extended period of cathode heating at temperatures of $\geq 100^{o}C$.

In addition to these findings, electron spectroscopy measurements have revealed that a period of conditioning results in a shift in the "non-metallic" emission spectra towards the Fermi level of the metal cathode. These hitherto unknown effects, which are not explicable by the traditional sputtering model of gas conditioning, have subsequently been interpreted in terms of an "electronic" conditioning model in which filled electron traps are created within an assumed metal-insulator (MI) emitting microregime, hence resulting in a "screening" effect at the critical MI interface region. Although this model is necessarily speculative, due to the lack of detailed knowledge of the electronic/physical properties of emission sites, it does, however, provide an explanation for the "voltage" and "temperature" effects outlined above. For future studies, it is anticipated that the development of a high-resolution UV photon / field emission imaging system, proposed by Latham [212] for the dynamic observation of the microtopography of an emitting microstructure, could provide an insight into the details of both the underlying emission, and hence the conditioning mechanisms. Moreover, from a theoretical viewpoint, it is apparent that the present analysis of the ion-induced interactions with an emitting microstructure would also benefit from a complementary analysis of the ion energy distributions, and the charge states etc, obtained under these conditions.

In the technological context, the present study has revealed the need for adopting a more sophisticated conditioning procedure in which the conditioning gas, or gases, are chosen to "match" the corresponding operating voltage of a particular

electrode assembly. Furthermore, as iterated in point (iii) above, the present findings also suggest that elevated cathode temperatures should be avoided at all times following the routine conditioning of a HV device. In fact, this limitation imposes a constraint on the use of the gas conditioning procedure in the case of HV systems which are routinely exposed to temperature fluctuations, e.g. space power systems.

In order to advance both our understanding of the conditioning mechanism and its wider potential technological applications, it is suggested that two important aspects should be further explored. Firstly, it would be beneficial to assess the relative conditioning efficiencies of a wider range of gases, particularly the heavier species, since this could well result in an extension of the present conditioning voltage limit beyond 25kV. Secondly, there is a need for a detailed investigation into the effect of annealing temperature and annealing time on the reversal of the conditioning effect. However, it should be noted that, although gas conditioning has been shown to reliably reduce the prebreakdown currents in HV electrode assemblies by typically one order of magnitude at a constant voltage, it is important to appreciate that this often compulsory measure should not undermine the current trend towards "clean room" processing of electrodes [26] to reduce the incidence of contaminant particles, and hence potential emission sites.

7.2 Metal-insulator Composite-coated Cathodes

The central finding of this study was to demonstrate that by coating a planar metal cathode with a two-phase resin-conducting particle composite film, it is possible to achieve an increase of greater than four orders of magnitue in the total emission current when compared with an uncoated cathode tested under identical field conditions. In this investigation, composite-coated cathodes composed of geometrically irregular Au, C, Fe, MoS_2, S, Si and SiC particles, typically 50-400μm in diameter, have been shown to exhibit an initial switch-on phenomenon in the field range 5-10MVm^{-1}, which subsequently gives rise to

(i) emission site densities of typically 10-30 sites per cm^2,

(ii) reversible current-voltage (I-V) characteristics and a linear F-N behaviour (β~500-3000), and

(iii) total emission currents of $\geq 100\mu A$ for applied fields of typically $\leq 20 MVm^{-1}$.

For most composites, this high-current emission phenomenon has also been associated with a "size effect" relationship, in which the larger particles are typically found to switch-on and emit at the lower values of applied field. However, there is one notable exception to this rule, in that the smaller particle C-composites are consistently the most prolific emitters, where total currents of $\geq 1mA$, and average site currents $\geq 15\mu A$, are readily obtained for fields as low as $10 MVm^{-1}$. In addition to the characteristic site switch-on process observed with the composite-coated cathodes, i.e. similar to the well-known metal-insulator switching phenomenon, further evidence of a "non-metallic" emission mechanism has been afforded by electron spectroscopy measurements, which reveal a characteristic field dependence of the spectral shift and half-width. From a cross-section optical microscopy study of the composite-coating microstructures, it has been suggested that the emission phenomenon is associated with a two-stage metal-insulator-metal-insulator-vacuum (MIMIV) mechanism involving dielectric switching in the MIM and MIV regions of a microstructure. However, although this model has been shown to provide a qualitative explanation of the observed "size effect", i.e. in terms of a the field-probing "antenna" properties of the electricallly-isolated conducting particles, it is apparent that any future models of this type of electron emission should consider in more detail the electronic, physical, or even thermal properties of the conducting particle species, particularly C.

The present study has also indicated that the C-composite emitters possess a number of operational qualities which warrant a further investigation into their potential use as cold-cathode electron sources. These features include (i) individual site currents

in excess of 15μA, (ii) an estimated equivalent current density of ≥0.1Acm^{-2} over extended areas, (iii) insensitivity to poor vacuum conditions (≤10^{-4}mbar), and (iv) low-cost and ease of fabrication. However, with the exception of the Si-cathodes, the composite emitters are found to exhibit an undesirable level of site switching instability which ultimately limits their use in, for example, multiemitter array applications. In this context, it is suggested that a future investigation should aim to improve the present fabrication stages with particular emphasis on the particle species, size, geometry, and resin processing methods (e.g. the curing temperature and cycle). Whilst such an investigation would be beneficial from a cold-cathode electron source viewpoint, it is also anticipated that a controlled cathode fabrication technique will provide the basis for testing the fundamental assumptions of the two-stage switch-on model described section 5.4.1. Finally, reference should be made to the implications of the present findings on the technology of high-voltage vacuum insulation. Thus, it has been demonstrated that it is imperative to avoid particulate contamination on HV electrode surfaces at all costs - particularly carbon deposits.

7.3 LB Dielectric-coated Cathodes

Somewhat remarkably, this study showed that, in common with the composite-coated cathodes, a similar emission-enhancing effect results from the coating of a planar cathode with a thin (100-1000Å) dielectric LB-film. Thus, a microscopically localised field-induced electron emission phenomenon is stimulated at fields which are typically an order of magnitude below that required to obtain emission from an equivalent uncoated electrode. The initial switch-on process for the LB-coated cathodes, which typically occurs in the field range 10-20MVm^{-1}, is subsequently found to give rise to a stable distribution of ~10-30 sites cm^{-2} which are permanently "formed" on the cathode, even after prolonged periods (≥200 hours) of exposure to atmosphere. Following an initial hysteresis behaviour, the cathodes are found to

exhibit a reversible, high-β, I-V characteristic, where average site currents as high as 10μA are obtainable at fields of ≤10MVm^{-1}. Complementary electron spectroscopy measurements have revealed that the emission process is characteristic of "conducting filaments" having been formed within a dielectric medium, i.e. where individual sites display both field dependent shifts of ≥1eV below the Fermi level of the metallic substrate and broad energy distributions of ≥0.5eV. Significantly, these measurements have also revealed a hitherto unobserved "oscillatory" behaviour associated with the above field dependencies.

The study of field-induced electron emission from the LB-coated cathodes reported in this thesis has been found to show significant similarities to the switch-on and I-V characteristics of MIM devices using a similar LB multilayer insulating medium. However, in contrast to the MIM study, which implicated a metallic conduction process, it is not fully understood at this stage whether the conducting filaments which promote the LB-film emission phenomenon are metallic or non-metallic in nature. By assuming that the filaments are formed within an idealised planar metal-LB film structure, it found to be necessary, from the spectral shift data of section 6.3.4, to assume a field enhancement of ~10 times within the dielectric film, i.e. at the location of an emission site. From this evidence, it has been shown how the field enhancement, and hence the filamentary emission mechanism, could be influenced by, for example, the enhancement factors associated with particulate contamination, induced charging in either the bulk or interface regions of an emitting channel, or alternatively, the formation of electromigrated metallic filaments.

Whilst the physical basis of the emission mechanism remains unclear, it is apparent that, from the viewpoint of high voltage insulation, thin (≤1000Å) dielectric coatings have the degrading effect of lowering the applied field threshold for the onset of significant emission, or leakage, currents across a HV electrode gap. However, since it is well established that thick (≥1μm) dielectric coatings have the opposite effect of suppressing electron emission processes, i.e. a procedure that has been exploited by high-voltage engineers [37,38], it is suggested that a future investigation into the LB-

coated electrodes should include a wider range of film thicknesses (possibly 100Å to a few microns) to determine the thicknesses over which a "transition" occurs from the emission "enhancing" to the "suppressing" effects of surface coatings. From an alternative viewpoint, the LB-cathode coating technique has been shown to give rise to very stable, high-current emission sources which are relatively insensitive to poor vacuum conditions. However, in order to fulfil this potential in, for example, single, high-brightness cold-cathode emitters, or multiemitter array cathodes etc, it is apparent that techniques must be developed which enable emission sites to be "written" at a particular, pre-programmed location in the dielectric coating. It follows that if the assumptions of the sub-micron particle contamination or charge-induced emission mechanisms are correct, then an appropriate "doping" technique based on these parameters may be achieved with some degree of control. The accomplishment of this latter proposal remains an on-going objective of the present study.

7.4 Technological Overview

In this final section, we will briefly highlight some general properties of the above cold-cathode regimes, and offer some further remarks on the technological implications of the present findings. Table 7.1 collates a number of characteristics obtained for the uncoated, C-composite and LB-coated cathodes described respectively in chapters 4, 5 and 6. As a general observation, it will be seen that although the C-composite emitters have been shown to offer a desirable high-current characteristic, it appears that the inherent instability of this regime ultimately limits its present use in devices which require a cold-cathode electron source. In contrast, the LB-coated cathodes show every promise of achieving the required stability for these applications, although future objectives should include the development of a technique to control the spatial location of sites on these cathodes, i.e. as can be achieved with the composite-coated emitters.

	Uncoated Cu-cathode	C-composite cathode	LB-cathode cathode
Emission site density (E_g=20MVm^{-1})	typically ≤5cm^{-2}	≥50cm^{-2}	10-20cm^{-2}
Average site currents (E_g=15MVm^{-1})	≥1μA	≥10μA	≥5μA
Current stability (I_g=100μA)	5%	10-20%	≤2%
Site distributions	Relatively stable	Unstable	Very stable
Effect of He-conditioning (10kV)	Order of magnitude reduction in current	No effect	No effect

Table 7.1 Some general characteristics of the three cathode-types considered in this thesis.

Whilst the "resistance" of the composite and LB-coated cathodes to gas conditioning is a significant attribute as far as cold-cathode operation under poor-vacuum (≥10^{-5}mbar) conditions is concerned, it should be noted, however, that this may have a detrimental effect in HV systems which employ dielectric-coated electrodes. Thus, although dielectric coatings have been used to suppress electron emission processes on HV electrodes [37,38,177], it follows that if sites are switched-on during operation of a coated HV device, then gas conditioning may be ineffective as a back-up procedure for regaining the insulating capability of the system; this would necessitate the costly and time consuming procedure of replacing the rogue electrode.

Finally, as a "rule of thumb" guide to the effects of dielectric-coatings and particulate contamination on planar metallic electrodes, Figure 7.1 compares, schematically, the levels of prebreakdown emission that are likely to result from various combinations of conducting and insulating materials on a cathode surface. In the context of high-voltage insulation, it is clear that the shift from the uncoated characteristic, i.e. a shift to the left in this figure, indicates the level of risk induced by

the presence of these structures on HV electrode surfaces. As discussed in chapter 6, it is also important to note that thin (≤1000Å) dielectric-coatings are likely to degrade the insulating capabilities of HV electrodes, i.e. in contrast to the improvements in voltage hold-off capability obtained using thicker surface coatings [37,38,177].

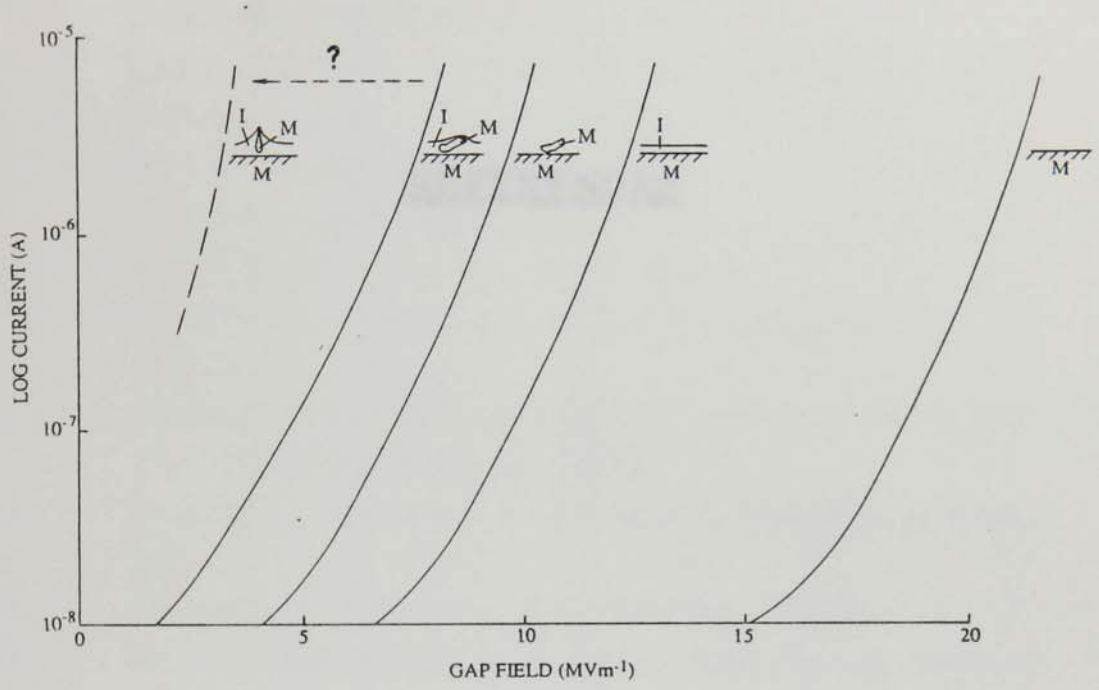

Figure 7.1 A schematic of the relative effects of dielectric surface coatings and/or particulate contamination on the emission characteristics of a metallic electrode. M-metal, I-insulator.

REFERENCES

1. Fowler, R. H. and Nordheim, L., Proc. Roy. Soc. A119, 173-81, 1928.
2. Swanson, L. W., Strayer, R. W. and Charbonnier, F. M., Surface Sci., 2, 177-82, 1964.
3. Latham, R. V., "High Voltage Vacuum Insulation: The Physical Basis", London/New York, Academic Press, 1981.
4. Hurley, R. E., J. Phys. D: Appl. Phys. 12, 2229-45, 1979.
5. Hurley, R. E., J. Phys. D: Appl. Phys. 12, 2247-52, 1979.
6. Halbritter, J., Appl. Phys. A39, 49-57, 1986.
7. Halbritter, J., IEEE Trans. EI-18, 204, 1983.
8. Latham, R. V. , Vacuum 32, 137-40, 1982.
9. Bayliss, K. H. and Latham, R. V., Proc. Roy. Soc., A403, 285-311, 1986.
10. Athwal, C. S., Bayliss, K. H., Calder, R. S. and Latham, R. V., IEEE Trans. Plasma Sci., PS-13, 226-9, 1985.
11. Latham, R. V. and Mousa, M. S., J. Phys. D: Appl. Phys. 19, 699-713, 1986.
12. Mousa, M. S., Ph.D. Thesis, Aston University, UK, 1984.
13. Xu, N. S. and Latham, R. V.., J. Phys. D: Appl. Phys. 19, 477-82, 1986.
14. Bajic, S. and Latham, R. V., J. Phys. D: Appl. Phys. 21, 200-4, 1988.
15. Spindt, C. A., Holland, C. E. and Stowell, R. D., Applications of Surface Sci., 16, 268-76, 1983.
16. Forman, R., Applications of Surface Sci., 16, 277-91, 1983.
17. Holland, C. E., Spindt , C. A. Brodie, I., Mooney, J. B. and Westerberg, E. R., "Spindt Cold--Cathode Vacuum Flourescent Display", (SRI International, USA), EuroDisplay '87, London, September 1987.
18. Gray, H. F., Campisi, G. J. and Greene, R. F., Proc. IEDM 86, 776-9, 1986.
19. Mead, C. A., Proc. I.R.E., 48, 359, 1960.
20. Biedermann, H., Vacuum, 26, 513-23, 1976.
21. Yankelevitch, Yu. B., Vacuum, 30, 97-107, 1979.
22. Baker, F. S., Osborn, A. R. and Williams, J., Nature, 239, 96-7, 1972.
23. Erikson, G. F. and Mace, P. N., Rev. Sci. Instrum., 54, 586-90, 1983.

24. Latham, R. V. and Salim, M. A., J. Phys. E: Sci. Instrum., 20, 181-188, 1987.
25. Chatterton, P. A., Proc. Phys. Soc. (London), 88, 231-45, 1966.
26. Bloess, D., Proc. 2nd Workshop on RF Superconductivity, Geneva (Switzerland), pp. 409-426, July 1984.
27. Lyman, E. M., Lee, D. A., Tomaschke, H. E. and Alpert, D., Proc. II - DEIV, 33-9, 1966.
28. Alpert, D., Lee, D. A., Lyman, E. M. and Tomaschke, H. E., J. Appl. Phys., 38, 880-1, 1967.
29. Ettinger, S. Y. and Lyman, E. M., Proc. III-DEIV, 128-33, 1968.
30. Beukema, G. P., J. Phys. D: Appl. Phys., 7, 1740-55, 1974.
31. Beukema, G. P., Physica C, 61, 259-74, 1972.
32. Maitland, A., Brit. J. Appl. Phys., 13, 122-5, 1962.
33. Steib, G. F. and Moll, E., J. Phys. D: Appl. Phys., 6, 243-55, 1973.
34. Hackman, R. and Govindra Raju, G. P., J. Appl. Phys., 45, 4784-94, 1974.
35. Miller, H. C. and Farrall, G. A., J. Appl. Phys., 36, 1338-44, 1965.
36. Cox, B. M., J. Phys. D: Appl. Phys., 7, 143-51, 1974.
37. Rohrbach, F., Proc. I - IHVV, 393-429, 1964.
38. Germain, C., Jeannerot, L., Rohrbach, F., Simon, D. and Tinquely, R., Proc. II - IHVV, 279-91, 1966.
39. Schottky, W., Z. Physik., 14, 63, 1923.
40. Good, R. H. and Muller, E. W., In "Handbuch der Physik" (Springer-Verlag, Berlin), 21, 176-231, 1956.
41. Van Oostrom, A. G. J., Philips Research Reports, Suppl. No. 1, 1966.
42. Bohm, D., "Quantum Theory", p. 264, Prentice-Hall, New Jersey, 1951.
43. Haefer, R., Z. Physik., 116, 604-22, 1940.
44. Dyke, W. P., Proc. IRE, 43, 162, 1955.
45. Henderson, J. E. and Badgley, R. E., Phys. Rev., 38, 590, 1931.
46. Muller, E. W., Z. Physik., 102, 734-61, 1936.
47. Young, R. D. and Muller, E. W., Phys. Rev., 113, 115-20, 1959.
48. Young, R. D., Phys. Rev., 113, 110-14, 1959.
49. Gadzuk, J. W. and Plummer, E. W., Rev. Mod. Phys., 45, 487-548, 1973.
50. Ermrich, W., Philips Research Report, 20, 94, 1965.
51. Duke, C. B. and Alferieff, M. E., J. Chem. Phys., 46, 923, 1967.

52. Merzebacher, E., "Quantum Mechanics", Wiley, New York, 121-30, 1961.
53. Modinos, A., "Field, Thermionic and Secondary Electron Emission Spectroscopy", Plenum Press, 1983.
54. Noer, R. J., Appl. Phȳs., A28, 1, 1982.
55. Cox, B. M., CEGB Laboratory Note R/M/N, 1021, 1979.
56. Hurley, R. E., J. Phys., D: Appl. Phys., 13, 1121-8, 1980.
57. Athwal, C. S. and Latham, R. V., J. Phys. D: Appl. Phys., 17, 1029-34, 1984.
58. Cox, B. M., J. Phys. D: Appl. Phys., 8, 2065-73, 1975.
59. Hurley, R. E., J. Phys., D: Appl. Phys., 12, 2247-52, 1979.
60. Athwal, C. S. and Latham, R. V., Physica, 104C, 46-9, 1981.
61. Niedermann, Ph., Sankarraman, N., Noer, R. J. and Fischer, O., J. Appl. Phys., 59, 892-905, 1986.
62. Niedermann, Ph., Ph.D. Thesis, Geneva University, Switzerland, 1986.
63. Allen, N. K., Cox, B. M. and Latham, R. V., J. Phys. D: Appl. Phys., 12, 969-77, 1979.
64. Hurley, R. E. and Dooley, P. J., J. Phys. D: Appl. Phys., 10, L195-201, 1977.
65. Hurley, R. E. and Dooley, P. J., Vacuum, 28, 147-149, 1978.
66. Klyarfell, B. N. and Pokrovskaya-Soboleva, A. S., Sov. Phys. 15, 149-52, 1970.
67. Alfrey, G. F. and Taylor, J. B., Brit. J. Appl. Phys., 6, Suppl. 4, S44-9, 1955.
68. Hurley, R. E., J. Phys. D: Appl. Phys., 12, 2229-45, 1979.
69. Fielding, T. J., Ph.D. Thesis, Aston University, UK, 1986.
70. Braun, E., Forbes, R. G., Pearson, J., Pelmore, J. M. and Latham, R. V., J. Phys. E: Sci. Instrum., 11, 222-8, 1978.
71. Allen, N. K., Ph.D. Thesis, Aston University, UK, 1979.
72. Allen, N. K., Athwal, C. S. and Latham, R. V., Vacuum, 32, 325-32, 1982.
73. Allen, N. K. and Latham, R. V., J. Phys. D: Appl. Phys., 11, L55-57, 1978.
74. Athwal, C. S. and Latham, R. V., Physica, 104C, 189-95, 1981.
75. Bayliss, K. H. and Latham, R. V., Vacuum, 35, 211-7, 1985.
76. Ovshinsky, S. R., Phys. Rev. Lett., 21, 1450-3, 1968.

77. Dearnaley, G., Stoneham, A. M. and Morgan, D. V., Rep. Prog. Phys., 33, 1129-91, 1970.
78. Adler, D., Henisch, H. K. and Mott, N. F., Rev. Mod. Phys., 50, 209-20, 1978.
79. Dearnaley, G., Thin Solid Films, 3, 161-174, 1969.
80. Hickmott, T. W., J. Appl. Phys., 37, 4380-8,. 1966.
81. Halbritter, J., Appl. Phys., A39, 49-57, 1986.
82. Fischetti, M. V., DiMaria, D. J., Brorson S. D., Theis, T. N. and Kirtley, J. R., Phys. Rev. B, 311, 8124-42, 1985.
83. Athwal, C. S., Ph.D. Thesis, Aston University, UK, 1981.
84. Latham, R. V., Vacuum, 32, 137-40, 1982.
85. Halbritter, J., IEEE Trans. EI-18, 204, 1983.
86. Bayliss, K. H., Ph.D. Thesis, Aston University, UK, 1984.
87. Mott, N. F., Phil. Mag., 32, 159-71, 1975.
88. Murphy, E. L. and Good, R. H., Phys. Rev., 102, 1464-73, 1956.
89. Simmons, J. G., Phys. Rev., 155, 657-62, 1967.
90. Simmons, J. G., Phys. Rev., 166, 912-20, 1968.
91. Simmons, J. G., J. Phys. D: Appl. Phys., 4, 613-57, 1971.
92. Mott, N. F. and Davies, E. A., "Electronic Processes in Non-Crystalline Materials", Clarendon Press, Oxford, 1979.
93. Simmons, J. G., Verderber, R. R., Lytollis, J. and Lomax, R., Phys. Rev. Lett., 17, 675-77, 1966.
94. Xu, N. S. and Latham, R. V., J. de Physique, 47, 67-72, 1986.
95. Xu, N. S. and Latham, R. V., J. de Physique, 47, 95-9, 1986.
96. Xu, N. S. , Ph.D. Thesis, Aston University, UK, 1986.
97. Muller, E. W., Z. Physik, 106, 541-550, 1937.
98. Swanson, L. W. and Crouser, L. C., J. Appl. Phys., 40, 4741-9, 1969.
99. Skellet, A. M., Firth, B. G. and Mayer, D. W., Proc. IRE, 47, 1704, 1959.
100. Nosov, A. A., Nosova, D. I., Ovsyannikov, N. P. and Chadayev, N. N., Sov. J. Commun. Technol. Electron., 31, 220-1, 1988.
101. Feist, W. M., Advances in Electronics and Electron Phys., Suppl. 4, Academic Press, New York, p. 1-59, 1968.
102. Rivlin, V. G., Stewart, D. and Wilson, P. D., Interim Sci. Report AFOSR-77-3292, 1979.

103. Gray, H. F., Ardis, L. and Campisi, G. J., Rev. Sci. Instrum., 58, 301-4, 1987.
104. Spindt, C. A., Brodie, I., Humphrey, L. and Westerberg, E. R., J. Appl. Phys., 47, 5248, 1976.
105. Baker, F. S., Osborn, A. R. and Williams, J., J. Phys. D: Appl. Phys., 7, 2105-15, 1974.
106. Lea, C., J. Phys. D: Appl. Phys., 6, 1105-14, 1973.
107. English, T. H., Lea, C. and Lilburne, M. T., Scanning Electron Microscopy: Systems and Applications (Inst. Phys. Conf. Ser. 18, pp. 12-14), 1973.
108. Hosoki, S., Yamamoto, S., Futamoto, M. and Fukuhara, S., Surface Sci., 86, 723-33, 1979.
109. Yamamoto, S., Hosoki, S., Fukuhara, S. and Futamoto, M., Surface Sci., 86, 734-42, 1979.
110. Latham, R. V. and Wilson, D. A., J. Phys. D: Appl. Phys., 14, 2139-45, 1981.
111. Latham, R. V. and Wilson, D. A., J. Phys. D: Appl. Phys., 16, 455-63, 1983.
112. Barnet, F. R. and Norr, M. K., Composites, 7, 93-9, 1976.
113. Latham, R. V. and Wilson, D. A., J. Phys. E: Sci. Instrum., 15, 1083-92, 1982.
114. Gomer, R., "Field Emission and Field Ionisation", (Oxford: OUP), 1961.
115. Mousa, M. S. and Latham, R. V., J. de Physique, 47, 139-44, 1986.
116. Mousa, M. S., Vacuum, 38, 835-8, 1988.
117. Stratton R., Phys. Chem. Solids, 23, 117, 1962.
118. Simmons, J. G., J. Appl. Phys., 34, 1793 and 3581, 1963.
119. Mead, C. A., J. Appl. Phys., 32, 646-52, 1961.
120. Chopra, K. L., "Thin Film Phenomena", McGraw-Hill Inc., pp. 508-14, 1969.
121. Kanter, H. and Feibelman, W. A., J. Appl. Phys., 33, 3580, 1962.
122. Savoye, E. D. and Anderson, D. E., J. Appl. Phys., 38, 3245, 1967.
123. Eckertova, L., J. Vac. Sci. Technol., 6, 508-18, 1969.
124. Hickmott, T. W., J. Appl. Phys., 33, 2669, 1962.
125. Hickmott, T. W., J. Appl. Phys., 35, 2118 and 2679, 1964.
126. Hickmott, T. W., Thin Sol. Films, 9, 431, 1972.

127. Emmer, L., Thin Solid Films, 20, 43-52, 1974.
128. Biederman, H., Thin Solid Films, 18, 127, 1971.
129. Hickmott, T. W., J. Appl. Phys., 36, 1885, 1965.
130. Gould, R. D., Hogarth, C. A. and Collins, R. A., J. Non-Cryst. Solids, 12, 131, 1973.
131. Biederman, H., Phys. Status Solidi (a), 36, 783, 1976.
132. Simmons, J. G. and Verderber, R. R., Proc. Roy. Soc., A301, 77, 1967.
133. DiMaria, D. J., in "Insulating Films on Semiconductors", edited by M. Schulz and G. Pensl, (Springer, Berlin), pp. 88-103, 1981.
134. DiMaria, D. J. and Dong, D. W., J. Appl. Phys., 51, 2722-35, 1980.
135. DiMaria, D. J., Theis, T. N., Kirtley, J. R., Pesavento, F. L., Dong, D. W. and Brorson, S. D., J. Appl. Phys., 57, 1214-38, 1985.
136. Fischetti, M. V., DiMaria, D. J., Brorson, S. D., Theis, T. N. and Kirtley, J. R., Phys. Rev. B, 31, 8124-42, 1985.
137. Brorson, S. D., DiMaria, D. J., Fischetti, M. V., Pesavento, F. L., Solomon, P. M. and Dong, D. W., J. Appl. Phys., 58, 1302-13, 1985.
138. Hamasaki, M., Adachi, T., Wakayama, S. and Kikuchi, M., J. Appl. Phys., 49, 3987, 1978.
139. Abeles, B., Sheng, P., Couths, M. D. and Arie, Y., Advances in Physics, 24, 407, 1975.
140. Pfeilsticker, R., Kalbitzer, S. and Muller, G., Nuclear Instrum. and Methods, 182/183, 603-8, 1981.
141. Brander, R. W. and Todkill, A., Materials Research Bull., 4, S303-10, 1969.
142. Brander, R. W., 3rd Int. Conf. Silicon Carbide, pp. 584-592, 1973.
143. Schade, H., Nelson, H. and Kressel, H., Appl. Phys. Lett., 20, 385, 1972.
144. Wolff, P. A., Phys. Rev., 95, 1415, 1954.
145. Hodgkinson, R. J., Solid-State Electron., 5, 269, 1962.
146. Choyke, W. J. and Patrik, L. A., US Patent No. 3,105,166.
147. Bell, R. L., "Negative Electron Affinity Devices", Clarendon Press, Oxford, 1973.
148. Swanson, L. W. and Strayer, R. W., J. Chem. Phys., 48, 2421, 1968.
149. Sommer, A. H., "Photoemissive Materials", Wiley and Sons, New York, 1968.
150. Tuck, R. A., Vacuum, 33, 715, 1983.

151. Woratschek, B., Ertl, G., Kuppers, J., Sesselmann, W. and Haberland, H., Phys. Rev. Lett., 57, 1484-7, 1986.

152. Norman, D., Tuck, R. A., Skinner, H. B., Wadsworth, P. J., Gardiner, T. M., Owen, I. W., Richardson, C. H. and Thornton, G., Phys. Rev. Lett., 58, 519-22, 1987.

153. Kohn, E. S., Appl. Phys. Lett., 18, 272, 1971.

154. Bischopf, M. and Pagnia, H., Thin Solid Films, 29, 303, 1975.

155. Blessing, R. and Pagnia, H., Phys. Stat. Sol. B, 110, 537, 1982.

156. Araki, H. and Hanawa, T., Thin Solid Films, 121, 17-27, 1984.

157. Araki, H. and Hanawa, T., Vacuum, 38, 31-5, 1988.

158. Brand, F. A. and Jacobs, H., Phys. Rev., 97, 81, 1955.

159. Johannes, R., Ramanathan, K, Cholet, P. and Haas, W., Proc. IEEE Trans., ED-10, 258, 1963.

160. Kenward, M., New Scientist, No. 1559, pp. 46-51, May 1987.

161. Young, R. W., Vacuum, 24, 167-72, 1973.

162. Latham, R. V., Bayliss, K. H. and Cox, B. M., J. Phys. D: Appl. Phys., 19, 219-31, 1986.

163. Kuyatt, C. E. and Plummer, E. W., Rev. Sci. Instrum., 43, 108-11, 1972.

164. Young, R. D., Phys. Rev., 113, 110-4, 1959.

165. Young, R. D. and Kuyatt, C. E., Rev. Sci. Instrum., 39, 1477-80, 1968.

166. Schwab, A. J. "High Voltage Measurement Techniques", Chapter 2, MIT Press, Cambridge, Mass., 1972.

167. Johnson, R. H., J. Inst. Elect. Engrs., IIIA, 93, 1043, 1946.

168. Craggs, J. D. and Meek, J. M., "High Voltage Laboratory Technique", Butterworths, London, p. 205, 1954.

169. Bloomer, R. N. and Cox, B. M., Vacuum, 18, 379-82, 1968.

170. Cox, B. M. and Bloomer, R. N., CEGB Report No. RD/M/R91, 1968.

171. Bajic, S. and Latham, R. V., IEEE Trans, EI-23, 27-32, 1988.

172. Bajic, S. and Latham, R. V., J. Phys. D: Appl. Phys., 21, 943-50, 1988.

173. Bajic, S., Abbot, A. M. and Latham, R. V., Proc. XIII DEIV, pp. 8-12, 1988.

174. Bernard, P., Cavallari, G., Chiaveri, E., Haebel, E., Lengeler, H., Padamsee, H., Picciarelli, V., Proch, D., Schwettman, A., Tuckmantel, J., Weingarten, W. and Piel, H., Nuc. Instrum. and Methods, 206, 47-56, 1983.

175. Padamsee, H., Hartung, W., Noer, R., Rees, C. and Shu, Q. S., Proc. 3rd Workshop on RF Superconductivity, New York (USA), July 1986.

176. Sze, S. M., "Semiconductor Devices: Physics and Technology", John Wiley and Sons, 1985.

177. Jedynak, L., J. Appl. Phys., 35, 1727, 1964.

178. Smith, B., "Ion Implantation Range Data for Silicon and Germanium Device Technologies", Learned Information Limited, Oxford/New York, 1977.

179. Townsend, P. D., Kelly, J. C., Hartley, N. E. W., "Ion Implantation, Sputtering and their Applications", Academic Press, 1976.

180. Kaye, G. W. C. and Laby, T. H., "Tables of Physical and Chemical Constants", 14th Edition, (Longman, London), 1973.

181. Smith, R., J. Phys. D: Appl. Phys., 17, 1045-53, 1984.

182. Schiott, H. E., Rad. Eff., 6, 107, 1970.

183. Saitou, N., Surface Sci., 66, 346-56, 1977.

184. DiMaria, D. J., in "Physics of SiO_2 and its Interface", Pergamon, New York, pp. 160-78, 1978.

185. Drechsler, M., Proc. Int. Symp. on Discharges in Vacuum, Supplement, Poznan, Poland, 1972.

186. Cavaille, J. Y. and Drechsler, M., Surface Sci., 75, 342-54, 1978.

187. Calder, R. S., Dominichini, G. and Hilleret, N., Proc. XIII DEIV, 495-7, 1988.

188. Ghani, A., Ph.D. Thesis, University of London, UK, 1971.

189. Swann, D. J. and Smith, K. C. A., Proc. 6th Ann. Scanning Electron Microscope Symp., Pt. 1, pp. 44-56, 1973.

190. Mills, K., Davies, J. R., Destefani, J. D., Dieterich, D. A., Crankovich, G. M. and Frisell, H. J., (ed)., "Metals Handbook", Vol. 9, 9th Edition, (Ohio: American Society for Metals), 1985.

191. Bajic, S., "The Development of a New-Generation Cold-Cathode", Aston University Internal Report, 1986.

192. Latham, R. V., Proc. 2nd Workshop on RF Superconductivity, CERN (Geneva), pp. 533-550, 1984.

193. Klein, N., Adv. Phys., 21, 605-45, 1972.

194. Richards, B. P. and Footner, P. K., GEC J. Res., 2, 157, 1984.

195. Couch, N. R., Movaghar, B. and Girling, I. R., Solid State Commun., 59, 7, 1986.
196. Couch, N. R., Montgomery, C. M. and Jones, R., Thin Solid Films, 135, 173, 1986.
197. Cade, N. A., Cross, G. H., Lee, R. A., Bajic, S. and Latham, R. V., J. Phys. D: Appl. Phys., 21, 148-53, 1988.
198. Xu, N. S. and Latham, R. V., J. de Physique, 47, 73-7, 1986.
199. Roddy, D., "Microwave Technology", Reston, Va. Reston Pub. Co., 1986.
200. Kuroda, K., Hosoki, S. and Komoda, T., Scanning Microscopy, 1, 911-7, 1987.
201. Peterson, I. R. and Girling, I. R., Sci. Prog. Oxf., 69, 533-50, 1985.
202. Barnes, W. L. and Sambles, J. R., Thin Solid Films, 143, 237, 1986.
203. Veale, G., Girling, I. R. and Peterson, I. R., Thin Solid Films, 127, 293, 1985.
204. Long Range Group, GEC Hirst Research Centre, East Lane, Wembley, Middlesex, HA9 7PP, UK.
205. Peterson, I. R., Thin Solid Films, 116, 357, 1984.
206. Less, K. J. and Wilson, E. G., J. Phys. C: Solid State Phys., 6, 3110, 1973.
207. Hibbert, D. B. and Goodman, A., Int. J. Electron, 59, 701, 1985.
208. Tagawa, M., Takenobu, S., Ohmae, N. and Umeno, M., Appl. Phys. Lett., 53, 626-7, 1988.
209. Ridley, B. K., "Quantum Theory of Semiconductors", Clarendon Press, Oxford, 1982.
210. Solymar, L. and Walsh, D., "Lectures on the Electrical Properties of Materials", Oxford University Press, 1984.

APPENDICES